

UNIVERSITÀ DEGLI STUDI DI PADOVA
DIPARTIMENTO DI FISICA E ASTRONOMIA “GALILEO GALILEI”

Corso di Dottorato in Astronomia – Ciclo XXXVII

Studying galaxy evolution through strong gravitational lensing

COORDINATORE: Ch.mo Prof. Giovanni Carraro

SUPERVISORE: Dr. Anita Zanella

Co-SUPERVISORE: Prof. Claudio Grillo

Co-SUPERVISORE: Dr. Joël Vernet

DOTTORANDO:
Andrea Bolamperti

Anno Accademico 2023/2024

The work that led to the results presented in this thesis was supported by
the University of Padova, the Istituto Nazionale di Astrofisica (INAF),
and the European Southern Observatory (ESO, Garching bei München, Germany).

Contents

Contents	I
List of Figures	V
List of Tables	IX
List of publications	XI
List of Publications	XI
Summary	XI
1 Introduction	1
1.1 Brief history of gravitational lensing	2
1.2 Strong lensing modeling	4
1.3 Magnified compact and faint sources at high- z	8
1.4 An overview on spectropolarimetry	11
1.5 Thesis aims and structure	17
2 An introduction to strong gravitational lensing formalism	21
2.1 The lens equation	22
2.2 Magnification, critical curves and caustics	24
2.3 Time delays	26
2.4 Multi-plane formalism	27
3 Studying the most massive early-type galaxies acting as strong gravitational lenses at intermediate redshift	29
3.1 Introduction	29
3.2 Observations and data reduction	31
3.2.1 HST imaging	31
3.2.2 NOT imaging	31
3.2.3 VLT/X-Shooter spectroscopy	32
3.3 The SDSS J0100+1818 deflector	33
3.3.1 Stellar mass	34
3.3.2 Luminosity profile	35
3.3.3 Stellar kinematics	37
3.3.4 Environment	37
3.4 Point-like source modeling	37

3.4.1	Modeling with A and B	39
3.4.2	Modeling with A, B, and C	40
3.4.3	Total mass profile of the deflector	45
3.5	Extended source modeling	45
3.5.1	Modeling the deflector and the arcs	47
3.5.2	Total mass profiles of the deflector	49
3.5.3	Source SB reconstruction	49
3.6	Discussion and summary	55
4	Cosmography from accurate mass modeling of the lens group SDSS J0100+1818: five sources at three different redshifts	61
4.1	Introduction	61
4.2	Observations and data reduction	63
4.2.1	Ancillary data	63
4.2.2	Integral field spectroscopy observations with VLT/MUSE	64
4.3	The SDSS J0100+1818 system	65
4.3.1	Multiple images of A and B	65
4.3.2	Multiple images of C	65
4.3.3	Multiple images of E and F	68
4.3.4	Discussion on system D	68
4.3.5	Group members	69
4.3.6	Velocity dispersion profile	70
4.4	Lensing modeling	70
4.4.1	Inclusion of group members	72
4.4.2	Dark matter halo	73
4.4.3	Mass models and results	74
4.4.4	Mass profiles of the deflectors	75
4.5	Strong lensing models with variable cosmology	78
4.5.1	Multi-plane approach	79
4.6	Discussion	82
4.6.1	An enhanced model for SDSS J0100+1818	82
4.6.2	SDSS J0100+1818 as a fossil system	84
4.6.3	The values of Ω_m and w from multi-plane strong lensing systems	84
4.7	Summary and conclusions	85
5	UV-continuum β slopes of individual $z \sim 2 - 6$ clumps and their evolution	89
5.1	Introduction	89
5.2	Sample selection and ancillary data	91
5.2.1	<i>HST</i> data	91
5.2.2	VLT/MUSE data	91
5.2.3	Lensing model	92
5.2.4	Clumps identification	92
5.2.5	Sample	94
5.3	Photometric β slopes	94
5.3.1	Photometric measurements	94
5.3.2	Photometric β slopes	95
5.3.3	Robustness of the photometric and β slopes measurements	97
5.3.4	β slopes measurements	99

5.3.5	Uncertainty estimates on β	99
5.3.6	Comparison with ASTRODEEP	100
5.4	Spectroscopic β slopes	100
5.4.1	Comparison with photometric β slopes	101
5.5	Results and discussion	102
5.5.1	Comparison with galaxy-integrated β slopes	102
5.5.2	Trends with M_{UV} and redshift	102
5.5.3	Extremely blue β slopes	104
5.5.4	Caveats	109
5.6	Summary and conclusions	109
6	Constraining the geometry of the gas surrounding a typical galaxy at $z = 3.4$ with Lyα polarization	111
6.1	Introduction	111
6.2	Data	113
6.2.1	Our target galaxy and its ancillary data	113
6.2.2	FORS2 PMOS observations and data reduction	115
6.3	Analysis	117
6.3.1	Intensity spectrum of Abell 2895a and dilution correction	117
6.3.2	The reduced Stokes parameters q , u , and P spectra and variance spectra	117
6.4	Radiative transfer models for Ly α	119
6.4.1	Ly α spectrum in the wind model	121
6.4.2	Polarization of Ly α in the wind model	122
6.4.3	Comparing observations and models	123
6.5	Discussion	124
6.5.1	Origin mechanisms of the Ly α	124
6.5.2	Spatially resolved observations and future perspectives	127
6.5.3	Polarization of other resonant lines	127
6.6	Summary and conclusions	128
7	Conclusions and future prospects	131
Acknowledgements		135
Bibliography		137
A Appendix of “Studying the most massive early-type galaxies acting as strong gravitational lenses at intermediate redshift”		157
A.1	Spectra of the multiple images	157
A.2	Spectrum of the main deflector	157
B Appendix of “UV-continuum β slopes of individual $z \sim 2 - 6$ clumps and their evolution”		159
B.1	Location of the mock clumps in the simulation	159
B.2	Comparison with ASTRODEEP	159
B.3	Comparison between photometric and spectroscopic β slopes	159
C Appendix of “Constraining the geometry of the gas surrounding a typical galaxy at $z = 3.4$ with Lyα polarization”		163

C.1 Ly α polarization measured in the three-bin case	163
---	-----

List of Figures

1.1	Scheme of the deflection of the light coming from a star, observed in an apparent position	1
1.2	The first strongly lensed system observed and examples of an Einstein cross and Einstein ring geometries	4
1.3	Improvement of the strong lensing modeling thanks to the advent of IFU: the example of MACS J0416.1–2403	6
1.4	The maximum physical scale that we can study with and without strong gravitational lensing	9
1.5	Example of clumpy galaxies, differently magnified	10
1.6	Resulting UV-continuum β slope from models for different metallicity, age, and LyC escape values	12
1.7	Scheme and picture of a Wollaston prism	14
1.8	Measurements of Q , U , and P , showing the importance of the two-exposures method	15
2.1	Sketch of a typical gravitational lensing system	22
2.2	Contour levels of the Fermat potential with a fixed source position and increasing surface density of the lens	23
2.3	Illustration of the effects of convergence and shear on a circular source	25
2.4	Compact source moving away from the center of an elliptical lens	26
2.5	Sketch of a multi-plane lensing system	28
3.1	F160W image of the strong lensing system SDSS J0100+1818	32
3.2	Spectral energy distribution fitting of the main lens galaxy of SDSS J0100+1818 .	33
3.3	Photometric modeling of SDSS J0100+1818 with GALFIT	36
3.4	Cumulative stellar mass (M_*) profile of the main lens	36
3.5	Photometric redshift distribution of galaxies around the SDSS J0100+1818 main lens	38
3.6	comparison between the observed and predicted by the strong lensing model multiple images of sources A, B, and C	41
3.7	Probability density distributions of the parameters of the PIEMD+rc and SPEMD models	43
3.8	Probability density distribution of the parameters of the SPEMD model considering the multiple image positions of A and B only and of A, B, and C	44
3.9	Cumulative projected total mass profiles for the PIEMD+rc and SPEMD models obtained by modeling the multiple images of A, B, and C as point-like objects . .	46
3.10	Cumulative projected stellar-over-total mass fraction profiles for the PIEMD+rc and SPEMD models obtained by modeling the multiple images of A, B, and C as point-like objects	46

3.11	Probability density distribution for the SPEMD model with two sources (source AB and source C)	50
3.12	SB results of the extended modeling and source reconstruction with the PIEMD model	51
3.13	As in Fig. 3.12 for the SPEMD model with one source	51
3.14	As in Fig. 3.12 for the SPEMD model and for both AB and C	52
3.15	Cumulative projected total mass profiles for the PIEMD+rc model with point-like and extended source modeling	53
3.16	Cumulative projected stellar-over-total mass fraction profiles for the PIEMD+rc model with point-like and extended source modeling	53
4.1	HST F160W image of the SDSS J0100+1818 strong lensing system with sources AB, C, and EF	63
4.2	Group members and regions used to extract the spectra, within the MUSE field of view	66
4.3	MUSE 1D spectra of the multiple images A1+B1, A2+B2, A3+B3, A4+B4, and stacked	67
4.4	MUSE 1D spectrum of the multiple images C1 and C2 (stacked)	67
4.5	Ly α contours of EF and MUSE 1D spectra of the multiple images E1, E2, E3, E4, and stacked, and F1, F2, F3 and F4, and stacked	68
4.6	Stellar velocity dispersion profile of the main deflector	71
4.7	Cumulative projected total mass profiles for the PIEMD, SPEMD, PIEMD+BGG and SPEMD+BGG models, relative to the total mass, and they are divided into the halo (M_{halo}) and the galaxy member (M_{gal}) components	77
4.8	Cumulative projected stellar-over-total mass fraction profiles for the PIEMD, SPEMD, PIEMD+BGG and SPEMD+BGG	78
4.9	Probability density distributions of the cosmological parameters Ω_m and w in the PIEMD $_{\Omega_m w}$ and SPEMD $_{\Omega_m w}$ models	81
4.10	Marginalized 1D probability density distributions of the cosmological parameters Ω_m and w in the PIEMD $_{\Omega_m}$, SPEMD $_{\Omega_m}$, and MP-PIEMD $_{\Omega_m}$ models, and PIEMD $_{\Omega_m w}$, SPEMD $_{\Omega_m w}$, and MP-PIEMD $_{\Omega_m w}$	83
5.1	RGB image of the HFF cluster MACS J0416 with the position of the clumps in the sample	93
5.2	Properties of the sample of clumps	95
5.3	Scheme of the rest-frame UV coverage of each available HST filter, as a function of the redshift	97
5.4	Difference between the measured and the injected β slopes as a function of the magnitude	98
5.5	Distribution of the measured photometric β slopes as a function of the photometric points used in the fit	99
5.6	Distribution of the measured photometric β slopes for clumps and comparison with galaxy systems	103
5.7	Relation between β and M_{UV} in different redshift bins	104
5.8	β - z relation	105
5.9	Measured magnitudes and the UV-continuum slope for eight selected clumps with $\beta \lesssim 2.7$	106
5.10	UV continuum β slopes as a function of the age and metallicity obtained with the synthetic spectra	108

6.1	HST F606W image of Abell 2895a, with the Ly α contours and FORS2 slit superimpose, and FORS2/PMOS 2D spectra	115
6.2	$I(\lambda)$ spectrum, before and after subtracting $I_{BCG}(\lambda)$, and the measured degree of polarization before and after the dilution correction	118
6.3	Schematic illustration of the assumed wind model in Ly α radiative trasfer modeling	120
6.4	Comparisons between observed and simulated Ly α spectra	120
6.5	The degree of polarization P for models with θ_{LOS} from 0° to 90° , with steps of 10°	121
6.6	Comparison between the observed Abell 2895a Ly α spectrum and polarization, and those from a large variety of models	125
6.7	Representation of the constraint we can put with a joint analysis of the Ly α spectrum and degree of polarization	126
A.1	X-Shooter 1D spectra of the multiple images A1 and B1	157
A.2	X-Shooter 1D spectra of the multiple images A3 and B3	158
A.3	X-Shooter 1D spectra of the multiple images A4 and B4	158
A.4	X-Shooter 1D spectrum of the main lens galaxy	158
B.1	Location of the 50 mock clumps	160
B.2	Comparison between the β slopes measured from the ASTRODEEP collaboration and in this work	161
B.3	Location of the 37 clumps whose spectra have $S/N \gtrsim 2$	161
C.1	$I(\lambda)$ spectrum, before and after subtracting $I_{BCG}(\lambda)$, and the measured degree of polarization before and after the dilution correction, in the three-bins case	164

List of Tables

1.1	Improvement of the strong lensing modeling thanks to the advent of IFU: the example of MACS J0416.1–2403.	5
3.1	Modeling of the deflector total mass distribution using the observed multiple image positions.	42
3.2	Modeling of the deflector total mass distribution using the extended source modeling. .	48
3.3	Angular separation and sizes of the reconstructed sources	55
3.4	Median and 68% confidence level uncertainty values of the parameters of the different models	56
4.1	Right ascension and declination, redshift, and distance in projection from the brightest group galaxy center of the detected multiple images	69
4.2	Results obtained for the deflector total mass distribution from the four adopted models.	76
4.3	Cosmological parameters Ω_m and w from the six adopted strong lensing models with variable cosmology.	80
5.1	Summary of the HST filters used to fit Eq. 5.1 in each redshift interval	96
5.2	Rest-frame UV ten spectral windows used to measure the spectroscopic β slopes and the relative redshift range in which they can be exploited.	101
5.3	The selected eight clumps with robust extremely blue slopes ($\beta \lesssim -2.7$)	106
6.1	Values of the parameters describing the bipolar wind model adopted in our simulations.	123

X

List of Publications

This thesis work is mostly based on the following peer-reviewed first-author papers:

- Bolamperti, A., et al. (2024), “Constraining the geometry of the gas surrounding a typical galaxy at $z = 3.4$ with Ly α polarization”, submitted to A&A in September
- Bolamperti, A., et al. (2024), “Cosmography from accurate mass modeling of the lens group SDSS J0100+1818: five sources at three different redshifts”, accepted for publication in A&A, arXiv:2411.07289
- Bolamperti, A., et al. (2023), “UV-continuum β slopes of individual $z \sim 2 - 6$ clumps and their evolution”, MNRAS, 526, 5263
- Bolamperti, A., et al. (2023), “Reconstructing the extended structure of multiple sources strongly lensed by the ultra-massive elliptical galaxy SDSS J0100+1818”, A&A, 671, A60

and also on the following co-author papers led by collaborators:

- Acebron A., et al. (2024), “The Next Step in Galaxy Cluster Strong Lensing: Modeling the Surface Brightness of Multiply Imaged Sources”, ApJ, 976, 110
- Messa, M., et al. (2024), “Anatomy of a $z = 6$ Lyman- α emitter down to parsec scales: extreme UV slopes, metal-poor regions and possibly leaking star clusters”, arXiv:2407.20331
- Vanzella, E., et al. (2024), “Extreme Ionizing Properties of Metal-Poor, $M_{\text{UV}} \simeq -12$ Star Complex in the first Gyr”, A&A, 691, A251
- Zanella, A., et al. (2024), “Unveiling [C II] clumps in a lensed star-forming galaxy at $z \sim 3.4$ ”, A&A, 685, A80
- Vanzella, E., et al. (2023), “An extremely metal-poor star complex in the reionization era: Approaching Population III stars with JWST”, A&A, 678, A173
- Zanella, A., et al. (2023), “The large molecular gas fraction of post-starburst galaxies at $z > 1$ ”, MNRAS, 524, 923
- Meštrić, U., et al. (2023), “Clues on the presence and segregation of very massive stars in the Sunburst Lyman-continuum cluster at $z = 2.37$ ”, A&A, 673, A50
- Iani, E., et al. (2023), “Scrutiny of a very young, metal-poor star-forming Ly α emitter at $z \approx 3.7$ ”, MNRAS, 518, 5018

Abstract

The path of photons emitted by a distant source is perturbed when passing in proximity of a massive structure (a “lens”, or “deflector”) like a galaxy, a group, or a cluster of galaxies. This effect, called “strong gravitational lensing” makes the source appear brighter, displaced, distorted and, sometimes, multiply imaged.

Nowadays, strong gravitational lensing represents a powerful probe in extragalactic astrophysics, thanks to two main properties. Firstly, the deflection of light rays only depends on the total mass distribution of the deflector (i.e., on its gravitational potential), and on the mutual angular-diameter distances between the source, the deflector, and the observer. Thus, the strong lensing observables - like the positions, the flux ratios, and the time delays between the multiple images - can be exploited to study the total, dark matter, and baryonic mass profiles of the deflectors and the geometry and content of the Universe. Secondly, the magnification effect can significantly boost the flux coming from distant sources, allowing us to study objects that would otherwise be too faint or too small to be resolved with the current instrumentation.

In this thesis, I exploit both these aspects, to achieve three goals: i) measure the total mass profiles of extremely massive early-type galaxies that act as lenses at intermediate redshift, and employ them to measure the values of the cosmological parameters; ii) characterize the stellar population of the star-forming clumps that we observe in high- z , lensed galaxies; and iii) employ the Lyman- α (Ly α) emission from distant galaxies to constrain the geometry of the circumgalactic medium surrounding typical high- z galaxies.

i) In the first part, I study the total and baryonic mass distributions of SDSS J0100+1818, a group-scale system at $z = 0.581$ with five lensed sources, from $z = 1.698$ to 4.95 . The deflector is composed by a central brightest group galaxy (BGG) with a stellar velocity dispersion of $(380.5 \pm 4.4) \text{ km s}^{-1}$, and 18 fainter group members. With a full strong lensing analysis, modeling the sources both as point-like and extended, I accurately measure the total mass profile and infer the stellar over total mass profile of the deflector all over the remarkably wide radial interval where the multiple images are observed, ranging from 15 to 77 kpc from the BGG. They result in a total mass of $(1.55 \pm 0.01) \times 10^{13} M_{\odot}$ within 50 kpc and a stellar over total mass profile decreasing from $45.6_{-8.3}^{+8.7}\%$ at the BGG effective radius to $(6.6 \pm 1.1)\%$ at $R \approx 77$ kpc. Thanks to the spread in redshift of the five background sources, I am able to measure the values of the cosmological parameters, $\Omega_m = 0.14_{-0.09}^{+0.16}$ in a flat Λ cold dark matter (CDM) model, and $\Omega_m = 0.19_{-0.10}^{+0.17}$ and $w = -1.27_{-0.48}^{+0.43}$ in a flat w CDM model. Given the presence of different sources angularly close in projection, I quantify through a multi-plane approach their impact on the inferred values of the cosmological parameters, obtaining consistent median values, with uncertainties for only Ω_m increased by approximately a factor of 1.5.

ii) In the second part, I study the ultraviolet (UV) continuum β slope of a sample of 166 clumps, individual star-forming regions observed in high- z galaxies. They are hosted by 67 galaxies with

redshift between 2 and 6.2, strongly lensed by the Hubble Frontier Fields cluster of galaxies MACS J0416.1–2403. The value of β depends on different physical properties, such as the metallicity, the age of the stellar population, the dust attenuation throughout the galaxy, the stellar initial mass function (IMF), and the star-formation history (SFH). I find a median value of $\beta \sim -2.4$ for the sample of clumps, lower than the typical $\beta \sim -2$ of integrated galaxies in the same redshift range. This result confirms that clumps are sites of intense star formation, populated by young, massive stars, whose spectrum strongly emits in the UV. I find that the β slopes of clumps follow the same relations with the redshift and UV magnitude (M_{UV}) as those of integrated galaxies, extended to much fainter magnitudes ($M_{\text{UV}} < -13$). I also find evidence of eight clumps with extremely blue ($\beta \lesssim -2.7$) slopes, that are not reproducible with standard stellar population models, and require extremely metal-poor or young stellar populations.

iii) In the third part, I exploit the lensing magnification power to understand the origin of the Ly α emission and the circumgalactic medium (CGM) geometry in high- z galaxies, by measuring the polarization of the Ly α emission line of a typical star-forming galaxy at $z \sim 3.4$, that is observationally very demanding. The Ly α emission is the strongest tracer of recombining ionized hydrogen in young, star-forming galaxies, but its origin is still debated. Ly α arises when emitted photons scatter in neutral hydrogen, with each scattering event changing their propagation direction and frequency. The resulting spectrum depends on the neutral hydrogen column density, geometry, kinematics, powering mechanism and on the region from which the photons are emitted. Although different processes produce similar spectra, they have different degrees of polarization, that I can use to discriminate between them and thus to put stringent constraints on the geometry of the galaxy and its CGM where Ly α photons scatter, and on their emission mechanism. I measure a Ly α degree of polarization 1σ upper limit of 4.6%, and I develop Ly α radiative transfer models assuming a biconical outflow geometry to reproduce the observations. I find that they can be explained by assuming the star-forming galaxy being embedded in a CGM with a biconical outflow geometry, with an opening angle of the wind $\theta_{\text{o, Wind}} \sim 30^\circ$ for line-of-sight angles $\theta_{\text{LOS}} \leq 20^\circ$, $\theta_{\text{o, Wind}} \sim 45^\circ$ for $\theta_{\text{LOS}} \leq 20^\circ$, $\theta_{\text{o, Wind}} \sim 60^\circ$ for $\theta_{\text{LOS}} \leq 20^\circ$, and $\theta_{\text{o, Wind}} \sim 75^\circ$ for $\theta_{\text{LOS}} \leq 40^\circ$, where $\theta_{\text{LOS}} = 0^\circ$ means observing in the direction of the outflow.

In this thesis I have employed strong gravitational lensing to investigate three different aspects of galaxy evolution, from the smallest scales of the star-forming clumps in high- z galaxies, through the properties of the gas around them, up to the large scales of group and cluster of galaxies and of the entire Universe. I have tackled some of the most compelling open questions in extragalactic astrophysics, by complementing archival data with new and proprietary observations taken with state-of-the-art instruments mounted on cutting edge facilities, like the Very Large Telescope's (VLT) Multi Unit Spectroscopic Explorer (MUSE), XShooter, and the visual and near UV FOcal Reducer and low dispersion Spectrograph (FORS), the James Webb Space Telescope's (JWST) Near Infrared Camera (NIRCam) and Near-Infrared Spectrograph (NIRSpec), and the Hubble Space Telescope's (HST).

I will advance these studies by i) including the kinematics of the BGG and of the brightest group members, to refine the strong lensing analysis, and further characterizing the background sources, with their morphology and kinematics; ii) enlarging the sample of clumps, including new fields and new infrared observations, and spectroscopically following-up the most promising clumps with extremely blue β slopes, to investigate their stellar populations and put them in the context of the evolution of the first galaxies; and iii) studying the Ly α polarization fraction of extremely magnified and distorted arcs, that would allow us to perform a spatially and spectrally resolved study to conclusively understand the origin of the Ly α emission and the CGM geometry.

Introduction

When photons from a distant source travel across the Universe, their paths are modified by the distribution of matter, so that their source can appear displaced and distorted; this phenomenon is called *gravitational lensing*. There are two main gravitational lensing regimes, namely ‘strong’ and ‘weak’ lensing, that mostly differ for the level of distortion. While the latter originates coherently elongated and tangentially distorted images of the sources ([Tyson et al. 1990](#)), strong lensing is usually due to the most massive bounded structures in the Universe (such as galaxies, groups of galaxies and clusters of galaxies) and generates multiple, and significantly distorted, images. In this thesis, we focus on the strong lensing regime.

This chapter is structured as follows. In Section 1.1, we summarize the historical steps that brought gravitational lensing from being a theoretical speculation to one of the most competitive tools in extragalactic astrophysics. In the following sections, we describe in particular the basics of the three main applications that we used in this thesis: we discuss (i) how we can build strong lensing models from the observables, and how we can use it to learn about galaxy formation and evolution and the geometry of the Universe (Section 1.2), (ii) how strong lensing can help us to delve into the most compact and faint sources in the distant Universe, and allow us to study, in particular, the properties of the star-forming regions in distant galaxies (Section 1.3), and (iii) the basics of spectropolarimetry (Section 1.4), an extremely time-demanding observational technique that needs strong lensing to reach its full potential. Finally, in Section 1.5, we summarize the aims of this thesis, the main questions we address, and describe the structure of this thesis.

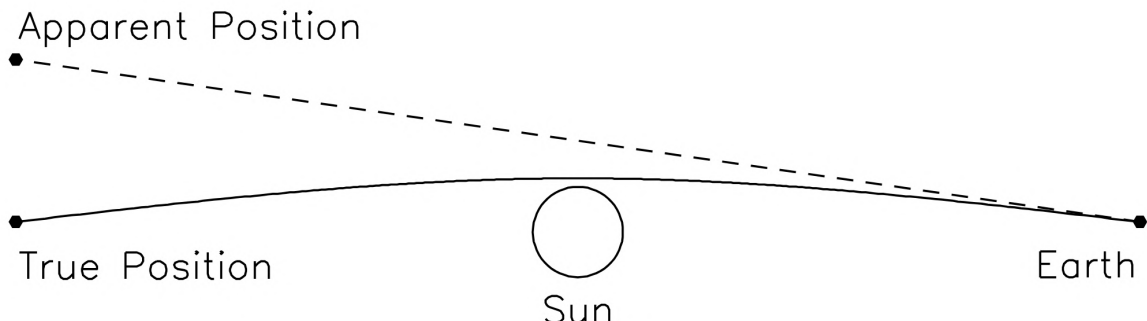


Figure 1.1: The light coming from a star is deflected by the mass of the Sun, that creates an image of the emitting star in an apparent position. From [Narayan & Bartelmann \(1996\)](#).

1.1 Brief history of gravitational lensing

About two centuries ago light was thought to be made of particles, and several physicists speculated that the trajectories followed by such particles could be influenced by the gravitational field in which they travel (Newton 1704). In 1784, in a letter to the English natural philosopher and scientist Henry Cavendish¹, the English natural philosopher and clergyman John Mitchell² calculated, according to the laws of classical mechanics, that light propagating near a spherical mass M would be deflected by an angle (Michell 1784)

$$\hat{\alpha}_N = \frac{2GM}{c^2\xi}, \quad (1.1)$$

where ξ is the impact parameter of the trajectory and G is the gravitational constant. Later, the German physicist, mathematician and astronomer Johann von Soldner³ independently obtained the same result (von Soldner 1804); additionally, he stated that this effect should have been taken into account when observing fixed stars close to the Sun. However, such observations were not possible at that time - hence he concluded this deflection to be negligible (see also Will 1988, for a review).

As these conclusions were reached considering light as composed of massive particles, they lost appeal after the discovery of photons. Only in 1915, after the formulation of the theory of General Relativity by Albert Einstein⁴ (Einstein 1915, 1916, 1917), the trajectory of a light ray in a gravitational field could be studied in a more comprehensive way. After confirming Mitchell and Soldner's results in Einstein (1911), making use of the principle of equivalence, Einstein repeated their calculations and found a difference of a factor of 2,

$$\hat{\alpha}_{GR} = \frac{4GM}{c^2\xi}. \quad (1.2)$$

The total solar eclipse of May 29th, 1919 offered the opportunity to test Einstein's prediction, by measuring the deflection of light caused by the Sun on stars angularly close to its surface. The experiment, lead by the British astronomers Frank Dyson⁵ and Arthur Eddington⁶ was divided in two expeditions, to carry out observations from the West African island of Príncipe and the Brazilian town of Sobral. Thanks to the eclipse, they could observe the bright group of stars of the "Hyades" during daylight (while the sky is normally too bright) and compare their observed and unperturbed positions. They measured a displacement of approximately 1.75'', confirming the prediction obtained applying Einstein's theory of General Relativity (Dyson et al. 1920; Eddington 1919; Dyson et al. 1920; Eddington 1920). Their results were additionally confirmed with new measurements taken during the solar eclipse of September 21th, 1922 in Australia, with a larger sample of approximately 200 (Campbell & Trumpler 1923) and 3000 (Trumpler 1928) deflected stars.

The term *gravitational lens* was used for the first time in 1919 (Lodge 1919). In the following years, Chwolson (1924) theoretically analysed a system with a lens and a source perfectly aligned and found that the source would be imaged as a ring around the lens, later named *Einstein ring*,

¹Henry Cavendish (Nice, 10 October 1731 – London, 24 February 1810)

²John Mitchell (Eakring, 25 December 1724 – Thornhill, 21 April 1793)

³Johann Georg von Soldner (Feuchtwangen, 16 July 1776 – Bogenhausen, 13 May 1833)

⁴Albert Einstein (Ulm, 14 March 1879 – Princeton, 18 April 1955)

⁵Sir Frank Watson Dyson (Measham, 8 January 1868 – At sea, 25 May 1939)

⁶Sir Arthur Stanley Eddington (Kendal, 28 December 1882 – Cambridge, 22 November 1944)

whose radius is the so-called *Einstein radius*. If the alignment is not perfect, it is possible to see multiple images; in 1912, Einstein had already speculated the possibility of observing multiple images of the same background source (although these calculations were published only 24 years later, in [Einstein 1936](#)); however, he had only considered the effect of a single star as a deflector, concluding that observing such effect would be extremely unlikely due to the small angular separation between the multiple images and the difficulty of identifying such a rare, aligned system. As a consequence of this discouraging anticipation, the hope to observe multiple images faded until the late 1930s, when galaxies (at the time known as ‘nebulae’) were discovered as extragalactic objects. Fritz Zwicky⁷, recognizing that the angular separation is proportional to the mass of a lens, proposed that a galaxy could act as a lens and predicted possible separations on the order of $10''$: this new prediction, much more promising than Einstein’s earlier estimate, was observable with the telescopes available at the time - which led to concluding that a lens galaxy was likely to be found soon ([Zwicky 1937a,b](#)). However, the first observational evidence of gravitational lensing came more than 40 years later.

In the early 1960s, the discovery of quasars as extragalactic, distant, and extremely bright objects renewed the interest in gravitational lensing, as they were identified as ideal background sources to be observed lensed into multiple images ([Klimov 1963](#); [Liebes 1964](#); [Refsdal 1964c](#)). At the same time, the development of the theory of gravitational lensing included more complicated and realistic geometries, beyond the spherically symmetric mass distribution and perfect alignment (see, e.g., [Schneider et al. 1992b](#); [Schneider 2014](#); [Meneghetti 2021](#)). Moreover, it was also discovered that gravitational lensing could be used as a cosmological probe, to investigate the geometry of the Universe or its expansion rate. In fact, [Refsdal \(1964a\)](#) calculated the time delay due to the different paths of light coming from different images of a same source: this depends on the mass of the lens and on the cosmological distances of the lensing system, so that a time delay measurement could in principle be used to calculate the mass of a lens and the value of Hubble constant, H_0 .

Finally, in 1979, [Walsh et al. \(1979\)](#) observed the first strong gravitational lensing system, the double quasar Q0957+561 (Fig. 1.2, left panel), during a campaign aiming at identifying radio sources. Shortly after, the first Einstein crosses ([Huchra et al. 1985](#); [Magain et al. 1988](#), see the central panel of Fig. 1.2), composed of four multiple images around the lens, and the first Einstein rings ([Hewitt et al. 1988](#); [Langston et al. 1989](#), see the right panel of Fig. 1.2) were observed.

After that, in the last 25 years, thousands of gravitational lensing systems have been discovered and studied, including multi-plane galaxy-scale systems (e.g., [Smith & Collett 2021](#); [Wang et al. 2022](#); [Bolamperti et al. 2023a](#)), extended and giant lensed arcs (e.g., [Vanzella et al. 2022](#); [Adamo et al. 2024](#)), cluster of galaxies that act as lenses for hundreds of background sources (e.g., [Bergamini et al. 2023a](#); [Schuldt et al. 2024](#)), and variable systems suitable for cosmological studies (e.g., [Suyu et al. 2017](#); [Birrer et al. 2024](#)). All these evidences make strong gravitational lensing a powerful tool for studying galaxy evolution and for exploring the properties of the Universe (e.g., [Bartelmann 2010](#); [Treu 2010](#)). Moreover, present day and future facilities, such as the James Webb Space Telescope (JWST), the Extremely Large Telescope (ELT), Euclid and the Vera C. Rubin Observatory - LSST, will allow us to further improve these studies, with larger statistics over broad redshift, size, and brightness ranges.

⁷Fritz Zwicky (Varna, 14 February 1898 – Pasadena, 8 February 1974)

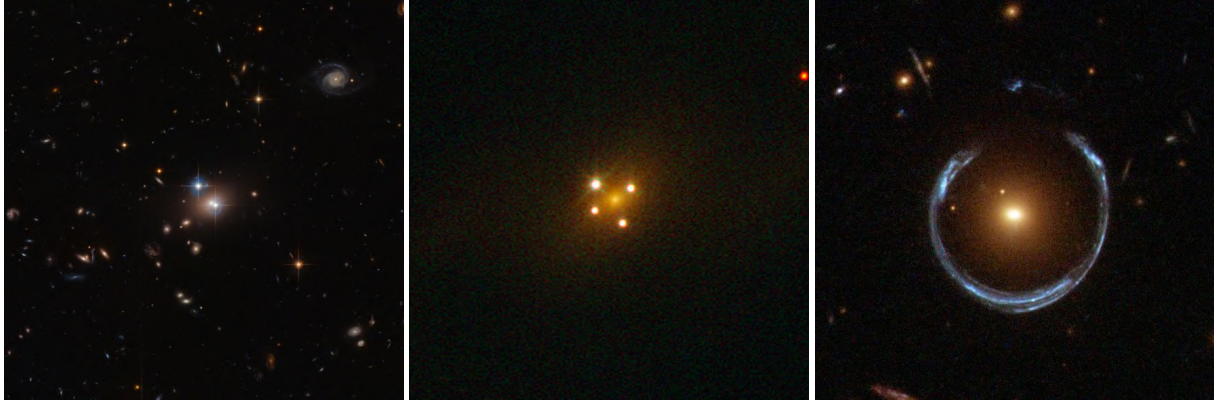


Figure 1.2: Left: The first strongly lensed observed system, the twin quasars QSO 0957+561, as seen with the Hubble Space Telescope. Credit: ESA/Hubble & NASA. Center: The QSO 2237+0305 system (also known as “Huchra’s Lens”), with the typical Einstein Cross configuration. Credit: ESA/Hubble & NASA. Right: the Einstein ring of the SDSS J114833.14+193003.2 system, known as the “Cosmic Horseshoe”, observed with the Hubble Space Telescope. Note that the fields of view of the three panels do not share the same angular scale.

1.2 Strong lensing modeling

One of the main applications of strong gravitational lensing is the study of the lens itself, given that the gravitational lensing observables - such as the positions, the fluxes, and the time delays - depend on the gravitational potential (i.e., the total mass) of the lens and on the mutual distances between the observer, the lens, and the background source. In this section I describe the principles of strong lensing modeling, that I employ in Chapters 3 and 4 to study the properties of galaxies and groups that act as lenses, and to learn about the geometry of the Universe.

- The positions of the multiple images are the most straightforward constraints to use when probing the lens’ deflection field, for two reasons: 1) they depend on the first derivative of the lensing potential (as I will extensively describe in Chapter 2; see, in particular, Eq. 2.10); 2) they can be quite easily measured from available deep and high-resolution observations, mainly with the state-of-the-art space-based Hubble Space Telescope (HST) and James Webb Space Telescope (JWST), at optical and near-infrared wavelengths. Given that multiple images of the same background source must share the same spectra, and that a precise measurement of their distance is crucial to correctly model the mass distribution of the lens, it is essential to confirm candidate multiple images with spectroscopy. In the last decades, thanks to the advent of the Integral Field Unit (IFU) instruments (e.g., the Multi Unit Spectroscopic Explorer, MUSE, mounted on the UT4 telescope of the Very Large Telescope, VLT; [Bacon et al. 2010](#)) hundreds of multiple images have been identified and confirmed. The power of MUSE is that the final result from an observation is a datacube with a field of view of $1' \times 1'$, where every pixel (called *spaxel*) has a spectrum from 4750 \AA to 9350 \AA ; therefore, it is possible to extract the spectrum of each object within the field of view, without pre-selecting it and following it up. To give an idea of the improvement that MUSE brought to the field, both in terms of strong lensing models and number of identified multiple images and background sources, one can consider the strong lensing modeling of the cluster of galaxies MACS J0416.1–2403 (MACS J0416). At $z = 0.396$,

Table 1.1: Improvement of the strong lensing modeling thanks to the advent of IFU: the example of MACS J0416.1–2403.

Reference	N_{img}	N_{src}	Δ_{rms}	N_{memb}	Main improvement
Grillo et al. (2015)	30	10	0.3''	175	CLASH-VLT spectroscopy (ID: 186.A-0798; PI: P. Rosati)
Hoag et al. (2016)	30	15	-	175	GLASS spectroscopy (ID: GO-13459; PI: T. Treu) and WL
Caminha et al. (2017)	102	37	0.59''	193	MUSE (2h North-East, 11h South-West)
Bonamigo et al. (2018)	102	37	0.59''	193	Inclusion of hot gas from X-ray
Bergamini et al. (2019)	102	37	0.61''	193	Inclusion of galaxy kinematics
Bergamini et al. (2021)	182	66	0.40''	213	MUSE deep (17.2h North-East)
Richard et al. (2021)	198	71	0.58''	213	Update
Bergamini et al. (2023b)	237	88	0.43''	213	Update, see details in Fig. 1.3.
Diego et al. (2023)†	343	119	1.07''	444	JWST NIRCam photometry (PEARLS, PI: R. Windhorst)
Rihtaršič et al. (2024)	303	111	0.53''	213	JWST NIRISS spectroscopy (CANUCS, PI: C. Willott)

Notes. For each work, I list the bibliographic reference, the number of multiple images N_{img} and background sources N_{src} exploited in the models, the mean displacement between the observed and predicted positions of the multiple images Δ_{rms} , the number of considered cluster members N_{memb} , and the main improvement (in the data or in the method). Unless differently indicated by the † symbol, all models are built based on only spectroscopically confirmed sources, and not including photometric redshifts. The main improvements, in terms of increasing N_{img} and N_{src} , coincides with the advent of MUSE IFU observations. The table does not include previous works exclusively based on photometric data (e.g., Zitrin et al. 2013; Jauzac et al. 2014; Diego et al. 2015).

MACS J0416 is one of the galaxy clusters acting as gravitational lenses with the largest number of observed multiple images (Zitrin et al. 2013) and is included in the Hubble Frontier Field (HFF; Lotz et al. 2017) program. In less than 10 years, we were able to go from exploiting the positions of 30 confirmed multiple images from 10 background sources to 303 multiple images from 111 background sources (Grillo et al. 2015; Hoag et al. 2016; Caminha et al. 2017; Bonamigo et al. 2018; Bergamini et al. 2019, 2021, 2023b; Diego et al. 2023; Rihtaršič et al. 2024, where the main improvement coincide with the advent of new MUSE observations, see Table 1.1) and Fig. 1.3, as well as a more precise and complete mapping of the cluster members.

- The fluxes (and thus the magnification) and the shapes of the multiple images and distorted arcs probe the higher-order (mostly the second) derivatives of the lensing potential; as a consequence, they are more sensitive to small-scale components and substructures, but also more delicate and difficult to model.
- Finally, the relative time delays between the multiple images are the only dimensional observable of gravitational lensing, and can probe the lensing potential, as described in Section 2.3. Unfortunately, there are three main limitations to their extensive use: they require a variable source (like a quasar, or a supernova), they are rare (with only a few tens known cases), and the time delays are difficult to measure and require extensive follow-ups and monitoring.

The method to convert all these observables into total mass distribution is called “lens inversion”. It is usually performed with some specific strong lensing programs (e.g., GLEE by Suyu & Halkola 2010, lenstool by Jullo et al. 2007, GLAFIC by Oguri 2010, PyAutoLens by Nightingale & Dye 2015, Gravity.jl by Lombardi 2024) and can be parametric or non-parametric (“free-form”), depending on how the lens mass distribution is described. I will focus on the parametric process,

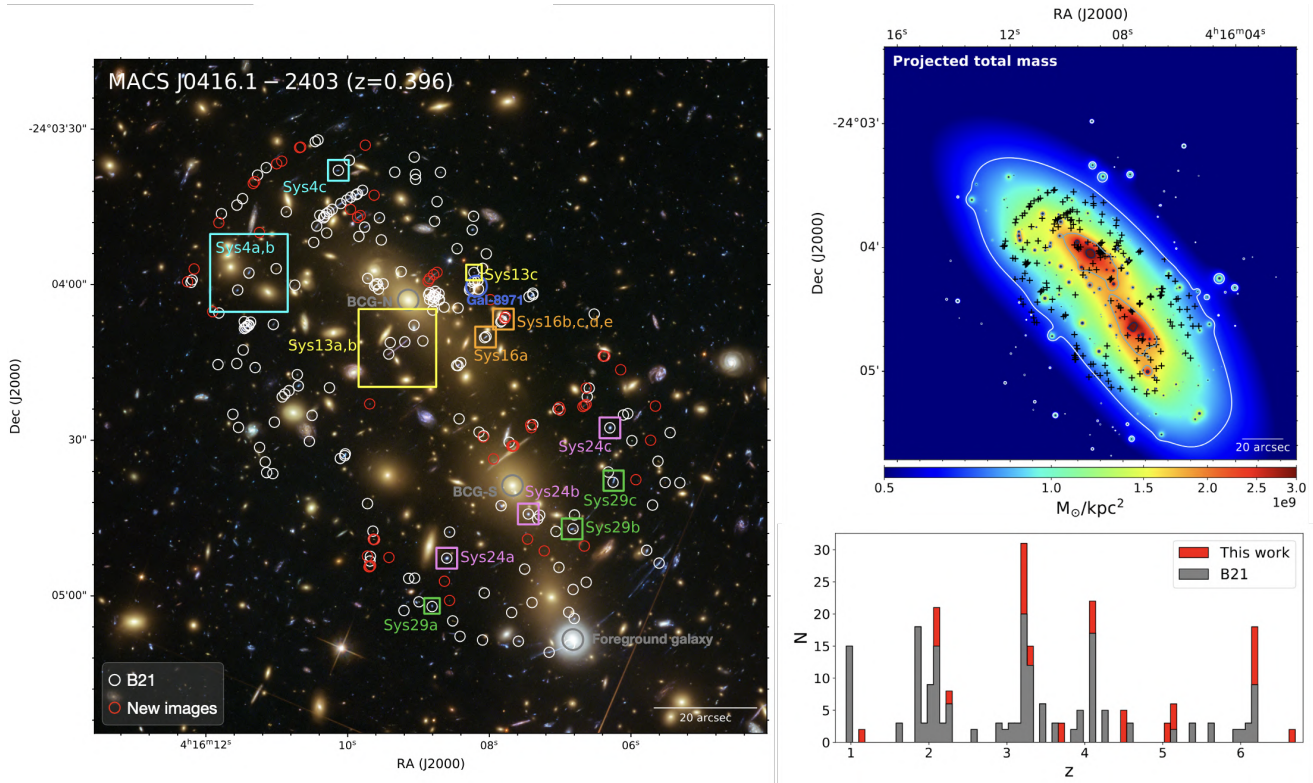


Figure 1.3: Left: RGB image of the MACS J0416 cluster of galaxies, where white circles show the positions of the 182 multiple images identified by Bergamini et al. (2021) (labeled in the figures as B21), while the red circles those of the new multiple images used in Bergamini et al. (2023b). Different squares and labels identify particular systems of multiple images. Top right: Projected total mass density distribution of MACS J0416 from the best-fit model of Bergamini et al. (2023b), composed both of cluster- and galaxy-scale halos. Contours encompass values of 0.70, 1.85, and $3.00 \times 10^9 M_\odot \text{ kpc}^{-2}$. Bottom right: Redshift distribution of the 237 multiple images adopted to build the strong lensing model with in red the newest multiple images. From Bergamini et al. (2023b).

where the mass distribution of the lens is reconstructed using different mass components with an assumed mass distribution described by a set of parameters, and usually assuming that the mass follows the light. Additionally, in some cases, this process also allows us to measure the values of the cosmological parameters, as they need a cosmological model to be assumed. The procedure, that aims at finding the best combination of parameters that reproduces the observed positions of the multiple images, can be qualitatively summarized into the following steps:

- Given an initial set of parameters (of the lens and the cosmology), we calculate the deflection angle and apply the lens equation (Eq. 2.5) and map the positions of the observed multiple images on the source plane;
- The resulting points are usually spread on the source plane (ideally, with a perfect model, they would be mapped in a single point), and we can measure the resulting source position as the (weighted) mean position of these points. We can use a χ^2_{src} metric to evaluate the goodness of the model on the source plane, by comparing the mean position with the individual ones. We usually refer to the minimization of this χ^2_{src} value as a source plane

optimization.

3. By using the ray tracing equation again, we map back the mean source position on the image plane, and compare the observed and predicted positions of the images, with a χ_{img}^2 metric (usually defined as in Eq. 3.2), in a image plane optimization. We stress that the optimization on the image plane is the only one that is reliable and meaningful, as allows us to compare the predictions from our model directly with the observations.
4. This process can be repeated varying the values of the set of parameters, \mathbf{p} , in order to maximize the likelihood, defined as

$$\mathcal{L}(\mathbf{p}) = \prod_{j=1}^{N_{\text{fam}}} \frac{1}{\prod_{i=1}^{N_{\text{img}}} \sigma_{ji} \sqrt{2\pi}} \exp \left(-\frac{\chi_{\text{img},j}^2(\mathbf{p})}{2} \right), \quad (1.3)$$

where $\chi_{\text{img},j}^2$ is relative to the j -th family of multiple images, σ_{ji} is the error on the position of the i -th image of the j -th family, N_{fam} and N_{img} are the total numbers of families and images. This is equivalent to minimizing the total $\chi_{\text{img,tot}}^2$, defined as

$$\chi_{\text{img,tot}}^2(\mathbf{p}) = \sum_{j=1}^{N_{\text{fam}}} \chi_{\text{img},j}^2(\mathbf{p}) \quad (1.4)$$

If other observables are included, $\chi_{\text{img,tot}}^2(\mathbf{p})$ can take the form

$$\chi_{\text{img,tot}}^2(\mathbf{p}) = \chi_{\text{pos}}^2(\mathbf{p}) + \chi_{\text{flux}}^2(\mathbf{p}) + \chi_{\text{time delay}}^2(\mathbf{p}) \quad (1.5)$$

Usually, different mass parametrizations are assumed to model different objects. For example, deflector galaxies are usually modeled with a single mass distribution (e.g., isothermal or power-law profile, see Chapter 3) and eventually an external perturbation, that are sufficient to reproduce the positions of the observed multiple images. On larger scales, groups and clusters of galaxies have complex mass distributions, are located in dense environments, and include several components, as suggested by observations (see the top right panel of Fig. 1.3). These components must be taken into account when building a strong lensing model. On cluster scales, for example, a dark-matter extended halo that dominates the mass budget is usually included, and is associated to the brightest cluster galaxy. If the mass distribution of the cluster is more complex or asymmetric, multiple large scale components are included, to reproduce the characteristic elongation. Additional mass can be included to reproduce the hot diffuse gas (e.g., Bonamigo et al. 2018), external perturbations to model the structures at different distances along the line of sight, and any other asymmetry on the lens plane. Finally, the cluster members are modeled with individual mass distributions, that can give rise to local galaxy-scale strong lensing events. A complete lens model is described by a large number of free parameters, that can vary from less than 10 in galaxy-scale systems to several hundreds in cluster-scale systems, making a proper optimization a time expensive process, but new codes and techniques can significantly lower this time (Lombardi 2024).

The characterization of the strong lenses and the geometry and structure of the Universe can be applied to a large variety of topics in the frame of galaxy formation and evolution. A non exhaustive list includes: to reconstruct the total and dark-matter mass distributions, thus the dark-matter over total mass fraction (Gavazzi et al. 2007; Grillo et al. 2009; Suyu & Halkola 2010; Sonnenfeld et al. 2015; Schuldt et al. 2019) and the mass density slopes (e.g., Treu & Koopmans

2002; Koopmans et al. 2009; Barnabè et al. 2011; Shu et al. 2015), to infer the most likely lens stellar initial mass function (IMF; e.g., Cañameras et al. 2017b; Barnabè et al. 2013; Sonnenfeld et al. 2019), and to identify dark-matter substructures (e.g., Vegetti et al. 2012; Hezaveh et al. 2016; Ritondale et al. 2019), to measure the values of some cosmological parameters in strong lensing systems with kinematic data of the lenses (e.g., Grillo et al. 2008; Cao et al. 2012) or in systems where two or more sources are multiply imaged by the same lens galaxy (Tu et al. 2009; Collett & Auger 2014; Tanaka et al. 2016; Smith & Collett 2021), once the mass sheet degeneracy is broken (Schneider 2014), to learn about the slope value of the mass density of the dark matter halos in inner regions of galaxy clusters (Sand et al. 2004; Grillo et al. 2015; Annunziatella et al. 2017; Bergamini et al. 2019), to measure the cosmological density parameter values (Jullo et al. 2010; Caminha et al. 2016; Grillo et al. 2020), and the value of the Hubble constant (Suyu et al. 2013, 2017; Grillo et al. 2024), and the study of the lensed background sources (e.g., Rigby et al. 2017; Cava et al. 2018; Dessauges-Zavadsky et al. 2019), and in particular of the most magnified and distorted ones (e.g. Vanzella et al. 2023; Welch et al. 2023; Adamo et al. 2024).

1.3 Lensing magnification enables the study of compact and faint sources at high- z

Thanks to their magnification, that depends on the total mass of the lens and on the mutual distances between the observer, the lens, and the source, galaxies and cluster of galaxies act as the most powerful natural telescopes (see, e.g., the Hubble Frontier Field program, Lotz et al. 2017). Depending on their position and alignment with the lens, background sources can be significantly magnified, if they lie close to the caustic lines, that represent the positions where the magnification theoretically diverges, and observationally can reach $\gtrsim 100$ values (for a complete view on the formalism, we refer to Chapter 2, and in particular to Section 2.2). In Fig. 1.4, we show the impact of strong gravitational lensing on the physical scale that we can study with different instruments, like HST (representing the past and present), JWST (the present) and MORFEO-MICADO, that will be mounted on the Extremely Large Telescope (ELT; future, ≈ 2030). MICADO⁸ will take high-resolution images of the Universe at near-infrared wavelengths, and will work with the ELT’s adaptive-optics module, MORFEO⁹ (Fiorentino et al. 2017). As shown in Fig. 1.4, in non-lensed fields we can today probe sub-kpc structures, mostly with unresolved sizes < 1 kpc (e.g., Förster Schreiber et al. 2011a; Guo et al. 2018; Zanella et al. 2019; Kalita et al. 2024). When we observe lensed objects (in the figure, for instance, with magnification factors from 20 to 30, we can probe scales of tens of pc, approaching those of star-forming complexes, at cosmological distances (e.g., Vanzella et al. 2022; Meštrić et al. 2022; Messa et al. 2022; Claeysens et al. 2023), down to few pc scales with future ELT/MORFEO-MICADO observations or today with extremely large magnification factors (Vanzella et al. 2017a,b, 2021; Welch et al. 2023; Adamo et al. 2024), exploring the physical scales of local star-forming complexes and star clusters.

The study of the smallest structures we can resolve, and the continuous improvement of the observations, has led to the discovery, in the last years, of the substructures present in the most distant galaxy that we observe. In particular, rest-frame UV and optical observations revealed that, galaxies at $z \sim 1 - 4$ have irregular morphologies (see Conselice 2014 for a review and, e.g., Conselice et al. 2004; Shibuya et al. 2016; Huertas-Company et al. 2024 and are dominated by bright, blue regions of active star formation, called “clumps” (e.g., Elmegreen & Elmegreen 2005;

⁸<https://elt.eso.org/instrument/MICADO/>

⁹<https://elt.eso.org/instrument/MORFEO/>

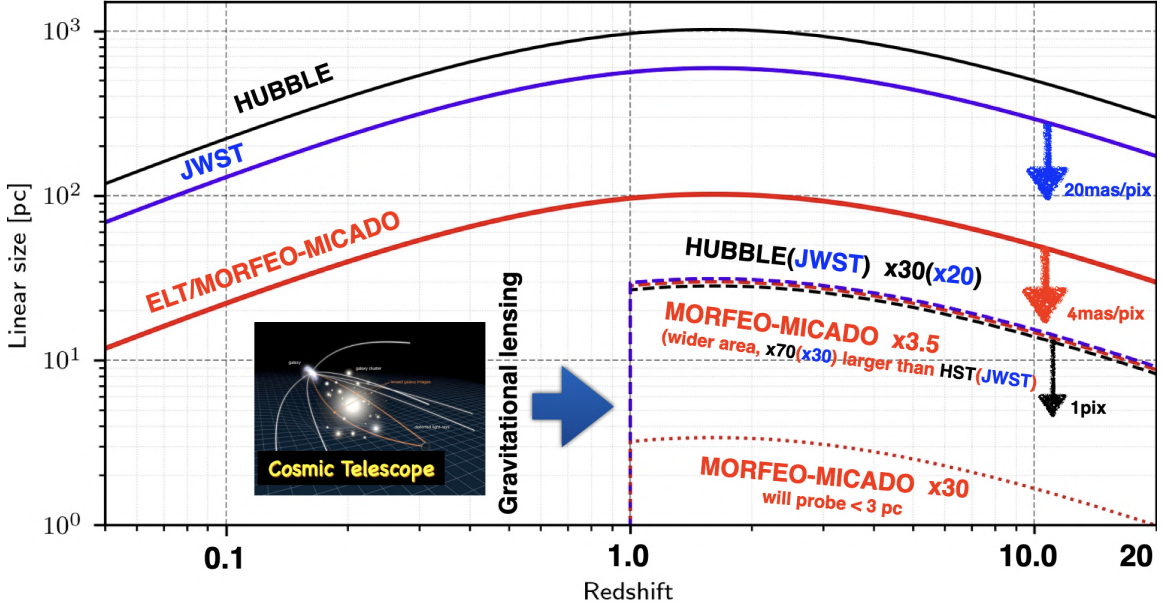


Figure 1.4: Physical scale that we can probe as a function of the redshift, for different instruments (solid lines, HST in black, JWST in blue, and ELT/MORFEO-MICADO in red). Thanks to strong gravitational lensing by galaxies and clusters of galaxies, we can resolve smaller scales (dashed curves, color-coded as the solid ones, assume a magnification factor of 30 for HST, 20 for JWST, and 3.5 for ELT/MORFEO-MICADO), from kpc scales to $\lesssim 10$ pc scales. A magnification factor of 30, observed with ELT/MORFEO-MICADO, will allow us to probe < 3 pc scales at cosmological distances (dotted red line). Image credits: courtesy of Eros Vanzella.

[Elmegreen et al. 2007, 2009a; Zanella et al. 2015; Guo et al. 2015](#)), shown in Fig. 1.5. Clumps in non lensed fields have typical stellar masses $M_\star = 10^7 - 10^9 M_\odot$, star formation rates (SFRs) of $0.1 - 10 M_\odot/\text{yr}$ and sizes < 1 kpc ([Förster Schreiber et al. 2011a; Guo et al. 2018; Kalita et al. 2024](#)) while, in lensed fields, we can observe down to $M_\star = 10^6 M_\odot$ and sizes of 10-100 pc ([Meštrić et al. 2022; Claeysens et al. 2023](#)). Moreover, they exhibit blue UV-continuum β slopes (defined as the slope of the UV-continuum if parametrized by a power law, [Calzetti et al. 1994](#)), suggesting that they are sites of intense star formation and host young stellar populations with relatively low metallicity ([Bolamperti et al. 2023b](#)).

The mechanisms of formation and evolution of clumps is strongly related to their hosts galaxy evolution, and it is still debated. Two main scenarios, that are contradictory, have been proposed. In the first one, they are remnants of mergers or accreted satellites that have not been completely disrupted (e.g., [Puech et al. 2009; Puech 2010; Hopkins et al. 2013; Wuyts et al. 2014; Guo et al. 2015; Straughn et al. 2015; Ribeiro et al. 2017](#)), while in the second they are star-forming regions formed *in situ*, due to the fragmentation and local collapse of high- z galaxies, that are rich of gas, and turbulent (e.g., [Elmegreen et al. 2007; Bournaud et al. 2008; Genzel et al. 2008, 2011; Guo et al. 2012, 2015; Hinojosa-Goñi et al. 2016; Mieda et al. 2016; Fisher et al. 2017](#)). The *in situ* scenario can also be tested as, according to it, we should be able to detect clumps during their formation, and thus with ages $\lesssim 10$ Myr. Currently, only a few candidates are present, as these extremely young ages require exceptional accuracy to be measured, and thus need deep spectroscopic data, and are not possible to address with photometry only.

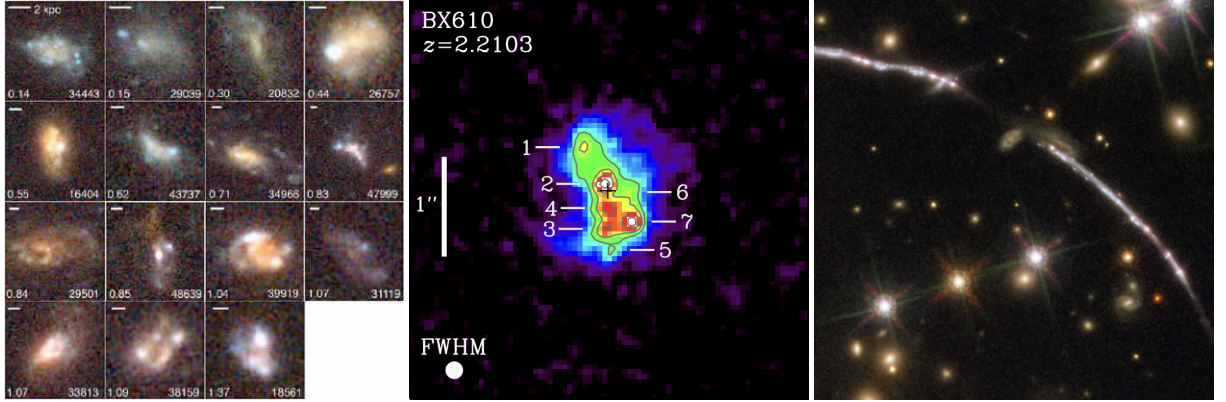


Figure 1.5: Left: Sample of clumpy galaxies, where it is possible to see the diffuse host galaxies and their bright clumps, from [Elmegreen et al. \(2009b\)](#). The white rulers indicate a physical size of 2 kpc. Center: Example of a clumpy galaxy in a non-lensed field, from [Förster Schreiber et al. \(2011b\)](#), where clumps have unresolved < 1 kpc sizes. Right: Particular of the Sunburst arc, from a galaxy at $z = 2.37$ that is extremely magnified and distorted, allowing us to observe stellar clusters (multiply imaged more than 10 times) with physical sizes $\lesssim 10$ pc ([Dahle et al. 2016](#); [Rivera-Thorsen et al. 2017](#); [Vanzella et al. 2020a, 2022](#); [Meštrić et al. 2023](#)), as the bright dots embedded in the extended arc.

Moreover, also the final fate of the clumps is still debated. This is due to the difficulty of observationally measuring the ages of the clumps, and on the contradictory results from the simulations, that are dependent on the initial conditions or the assumed recipes. One possibility is that clumps may be quickly disrupted, as they would not be able to survive the gas removal and unbinding of the system by strong stellar feedback and tidal forces in the host galaxies. In this case, we expect clumps to be short-lived (survive for $\lesssim 50$ Myr) and only partially influencing the structural evolution of their host galaxies (e.g., [Tamburello et al. 2015](#); [Buck et al. 2017](#); [Oklopčić et al. 2017](#)). A second possibility predicts that clumps, thanks their high star-formation efficiency, are able to quickly convert all the molecular gas content into stars, and remain bound for $\gtrsim 500$ Myr. In this long timescales, due to the effects of friction and tidal torques, clumps are expected to migrate toward the center of their host galaxy, contributing to the formation and accretion of their bulge, eventually feeding the central super massive black hole (e.g. [Ceverino et al. 2010](#); [Bournaud et al. 2014](#)). In principle, this scenario could be confirmed by the observation of a population of old ($\gtrsim 100$ Myr) clumps, and an evolution of their age and color with the distance from the center of the host ([Förster Schreiber et al. 2011b](#); [Guo et al. 2012](#); [Soto et al. 2017](#)). Understanding the formation and evolution of clumps, and their interplay with those of their host galaxy, is key for different aspects like, for instance, validating the feedback models we use in simulations, shedding light on the formation of the bulge in the center of the local galaxies, and characterize how the star-formation proceeds at high- z (see [Madau & Dickinson 2014](#)).

One of the main factors influencing and regulating the star-formation processes at high- z are the stellar populations in clumps and galaxies. As discussed above, clumps demonstrated to have young stellar populations, being active sites of star formation. This evidence is encoded in the UV-continuum β slope, that exhibits bluer values, with respect to that of their host galaxies ([Bolamperti et al. 2023b](#)). Moreover, the β slope was shown to evolve with the redshift and the intrinsic magnitude (see the detailed discussion in [Bouwens et al. 2012, 2014](#)), suggesting an

evolution of the stellar populations over cosmic time. Recent deep observations have additionally revealed the presence of robust, “extremely blue” $\beta \lesssim -2.7$ galaxies and clumps (e.g. Bouwens et al. 2010; Labb   et al. 2010; Zackrisson et al. 2013; Jiang et al. 2020; Maseda et al. 2020; Marques-Chaves et al. 2022; Bolamperti et al. 2023b), that gained attention because it is not possible to reproduce them with standard stellar populations models, and extreme physical conditions are required. Several studies tried to reproduce such blue β slopes (see Fig. 1.6): Bouwens et al. (2010) could reproduce slopes of ~ -3 with standard (Leitherer et al. 1999; Bruzual & Charlot 2003) stellar population models only for very young (< 5 Myr) star-forming systems and ignoring the nebular continuum emission, that is due to the ionized gas around young stars, and can redden the slopes up to $\Delta\beta \sim 0.5$ (Topping et al. 2022), making it difficult to reproduce slopes below -2.7 . This suggests that very low metallicity (Z) values, or a different IMF, are needed to reproduce more extreme slopes. Some studies (e.g., Raiter et al. 2010; Maseda et al. 2020) found that it is possible to reproduce slopes of about -3 with $Z < 10^{-2} Z_{\odot}$, but only for a limited range of ages, between 10 and 30 Myr. They conclude that very low metallicity values can explain part of the extremely blue slopes found, but the limited age range makes it unlikely to be the general explanation. Finally, an escape fraction of ionizing photons into the intergalactic medium of 0.3 can easily reproduce the observed blue spectra (Bouwens et al. 2010; Zackrisson et al. 2013; Chisholm et al. 2022), but this value is considerably larger than the usually assumed ~ 0.1 , sufficient for galaxies to reionize the Universe. Topping et al. (2022) explored the possibility that the introduction of binary stars could generate significantly bluer slopes, but could reproduce slopes down to -3.15 , similar to the ~ -3.2 limit reached with single stars, concluding that binaries are not the main responsible for the extremely blue slopes. In summary, several physical quantities can affect the resulting β slope but, in order to reproduce the extremely blue ones found in observations, one has to assume a dust-poor system, without nebular emission, and with young ages ($\lesssim 10$ Myr) and low metallicity ($\lesssim 1\% Z_{\odot}$ (Bolamperti et al. 2023b)). One of the possibilities, that fulfills these requirements, is the presence of Population III (PopIII) stars.

Simulations and theoretical studies have long been predicting the existence in the primordial Universe of the first populations of stars, PopIII, formed in pristine regions, from primordial hydrogen and helium (Wise et al. 2012; Dayal & Ferrara 2018; Nakajima & Maiolino 2022). PopIII stars are expected to have an exceptionally high effective temperature ($\sim 10^5$ K), emit a large fraction of their luminosity in the Lyman continuum, have masses of tens of solar masses, and live for 3-10 Myr (Schaerer 2002; Hirano et al. 2015). These properties result in an expected spectral energy distribution with a blue continuum slope and the lack of metal lines, but with strong hydrogen and helium lines, in particular the HeII1640 emission (Raiter et al. 2010; Inoue 2011). The observation of such a population of stars would be groundbreaking in our comprehension of the formation of the first galaxies (e.g., Wise 2019). In the last years, various studies yielded candidates of high- z systems dominated by PopIII populations (Kashikawa et al. 2012; Sobral et al. 2015, 2019; Vanzella et al. 2023), but they are still uncertain and controversial (Bowler et al. 2017; Shibuya et al. 2018). They are expected to form in compact, isolated regions (Zackrisson et al. 2015) such that lensed, high- z clumps with extremely blue beta slopes are ideal candidates to look for PopIII stars.

1.4 Using gravitational lensing for spectropolarimetric studies

Strong lensing, thanks to its magnification effect, acts as the most powerful natural telescope and allows some kind of studies that would not need gravitational lensing themselves, but would

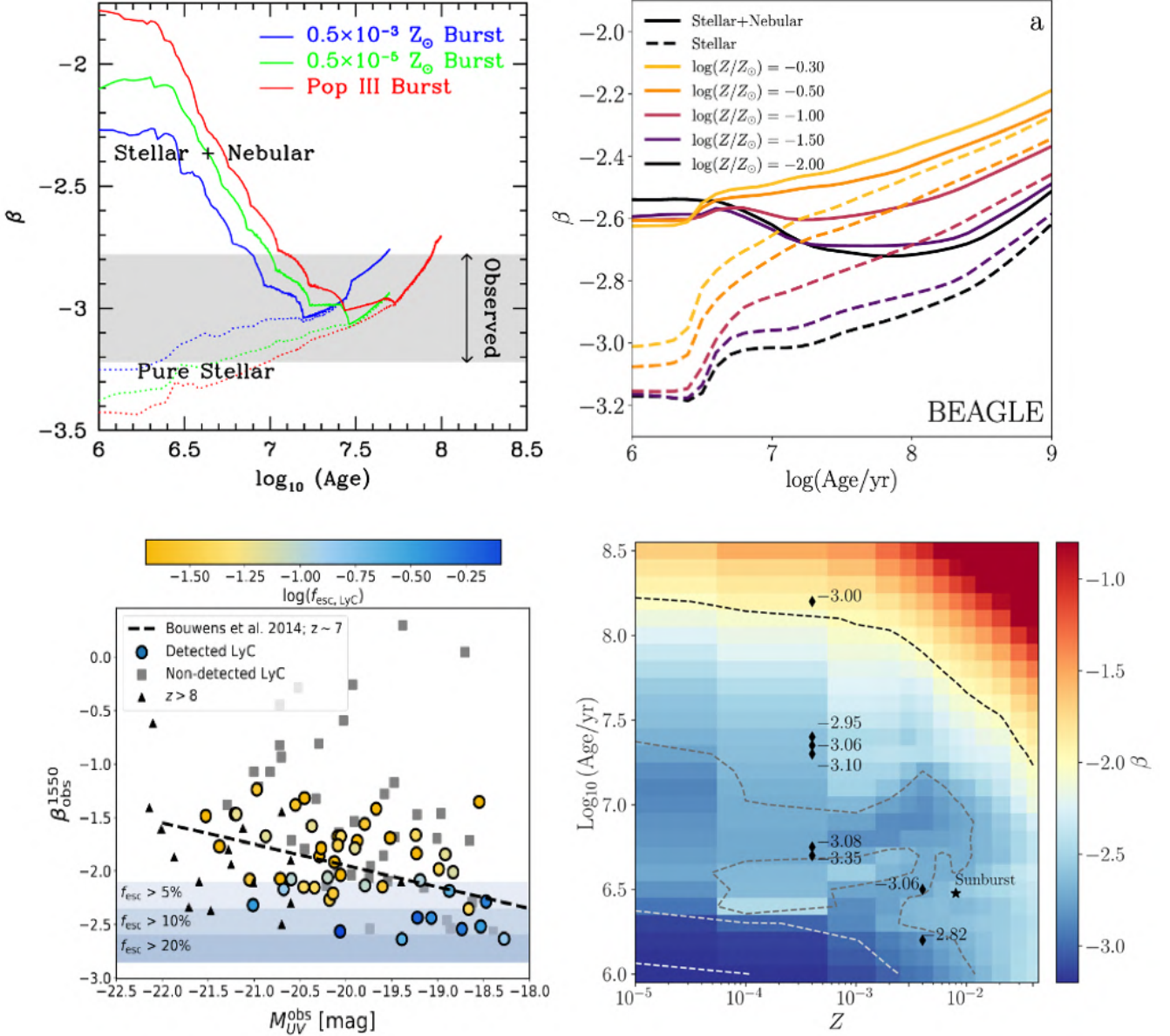


Figure 1.6: Resulting UV-continuum β slope from models with different metallicities as a function of the age (top left, [Bouwens et al. 2010](#), and top right, [Topping et al. 2022](#)), different Lyman-continuum (LyC) escape fractions as a function of observed magnitude (bottom left, [Chisholm et al. 2022](#)), and as a function of both metallicity and age (bottom right, [Bolamperti et al. 2023b](#)). The top panels show the models both with and without the nebular emission from ionized gas around young stars.

not be possible without the flux boost. One of them is spectropolarimetry of distant and faint star-forming galaxies. In this section, we give an overview on polarization, that we will exploit in Chapter 6 to learn about the geometry of the neutral gas surrounding galaxies at high- z .

The light is a transversal electromagnetic wave, and is thus characterized by three properties: the intensity, the wavelength, and the polarization. When the electric (\mathbf{E}) and magnetic (\mathbf{B}) fields vibrate preferentially in a given direction, the radiation is said to be linearly polarized. If the

fields describe a circular motion, then the polarization is said circular. If the vibrations have randomly distributed orientation, the signal is not polarized. Light polarization is ubiquitously present, both in modern technologies and in nature (see, e.g., [Können 1985](#), for a review of polarized light in nature).

Being \mathbf{E}_x and \mathbf{E}_y orthogonal components of the electric field \mathbf{E} , both orthogonal to the propagation direction, one can define the Stokes parameters I , Q , U , and V as

$$\begin{pmatrix} I \\ Q \\ U \\ V \end{pmatrix} = \begin{pmatrix} E_x E_x^* + E_y E_y^* \\ E_x E_x^* - E_y E_y^* \\ E_x E_y^* + E_y E_x^* \\ i(E_x E_y^* - E_y E_x^*) \end{pmatrix}, \quad (1.6)$$

where the E^* symbol represents the complex conjugate. A more appropriate definition, for the most general and not only monochromatic emission, considers the temporal mean of the quantities on the right hand of this equation. These parameters were firstly described by the Irish mathematician and physicist George Stokes¹⁰ ([Stokes 1851](#)), where I represents the total intensity, Q and U are related to linear polarization, and V to circular. If the light is not polarized, Q , U , and V are zero, while, if the light is fully polarized, $I^2 = Q^2 + U^2 + V^2$. In general, $0 < Q^2 + U^2 + V^2 < I^2$. It is then possible to define the degree of polarization, as

$$P = \frac{\sqrt{Q^2 + U^2 + V^2}}{I} \quad \text{if linear polarization} \quad P_{\text{lin}} = \frac{\sqrt{Q^2 + U^2}}{I}, \quad (1.7)$$

and the polarization angle

$$\theta = \frac{1}{2} \arctan \left(\frac{U}{Q} \right), \quad (1.8)$$

defined as the angle between \mathbf{E} and the North direction, increasing towards East.

The general principle to measure the polarization is to place a linear polarizer between the source we aim to observe and the detector, and to measure the intensity of the radiation for several orientations of the polarizer. What a polarizer does is to extract, for a given direction, the component that is linearly polarized in that direction. The most common technique used on today's most advanced telescopes is to use a birefringent prism, composed of a birefringent material (e.g., calcite, CaCO_3), which have different refractive indexes for light polarized in the parallel and perpendicular directions with respect to their optical axis. Thus, after refraction, the incident ray is split into two components with perpendicular polarizations, and deflected by different angles: the "Ordinary" ray is perpendicular to the axis of the prism, while the "Extraordinary" is parallel. Due to its symmetry, the most used prism is the Wollaston prism (Fig. 1.7), that deflects the two rays by the same angle, such that, if the prism is oriented with an angle α , we can measure at the same time the intensity in the α and $\alpha + 90^\circ$ directions (see the scheme in Fig. 1.7).

If we orient the prism such that $\alpha = 0^\circ$ and then 45° , it is possible to independently measure the couples (I, Q) and (I, U) , as

$$\begin{cases} I = I_0 + I_{90} \\ Q = I_0 - I_{90} \end{cases} \quad \text{and} \quad \begin{cases} I = I_{45} + I_{135} \\ U = I_{45} - I_{135} \end{cases}, \quad (1.9)$$

¹⁰Sir George Gabriel Stokes (13 August 1819 – 1 February 1903)

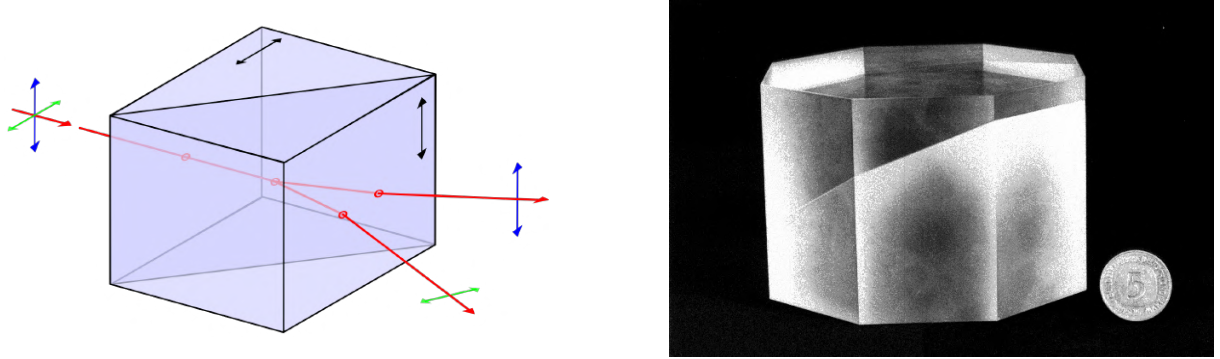


Figure 1.7: Left: Scheme of the deflection by a Wollaston prism. The orthogonal polarization directions are refracted by the same angle. Credits: Creative Commons, in Wikimedia Commons. Right: Wollaston prism mounted on VLT/FORS. Credits: ESO.

and thus reducing the measurements of the Stokes parameters Q and U , in the ideal case, to sums and differences of the total intensities of ordinary and extraordinary rays after the passage through a Wollaston prism.

In reality, this procedure is usually not sufficient because a difference in gain between the ordinary and extraordinary channels (that is inevitable from the difference in response of the gratings and mirrors), introduces an asymmetry that biases the measurements. Given that the gain factors are not known *a priori*, the classic workaround is to measure each Stokes parameter with two exposures instead of one, by rotating the polarimeter by 90° (or equivalently the half-wave plate angle α of 45°). Moreover, the atmospheric conditions, that can vary over timescales of minutes during observations, can introduce additional biases. Let G^o and G^e be the gains in the ordinary and extraordinary channels, and A_α the factor related to the atmospheric conditions. With two exposures, we can measure

$$\text{exposure 1 : } \begin{cases} I_0^o = \frac{1}{2}(I + Q) \times G^o \times A_0 \\ I_0^e = \frac{1}{2}(I - Q) \times G^e \times A_0 \end{cases} \quad (1.10)$$

$$\text{exposure 2 : } \begin{cases} I_{45}^o = \frac{1}{2}(I - Q) \times G^o \times A_{45} \\ I_{45}^e = \frac{1}{2}(I + Q) \times G^e \times A_{45} \end{cases} . \quad (1.11)$$

It is worth noting that all the quantities, I , Q , G , and A_α are a function of the wavelength. If one divides the ordinary and extraordinary equations, it is possible to measure the Stokes parameters and cancel the G and A_α factors, as

$$Q = \frac{R_Q - 1}{R_Q + 1} \quad \text{where } R_Q^2 = \frac{I_0^o / I_0^e}{I_{45}^o / I_{45}^e} \quad (1.12)$$

and, in the same way, considering $\alpha = 22.5^\circ$ and 67.5° , one can measure U as

$$U = \frac{R_U - 1}{R_U + 1} \quad \text{where } R_U^2 = \frac{I_{22.5}^o / I_{22.5}^e}{I_{67.5}^o / I_{67.5}^e} . \quad (1.13)$$

The benefits of this technique can be seen in Fig. 1.8, where [Vernet \(2001\)](#) compared the use of one or two exposures to measure the polarization of the standard star HD 251204.

One last step consists in correcting the polarization measurements, taking into account the presence of noise in the observations. In fact, the degree of polarization P is a biased estimator,

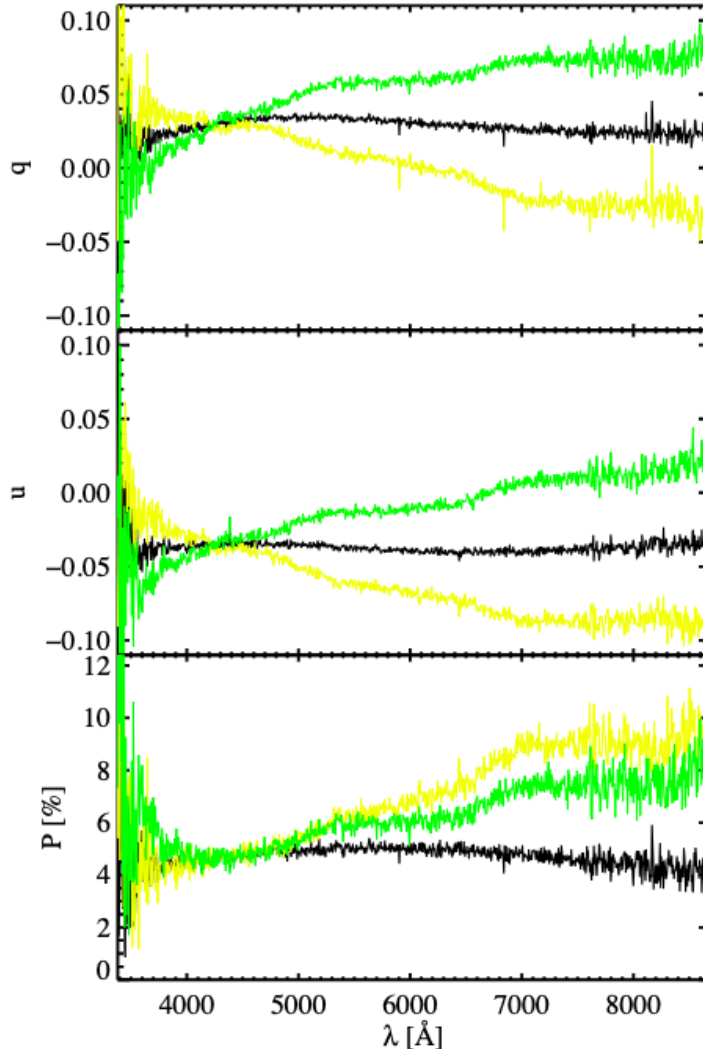


Figure 1.8: Measurements of $q = Q/I$, $u = U/I$, and P , showing the importance of the two-exposures method. In green, using only the observations with $\alpha = 0^\circ$ (for q) and 22.5° (for u). In yellow using only the observations with $\alpha = 45^\circ$ (for q) and 67.5° (for u). In black, their combination, using Eq 1.12 and 1.13. The three methods have very different results, as the green and yellow are dominated by the different gains contribution. This figure, from [Vernet \(2001\)](#), takes as example the standard star HD 251204 spectropolarimetric observations taken with VLT/FORS on the 1st December 1999.

and several studies have tackled the problem defining the best estimator (see, e.g., the review from [Clarke & Stewart 1986](#)), because P is, by definition, a positive quantity (see Eq. 1.7). It means that the presence of noise always increases the P value with respect to the “true” value, P_0 . [Vernet \(2001\)](#) showed, for example, that simulating 10000 observations of an unpolarized object, the measured degree of polarization distribution is not centered on $P = 0$, but approximately on 2 – 3%. In general, [Serkowski \(1958\)](#) showed that, if we assume the reduced Stokes parameters $q = Q/I$ and $u = U/I$ to be normally distributed with the same variance σ^2 around their unbiased values q_0 and u_0 , then the probability of obtaining a measured $p = P/\sigma$ given the true

p_0 is a Rice function, as

$$F(p, p_0) = p \exp\left(\frac{-(p^2 - p_0^2)}{2}\right) J_0(ipp_0), \quad (1.14)$$

where $p_0 = P_0/\sigma$ and J_0 is the Bessel function of order zero.

In conclusion, if we measure a value P from an observation, what is the best estimator for P_0 ? Different solutions have been proposed. We assume the correction by [Simmons & Stewart \(1985\)](#), that proposed, for different S/N regimes, four different possible methods to estimate P_0 (the average estimator from [Serkowski 1958](#), the [Wardle & Kronberg 1974](#) estimator, the maximum likelihood estimator, and the median estimator) and their uncertainties. In high ($\gtrsim 4$) S/N regimes all the four methods produce consistent results, while they are particularly effective in estimating P_0 in low S/N regimes.

In Chapter 6 we will leverage on 18 hours of VLT/FORS2 in spectropolarimetric mode to study the Ly α polarization of a relatively low-mass ($M_\star \sim 10^9 M_\odot$) galaxy at high redshift ($z \sim 3.5$). In this regime, this study is possible only thanks to gravitational lensing as, with a magnification factor of ~ 5.5 , the needed observing time without lensing would have been of approximately 500 hours. The degree of polarization of the Ly α line can tell us a lot about its emission mechanism and the geometry of the scattering medium, thanks to its resonant nature. In fact, a Ly α photon can experience a great number of scatterings after its emission. The number of scatterings that it experiences before being able to leave its emission site depends on the H I column density, geometry, and kinematics ([Adams 1972](#); [Dijkstra 2014](#)), on quantum mechanical probabilities ([Stenflo 1980](#)), and on the properties of the region where it originated. For instance, centrally emitted Ly α photons, e.g., created as nebular emission powered by star formation, scatter significantly before escaping, potentially giving rise to an observed spatially-extended Ly α emission. However, spatially-extended Ly α emission can also be produced by cooling gas ([Haiman et al. 2000](#)), gas that has been shock-heated by supernova explosions ([Mori et al. 2004](#)) and galactic winds ([Taniguchi & Shioya 2000](#)), fluorescent radiation from an external ionizing field ([Hogan & Weymann 1987](#); [Cantalupo et al. 2005](#)), or extended star formation ([Momose et al. 2016](#); [Mas-Ribas et al. 2017](#)). These features are encoded in the intensity spectrum of the source ([Ahn et al. 2002, 2003](#); [Verhamme et al. 2006](#); [Dijkstra & Loeb 2008](#); [Gronke et al. 2015](#)), causing the broadening and shifting of its Ly α line profile ([Neufeld 1990](#); [Dijkstra et al. 2006](#)). The spectrum, together with the Ly α surface brightness profile that reveals the spatial distribution of the Ly α emission and the diffusion process of Ly α photons, are the most frequently used observables embraced to investigate the nature of the Ly α emission. Thanks to its resonant nature, we can additionally leverage on the Ly α degree and direction of linear polarization. The Ly α degree of polarization increases if photons are scattered in a preferential direction, and the resulting value mainly depends on two fundamental factors: the production mechanism and the site where the Ly α photons are created, and the geometry of the gas where they scatter before escaping, being in particular sensitive to the isotropy and homogeneity of the emission and gas distribution (e.g., [Lee & Ahn 1998](#); [Ahn et al. 2002](#); [Eide et al. 2018](#)). Theoretical studies showed that different models may present similar spectra, but different degrees of polarization of the Ly α line (e.g., [Dijkstra & Loeb 2008](#); [Gronke et al. 2015](#); [Eide et al. 2018](#)).

1.5 Thesis aims and structure

In this thesis, we employ strong gravitational lensing to characterize both the deflector and the background sources in different systems, from galaxy- and group- to cluster-scales. We make use of new and proprietary observations taken with state-of-the-art instruments mounted on cutting edge facilities, like the Very Large Telescope’s (VLT) Multi Unit Spectroscopic Explorer (MUSE), XShooter, and the visual and near UV FOcal Reducer and low dispersion Spectrograph (FORS) instruments, the James Webb Space Telescope’s (JWST) Near Infrared Camera (NIRCam) and Near-Infrared Spectrograph (NIRSpec) instruments, and the Hubble Space Telescope’s (HST) Advanced Camera for Surveys (ACS) and Wide Field Camera 3 (WFC3). In particular, we leverage on the following observations: program ID 110.245R, PI: A. Bolamperti (VLT/MUSE); program ID 111.253B, PI: A. Bolamperti (VLT/X-Shooter); program ID 108.2260, PI: A. Zanella (VLT/FORS2); GO program 1908, PI: E. Vanzella (JWST/NIRSpec); program GO-15253, PI: R. Cañameras (HST); program ID 091.A-0852, PI: L. Christensen (VLT/XShooter). We complement them with archival data from the same facilities.

The thesis is organized as follows. In this chapter, we briefly introduced gravitational lensing, and the basics of strong lensing modeling, the study of background source, and of polarization, that will be discussed later. In Chapter 2 we give an introduction to the gravitational lensing theory and formalism. In the following chapters, namely Chapter 3, 4, 5, 6, we address the following questions:

Chapter 3: *How well can we measure the total mass profiles of extremely massive early-type galaxies that act as lenses at intermediate redshift, and how are their baryonic and dark matter components distributed? How can we reconstruct and characterize the background sources, thanks to spatially-extended strong lensing modeling?*

In this chapter, we study the total and baryonic mass distributions of the SDSS J0100+1818 deflector through a full strong lensing analysis. The system is composed by an ultra-massive early-type galaxy at $z = 0.581$, surrounded (at a distance of approximately 45 kpc) by ten multiple images of three background sources, two of which spectroscopically confirmed at $z = 1.880$ (initially, then in the following chapter we will expose new MUSE data and their improvements). The large angular separation between the multiple images and the very large stellar velocity dispersion value of (450 ± 40) km s $^{-1}$ initially measured with X-Shooter suggested that this galaxy could be the central galaxy of a (fossil) group, and between the most massive galaxies known at intermediate redshift, and could probe as a test for galaxy evolution models. We take advantage of high-resolution HST photometry and VLT/X-shooter spectroscopy to measure the positions of the multiple images and perform a strong lensing study with the software GLEE. We test different total mass profiles for the lens and model the background sources first as point-like and then as extended objects. We successfully predict the positions of the observed multiple images and reconstruct over approximately 7200 HST pixels the complex surface brightness distributions of the sources. We show the resulting total mass profile and dark matter distribution, from the effective radius ($R_e = 9.3$ kpc) to the outskirts ($R = 70$ kpc). We measure also the physical sizes of the lensed distant sources, resolving them down to a few hundreds of parsec. Finally, we quantify and discuss a relevant source of systematic uncertainties on the reconstructed sizes of background galaxies, associated to the adopted lens total mass model.

Chapter 4: *How can we develop an enhanced strong lensing model thanks to new MUSE data? What constraints can we put from such models to the values of the cosmological parameters? What*

is the impact on such values of multi-plane lensing, where additional deflection planes are introduced?

Integral Field Spectroscopy has had a tremendous impact on strong gravitational lensing studies, thanks to the possibility of obtaining the spectrum of all the sources over the field of view, without pre-selecting the targets. In this chapter we take advantage of new spectroscopic data from MUSE to securely measure the redshift of 65 sources, including five multiply imaged background sources (lensed into a total of 18 multiple images) and 19 galaxies on the deflector plane, all employed to build robust strong lensing models with the software **GLEE**. Two additional background sources, at $z = 4.95$, have been discovered thanks to their Ly α emission. We build an enhanced strong lensing model, employing the positions of all the 18 multiple images and modeling the deflector with group-scales halos (as previously done) but additionally adding all the group members with individual mass distributions. Thanks to the remarkably wide radial interval where the multiple images are observed, ranging from 15 to 77 kpc from the BGG, we accurately measure the total mass profile and infer the stellar over total mass profile of the deflector. Moreover, systems where multiple sources at different redshifts are strongly lensed by the same deflector allow one to directly investigate the evolution of the angular diameter distances as a function of redshift, and thus to learn about the geometry of the Universe. We present measurements of the values of the total matter density, Ω_m , and of the dark energy equation of state parameter, w , included in the strong lensing model as free parameters. Finally, given the presence of different sources angularly close in projection, we quantify through a multi-plane approach their impact on the inferred values of the cosmological parameters, and discuss such degeneracy in light of future surveys, like Euclid and Rubin-LSST.

Chapter 5: *What is the distribution of UV-continuum β slopes of the individual clumps we observe in high- z galaxies, and how does it evolve with the UV magnitude and the redshift? How can we reproduce and interpret the extremely slopes ($\beta \lesssim -2.7$) we observe?*

In this chapter, we study the ultraviolet (UV) continuum β slope of a sample of 166 clumps, individual star-forming regions observed in high redshift galaxies. They are hosted by 67 galaxies with redshift between 2 and 6.2, strongly lensed by the Hubble Frontier Fields cluster of galaxies MACS J0416.1–2403. The β slope value is sensitive to a variety of physical properties, such as the metallicity, the age of the stellar population, the dust attenuation throughout the galaxy, the stellar initial mass function (IMF), and the star-formation history (SFH). The aim of this chapter is to compare the β values of individual clumps with those measured on the entire galaxy, to investigate possible physical differences between these regions and their hosts. We investigate the evolution of β with the UV magnitude, M_{UV} , and the redshift, z . We conclude with a discussion on the most extreme slopes (“extremely blue slopes”, $\beta \lesssim -2.7$), making use of synthetic spectra to reproduce them, and infer their expected physical properties.

Chapter 6: *What is the origin of the (resonant) Ly α emission in a typical clumpy star-forming galaxy at high- z ? How can we use Ly α polarization to constrain between different models, that assume different physical properties of the scattering medium and its geometry?*

Ly α emission is the strongest tracer of recombining ionized hydrogen in young, star-forming galaxies, but its origin is still debated. Ly α arises when emitted photons scatter in neutral hydrogen, with each scattering event changing their propagation direction and frequency. So far, observational efforts have mostly focused on the Ly α surface brightness and spectral profile, which depend on the neutral hydrogen column density, geometry, kinematics,

powering mechanism and on the region from which the photons are emitted. Although different processes produce similar spectra, they have different degrees of polarization, that we can use to discriminate between them and to put stringent constraints on the geometry of the galaxy and its circumgalactic medium (CGM) where Ly α photons scatter, and on their emission mechanism. In this chapter, we present the first deep spectropolarimetric observations of a typical clumpy star-forming galaxy at $z \sim 3.4$, strongly lensed by the cluster of galaxies Abell 2895, taken with the Polarimetric Multi Object Spectroscopy (PMOS) mode of the VLT/FORS2 instrument. We develop a large set of new Ly α radiative transfer models, assuming a biconical outflow geometry, to reproduce the observations. We discuss what we can learn from such observations and comparison with the models, focusing on the different origin mechanisms that might originate the Ly α photons and on the geometry and symmetry of the scattering medium.

In Chapter 7, we draw the conclusions and discuss possible future perspectives. In the Appendixes A, B and C, we report additional material related to that presented in the Chapters 3, 5, and 6, respectively.

Unless differently specified, and in Section 4.5, throughout this thesis, we assume a flat cosmology with $H_0 = 70 \text{ km s}^{-1} \text{ Mpc}^{-1}$, $\Omega_m = 0.3$ and $\Omega_\Lambda = 0.7$. In this model, 1'' corresponds to a linear size of 6.585 kpc at the deflector redshift of $z = 0.581$, in Chapters 3 and 4. All magnitudes are given in the AB system (Oke 1974) and, in Chapters 3 and 4, are measured in the HST F160W filter.

CHAPTER 2

An introduction to strong gravitational lensing formalism

In General Relativity, light propagates along null geodetics of the space-time metrics. For the majority of the situations studied through gravitational lensing, the problem can be simplified by adopting the so-called gravitational lensing theory ([Schneider et al. 1992a, 2006; Narayan & Bartelmann 1996](#)).

The first approximation consists in assuming that the Newtonian gravitational potential is weak, i.e. $\frac{\phi_N}{c^2} \ll 1$. Space-time is in general described by the Minkowski metric,

$$g_{\mu\nu} = \text{diag}(1, -1, -1, -1) \quad (2.1)$$

that, if we include a weak perturbation, takes the form

$$g_{\mu\nu} = \begin{bmatrix} 1 + \frac{2\phi}{c^2} & 0 & 0 & 0 \\ 0 & -(1 - \frac{2\phi}{c^2}) & 0 & 0 \\ 0 & 0 & -(1 - \frac{2\phi}{c^2}) & 0 \\ 0 & 0 & 0 & -(1 - \frac{2\phi}{c^2}) \end{bmatrix}. \quad (2.2)$$

This weak field approximation implies that the light will be deflected by an angle $\hat{\alpha} \ll 1$, and thus in the following we will consider only small deflection angles. Moreover, we will examine exclusively cases where the velocity of the deflecting mass is small compared to the light speed c .

The second approximation consists in considering the deflecting mass as geometrically thin. Commonly, the physical linear scale of a lens along the line-of-sight (less than a Mpc¹) is much smaller than these distances (on the order of Gpc). For example, if we assume a standard flat Λ CDM cosmology with $H_0 = 70 \text{ km s}^{-1} \text{ Mpc}^{-1}$, $\Omega_m = 0.3$ and $\Omega_\Lambda = 0.7$, the angular-diameter distance of a deflector at $z = 0.581$ (the same of the system described in Chapter 3) is 1358.7 Mpc, and the angular-diameter distance between that deflector and a source at $z = 1.88$ is 990.7 Mpc. Both of them are much larger than the sub-Mpc scale, even considering the largest lenses. In this regime, the situation in which a light ray is smoothly curved near the lens plane can be approximated with two straight rays one traveling from the source to the deflector plane, and

¹The parsec (pc) is a unit of length used in astrophysics. A parsec is defined as the distance at which one astronomical unit (i.e., the distance between the Earth and the Sun) subtends an angle of one arcsecond.
1pc $\approx 3.086 \times 10^{16} \text{ m}$

the other from the deflector plane to the observer, that intersect the lens plane, with an angle $\hat{\alpha}$.

2.1 The lens equation

In the easiest case of a system composed by an observer, a deflector, and a source, like that shown in Fig. 2.1 (we will treat the case of multiple deflector planes in Section 2.4), there are three important angular-diameter distances: those from the observer to the deflector, D_d , from the observer to the source, D_s , and from the deflector to the source, D_{ds} . We note that, in general, $D_d + D_{ds} \neq D_s$.

A sketch of typical single-plane gravitational lensing system is shown in Fig.(2.1). We define the *optical axis* as the straight line perpendicular to the lens plane that connects the observer with the center of mass of the lens. Let η be the two-dimensional position of a source on the source plane and ξ the two-dimensional position of one of its images on the lens plane. Converting them into angular positions, we can state that

$$\eta = D_s \beta \quad \text{and} \quad \xi = D_d \theta \quad (2.3)$$

and we can write η in function of ξ and $\hat{\alpha}$.

$$\eta = \underbrace{\frac{\xi}{D_d}}_{\theta} D_s - \hat{\alpha}(\xi) D_{ds}. \quad (2.4)$$

Eq. 2.4 is known as the **ray-tracing equation** and we can use it to find the position of a source given the position of one of its images.

We can express it in angular units using the relations (2.3) as

$$\beta = \theta - \frac{D_{ds}}{D_s} \hat{\alpha}(D_d \theta) = \theta - \alpha(\theta), \quad (2.5)$$

where we define the scaled deflection angle $\alpha(\theta) = \frac{D_{ds}}{D_s} \hat{\alpha}(D_d \theta)$ in the last step.

If a lens is thin, the deflection is given by its distribution of mass $\rho(\xi, z)$ projected along the line-of-sight (let z be the coordinate along this direction and $\xi = (\xi_1, \xi_2)$ the two-dimensional vector in the lens plane defined above). We can define a surface mass density

$$\Sigma(\xi) = \int \rho(\xi, z) dz, \quad (2.6)$$

and the deflection angle can be expressed in terms of a surface mass density as

$$\hat{\alpha}(\xi) = \frac{4G}{c^2} \int d^2 \xi' \Sigma(\xi') \frac{\xi - \xi'}{||\xi - \xi'||^2}. \quad (2.7)$$

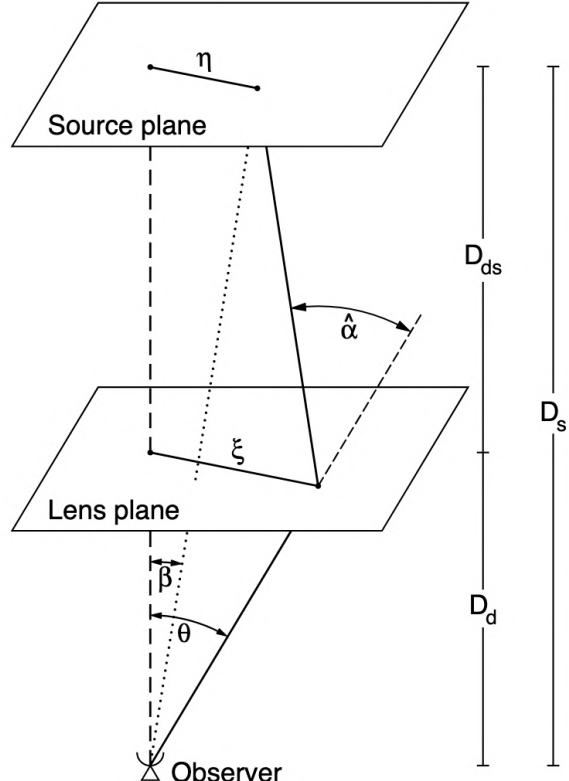


Figure 2.1: Sketch of a typical gravitational lensing system, from [Bartelmann & Schneider \(2001\)](#).

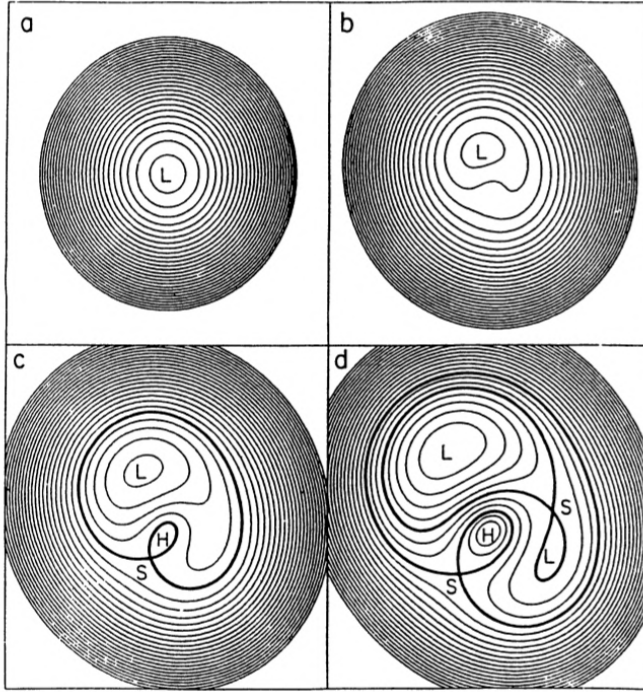


Figure 2.2: Contour levels of the Fermat potential with a fixed source position and increasing “strength” (i.e. surface density) of the lens. The letters indicate the stationary points: L is a minimum, H is a maximum and S is a saddle point. The strength is set to zero in (a) and it is weak in (b), in fact we can observe a single image distorted (weak lensing). In (c) and (d) we see the strong lensing regime with 3 and 5 images, respectively. From [Blandford & Narayan \(1986a\)](#).

Introducing the angular-diameter distances, we can write an expression for the scaled deflection angle:

$$\alpha(\boldsymbol{\theta}) = \frac{1}{\pi} \int d^2\boldsymbol{\theta}' \kappa(\boldsymbol{\theta}') \frac{\boldsymbol{\theta} - \boldsymbol{\theta}'}{||\boldsymbol{\theta} - \boldsymbol{\theta}'||^2}, \quad (2.8)$$

where we have defined the convergence (or dimensionless surface mass density) as

$$\kappa(\boldsymbol{\theta}) = \frac{\Sigma(D_d \boldsymbol{\theta})}{\Sigma_{cr}} \quad \text{with} \quad \Sigma_{cr} = \frac{c^2}{4\pi G} \frac{D_s}{D_d D_{ds}} \quad (2.9)$$

We note that Σ_{cr} only depends on the distances and it can be used to characterize weak and strong lensing. We can finally define the *lensing potential* as

$$\psi(\boldsymbol{\theta}) = \frac{1}{\pi} \int d^2\boldsymbol{\theta}' \kappa(\boldsymbol{\theta}') \ln ||\boldsymbol{\theta} - \boldsymbol{\theta}'||, \quad (2.10)$$

from which we obtain²

$$\nabla_{\boldsymbol{\theta}} \psi(\boldsymbol{\theta}) = \alpha(\boldsymbol{\theta}), \quad (2.11)$$

²Using

$$\nabla_{\boldsymbol{x}} \ln ||\boldsymbol{x}|| = \frac{\boldsymbol{x}}{||\boldsymbol{x}||^2}$$

i.e. the gradient of the lensing potential is the deflection angle. We can calculate the Laplace operator too³ as

$$\nabla_{\boldsymbol{\theta}}^2 \psi(\boldsymbol{\theta}) = 2\kappa(\boldsymbol{\theta}); \quad (2.12)$$

This is a Poisson equation that allows us to calculate $\psi(\boldsymbol{\theta})$ and then the deflection angle if we know the surface mass distribution of a lens.

We can finally introduce the *Fermat potential*, defined as

$$\Phi(\boldsymbol{\theta}, \boldsymbol{\beta}) = \frac{||\boldsymbol{\theta} - \boldsymbol{\beta}||^2}{2} - \psi(\boldsymbol{\theta}), \quad (2.13)$$

which depends on the position of the source and on the position of one of its images. If we calculate

$$\nabla_{\boldsymbol{\theta}} \Phi(\boldsymbol{\theta}, \boldsymbol{\beta}) = 0,$$

we obtain the ray-tracing equation 2.5: $\boldsymbol{\theta} - \boldsymbol{\beta} - \alpha(\boldsymbol{\theta}) = 0$. This shows that the position $\boldsymbol{\theta}$ where the image of a source located in $\boldsymbol{\beta}$ appears is a stationary point of the Fermat potential (see Fig. 2.2).

2.2 Magnification, critical curves and caustics

We can linearize the ray-tracing equation locally, defining the Jacobian matrix $\mathcal{A}(\boldsymbol{\theta}) \in \text{Mat}(2, 2)$ as

$$\mathcal{A}_{ij}(\boldsymbol{\theta}) \equiv \frac{\partial \boldsymbol{\beta}}{\partial \boldsymbol{\theta}} = \left(\delta_{ij} - \frac{\partial \alpha_i(\boldsymbol{\theta})}{\partial \theta_j} \right) = \left(\delta_{ij} - \frac{\partial^2 \psi(\boldsymbol{\theta})}{\partial \theta_i \partial \theta_j} \right) \equiv \mathcal{M}_{ij}^{-1}(\boldsymbol{\theta}), \quad (2.14)$$

such that

$$\boldsymbol{\beta} = \mathcal{A}(\boldsymbol{\theta}) \boldsymbol{\theta}. \quad (2.15)$$

$\mathcal{A}(\boldsymbol{\theta})$ is usually referred to as the *inverse magnification tensor*, as it is the inverse of the magnification tensor $\mathcal{M}(\boldsymbol{\theta})$. If we define the components of the so-called *shear* tensor $\boldsymbol{\gamma} = \gamma_1 + i\gamma_2$, that is responsible for the anisotropic distortion of the images of a source (see Fig. 2.3), as

$$\begin{aligned} \gamma_1(\boldsymbol{\theta}) &= \frac{1}{2} \left[\frac{\partial \psi}{\partial \theta_1 \partial \theta_1} - \frac{\partial \psi}{\partial \theta_2 \partial \theta_2} \right] \equiv \boldsymbol{\gamma}(\boldsymbol{\theta}) \cos [2\phi(\boldsymbol{\theta})], \\ \gamma_2(\boldsymbol{\theta}) &= \frac{\partial \psi}{\partial \theta_1 \partial \theta_2} = \frac{\partial \psi}{\partial \theta_2 \partial \theta_1} \equiv \boldsymbol{\gamma}(\boldsymbol{\theta}) \sin [2\phi(\boldsymbol{\theta})], \end{aligned} \quad (2.16)$$

we can explicitly write $\mathcal{A}(\boldsymbol{\theta})$ as

$$\begin{aligned} \mathcal{A}(\boldsymbol{\theta}) &= \begin{bmatrix} 1 - \kappa(\boldsymbol{\theta}) - \gamma_1(\boldsymbol{\theta}) & -\gamma_2(\boldsymbol{\theta}) \\ -\gamma_2(\boldsymbol{\theta}) & 1 - \kappa(\boldsymbol{\theta}) + \gamma_1(\boldsymbol{\theta}) \end{bmatrix} = \\ &= (1 - \kappa(\boldsymbol{\theta})) \begin{bmatrix} 1 & 0 \\ 0 & 1 \end{bmatrix} - \boldsymbol{\gamma} \begin{bmatrix} \cos[2\phi(\boldsymbol{\theta})] & \sin[2\phi(\boldsymbol{\theta})] \\ \sin[2\phi(\boldsymbol{\theta})] & -\cos[2\phi(\boldsymbol{\theta})] \end{bmatrix}, \end{aligned} \quad (2.17)$$

$\mathcal{A}(\boldsymbol{\theta})$ shows how sources are lensed into multiple images: the convergence κ produces an isotropic magnification of the source, that has the same shape but different size. Shear instead introduces anisotropy, that can be described by the shear magnitude $\gamma = \sqrt{\gamma_1 + \gamma_2}$ and the

³Using

$$\nabla_{\boldsymbol{x}}^2 \ln ||\boldsymbol{x}|| = 2\pi \delta^2(\boldsymbol{x})$$

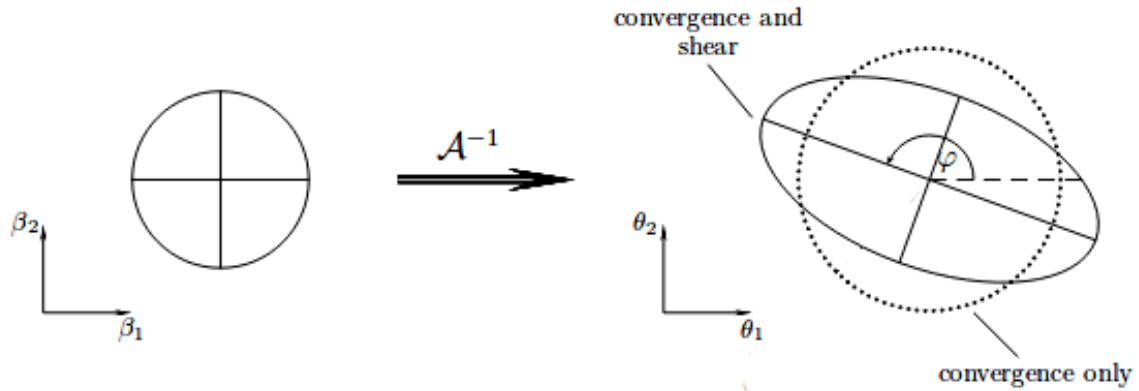


Figure 2.3: A circular source, shown at the left, is mapped by the inverse Jacobian \mathcal{A}^{-1} onto an ellipse. Without shear, the resulting image would still be a circle, but with modified radius, depending on κ . The semi-axes are $a_{\pm} = \frac{r}{1-\kappa \mp \gamma}$. The orientation of the resulting ellipse depends on the phase of the shear. From: [Narayan & Bartelmann \(1996\)](#).

orientation, ϕ . These effects are shown in Fig. 2.3. Thus, a circular source is mapped into ellipses, with axes $(1 - \kappa - \gamma)^{-1}$ and $(1 - \kappa + \gamma)^{-1}$, and orientation ϕ . The local solid angle distortion is given by the determinant of \mathcal{A} and transforms a solid angle $\delta\beta^2$ into $\delta\theta^2$, and thus the magnification factor ($\mu(\boldsymbol{\theta})$) is given by the determinant of $\mathcal{A}(\boldsymbol{\theta})$ as

$$\mu(\boldsymbol{\theta}) = \frac{1}{\det \mathcal{A}(\boldsymbol{\theta})} = \det \mathcal{M}(\boldsymbol{\theta}) = \frac{1}{(1 - \kappa(\boldsymbol{\theta}))^2 - |\gamma(\boldsymbol{\theta})|^2} \quad (2.18)$$

The sign of the magnification (see Eq. 2.18) defines the parity of the image: if it is negative, the images are mirror-symmetric compared to the source.

The points on the lens plane in which the Jacobian vanishes (i.e., $\det \mathcal{A}(\boldsymbol{\theta}) = 0$) describe closed and smooth curves, called *critical curves*. Mapping these curves onto the source plane, we find the *caustics*, which are not smooth and can have cusps. Observing the critical curves and caustics allows one to understand qualitatively the geometry and the characteristics of a lensing system (see Fig. 2.4).

A point-like image which lies on a critical curve has a magnification that mathematically diverges, but it does not have a physical meaning and all the magnifications that we observe are finite, mainly because the sources have a finite size. A source located near a caustic produces very magnified images located near the corresponding critical curve. Moreover, the weak or strong lensing regime depends on the position of a source with respect to the caustics. A source with large $\|\boldsymbol{\beta}\|$ will have only one image, at $\boldsymbol{\theta} \approx \boldsymbol{\beta}$. Noting that the lens mapping is invertible where $\det \mathcal{A}(\boldsymbol{\theta}) \neq 0$, unless a source moves across a caustic, the number of images will not change. When a caustic is crossed, towards the inner region, a pair of images is created. As anticipated, caustics are not necessarily smooth: it is possible to distinguish *cusp* and *fold caustics* (see Fig. 2.4). Finally, we obtain a qualitative scheme of the geometry of a lensing system from the critical curves and caustics. The critical curves divide the lens plane into regions of different image parity. Similarly, the corresponding caustics define regions of different image multiplicity.

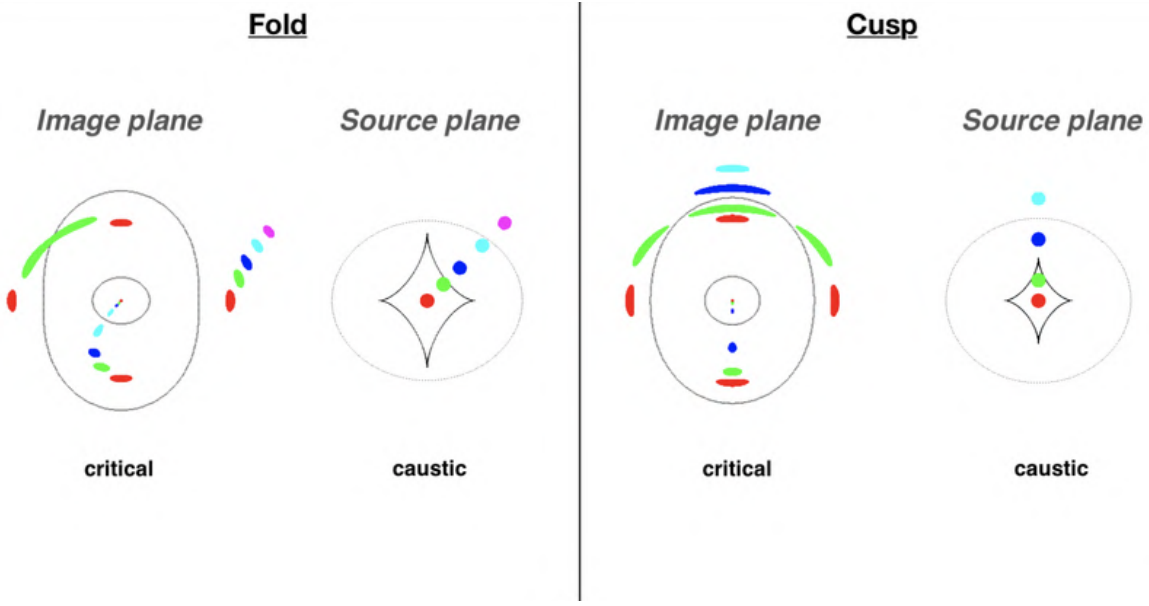


Figure 2.4: Compact source moving away from the center of an elliptical lens, crossing a fold (on the left) or crossing a cusp caustic (on the right). For each pair of images, it is shown on the right the caustics and the position of the source, and on the left the critical curves and the position of the corresponding images (with the same colors). Adapted from: [Narayan & Bartelmann \(1996\)](#).

2.3 Time delays

Time delays are the only observables of gravitational lensing, that are dimensional, and they are linked to the values of the angular-diameter distances, which are proportional to the value of the Hubble constant. Thus, the differences in propagation time are proportional to H_0^{-1} ([Refsdal 1964b](#)). These properties allow one, for instance, to distinguish two gravitational lensing systems which are identical, but one of them has all the distances doubled (fixing the value of the Hubble constant). In this situation, time delays are essential, because angular separations and flux ratios are the same. If a lens produces at least two images of a source, the light-travel-times will in general be different, and for variable sources, the differences are observable as time delays. There are two effects which contribute. First, the different paths will have different length (*geometrical time delay*). Second, different paths cross the gravitational field of the deflector in different regions, thus the light rays are delayed in different ways (*potential time delay*). From the weak-field metric (Eq. 2.2), the coordinate time interval dt for a ray to travel a length dl is

$$c \, dt \approx (1 - 2\phi) \, dl. \quad (2.19)$$

It can be expanded ([Schneider et al. 1992b](#)), in angular units, to

$$c \Delta t(\beta) = \frac{D_s D_d}{D_{ds}} (1 + z_l) \left[\Phi(\theta^{(1)}, \beta) - \Phi(\theta^{(2)}, \beta) \right]. \quad (2.20)$$

If we substitute the definition of the Fermat potential (Eq. 2.13), we see that the first term in the definition represents the deviation of the light ray from a straight path, i.e. the geometrical delay, and the second is the potential delay.

The first measurement of a time delay has been described by [Florentin-Nielsen \(1984\)](#), who studied the gravitational lens QSO 0957+561 and measured a time delay $\Delta t = 1.55 \pm 0.1$ yr

between two multiple images, for which he determined an Hubble constant value of $H_0 = 77 \text{ km s}^{-1} \text{ Mpc}^{-1}$. The basic procedure to measure a time delay consists on finding a variable source which is multiply lensed, and observing it for a time which is longer than that of its variability. This has been done for the first simple systems with a galaxy as lenses but, despite their complex mass distribution, systems with more images allow one to measure multiple time delays and to measure the value of H_0 with a lower uncertainty. In some particular cases, as for example for the multiply imaged supernova Refsdal (Refsdal 1964b), for which four of the predicted six multiple images were observed appearing at different times, it has been possible to build a model and predict when and where the next image would appear (Kelly et al. 2016; Grillo et al. 2016). This was then confirmed by later observations (see Grillo et al. 2024) There are usually three main problems in the measurement of the time delays: the first one is that, from the definition of the time delays, the observer has to measure very accurately the redshifts of the lens and of the source, and the relative positions of the multiple images with respect to the center of the lens. Today, with the latest instruments and telescopes, the required accuracy is usually reached, but it can be difficult in regions with strong dust extinction or in extremely dense environments. This is also the second main problem: the environment of the lens can make very difficult the lens modelling, because of neighbor objects that can affect significantly the time delays (Treu & Marshall 2016). The last problem is the degeneracy of the mass density of the deflector, known as the mass-sheet degeneracy: if one adds a sheet of constant mass density to the real total mass distribution of the lens, the image positions, flux ratios, and time delay do not change and there is no way to distinguish between the different mass densities.

2.4 Multi-plane formalism

In some cases, there is more than one deflecting mass distribution along the line of sight and a correct multi-plane approach is essential to properly reconstruct the path followed by the light rays and to perform a strong lensing analysis. Such systems, as will be described in Section 4, are particularly suitable for cosmography, i.e., to infer the values of the cosmological parameters defining the geometry of the Universe, namely Ω_m , Ω_Λ , and w . In fact, as shown in Section 2.1, the efficiency of a lens depends on the mutual distances between the source, the deflector, and the observer, and on the convergence κ of the lens. If we consider Eq. 2.10 and isolate the contributions that depend on the distance of a source, we can write it as

$$\psi(\boldsymbol{\theta}, z_s) \equiv \psi_0(\boldsymbol{\theta}) \frac{D_{ds}}{D_s} \quad \text{where} \quad \psi_0(\boldsymbol{\theta}) = \frac{4GD_d}{c^2} \int d^2\theta' \kappa(\boldsymbol{\theta}') \ln \|\boldsymbol{\theta} - \boldsymbol{\theta}'\|. \quad (2.21)$$

Thus, if we consider two multiple images at positions $\boldsymbol{\theta}_1$ and $\boldsymbol{\theta}_2$ of two sources at redshifts z_{s1} and z_{s2} , we can measure the ratio of the two distances (e.g., Bartelmann 2003; Schneider 2014; Gavazzi et al. 2008)

$$\eta \equiv \frac{\left(\frac{D_{ds}}{D_s}\right)_{z_{s1}}}{\left(\frac{D_{ds}}{D_s}\right)_{z_{s2}}}, \quad (2.22)$$

after assuming a model of the deflector, and thus giving assumptions on $\psi_0(\boldsymbol{\theta})$ and its derivatives defining the deflection, the convergence, and the shear.

In the multi-plane formalism, the total deflection angle is a suitable sum of all the deflection angles relative to the different deflector planes (see, e.g., Bartelmann 2003; Gavazzi et al. 2008). This approach has been used to model both different foreground and background deflectors at distances different from that of the primary lens (e.g., Chirivì et al. 2018; Schuldt et al. 2024,

Acebron et al., in prep.) and to assign mass to multiply imaged background sources, where several sources at different redshifts are lensed by the same deflector (e.g., Gavazzi et al. 2008; Schuldt et al. 2019; Collett & Smith 2020; Wang et al. 2022).

A light ray, in this formalism, follows straight paths between the different planes, but it is not deflected only once, but is rather deflected N times of an α_N angles, and the total deflection angle will be the vectorial sum of those angles. Hence, Eq. 2.4 can be generalized, and a light ray from the image plane at a physical coordinate ξ_1 will reach the source plane at a coordinate

$$\eta(\xi_1) = \frac{D_s}{D_1} \xi_1 - \sum_{i=1}^N \hat{\alpha}(\xi_i) D_{is}, \quad (2.23)$$

where D_i are the angular-diameter distances from the observer to the i -th lens plane, and D_{is} those from the i -th lens plane to the source plane. In angular coordinates, it can be written as

$$\theta_j(\theta_1) = \theta_1 - \sum_{i=1}^{j-1} \frac{D_{ij}}{D_j} \hat{\alpha}(\theta_i), \quad (2.24)$$

where again we defined the scaled deflection angle $\alpha(\theta) = \frac{D_{is}}{D_s} \hat{\alpha}(\theta_i)$. One of the j -th lens planes can also be a source plane, in cases where several sources are aligned and the light rays from the furthest one are deflected by the masses of the other sources, as shown in Fig. 2.5. We investigate the impact of mutual lensing of aligned sources in Section 4.5.1.

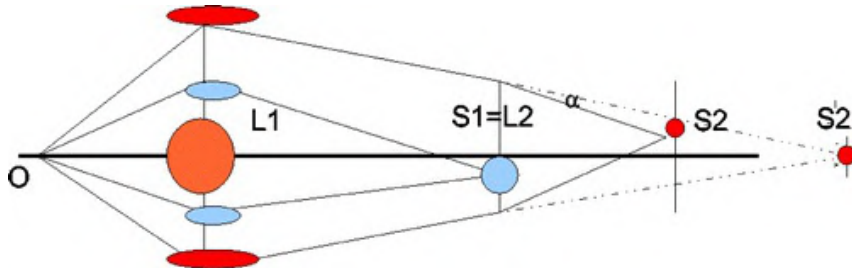


Figure 2.5: Sketch of a lensing system with source 1 (S1) and source 2 (S2) are lensed by a main lens (L1), but additionally S1 act as a perturbing lens ($S1=L2$) on S2, at $z_{s2} > z_{s1}$. From Gavazzi et al. (2008).

CHAPTER 3

Studying the most massive early-type galaxies acting as strong gravitational lenses at intermediate redshift

The results reported in this chapter have been described in:

the manuscript “Reconstructing the extended structure of multiple sources strongly lensed by the ultra-massive elliptical galaxy SDSS J0100+1818”, **Bolamperti A.**, Grillo C., Cañameras R., Suyu S. H., Christensen L., 2023, A&A, 671, A60 and the proceeding “Extended surface brightness modeling of three sources strongly lensed by an ultra-massive elliptical galaxy ”, **Bolamperti A.**, 2024, IAUS, 381, 113.

3.1 Introduction

In the last few decades, several studies have suggested the presence of a significant amount of dark matter (DM), both in elliptical (e.g., [Loewenstein & Mushotzky 2003](#)) and spiral (e.g., [Rubin 1983](#)) galaxies. These studies have measured total mass-to-light ratios considerably higher than the stellar ones and observed a remarkable difference between the visible, that is, stellar plus gas, and total mass estimated from galaxy dynamics (e.g., [Rubin & Ford 1970](#); [Gerhard et al. 2001](#); [Cappellari et al. 2006](#)). Since then, cosmological observations of the cosmic microwave background ([Smoot et al. 1992](#); [Hinshaw et al. 2013](#); [Planck Collaboration et al. 2020](#)), of baryon acoustic oscillations ([Efstathiou et al. 2002](#); [Eisenstein et al. 2005](#); [DESCollaboration et al. 2021](#)), and of Type Ia supernovae ([Riess et al. 1998](#); [Perlmutter et al. 1999](#); [Scolnic et al. 2018](#)) have all supported the currently accepted Λ cold dark matter (CDM) model, according to which $\approx 30\%$ of the Universe is composed of baryons and CDM and the remaining $\approx 70\%$ is a poorly understood component, known as dark energy, that is responsible for the accelerated expansion of the Universe. However, the Λ CDM model, which has been very successful at large scales ($\gtrsim 1$ Mpc), cannot accurately predict the properties of structures at smaller scales, such as the value of the inner slope of DM halos (e.g., [Gnedin et al. 2004](#); [Newman et al. 2013b,a](#); [Martizzi et al. 2012](#)). Hence, the interplay between DM and baryons on galactic scales is still being intensively investigated.

N -body simulations of DM particles show that, at equilibrium, they are distributed following an almost universal mass density profile, $\rho(r)$, first described by the Navarro-Frenk-White profile ([Navarro, Frenk, & White 1997](#)). This profile has a characteristic slope, which varies from $\rho_{r \ll r_s} \propto r^{-1}$ at small radii, and thus has a central cusp, to $\rho_{r \gg r_s} \propto r^{-3}$ at large radii. Recent

simulations with higher resolution (e.g., [Golse & Kneib 2002](#); [Graham et al. 2006](#); [Navarro et al. 2010](#); [Gao et al. 2012](#); [Collett et al. 2017](#); [Dekel et al. 2017](#)) and with realistic models that describe the baryonic components predict mass density profiles that deviate from the Navarro-Frenk-White one. This mainly depends on processes such as gas cooling, which allows baryons to condense toward the center of a galaxy (e.g., [Blumenthal et al. 1986](#); [Gnedin et al. 2004](#); [Sellwood & McGaugh 2005](#); [Gustafsson et al. 2006](#); [Pedrosa et al. 2009](#); [Abadi et al. 2010](#); [Sommer-Larsen & Limousin 2010](#)), active galactic nuclei feedback (e.g., [Peirani et al. 2008](#); [Martizzi et al. 2013](#); [Li et al. 2017](#)), dynamical heating in the central cuspy region, due to infalling satellites and mergers (e.g., [El-Zant et al. 2001, 2004](#); [Nipoti et al. 2004](#); [Romano-Díaz et al. 2008](#); [Tonini et al. 2006](#); [Laporte & White 2015](#)), and thermal and mechanical feedback from supernovae (e.g., [Navarro et al. 1996](#); [Governato et al. 2010](#); [Pontzen & Governato 2012](#)).

In this context, the observation of very massive (and DM-rich) galaxies and the measurement of their inner total, DM, and baryonic mass profiles represent a key step in understanding how the different mass components are distributed, and inferring how galaxies formed and evolved over cosmic time. These studies can be addressed by exploiting very massive galaxies that act as gravitational lenses.

Strong gravitational lensing represents a powerful tool for studying galaxy evolution and for exploring the properties of the Universe (e.g., [Bartelmann 2010](#); [Treu 2010](#)). Given the fact that the deflection of the light emitted by a source only depends on the total gravitational potential of the lens, gravitational lensing is sensitive to both luminous and DM mass and allows one to obtain some of the most precise total mass measurements, with relative errors on the order of a few percent, in extragalactic astrophysics (e.g., [Grillo 2010](#); [Zitrin et al. 2012](#)). Together with the results obtained by exploiting the most massive lenses, such as galaxy clusters, about the slope value of the mass density of the DM halos in their inner regions ([Sand et al. 2004](#); [Grillo et al. 2015](#); [Annunziatella et al. 2017](#); [Bergamini et al. 2019](#)), the measurements of the cosmological density parameter values ([Jullo et al. 2010](#); [Caminha et al. 2016](#); [Grillo et al. 2020](#)), and the value of the Hubble constant ([Grillo et al. 2018](#)), galaxy-scale strong gravitational lenses have provided several key results (e.g., [Suyu et al. 2013, 2017](#)). In particular, it has been possible to characterize the physical properties of the lens, for instance to reconstruct the total and DM mass distributions, and thus the DM over total mass fraction ([Gavazzi et al. 2007](#); [Grillo et al. 2009](#); [Suyu & Halkola 2010](#); [Sonnenfeld et al. 2015](#); [Schuldt et al. 2019](#)) and the mass density slopes (e.g., [Treu & Koopmans 2002](#); [Koopmans et al. 2009](#); [Barnabè et al. 2011](#); [Shu et al. 2015](#)), to infer the most likely lens stellar initial mass function (IMF; e.g., [Cañameras et al. 2017b](#); [Barnabè et al. 2013](#); [Sonnenfeld et al. 2019](#)), and to identify DM substructures (e.g., [Vegetti et al. 2012](#); [Hezaveh et al. 2016](#); [Ritondale et al. 2019](#)). It has also been shown how the values of some cosmological parameters can be measured in strong lensing systems using kinematic data of the lenses (e.g., [Grillo et al. 2008](#); [Cao et al. 2012](#)) or in systems where two or more sources are multiply imaged by the same lens galaxy ([Tu et al. 2009](#); [Collett & Auger 2014](#); [Tanaka et al. 2016](#); [Smith & Collett 2021](#)), once the mass sheet degeneracy is broken ([Schneider 2014](#)).

Moreover, gravitational lensing offers the opportunity to study the lensed background sources: they can be fully reconstructed by taking their surface brightness (SB) distribution into consideration during the strong lensing modeling (e.g., [Schuldt et al. 2019](#); [Rizzo et al. 2021](#); [Wang et al. 2022](#)). They can also be analyzed in detail thanks to high magnification factors, which allow one to investigate the local feedback mechanisms driving the evolution of the faintest and smallest high- z galaxies (e.g., [Fürster Schreiber et al. 2009](#); [Cañameras et al. 2017a](#); [Cava et al. 2018](#); [Iani et al. 2021](#)).

In this chapter, we show the measurements of the total and baryonic mass distributions of the deflector SDSS J010049.18+181827.7 (hereafter, SDSS J0100+1818) included in the Cambridge And Sloan Survey Of Wide ARcs in the skY (CASSOWARY) survey (Belokurov et al. 2009; Stark et al. 2013)¹. The exceptionally large Einstein radius of ≈ 42 kpc, together with the results from our follow-up observations with the Nordic Optical Telescope (NOT), the Very Large Telescope (VLT), and the *Hubble* Space Telescope (HST), presented in Sect. 3.2, suggests that the SDSS J0100+1818 deflector is an uncommonly strong lens and a candidate fossil system at intermediate redshift (Johnson et al. 2018b).

This chapter is organized as follows. In Sect. 3.2 we present the photometric and spectroscopic observations of SDSS J0100+1818. In Sect. 3.3 we focus on the main lens galaxy, showing the results of its stellar mass, kinematics, luminosity profile, and environment. In Sect. 3.4 we perform a strong lensing analysis by exploiting different sets of point-like multiple images and illustrate the best-fit models and the deflector total mass profile. We enhance the analysis in Sect. 3.5, where we model the deflector by considering the extended SB of the lensed sources. At the end of the section, we study the reconstructed sources assuming different models and comparing their reconstructed sizes. In Sect. 3.6 we summarize and discuss the main results.

3.2 Observations and data reduction

3.2.1 HST imaging

We observed SDSS J0100+1818 with the HST Wide Field Camera 3 (WFC3) in June and August 2018 (program GO-15253; PI: R. Cañameras), during one orbit in each of the two F438W and F160W filters. We used `astrodrizzle` from the `DrizzlePac` software package (Fruchter et al. 2010) to improve the correction for geometric distortion on the individual exposures calibrated with the standard HST pipeline. We also optimized both the rejection of cosmic rays with dedicated bad pixel masks, and the subtraction of the local sky background. Small regions with decreased sensitivity in the IR channel of WFC3 (blobs) were corrected using flat fields from the most recent version of the IR blob monitoring (Sunnquist 2018). The individual exposures were then re-drizzled and combined with inverse-variance weighting. For the F160W band, we adopted a pixel scale $0.066'' \text{ pix}^{-1}$ to adequately sample the point spread function (PSF), and a value `final_pixfrac` = 0.8 optimized for this pixel scale. For the F438W band, we used $0.033'' \text{ pix}^{-1}$ and `final_pixfrac` = 0.6. The PSF full widths at half maximum (FWHMs) measured on isolated stars in the field are $0.086''$ and $0.187''$ in F438W and F160W, respectively.

3.2.2 NOT imaging

We used the 2.5 m NOT (program 56-032, PI: R. Cañameras), to obtain color information for galaxies in the lens environment and to characterize their spectral energy distributions (SEDs). In October 2017, we obtained StanCam imaging in the B and R bands with good or average weather conditions, and total exposure times of 2400 and 3600 s, respectively. We added a 900 s long V-band exposure obtained with ALFOSC in October 2013 through the fast track service (program 47-426, PI: C. Grillo). Image reduction was conducted with standard `IRAF` routines. We then used the Scamp and SWarp software (Bertin 2006, 2010) to correct for geometric distortion,

¹The ID of this system has changed in the CASSOWARY survey in the past years. It was called CSWA 15 when we first targeted it, but it is currently identified as CSWA 115. In the main text, to avoid confusion, we refer to it as SDSS J0100+1818.

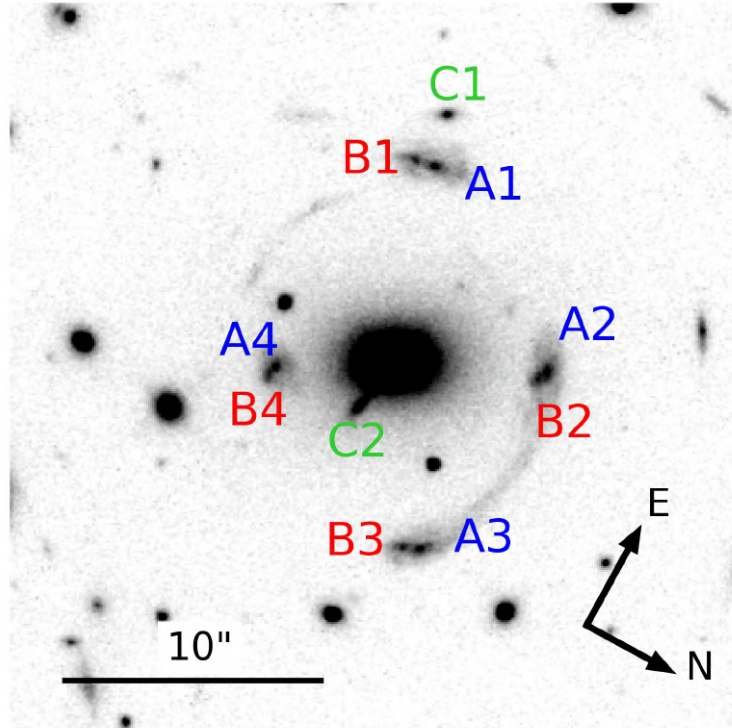


Figure 3.1: F160W image of the strong lensing system analyzed in this work. The multiple images corresponding to each of the three background sources considered in the analysis are labeled A1-A4, B1-B4, and C1-C2. Later in this study we show that sources A and B represent two emission peaks of a single extended source.

resample individual frames and align them with respect to the WCS, using the USNO-B1² catalog as reference, and to obtain relative alignments with a rms accuracy below $0.1''$. This resulted in a joint field-of-view of $2.5' \times 2.5'$, pixel sizes of $0.19''$, and PSF FWHMs of $1.05''$, $0.70''$, and $0.95''$, in B, V, and R, respectively. Photometric calibration was performed with respect to SDSS, using color corrections from Jester et al. (2005), and refined by fitting blackbody functions to stars in the field. The AB magnitudes of the main lens galaxy in B, V, and R bands are 22.57 ± 0.06 , 21.62 ± 0.10 , and 20.22 ± 0.12 , respectively.

3.2.3 VLT/X-Shooter spectroscopy

SDSS J0100+1818 was observed with VLT/X-Shooter (Vernet et al. 2011) (program 091.A-0852, PI: L. Christensen), in order to measure the lens and source spectroscopic redshifts, and to infer the lens stellar velocity dispersion. The main lens galaxy was observed in August and September 2013 with a $1.2''$ wide slit, seeing $\simeq 1''$, clear sky conditions, and with a total on-source integration time of 3.2 hours aimed at reaching a S/N of 5–10 per spectral bin in the VIS arm. The five individual OBs used a generic object, sky, object observing sequence with a $21''$ offset. As part of the same program, a separate one-hour long OB targeted two multiple images of the brightest lensed source, by nodding between the two images with a $19''$ offset.

After rejecting cosmic rays with Astro-SCRAPPY (McCully & Tewes 2019), the OBs were reduced

²tdc-www.harvard.edu/catalogs/ub1.html

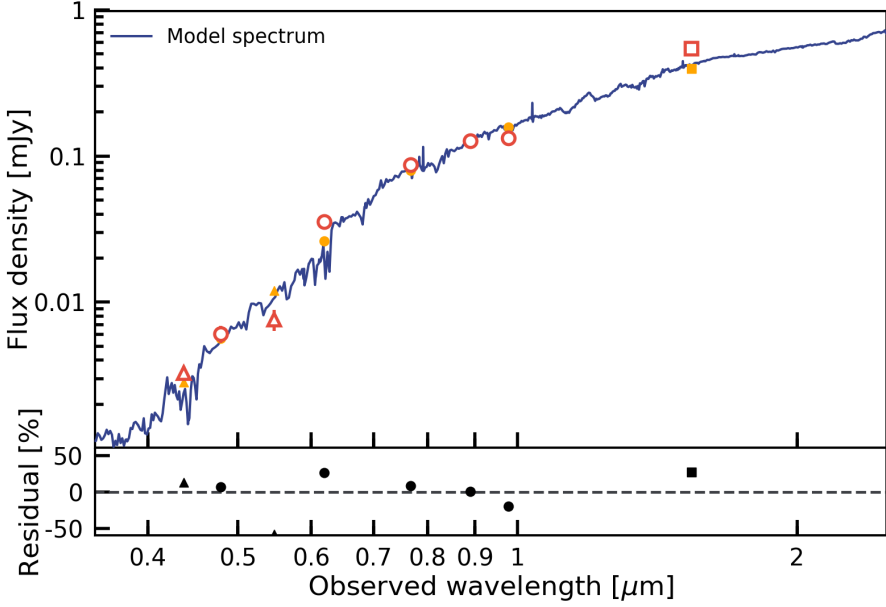


Figure 3.2: Spectral energy distribution of the main lens galaxy of SDSS J0100+1818. The observed flux densities from NOT (red triangles), Pan-STARRS (red circles), and HST (red square) are used to fit the SED with the CIGALE software. Error bars are smaller than the symbols. The best-fit stellar continuum template (blue curve) corresponds to the model fluxes plotted in orange and is used to infer the total stellar mass value of the deflector. The bottom panel shows the relative residuals of the fit.

with the X-Shooter pipeline (Modigliani et al. 2010) using the EsoReflex environment version 2.8.3 (Freudling et al. 2013). The OB nodding between the two lensed images was reduced in stare mode in order to measure the sky background directly from the frames. We used the observations of telluric standard stars taken within two hours of the science observations at similar airmass, to correct for telluric absorption using the atmospheric synthetic spectra from Molecfit (Smette et al. 2015; Kausch et al. 2015). The combination of individual exposures, the subtraction of residual sky emission, and the optimization of the wavelength calibration were then performed with separate scripts (see Selsing et al. 2019). The $0.1\text{--}1''$ offsets between the UVB and VIS arms resulting from the lack of atmospheric dispersion compensation at the time of the observations were also corrected on the 2D spectra. Finally, we conducted an optimal, profile-weighted extraction of the 1D spectrum of the lens galaxy of SDSS J0100+1818, and we extracted 1D spectra of multiple images using fixed apertures.

3.3 The SDSS J0100+1818 deflector

SDSS J0100+1818, (RA, dec) = (01:00:49.18, +18:18:27.79), was introduced in a late version of the CASSOWARY catalog, and was not included in the spectroscopic confirmation program from Stark et al. (2013). We therefore used the X-Shooter spectra to measure secure redshifts for the main lens elliptical galaxy and lensed source. The best-fit lens redshift of $z = 0.581$ was inferred from the most prominent rest-frame optical absorption lines, as part of the stellar kinematic analysis detailed in Sect. 3.3.3. We inferred a joint redshift of $z = 1.880$ for the two source components forming image families A and B visible in Fig. 3.1. Given the low S/N values of the lines detected in the 2D spectra, this source redshift estimate is obtained from a joint

analysis of the multiple images targeted by the X-Shooter OBs. The width of the lines detected at about 10740 in the binned 2D spectra of A1/B1, A3/B3, and A4/B4 is consistent with the $[\text{OII}]\lambda\lambda 3727$ doublet. Together with a faint detection of $[\text{OIII}]\lambda 5007$ in A3/B3 (Appendix A) and with the lack of additional line detections over the spectral range covered by X-Shooter, the detection of $[\text{OII}]\lambda\lambda 3727$ for the separate images ensures that the source redshift is robust. The 1D spectra of these multiple images are shown in the Appendix A.

By combining observations in the HST F160W and F438W filters with the first strong lensing models of the system, we identified another candidate background source, whose two multiple images are labeled with C1 and C2 in Fig. 3.1. Even though we are lacking spectroscopic confirmation, we include source C in our strong lensing models, with its redshift value as a free parameter, because the observation of two images with similar colors, robustly predicted at the same positions by the strong lensing models makes its multiply imaged nature highly likely. However, without a spectroscopic redshift measurement for source C, we cannot determine whether AB or C is the most distant source, so we will not be able to perform a multiplane lensing analysis here, and thus the light emitted by each source will be deflected only by the total mass distribution of the main lens, and not by any other background source. Then, thanks to the available photometric data and lensing model predictions, we also hypothesize the presence of an additional background source, with four multiple images. These images are barely detected in the HST data and two of the multiple images appear angularly very close to candidate group members. Thus, the one-component mass models we develop in this study might not be able to properly reconstruct these images. For these reasons, we do not consider this extra background source in the strong lensing models presented in this chapter, where we focus on the multiple images A, B, and C. We postpone to a future study a more detailed analysis of this fourth multiple-image family, when new data will possibly become available (see the last point in Sect. 3.6).

In the following we present the physical properties of the main deflector, such as its stellar mass, luminosity profile and stellar kinematics, measured from the full photometric and spectroscopic data set. The last subsection is dedicated to the study of the lens environment, discussing the possible group nature of this system.

3.3.1 Stellar mass

The SED of the main lens galaxy is modeled with the Code Investigating GAlaxy Emission (CIGALE; [Burgarella et al. 2005](#); [Noll et al. 2009](#); [Boquien et al. 2019](#)). We use the multiband photometry from the Panoramic Survey Telescope & Rapid Response System (Pan-STARRS), NOT, and HST, taking the F160W flux corrected from contamination by neighboring sources. The magnitudes are measured with SExtractor ([Bertin & Arnouts 1996](#)), using ISOCORR down to 3σ isophotes in all bands for the main lens galaxy, except for the magnitude in HST F160W filter, measured from its luminosity profile, as described in the next subsection. The grid of models to conduct SED fitting relies on [Bruzual & Charlot \(2003\)](#) single stellar population templates, and assume delayed star formation histories with exponential bursts and e-folding times in the range 0.1–1 Gyr, ages between 0.5 and 8 Gyr, and the modified [Charlot & Fall \(2000\)](#) extinction law. We assume a Salpeter ([Salpeter 1955](#)) stellar IMF and fix the metallicity to solar values, as expected for massive early-type galaxies at $z \sim 0.6$ ([Sonnenfeld et al. 2015](#); [Conroy et al. 2013](#); [Gallazzi et al. 2014](#)). The best-fit SED shown in Fig. 3.2 results in a total stellar mass value of $(1.5 \pm 0.3) \times 10^{12} M_{\odot}$.

3.3.2 Luminosity profile

We perform the photometric modeling of the system using the public software GALFIT (Peng et al. 2002, 2010). Considering the HST image in the F160W band, we extracted a cutout centered on the deflector with size of approximately $30'' \times 30''$ (see Fig. 3.3). Then, we decided to model the main lens and two other bright galaxies, located between the main lens and the multiple figures/lensing1/arcs. We masked out the external regions, where some bright objects are present, and the arcs, including the multiple image C2 (see the masked pixels, in white, in the right-hand panel of Fig. 3.3). In particular, C2 is too close to the main lens and radially distorted to be separately and adequately modeled. The very low values of the normalized residuals, without any clear pattern, confirm the goodness of our modeling choices.

We assume Sérsic (Sérsic 1963) profiles for the galaxies, and a uniform distribution for the background. The parameter values are optimized by minimizing a standard χ^2 function, defined as

$$\chi^2 = \sum_i^{N_{\text{pix}}} \frac{(f_i^{\text{data}} - f_i^{\text{model}})^2}{\sigma_i^2}, \quad (3.1)$$

where the index i runs over all the non-masked pixels, up to N_{pix} , f_i^{data} is the intensity value of the i -th pixel in the input data image and f_i^{model} is the intensity value in the same pixel predicted by the model, after the convolution with the estimated PSF. The PSF we use was obtained by combining several non-saturated bright stars in the field-of-view, stacking them, subtracting the background, and then normalizing the resulting image.

To better reproduce the observations, and thus to reduce the residuals in the inner regions, the main lens galaxy has been modeled with a combination of two Sérsic profiles. The centers of the two components are not forced to coincide, but the best-fit centers differ by less than 1 pixel. In Fig. 3.3, the considered cutout is shown in the left panel, the best-fit model in the middle one, and the normalized residuals in the right one. The number of degrees of freedom is evaluated from the number of considered (non-masked) pixels N_{pix} and the number of free parameters of the model N_{par} , as $\text{ndof} = N_{\text{pix}} - N_{\text{par}}$. The minimum χ^2 value is 13899, which, with a number of degrees of freedom $\text{ndof} = 46752$, corresponds to a reduced χ^2 value of ~ 0.3 .

We made use of the best-fit model of the main lens galaxy for three purposes: (1) We worked with lens-subtracted images in the strong gravitational lensing modeling, explained in the following sections, to avoid the lens light contaminating the multiple images and the arcs. This will be particularly important when considering source C, for which the multiple image C2 is angularly very close to the lens center.

(2) We built the cumulative luminosity profile of the deflector, from which we measure a total F160W magnitude value of $m_{\text{F160W}} = 17.06 \pm 0.05$, and an effective (i.e., half-light) radius value of $(1.42 \pm 0.02)''$, corresponding to (9.32 ± 0.12) kpc at $z = 0.581$. The value of the total magnitude was considered in the SED fitting (see Fig. 3.2), from which we measured the total stellar mass value.

(3) We converted the luminosity profile into a stellar mass profile, shown in Fig. 3.4, by assuming a constant stellar mass-to-light-ratio. In detail, we considered the galaxy cumulative luminosity profile, normalized it with the total luminosity value, and then multiplied this adimensional profile by the value of the total stellar mass of the central galaxy, obtained from its SED fitting. The figure also shows the 1σ uncertainty and the value of the effective radius.

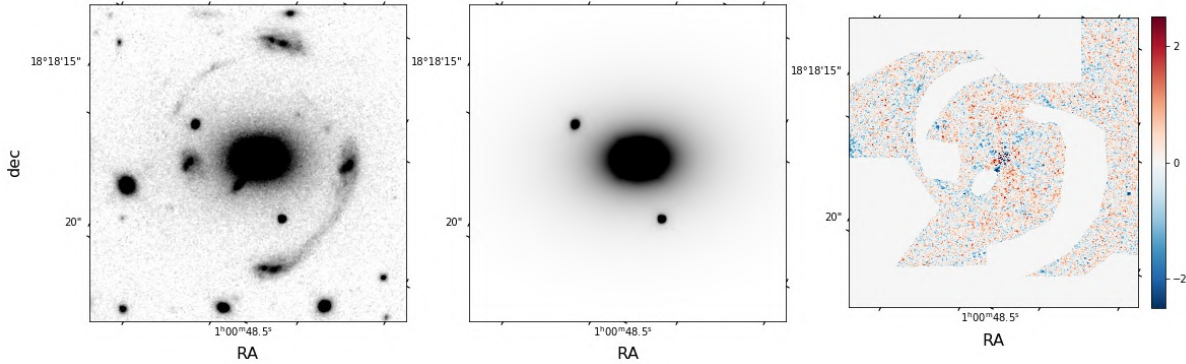


Figure 3.3: Results of the photometric modeling of the system with GALFIT. Left: Considered cutout of the HST image in the F160W band. Center: Best-fit model, consisting of a combination of two Sérsic profiles for the main lens in the middle, and a single Sérsic profile for each of the neighboring galaxies. Right: Normalized residuals on a color scale from approximately -2σ to $+2\sigma$. The white pixels, with values of 0.0, show the regions masked during the luminosity profile modeling.

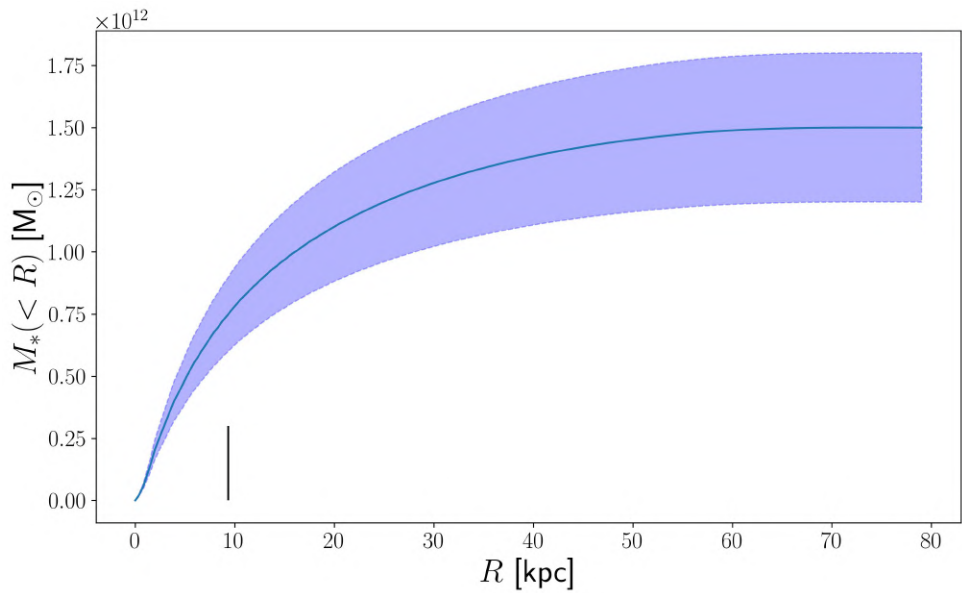


Figure 3.4: Cumulative stellar mass (M_*) profile (solid blue line) and $\pm 1\sigma$ uncertainties (shaded area) of the main lens. It is measured from the total stellar mass measured through the SED fitting and assuming a constant stellar mass-to-light ratio. The vertical black line shows the half-light radius of the lens galaxy.

3.3.3 Stellar kinematics

We used the penalized Pixel Fitting software (pPXF; [Cappellari & Emsellem 2004a; Cappellari 2017a](#)) that follows a maximum penalized likelihood method to determine the stellar velocity dispersion σ_* of the foreground lens galaxy. The X-Shooter spectrum has a resolution of $\simeq 6500$ in the VIS arm, where the main absorption lines fall. We masked the strong telluric absorption windows that could affect the analysis, and re-binned by two spectral pixels in order to obtain a $S/N > 10$ per bin and ensure reliable measurements of the stellar kinematics. We used the SYNTHE high-resolution template library ([Munari et al. 2005](#)) that covers the entire 2500–10500 Å wavelength range, with 1 Å pix $^{-1}$ sampling and a constant resolution FWHM of 2 Å pix $^{-1}$. Given the large size of the library, we extracted a subset of spectra representing the overall range of effective temperatures. The template spectra were then matched to the resolution of the binned X-Shooter spectrum. The pPXF fit was conducted in the rest-frame wavelength range 3800–5300 Å that covers the main absorption lines, Ca H and K at 3935 and 3970 Å, the G band at 4305 Å, H β at 4863 Å, the MgI triplet at 5167, 5173, and 5184 Å, as well as the strong continuum break at 4000 Å. This results in a stellar velocity dispersion value of (451 ± 37) km s $^{-1}$, confirming that the main lens galaxy of SDSS J0100+1818 is among the rarest, most massive elliptical galaxies ([Loeb & Peebles 2003](#)).

3.3.4 Environment

Given the large angular separation between the multiple images, we must consider the possibility that the main lens galaxy is located within a rich and overdense environment, as for other high-mass lens early-type galaxies at intermediate redshift (e.g., [Newman et al. 2015; Johnson et al. 2018b; Wang et al. 2022](#)). We estimate photometric redshifts using the template-fitting BPZ package ([Benítez 2000](#)) to study the source distribution over the $2.5' \times 2.5'$ field-of-view covered by our multiband images. In particular, we use the *grizy* bands from Pan-STARRS and BVR from NOT. At this stage, to avoid the possible introduction of systematics, we do not include the F160W band from HST, which only covers the central part of the considered field. The combination of optical and near-IR bands cover the 4000 Å break for early-type galaxies up to $z \sim 1$. We obtain redshift estimates for a total of 142 galaxies over the field, with a typical uncertainty of ± 0.2 , and 53 of the most reliable redshifts are consistent at the 2σ level with $z = 0.581$. Fig. 3.5 shows the difference between the redshift probability distribution functions of sources within 0.5' of the main lens (about 200 kpc at $z = 0.581$), and over the rest of the field, both normalized to the same area. Our analysis is broadly consistent with the presence of an overdensity around the main deflector, and possible galaxy members mostly have R-band AB magnitudes of 22–24 mag. Definite confirmation of this structure nonetheless requires spectroscopic follow-up and, given the large spread of candidate members over the field, we simply model its effect on the light deflection with an external shear component.

3.4 Point-like source modeling

We used the Gravitational Lens Efficient Explorer (**GLEE**; [Suyu & Halkola 2010; Suyu et al. 2012](#)) software to perform our strong lensing modeling of the system. **GLEE** supports several types of mass and light profiles and uses Bayesian analyses, such as simulated annealing and Markov chain Monte Carlo (MCMC), to infer the probability distributions of the parameter values and thus characterize the deflector. It also employs the Emcee package, developed by [Foreman-Mackey et al. \(2013\)](#), for sampling the model parameter posterior.

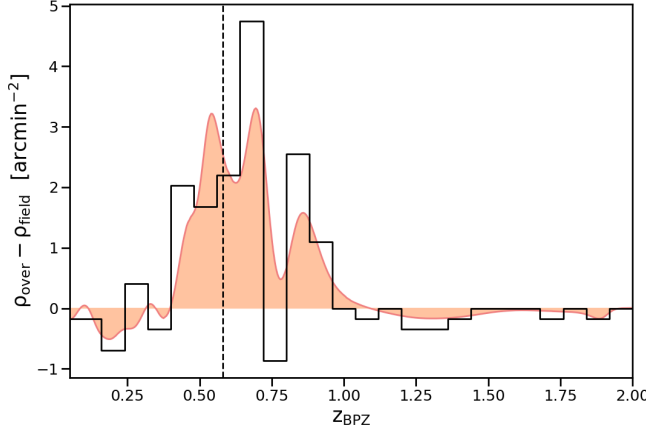


Figure 3.5: Difference between the redshift distribution functions of galaxies located within $0.5'$ of the main ultra-massive lens galaxy at $z = 0.581$, and over the rest of the $2.5' \times 2.5'$ field, after normalizing to the same area (orange curve). The black histogram is obtained from the peak of the redshift distribution of each source. A total of 14 galaxies within $0.5'$ of the main deflector have redshifts consistent, at the 2σ confidence level, with $z = 0.581$, and 39 over the rest of our analyzed field.

We started our modeling by making use of point-like images, that is, considering each multiple image position as that of its brightest pixel, with an uncertainty of one pixel. The best-fit values of the parameters of each model were estimated through a multistep simulated annealing technique, first minimizing the χ^2 on the source plane, and then on the deflector plane. Furthermore, the median values and the uncertainties (mainly at the 68% confidence level) were extracted from MCMC chains of 10^6 total steps, with acceptance rates between 20% and 30%, and the first 10% of the burn-in steps rejected. The results shown in Table 3.4 are extracted from the final chains of a sequence, in which each intermediate chain is used to estimate the covariance matrix of the model parameters and to extract the starting point for the following one.

We model the total mass distribution of the lens by assuming different mass profiles. The goodness of each model is evaluated by comparing the number of degrees of freedom (dof) and the value of the minimum χ^2 , computed by comparing the observed, $\boldsymbol{\theta}_i^{\text{obs}}$, and model-predicted, $\boldsymbol{\theta}_i^{\text{pred}}$, multiple image positions with the following statistics:

$$\chi^2 = \sum_{i=0}^N \frac{|\boldsymbol{\theta}_i^{\text{obs}} - \boldsymbol{\theta}_i^{\text{pred}}|^2}{\sigma_i^2}, \quad (3.2)$$

where N is the total number of multiple images and σ_i is the positional uncertainty relative to the i -th image. To compare different models, we considered three statistical estimators, often employed in similar strong lensing studies (see, e.g., Acebron et al. 2017; Mahler et al. 2018; Caminha et al. 2022): (1) the root-mean-square (rms) between the observed and model-predicted image positions, defined as

$$\text{rms} = \sqrt{\frac{1}{N} |\boldsymbol{\theta}_i^{\text{obs}} - \boldsymbol{\theta}_i^{\text{pred}}|^2}; \quad (3.3)$$

(2) the Bayesian information criterion (BIC; Schwarz 1978), given by

$$\text{BIC} = k \ln n + \chi^2, \quad (3.4)$$

where k is the number of free parameters; and (3) the corrected Akaike information criterion (AICc; [Akaike 1974](#); [Cavanaugh 1997](#)), defined as

$$\text{AICc} = 2k + \chi^2 + \frac{2k(k+1)}{n-k-1}. \quad (3.5)$$

The BIC and AICc estimators penalize models with increasing number of free parameters, to contrast overfitting. Thus, models with lower BIC and AICc values are preferred.

3.4.1 Modeling with A and B

At the beginning, we consider in the strong lensing modeling only the positions of the spectroscopically-confirmed eight multiple images of sources A and B.

First, we assume a pseudo-isothermal total mass distribution (PIEMD; [Kneib et al. 1996](#)) for the main lens. In **GLEE**, it is described by six parameters: the x and y coordinates of the center, the semimajor (a) to semiminor (b) axis ratio $q = b/a$, the position angle θ , the Einstein radius θ_E , and the core radius r_{core} . Here, we fix $r_{\text{core}} = 0$. We note that the value of θ_E is defined for a source at $z = \infty$ and does not correspond to that of the Einstein radius of the system, which should be nearly independent of the mass modeling details. The value of θ_E is a parameter that describes the lens strength and enters the dimensionless surface mass density κ_{PIEMD} as

$$\kappa_{\text{PIEMD}}(x, y) = \frac{\theta_E}{2\sqrt{r_{\text{core}}^2 + \frac{x^2}{(1+e)^2} + \frac{y^2}{(1-e)^2}}}, \quad (3.6)$$

where the ellipticity $e = \frac{1+q}{1-q}$. The value of the physical Einstein radius, as well as being estimated from this equation, would be clearly estimated from the total mass profiles presented in the following.

Then, we assume a singular power law elliptical mass distribution (SPEMD; [Barkana 1998](#)). In **GLEE**, it is described by seven parameters: the first six are in common with the PIEMD profile, and the slope g , which is related to the 3D logarithmic density slope $\gamma' = d \log[\rho(r)] / d \log(r)$ (i.e., $\rho \propto r^{-\gamma'}$) through $\gamma' = 2g+1$ (i.e., an isothermal profile corresponds to $\gamma' = 2$ and $g = 0.5$). In the following we refer to the physical parameter γ' . Similarly to the PIEMD case, θ_E is a parameter of the mass distribution introduced in the dimensionless surface mass density κ_{SPEMD} as

$$\kappa_{\text{SPEMD}}(x, y) = \theta_E \left(x^2 + \frac{y^2}{q^2} + \frac{4r_{\text{core}}^2}{(1+q)^2} \right)^{-\frac{\gamma'-1}{2}}. \quad (3.7)$$

In both total mass distributions, we included an external shear component. In **GLEE**, this is described by two parameters: the shear strength, γ_{ext} , and its position angle, ϕ_{ext} (where 0 means that images are stretched horizontally, along the x -axis, and $\pi/2$ means images are stretched vertically, along the y -axis).

The best-fit values of the parameters for these first two models are reported in the two upper entries of Table 3.1. The values of the x and y coordinates are in arcseconds, relative to the center of light of the elliptical lens galaxy, identified as its brightest pixel. For each model, we list the best-fit parameter values, the number of observables (N_{obs}), the number of degrees of freedom (dof), and the value of the minimum (χ_{min}^2).

3.4.2 Modeling with A, B, and C

Then, we add the two multiple images of source C, and use the same two mass density profiles defined in the previous section to fit the positions of all ten multiple images. The introduction of C requires an additional free parameter, its unknown redshift. In **GLEE**, this is parametrized with the value of D_{ds}/D_s , which is the ratio between the distances between the deflector and the source and between the observer and the source. Below, we convert the values (and the posterior probability distribution) of D_{ds}/D_s into those corresponding to the redshift of the source, z_C , and we always refer to this parameter. The best-fit parameter values are reported in the third and fourth entries of Table 3.1.

Since the position of the multiple image C2 is angularly very close to the main lens galaxy, we decide to try also PIEMD and SPEMD mass density profiles with the value of r_{core} free to vary. We refer to these models as PIEMD+rc and SPEMD+rc. We expect that C2 can affect the reconstructed lens total mass distribution in the inner region, depending mainly on the values of r_{core} and γ' . In fact, from strong lensing data, one can accurately measure the total mass distribution of a lens at the radii where the multiple images are observed. The presence of source C allows us to expand the radial interval from approximately (30–50) to (15–63) kpc. The best-fit values of the parameters of the models PIEMD+rc and SPEMD+rc are reported in the two lower entries of Table 3.1.

By comparing the best-fit parameter values of these different models, we notice that the center of the total mass is always shifted with respect to the luminosity center, along the positive x -axis and the negative y -axis. Furthermore, the values of the angles θ and ϕ_{ext} are similar and approximately orthogonal in almost all the models. When source C is included, the total mass of the deflector becomes more elliptical (i.e., the value of q decreases), unless a nonvanishing core radius is considered. Moreover, the introduction of source C and of a possible core radius changes significantly the best-fit values of the Einstein radii, suggesting a degeneracy between the values of the θ_E , r_{core} , γ' , and z_C parameters. Finally, the best-fit SPEMD profiles without a core radius are shallower than the corresponding isothermal profiles ($\gamma' \approx 1.5$ vs. $\gamma' = 2$); the best-fit values of the core radius and slope are very similar when the former is allowed to vary.

The low values of the minimum χ^2 suggest that we can accurately reproduce the positions of the observed multiple images by assuming a one-component total mass distribution for the deflector. In fact, the average distance between the observed and model-predicted positions of the multiple images is only of 0.02''. In Fig. 3.6, we show the observed (filled circles) and the model-predicted (crosses) positions of the multiple images for the PIEMD+rc model. All the considered models would result in very similar figures.

Furthermore, on the top of Table 3.4 we report the median and the 68% confidence level uncertainty values of the parameters of the different models. They are extracted from MCMC posteriors with 10^6 steps, with acceptance rates between 20% and 30%, after excluding the first 10% steps (considered as the burn-in phase). To correctly compare different models with different numbers of observables and degrees of freedom, for each model we rescaled the errors on the observed multiple images so that the value of χ^2_{min} is approximately equal to that of dof.

In Fig. 3.7, we show the posterior probability density distributions of the parameters of the PIEMD+rc (in blue) and SPEMD (in red) models, with sources A, B, and C included in the modeling. In order to compare them, only the common parameters are plotted, and thus γ' and r_{core} are not included. The x , y , q and θ distributions of the PIEMD+rc and SPEMD models are consistent. The Einstein radius distributions are centered on different values, but this is

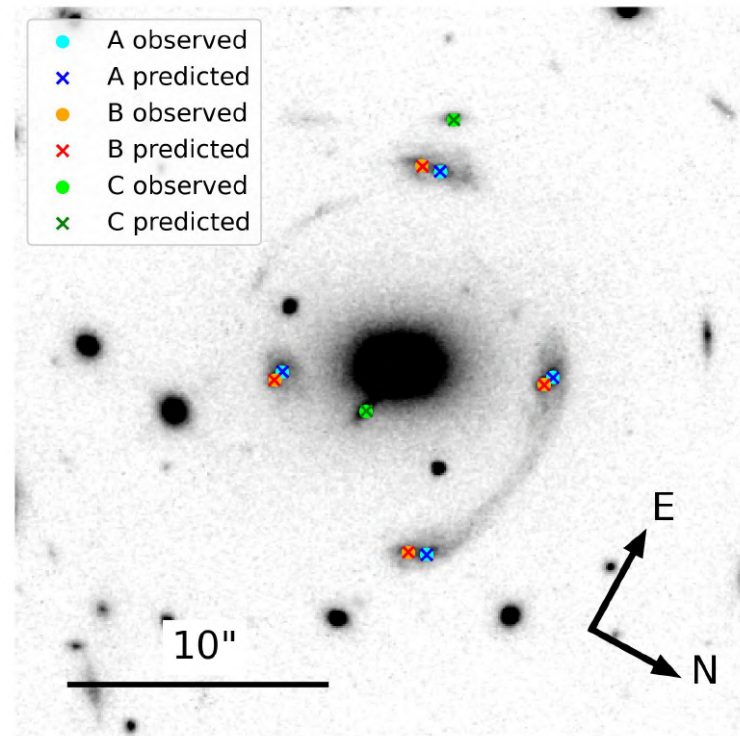


Figure 3.6: HST/F160W image of SDSS J0100+1818 and comparison between the observed multiple images of sources A (blue), B (red), and C (green), represented with circles, and those predicted by the best-fit PIEMD+rc model (fifth entry of Table 3.1), represented with crosses in the corresponding colors.

Table 3.1: Modeling of the deflector total mass distribution using the observed multiple image positions.

Multiple images A, B											
PIEMD											
x ["]	y ["]	q	θ [rad]	θ_E ["]	r_{core} ["]						
0.27	-0.13	0.69	0.07	11.1	[0.0]						
shear	γ_{ext}	ϕ_{ext} [rad]									
	0.21	1.44									
	$N_{\text{obs}} = 16$		dof = 5	$\chi^2_{\text{min}} = 1.29$							
	$\text{BIC} = 31.8$		AICc = 89.3	$\text{rms} = 0.028''$							
SPEMD											
x ["]	y ["]	q	θ [rad]	θ_E ["]	r_{core} ["]	γ'					
0.25	-0.11	0.77	0.10	3.8	[0.0]	1.55					
shear	γ_{ext}	ϕ_{ext} [rad]									
	0.06	1.08									
	$N_{\text{obs}} = 16$		dof = 4	$\chi^2_{\text{min}} = 0.63$							
	$\text{BIC} = 33.9$		AICc = 128.6	$\text{rms} = 0.020''$							
Multiple images A, B, C											
PIEMD											
x ["]	y ["]	q	θ [rad]	θ_E ["]	r_{core} ["]						
0.17	-0.22	0.41	0.01	12.9	[0.0]						
shear	γ_{ext}	ϕ_{ext} [rad]									
	0.06	1.22									
source	$D_{\text{ds}}/D_s = 0.477$		(corresponding to $z_C = 1.37$)								
	$N_{\text{obs}} = 20$		dof = 6	$\chi^2_{\text{min}} = 4.04$							
	$\text{BIC} = 46.0$		AICc = 116.0	$\text{rms} = 0.044''$							
SPEMD											
x ["]	y ["]	q	θ [rad]	θ_E ["]	r_{core} ["]	γ'					
0.14	-0.14	0.60	0.04	4.0	[0.0]	1.53					
shear	γ_{ext}	ϕ_{ext} [rad]									
	0.12	0.17									
source	$D_{\text{ds}}/D_s = 0.548$		(corresponding to $z_C = 1.72$)								
	$N_{\text{obs}} = 20$		dof = 5	$\chi^2_{\text{min}} = 1.78$							
	$\text{BIC} = 46.7$		AICc = 151.8	$\text{rms} = 0.030''$							
PIEMD+rc											
x ["]	y ["]	q	θ [rad]	θ_E ["]	r_{core} ["]						
0.18	-0.09	0.81	0.12	17.2	2.8						
shear	γ_{ext}	ϕ_{ext} [rad]									
	0.10	1.32									
source	$D_{\text{ds}}/D_s = 0.583$		(corresponding to $z_C = 1.98$)								
	$N_{\text{obs}} = 20$		dof = 5	$\chi^2_{\text{min}} = 1.08$							
	$\text{BIC} = 46.0$		AICc = 151.1	$\text{rms} = 0.023''$							
SPEMD+rc											
x ["]	y ["]	q	θ [rad]	θ_E ["]	r_{core} ["]	γ'					
0.18	-0.11	0.78	0.09	10.9	2.5	2.10					
shear	γ_{ext}	ϕ_{ext} [rad]									
	0.11	1.36									
source	$D_{\text{ds}}/D_s = 0.577$		(corresponding to $z_C = 1.93$)								
	$N_{\text{obs}} = 20$		dof = 4	$\chi^2_{\text{min}} = 0.62$							
	$\text{BIC} = 48.6$		AICc = 213.9	$\text{rms} = 0.017''$							

Notes. Modeling of the deflector total mass distribution using the observed multiple image positions. The two upper models were optimized by exploiting the eight observed positions of the spectroscopically confirmed background sources A and B, while the four bottom models include also the observed positions of the two multiple images of source C, without a spectroscopic redshift measurement. For each model, we show the best-fit values of the parameters, the number of degrees of freedom (dof), the minimum chi-square (χ^2_{min}) value, and the resulting BIC, AICc and rms values. The values of the x and y coordinates are referred to the center of light of the main elliptical lens galaxy, i.e., to its brightest pixel. The position angle θ is measured counterclockwise from x . Values in square brackets are kept fixed.

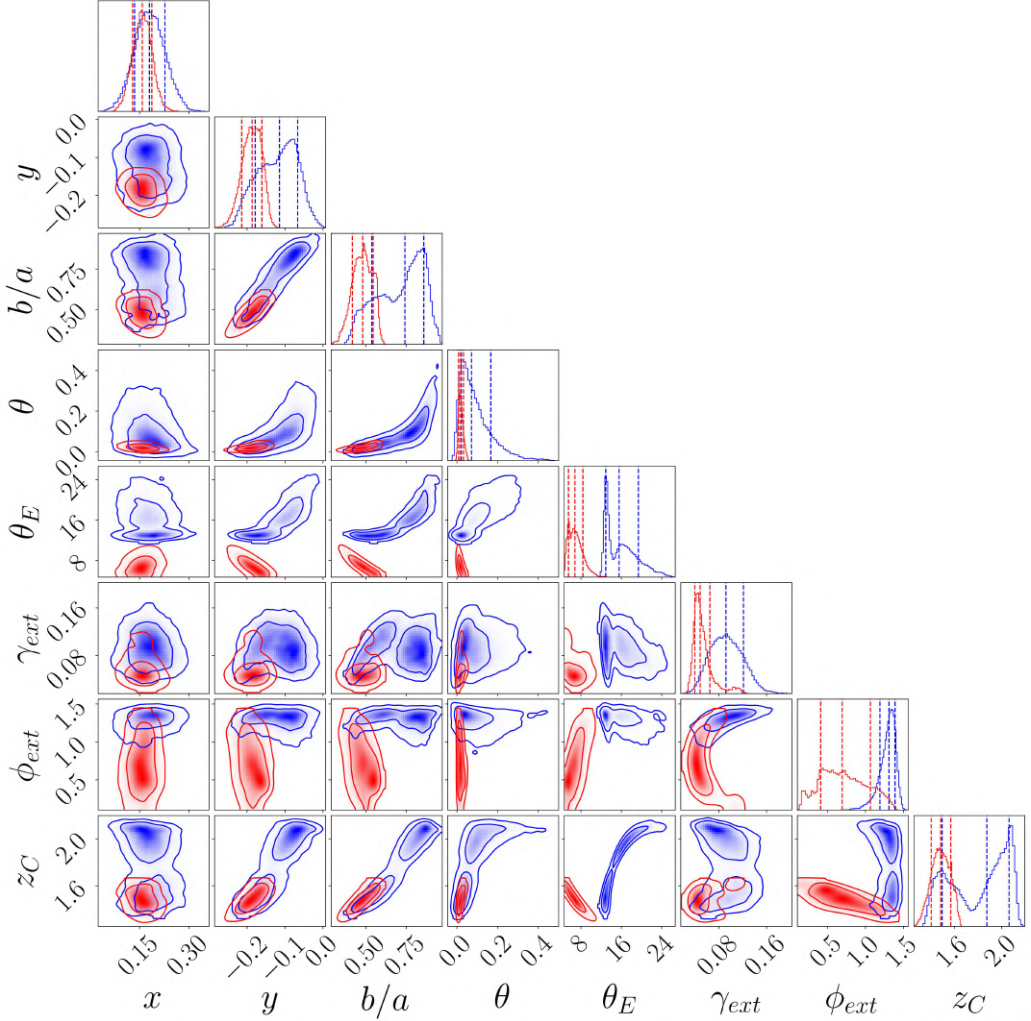


Figure 3.7: Probability density distributions of the parameters of the PIEMD+rc (in blue) and SPEMD (in red) models. The marginalized 1D histograms of each parameter are shown along the diagonal, while the other panels show the joint 2D probability distributions of the two parameters reported on the horizontal and vertical axes. The parameters plotted are those introduced in Sect. 3.4.1. The vertical dashed lines in the 1D histograms represent the 16th, 50th, and 84th percentiles, while the solid lines in the 2D distributions represent the 0.68 and 0.95 contour levels.

not surprising: its value is degenerate with those of the slope γ' (see Fig. 3.11) and of the core radius r_{core} . Finally, we remark that the SPEMD model shows a unimodal probability density distribution for z_C , as opposed to the bimodal one of the PIEMD+rc model. Finally, we show in Fig. 3.8 the comparison between two models with the same total mass parameterization (i.e., SPEMD), optimized first with the eight multiple images of sources A and B (in purple) and then with the ten multiple images of sources A, B, and C (in green). We can conclude that the results obtained with only two sources are consistent with those obtained with three sources and that the introduction of source C, at a different redshift, significantly reduces all but one confidence intervals.

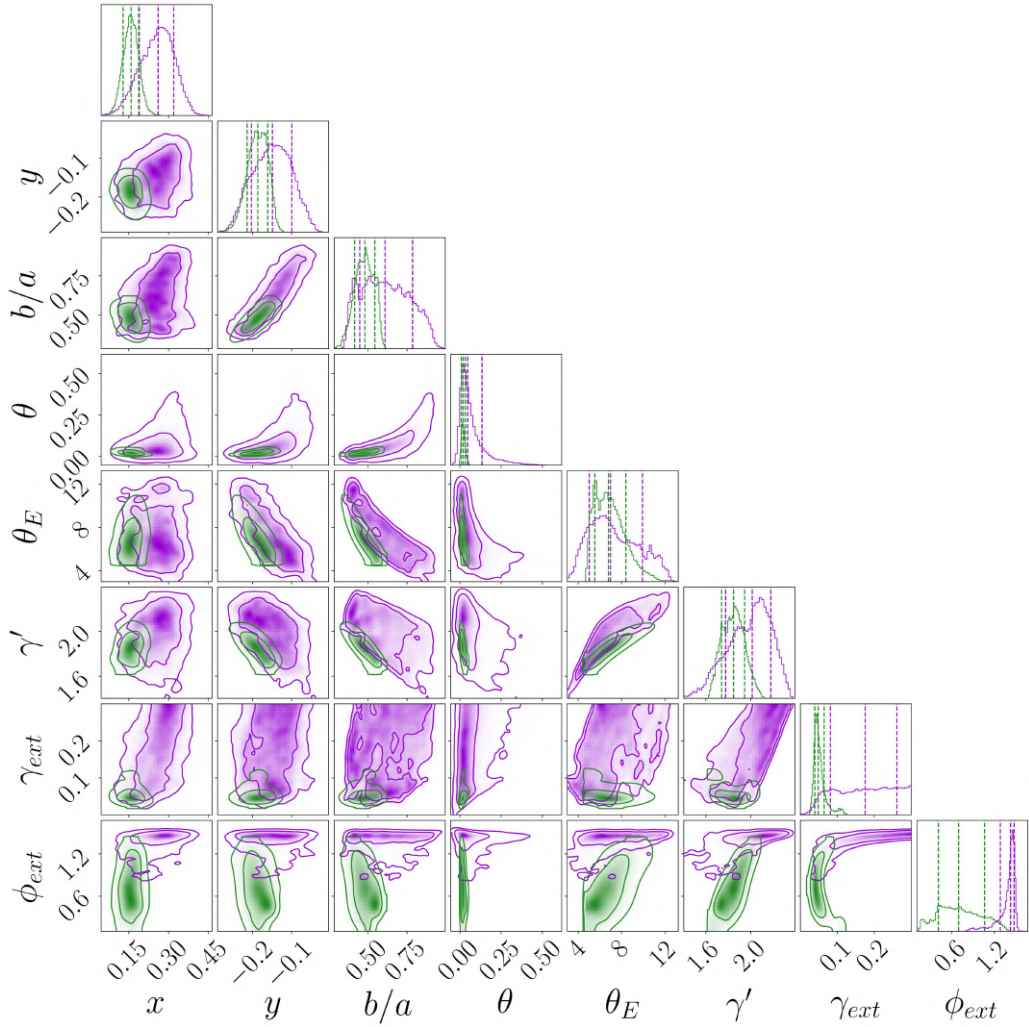


Figure 3.8: Probability density distribution of the parameters of the SPEMD model considering the multiple image positions of sources A and B only (in purple) and of sources A, B, and C (in green). The panels show the probability distributions as described in Fig. 3.7.

3.4.3 Total mass profile of the deflector

For each model, we estimate the total mass (M_T) distribution of the deflector by extracting randomly 1000 models from the 10^6 steps of the last MCMCs described above. First, we convert the convergence maps provided by **GLEE** into the corresponding total mass maps. Then, we sum up the contribution of all the pixels within circular apertures centered on the brightest pixel of the main lens galaxy, with a step of 0.5 pixels, to obtain the cumulative total mass profiles that are presented in the following. Within each fixed aperture, we consider the distribution of the total mass values of all the 1000 random models, from which we measure the median value and the 16th and 84th percentiles, as the uncertainties at the 1σ confidence level.

We started comparing the cumulative total mass profiles of each different mass model reconstructed by using the multiple images of sources A and B only and A, B, and C. We find that the profiles show consistent median values and that the introduction of source C significantly reduces the statistical uncertainties in the inner and outer regions. For example, for the SPEMD model, when source C is considered, the relative uncertainties are reduced from about 32% to 17% and from 9% to 5% in the inner ($R \approx 15$ kpc) and outer ($R \approx 63$ kpc) regions, respectively. Thus, in the following discussion and figures, we refer only to the models optimized by taking the observed multiple image positions of sources A, B, and C into account.

In Fig. 3.9 we show the cumulative projected total mass profiles of the deflector for the PIEMD+rc and SPEMD models. Despite the different total mass density parameterizations, and the slightly different optimized values of the parameters, the profiles are very similar and agree on the same mass value, with the smallest statistical errors, at the mean distance ($R \approx 42$ kpc) of the multiple images from the lens center, which represents approximately the physical Einstein radius of the system. The relative uncertainties at the distances of the innermost (C2, $R \approx 15$ kpc) and outermost (C1, $R \approx 63$ kpc) multiple images are, respectively, about 17% and 5% for the SPEMD model, while its minimum of approximately 1% is reached at $R \approx 42$ kpc. The total projected mass value measured within this radius is $(1.158 \pm 0.005) \times 10^{13} M_\odot$ for the PIEMD+rc model and of $(1.163 \pm 0.006) \times 10^{13} M_\odot$ with the SPEMD model. In the same figure, we also include the stellar mass profile of the system we described above.

Finally, in Fig. 3.10, we plot the cumulative projected stellar-over-total mass fraction profiles for the PIEMD+rc and SPEMD models. The two profiles are consistent, given the uncertainties, and differ mainly in the inner regions. At the lens galaxy effective radius, we estimate values of $(55 \pm 23)\%$ and $(38 \pm 9)\%$ for the PIEMD+rc and SPEMD models, respectively. According to both models, the fraction values are of $(12 \pm 2)\%$ and $(8 \pm 2)\%$ at $R \approx 42$ kpc and $R \approx 63$ kpc, respectively.

3.5 Extended source modeling

In this section we describe the reconstruction of the extended SB of the lensed sources that we performed with **GLEE**. At this stage, we merge sources A and B into a single, double-peaked source, at $z = 1.88$. Thus, in the following, we refer to “single source” models as the analogous of modeling with A and B in the point-like source modeling, and to “two source” models as of modeling with A, B, and C.

To model the SB of extended images, **GLEE** needs as input a mask with the pixels containing the observed multiple images and possible arcs of the lensed sources. These pixels are mapped onto the source plane through the ray-tracing equation, where the source SB is reconstructed on a

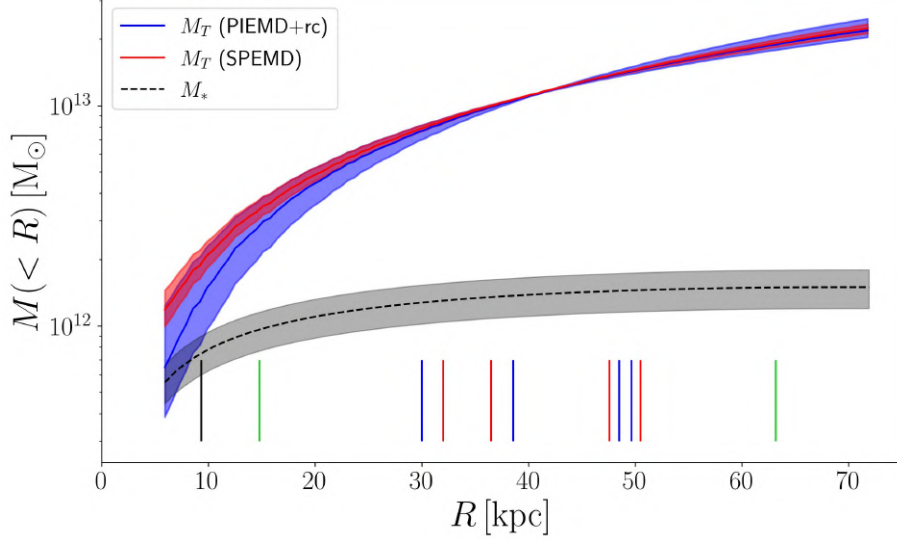


Figure 3.9: Cumulative projected total mass profiles for the PIEMD+rc (blue) and SPEMD (red) models with $\pm 1\sigma$ uncertainties (shaded areas), obtained by modeling the multiple images of A, B, and C as point-like objects. The cumulative projected stellar mass profile from Fig. 3.4 is shown in dashed black. The vertical lines close to the x -axis locate the distances from the lens galaxy center of the different multiple images, color-coded following Figs. 3.1 and 3.6. The black line shows the effective radius of the main lens galaxy.

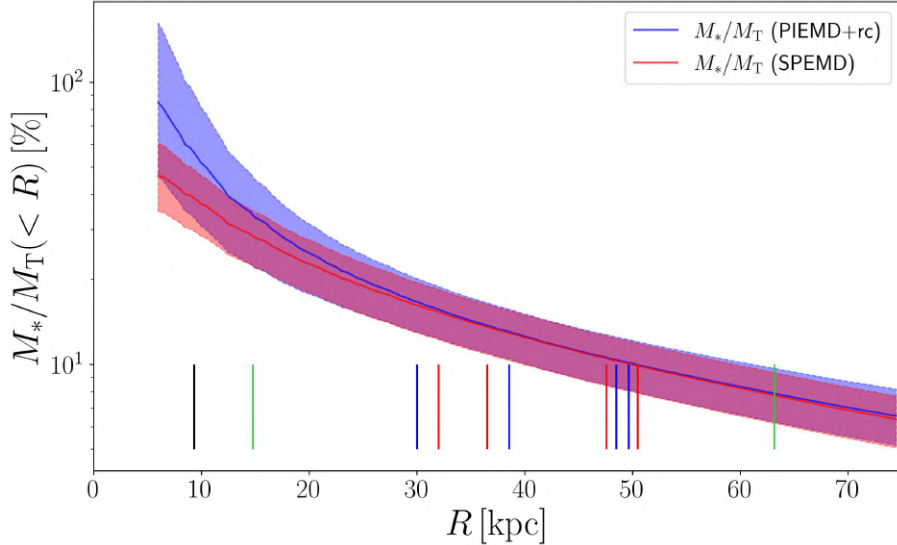


Figure 3.10: Cumulative projected stellar-over-total mass fraction profiles for the PIEMD+rc (blue) and SPEMD (red) models with $\pm 1\sigma$ uncertainties (shaded areas), obtained by modeling the multiple images of A, B, and C as point-like objects. The vertical lines are the same as in Fig. 3.9.

regular grid of pixels. The ray-tracing equation depends on the total mass distribution of the lens and on the angular diameter distances between the lens and the sources. When we model the observed images of a single source (i.e., A and B), with its spectroscopic redshift value measured and considered fixed, GLEE finds the best-fit model by varying the values of the parameters of

the mass distribution of the lens, and optimizing the posterior probability distribution, which is proportional to the product of the likelihood and the prior of the lens mass parameters (Suyu & Halkola 2010). Instead, when we model the images of the two sources, the mapping also depends on the relative distances between the observer, the deflector, and source C, and thus its redshift is introduced as an additional free parameter.

In the optimization process, the pixelated SB distributions of the sources are mapped back onto the image plane to obtain the model-predicted images, with flux intensity f_{ij}^{pred} , and compared with those observed, f_{ij}^{obs} . The χ^2_{SB} is thus defined as

$$\chi^2_{\text{SB}} = \sum_{i,j} \frac{(f_{ij}^{\text{obs}} - f_{ij}^{\text{pred}})^2}{\sigma_{ij}^2}, \quad (3.8)$$

where i and j identify the position of each pixel. During the optimization, we impose a curvature regularization on the values of the source SB pixels, weighted by the value of the parameter $\hat{\lambda}$, which is included in the χ^2_{SB} evaluation, as described in Suyu et al. (2006). This parameter penalizes physically less plausible solutions with very irregular SB distributions for the sources. The number of degrees of freedom is here computed as

$$\text{dof} = n_{\text{mask}} - n_{\text{lens}} - n_{\text{source}}, \quad (3.9)$$

where n_{mask} is the number of pixels on the image plane included in the mask as observables, n_{lens} is the number of free parameters related to the total mass distribution of the lens, and n_{source} is the effective number (i.e., smaller than the adopted one) of pixels onto which the source is reconstructed on the source plane. At the beginning, we consider the SB of a source on a regular grid of 25×25 pixels. Then, we refine (and show here) the results adopting a 40×40 grid on the source plane. We note that GLEE, after mapping the pixels included in the mask onto the source plane, reconstructs the source SB on a regular grid of pixels, with dimensions chosen by the user. Given that the maximum physical distance of the mapped pixels along the two coordinate axes is not known a priori, the SB source reconstructions usually have different pixel scales on the x and y axes, as can be observed in the plots presented in the following.

3.5.1 Modeling the deflector and the arcs

We started from the best-fit models achieved with the point-like source modeling, described in Sect. 3.4. In Table 3.1, we observe that the χ^2_{min} value decreases significantly, from approximately 4 to 1, when the number of degrees of freedom is reduced from 6 to 5 (from the PIEMD to the SPEMD and PIEMD+rc models). On the contrary, when dof is further reduced to 4 (for the SPEMD+rc model), the value of χ^2_{min} shows only a minor decrement. Furthermore, the SPEMD+rc model has the largest values for both the BIC and AICc estimators. This suggests that this model is the least favored one and, thus, that its extra complexity is statistically not fully justified. For these reasons, in the extended source modeling with two sources (AB and C), we decide to consider only the SPEMD and PIEMD+rc lens mass models, both with $\text{dof} = 5$ in the point-like source approximation. The free parameters of each mass distribution are the same as described previously. In Table 3.2, we report the best-fit values from the χ^2_{SB} minimization with a 40×40 pixelated source. As before, we can observe some trends in the values of the reconstructed parameters. The center of the total mass distribution is slightly shifted from the light peak, along the positive x and negative y directions. The value of the magnitude of the external shear is high in the PIEMD model with a single source, but it significantly decreases when considering a

Table 3.2: Modeling of the deflector total mass distribution using the extended source modeling.

Multiple images A, B									
PIEMD									
x ["]	y ["]	q	θ [rad]	θ_E ["]	r_{core} ["]				
0.24	-0.14	0.79	0.14	10.9	[0.0]				
shear	γ_{ext}	ϕ_{ext} [rad]							
	0.25	1.45							
$N_{\text{obs}} = 5831$			dof = 4576	$\chi^2_{\text{SB},\min} = 2650.5$					
SPEMD									
x ["]	y ["]	q	θ [rad]	θ_E ["]	r_{core} ["]	γ'			
0.18	-0.14	0.75	0.09	3.9	[0.0]	1.57			
shear	γ_{ext}	ϕ_{ext} [rad]							
	0.06	1.07							
$N_{\text{obs}} = 5831$			dof = 4571	$\chi^2_{\text{SB},\min} = 2429.0$					
Multiple images A, B, C									
SPEMD									
x ["]	y ["]	q	θ [rad]	θ_E ["]	r_{core} ["]	γ'			
0.05	-0.17	0.62	0.04	4.2	[0.0]	1.58			
shear	γ_{ext}	ϕ_{ext} [rad]							
	0.08	0.28							
source	$D_{\text{ds}}/D_s = 0.543$		(equals to $z_C = 1.69$)						
$N_{\text{obs}} = 7195$			dof = 5396	$\chi^2_{\text{SB},\min} = 3188.3$					
PIEMD+rc									
x ["]	y ["]	q	θ [rad]	θ_E ["]	r_{core} ["]				
0.09	-0.12	0.84	0.15	18.7	3.4				
shear	γ_{ext}	ϕ_{ext} [rad]							
	0.09	1.25							
source	$D_{\text{ds}}/D_s = 0.590$		(equals to $z_C = 2.04$)						
$N_{\text{obs}} = 7195$			dof = 5583	$\chi^2_{\text{SB},\min} = 4400.9$					

Notes. The two upper models were optimized by exploiting the double-peak source AB, while the two bottom models also include source C. The parameters are defined as in Table 3.1.

SPEMD model or when source C is introduced. The value of θ is approximately the same for all models, while the value of q decreases for the SPEMD models, where the deflector is found to be more elliptical. Finally, both the SPEMD models suggest a lens total mass profile shallower than an isothermal one, and the value of γ' is almost identical, when a single or two background sources are considered.

A comparison with the best-fit values of the point-like models shows that the center of the total mass distribution is always shifted in the same direction from the light distribution center. Moreover, the values of axis ratio, position angle, Einstein and core radii do not differ significantly when comparing each extended model with its corresponding point-like model. The main differences for the lens reconstruction between the two ways of modeling the background sources can be observed in Table 3.4, where we list the median values and the statistical uncertainties extracted from MCMCs of 10^6 steps, tuned to have $\chi^2_{\min} \approx \text{dof}$. The larger number of observables (approximately 7200, instead of 20) makes the marginalized probability distributions of the parameters much narrower when the sources are modeled as extended, as visible from the uncertainty values reported in the table. We show in Fig. 3.11 the probability density distribution of the SPEMD model with two sources. There, we can observe the expected degeneracies between the values of θ_E , γ' and z_C , found also in the point-like modeling. The values of the

shear parameters show some significant degeneracies with those of several other parameters, like q and θ .

Similarly to Fig. 3.6, we show the comparison between the observations and the model predictions for the extended modeling. It is now possible to compare directly, pixel by pixel, the observed and predicted arcs. We show the results for the PIEMD (Fig. 3.12) and SPEMD (Fig. 3.13) models when considering the single source AB, and for the SPEMD model when including also source C (Fig. 3.14). In the first panels from the left, we show the pixels of the observed images included in the masks as observables. In the second panels, we plot the extended images predicted by the best-fit models and, in the third panels, the normalized residuals in the $(-5\sigma, +5\sigma)$ interval. When a single source is reconstructed, we observe that the arcs are very well reproduced with the PIEMD model and the residuals do not exceed in absolute value 2.5σ . The results are even better with the SPEMD model, which is able to further reduce the residuals, in particular of the A2B2 and of A4B4 images. Besides the expected increase of the residuals (up to about 3.5σ around the images A3B3) when source C is added, the model can predict remarkably well the radial arc (C1). As already discussed, this multiple image is the most sensitive to the deflector inner total mass density profile and its good reconstruction supports the reliability of the strong lensing modeling results and of the lens SB modeling and subtraction. In the panels on the right, we show the reconstructed SB of the sources, which are discussed in Sect. 3.5.3.

3.5.2 Total mass profiles of the deflector

We measure the lens projected total mass distribution from the extended source modeling using the same procedure described for the point-like source modeling. In Fig. 3.15, we show the cumulative projected total mass profile of the deflector measured with the PIEMD+rc model and two extended sources (solid red line, the 1σ uncertainties are smaller than the linewidth), compared to its corresponding point-like source model (solid black and 1σ uncertainties as shaded area). The very small statistical uncertainties on the lens total mass profile from the extended source modeling, which are a factor of $\gtrsim 10$ smaller than those presented in Sect. 3.4.3, are related to the small uncertainties on the values of all the model parameters discussed above. In addition to the statistical uncertainties, we can estimate the systematic uncertainties by comparing the results of the different models, which fit the data almost equally well. Within $R \approx 42$ kpc, we measure a projected total mass value of 1.12 , 1.15 , 1.16 , and $1.16 \times 10^{13} M_\odot$ for the PIEMD and SPEMD (single source), SPEMD and PIEMD+rc (two sources) models, respectively.

On the contrary, the statistical uncertainties on the cumulative projected stellar-over-total mass fraction profiles for corresponding point-like and extended models are very similar, because the uncertainty on the stellar mass profile dominates over that on the total mass profiles. In Fig. 3.16, we show the profiles for the PIEMD+rc models. They present slightly different slopes, but they both result in a stellar-over-total mass fraction value of $(12 \pm 2)\%$ within 42 kpc. From a comparison with the PIEMD+rc point-like model, we find that the extended one predicts a higher value of $(85 \pm 17)\%$ consistent with one, at the effective radius, and a lower value of $(7 \pm 1)\%$ in the outermost regions ($R \approx 63$ kpc).

3.5.3 Source SB reconstruction

The source SB reconstructions are shown in the fourth panels of Figs. 3.12, 3.13, and 3.14. In each image, there are two different rods along the x and y directions, representing a scale of $0.5''$, as discussed above. By observing them, we note that, despite recovering the same morphology,

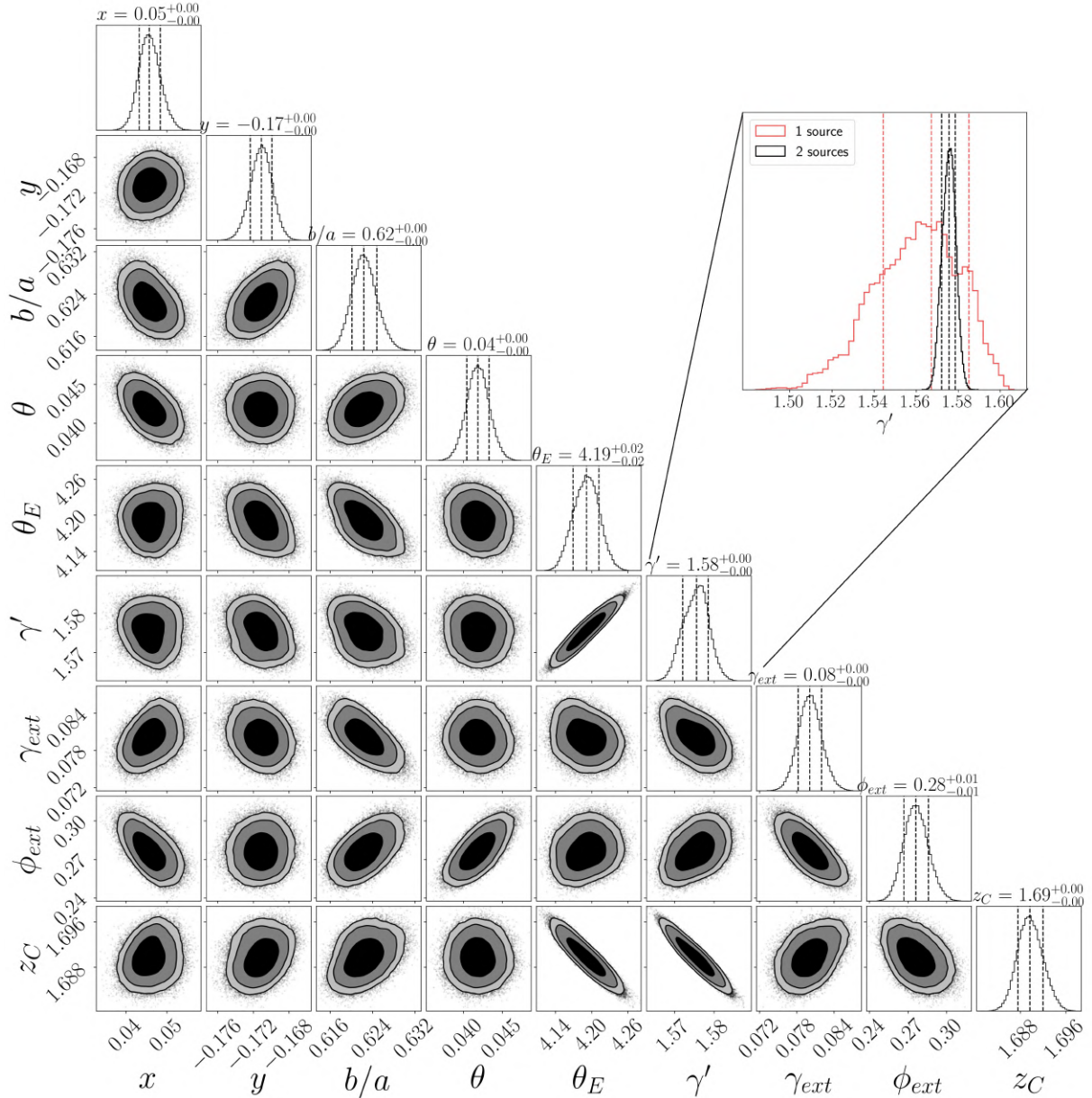


Figure 3.11: Probability density distribution for the SPEMD model with two sources (source AB and source C). The marginalized 1D histograms of each parameter are shown along the diagonal, while the other panels show the joint 2D probability distributions of the two parameters reported on the x and y axes. The parameters are those described in Sec. 3.4.1. The vertical dashed lines in the 1D histograms represent the 16th, 50th and 84th percentiles, which are also reported on top of each 1D histogram, while the solid lines and shaded areas in the 2D distributions represent the 0.68, 0.95, and 0.99 contour levels. In the floating panel, we zoom in the marginalized 1D histogram of the γ' parameter (in black), and compare it with its distribution for the model with the AB source only (in red). The introduction of source C provides tighter constraints on the value of the γ' parameter.

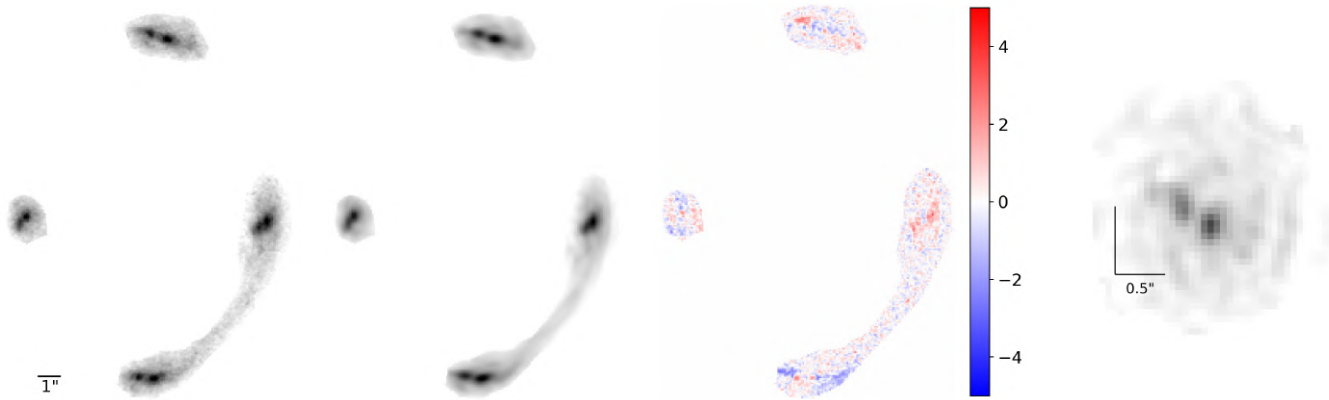


Figure 3.12: PIEMD model with one source. From the left to the right: observed SB in the F160W band of the multiple images considered in the extended source modeling; model-predicted SB; normalized residuals in the range from -5σ to $+5\sigma$; reconstructed SB of the source on a 40×40 pixel grid. Angular scales of $1''$ and of $0.5''$ are represented on the lens and source plane, respectively.

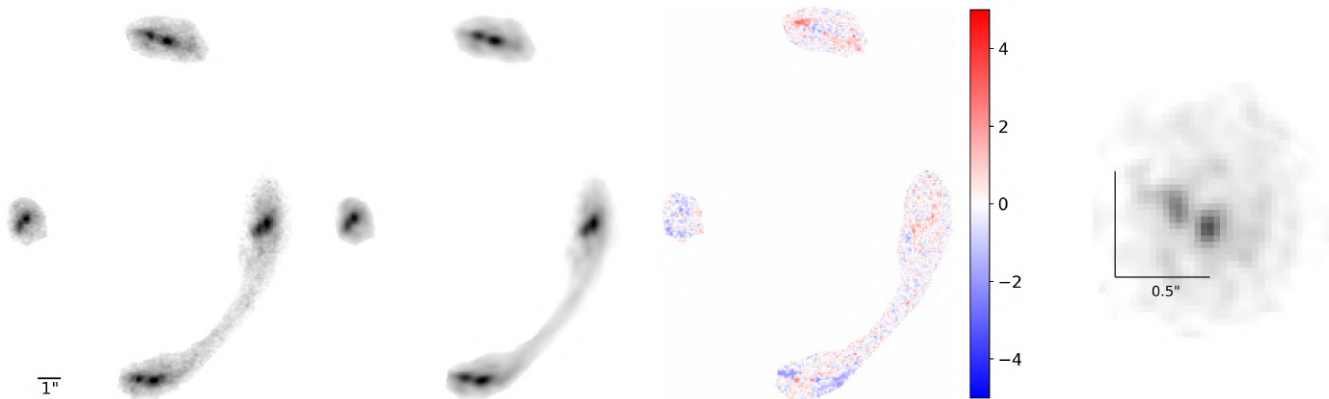


Figure 3.13: As in Fig. 3.12 for the SPEMD model with one source.

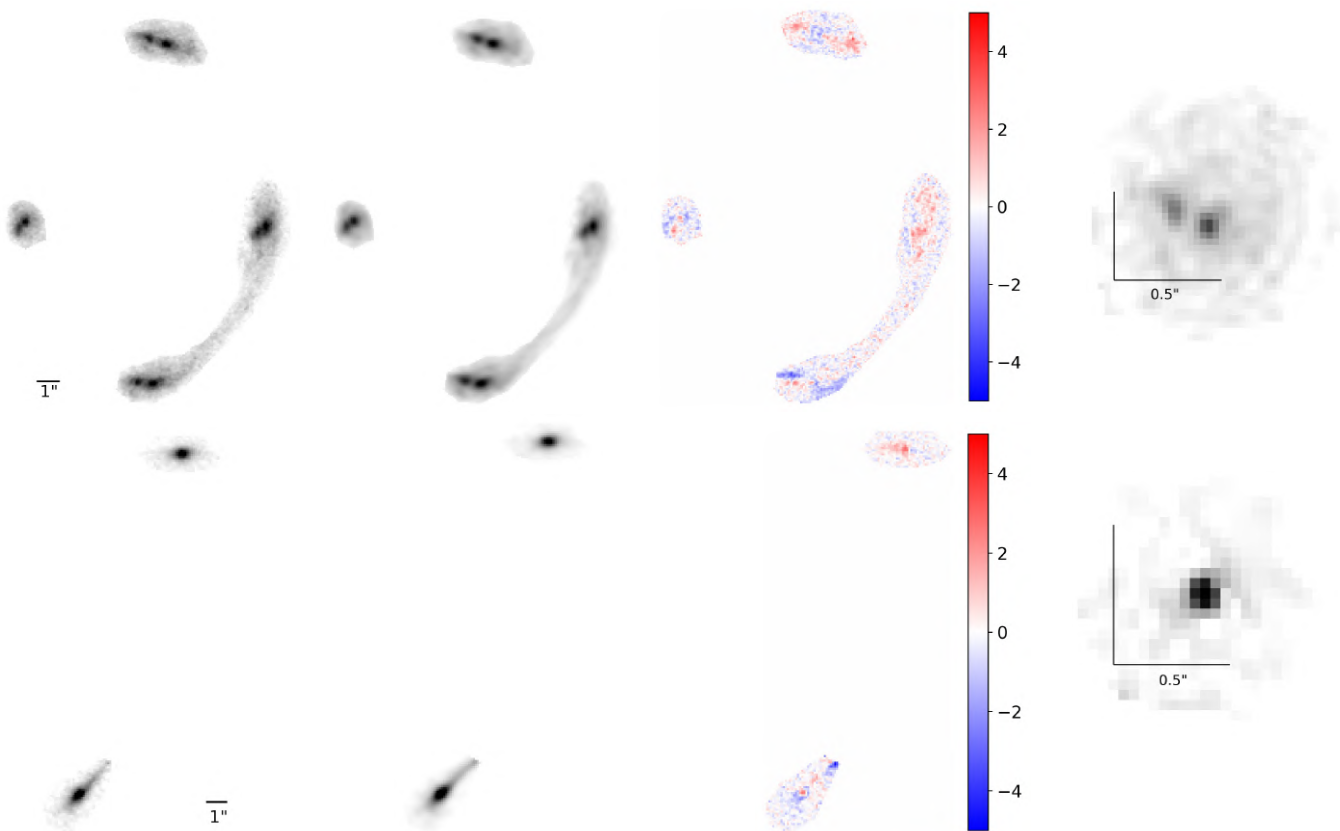


Figure 3.14: As in Fig. 3.12 for the SPEMD model with two sources. The top row shows sources A and B and their SB is reconstructed on a 40×40 pixel grid, while the bottom row shows source C and its SB is reconstructed on a 25×25 pixel grid.

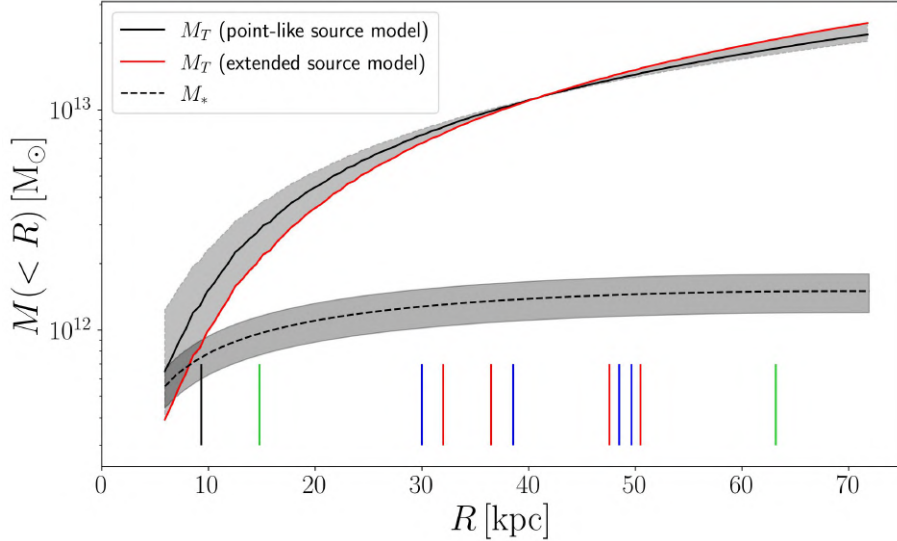


Figure 3.15: Cumulative projected total mass profiles for the PIEMD+rc model with point-like (solid black) and extended source (red) modeling, with $\pm 1\sigma$ uncertainties (shaded areas), obtained by modeling the multiple images of A, B, and C. For the extended source modeling, the uncertainties are smaller than the linewidth. The vertical lines close to the x -axis locate the distances from the lens galaxy center of the different multiple images, color-coded following Figs. 3.1 and 3.6. The black line shows the effective radius of the main lens galaxy.

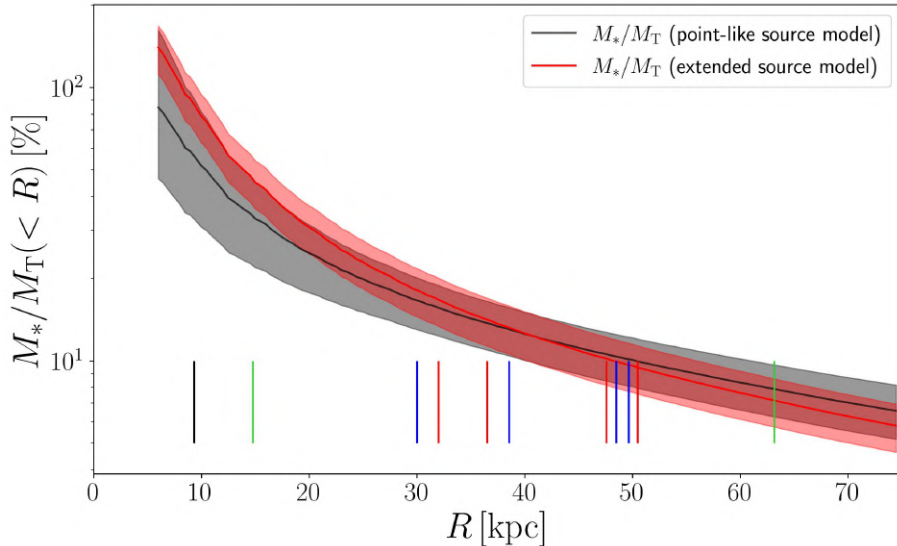


Figure 3.16: Cumulative projected stellar-over-total mass fraction profiles for the PIEMD+rc model with point-like (black) and extended source (red) modeling, with $\pm 1\sigma$ uncertainties (shaded areas), obtained by modeling the multiple images of A, B, and C. The vertical lines are the same as in Fig. 3.9.

the sizes of the background sources vary by a factor of ~ 2 , when the different total mass profiles for the lens are assumed.

We investigate this difference by measuring the angular separation between the sources A and

B, at redshift $z = 1.880$, and by estimating the half-light radii of the sources A, B, and C. In the first case, we compare the angular separations predicted by the different point-like and extended models. In particular, the positions of the point-like sources are optimized directly by **GLEE**, while, when considered as extended, we measure the angular separation between the brightest pixels associated with the sources. The results are shown in Table 3.3. First, we observe that each model predicts approximately the same angular distance, when the point-like or extended modeling is adopted. This test further proves the consistency of the two methods. Then, we confirm quantitatively what we observed from the reconstructed images: both the PIEMD and SPEMD models can reproduce well the observed multiple images, but they predict angular separations between the sources A and B that differ by a factor of approximately 2. This shows that the choice on the lens total mass distribution has a significant impact on the inferred properties of the background sources. This effect might be very relevant for lens clusters, where hundreds of background lensed sources are detected and the total mass distribution of the lens is more complex. However, in this strong lensing system, even if both the PIEMD and SPEMD models can reproduce successfully the observed multiple images and have approximately the same number of degrees of freedom, the SPEMD model results in a lower χ^2_{\min} value. We remark that the PIEMD+rc and SPEMD models, with sources A, B, and C, have the lowest χ^2_{\min} values and predict consistent angular distances. Considering the limited number of different models that can be tested in a strong lensing analysis, we highlight that this effect should be quantified and quoted as a possible source of systematic uncertainty on the reconstructed sources.

Next, we measured the effective radii of the two components A and B of the first source, and of source C. We computed the luminosity growth curve of each reconstructed source, measuring the flux included within concentric circular apertures, centered on the brightest pixel, with a step of 0.5 pixels (which corresponds to approximately $0.03''$ for all the sources). The apertures were corrected to take into account the different pixel sizes along the x - and y -axes. For the peaks of the composite AB source, we consider semicircular apertures, to avoid the contribution of source B being included in the measurement of the half-light radius of source A, and vice versa. Hence, we build the luminosity cumulative profiles and infer the half-light radii by considering only the halves of the plane less affected by the other peaks.

We observe that the cumulative luminosity profiles do not converge to a plateau, because of the noise in which the reconstructed sources are immersed. Because of that, we had to choose a maximum radius for the two sources, on the visual inspection of the images, of 4 and 3 pixels for the sources A and B, respectively. For source C instead, the cumulative luminosity profile converges to a plateau. The results are summarized on the left part in Table 3.3.

We check our results with another test. We analyze the multiple images A1 and B1, which are the less distorted and better resolved, and consider a rectangular cutout of $2.1'' \times 1.3''$ around them. We fit the SB of the background arc with an extended Sérsic component, and the SB of the two images A1 and B1 with two additional Sérsic profiles. From the best-fit model, we measure the values of the effective radii $r_{eA1} = 0.23''$ and $r_{eB1} = 0.17''$. Then, we estimate the local magnification factor around the multiple images A1 and B1 to infer their intrinsic sizes on the source plane. For each model, we compute the median magnification map from 1000 models randomly extracted from the final MCMCs (see Sect. 3.4.3). For each pixel of coordinates (i, j) of each model, we compute the local magnification factor as

$$\mu_{i,j} = \frac{1}{(1 - \kappa_{i,j})^2 - \gamma_{1i,j}^2 - \gamma_{2i,j}^2}, \quad (3.10)$$

where $\kappa_{i,j}$, $\gamma_{1i,j}$ and $\gamma_{2i,j}$ are the values of the convergence and shear components, respectively.

Table 3.3: Angular separation and sizes of the reconstructed sources

	Model	d_{AB} ["]	r_e ["] (A)	r_e ["] (B)	r_e ["] (C)	$\bar{\mu}_{A1}$	$\bar{\mu}_{B1}$	$r_{e,A}$ ["]	$r_{e,B}$ ["]	
Point-like	A,B	PIEMD	0.34 (2.87 kpc)			$2.59^{+0.12}_{-0.10}$	$2.49^{+0.11}_{-0.09}$	$0.14^{+0.01}_{-0.01}$ ($1.18^{+0.02}_{-0.03}$ kpc)	$0.11^{+0.01}_{-0.01}$ ($0.89^{+0.02}_{-0.02}$ kpc)	
		SPEMD	0.19 (1.58 kpc)			$3.84^{+4.46}_{-1.21}$	$3.68^{+4.13}_{-1.14}$	$0.12^{+0.02}_{-0.07}$ ($0.97^{+0.15}_{-0.56}$ kpc)	$0.09^{+0.01}_{-0.05}$ ($0.73^{+0.11}_{-0.41}$ kpc)	
	A,B,C	PIEMD+rc	0.19 (1.62 kpc)			$3.60^{+4.44}_{-1.15}$	$3.44^{+4.06}_{-1.07}$	$0.12^{+0.02}_{-0.07}$ ($1.00^{+0.16}_{-0.62}$ kpc)	$0.09^{+0.01}_{-0.05}$ ($0.75^{+0.12}_{-0.44}$ kpc)	
		SPEMD	0.19 (1.61 kpc)			$3.21^{+0.79}_{-0.58}$	$3.11^{+0.75}_{-0.55}$	$0.13^{+0.01}_{-0.02}$ ($1.06^{+0.10}_{-0.13}$ kpc)	$0.09^{+0.01}_{-0.01}$ ($0.79^{+0.07}_{-0.10}$ kpc)	
Extended	A,B	PIEMD	0.28 (2.41 kpc)	0.14 (1.18 kpc)	0.10 (0.87 kpc)	$2.80^{+0.10}_{-0.10}$	$2.69^{+0.01}_{-0.01}$	$0.14^{+0.01}_{-0.01}$ ($1.14^{+0.02}_{-0.02}$ kpc)	$0.10^{+0.01}_{-0.01}$ ($0.85^{+0.01}_{-0.01}$ kpc)	
		SPEMD	0.18 (1.55 kpc)	0.08 (0.70 kpc)	0.06 (0.51 kpc)	$7.27^{+0.50}_{-0.28}$	$6.93^{+0.47}_{-0.26}$	$0.08^{+0.01}_{-0.01}$ ($0.71^{+0.02}_{-0.02}$ kpc)	$0.06^{+0.01}_{-0.01}$ ($0.53^{+0.01}_{-0.02}$ kpc)	
	A,B,C	PIEMD+rc	0.16 (1.36 kpc)	0.07 (0.60 kpc)	0.05 (0.46 kpc)	0.10 (0.81 kpc, $z = 1.69$)	$7.64^{+0.08}_{-0.09}$	$7.16^{+0.07}_{-0.12}$	$0.08^{+0.01}_{-0.01}$ ($0.69^{+0.01}_{-0.01}$ kpc)	$0.06^{+0.01}_{-0.01}$ ($0.52^{+0.01}_{-0.01}$ kpc)
		SPEMD	0.18 (1.49 kpc)	0.09 (0.75 kpc)	0.06 (0.52 kpc)	0.06 (0.50 kpc, $z = 2.04$)	$6.22^{+0.08}_{-0.06}$	$5.96^{+0.07}_{-0.06}$	$0.09^{+0.01}_{-0.01}$ ($0.76^{+0.01}_{-0.01}$ kpc)	$0.07^{+0.01}_{-0.01}$ ($0.57^{+0.01}_{-0.01}$ kpc)

Notes. First column: angular separation between the sources A and B. In the point-like source modeling (top), this is computed as the distance between the best-fit source positions optimized by **GLEE**, while in the extended modeling (bottom), it is computed as the distance between the brightest pixels associated with each source in the reconstructed SBs. The second, third and fourth columns show the half-light radii of the reconstructed sources estimated through their cumulative luminosity profiles. Fifth and sixth columns: local median magnification factors of the multiple images A1 and B1 and 1σ statistical uncertainties. They are measured as the median value of the median magnification maps within circles of radii $r_{e,A1}$ and $r_{e,B1}$, centered on A1 and B1. Last two columns: half-light radii of the sources A and B measured from the results $r_{e,A1} = 0.23''$ and $r_{e,B1} = 0.17''$ of the SB modeling of the multiple images A1 and B1, and demagnified with Eq. (3.11). The uncertainties are propagated from those on the magnification factors. The angular quantities are converted to physical ones for $z = 1.880$, unless otherwise specified.

Then, from the 1000 values of magnification estimated on each pixel, we consider the median value and build the median magnification map $\bar{\mu}_{i,j}$. With the 16th and 84th percentile values of the same distribution, we quantify the $\pm 1\sigma$ uncertainties. Finally, we measure the local magnification factors for the multiple images A1 and B1 by taking the median value within circles centered on them and with radii equal to $r_{e,A1}$ and $r_{e,B1}$. The measured local magnification factors around A1 and B1 are reported in Table 3.3. If we correct the observed effective radii on the lens plane according to

$$r_e^{\text{source}} = \frac{r_e^{\text{image}}}{\sqrt{\bar{\mu}}}, \quad (3.11)$$

we find that these results (see the last two columns of Table 3.3) are consistent, given the uncertainties, with those obtained on the source plane with the luminosity growth curve of the SB reconstructions.

3.6 Discussion and summary

In this chapter we have studied SDSS J0100+1818, a strong lensing system consisting of a massive early-type galaxy with a spectroscopic redshift of $z = 0.581$, which acts as a gravitational lens on two background sources, AB and C. One of the sources (AB), spectroscopically confirmed at $z = 1.880$, has four multiple images, visible around the deflector at a projected distance of about

Table 3.4: Median and 68% confidence level uncertainty values of the parameters of the different models

	Parameters	x ["]	y ["]	q	θ [rad]	θ_E ["]	r_{core} ["]	γ'	γ_{ext}	ϕ_{ext} [rad]	z_C
Point-like A,B	PIEMD	$0.27^{+0.03}_{-0.03}$	$-0.14^{+0.02}_{-0.03}$	$0.67^{+0.09}_{-0.10}$	$0.07^{+0.05}_{-0.03}$	$11.2^{+0.4}_{-0.2}$	[0.0]		$0.20^{+0.04}_{-0.05}$	$1.44^{+0.02}_{-0.03}$	
	SPEMD	$0.26^{+0.06}_{-0.07}$	$-0.15^{+0.05}_{-0.06}$	$0.61^{+0.18}_{-0.16}$	$0.05^{+0.09}_{-0.04}$	$7.0^{+2.9}_{-2.0}$	[0.0]	$2.01^{+0.17}_{-0.24}$	$0.18^{+0.09}_{-0.09}$	$1.43^{+0.05}_{-0.15}$	
Extended A,B,C	PIEMD+rc	$0.18^{+0.05}_{-0.05}$	$-0.12^{+0.05}_{-0.06}$	$0.74^{+0.12}_{-0.21}$	$0.07^{+0.10}_{-0.05}$	$15.6^{+3.9}_{-2.6}$	$2.1^{+1.6}_{-1.6}$		$0.09^{+0.03}_{-0.03}$	$1.31^{+0.08}_{-0.12}$	$1.88^{+0.38}_{-0.19}$
	SPEMD	$0.16^{+0.03}_{-0.03}$	$-0.19^{+0.03}_{-0.03}$	$0.48^{+0.07}_{-0.07}$	$0.02^{+0.01}_{-0.01}$	$6.8^{+1.6}_{-1.3}$	[0.0]	$1.85^{+0.10}_{-0.11}$	$0.05^{+0.01}_{-0.01}$	$0.70^{+0.37}_{-0.29}$	$1.48^{+0.09}_{-0.08}$
Extended A,B	PIEMD	$0.24^{+0.01}_{-0.01}$	$-0.14^{+0.01}_{-0.01}$	$0.79^{+0.01}_{-0.01}$	$0.14^{+0.01}_{-0.01}$	$10.9^{+0.1}_{-0.1}$	[0.0]		$0.25^{+0.01}_{-0.01}$	$1.45^{+0.01}_{-0.01}$	
	SPEMD	$0.18^{+0.01}_{-0.01}$	$-0.14^{+0.01}_{-0.01}$	$0.76^{+0.01}_{-0.01}$	$0.09^{+0.01}_{-0.01}$	$3.9^{+0.1}_{-0.1}$	[0.0]	$1.57^{+0.02}_{-0.02}$	$0.06^{+0.01}_{-0.01}$	$1.06^{+0.06}_{-0.08}$	
A,B,C	PIEMD+rc	$0.09^{+0.01}_{-0.01}$	$-0.13^{+0.01}_{-0.01}$	$0.84^{+0.01}_{-0.01}$	$0.15^{+0.01}_{-0.01}$	$18.7^{+0.1}_{-0.1}$	$3.4^{+0.1}_{-0.1}$		$0.09^{+0.01}_{-0.01}$	$1.25^{+0.01}_{-0.01}$	$2.04^{+0.02}_{-0.01}$
	SPEMD	$0.05^{+0.01}_{-0.01}$	$-0.17^{+0.01}_{-0.01}$	$0.62^{+0.01}_{-0.01}$	$0.04^{+0.01}_{-0.01}$	$4.2^{+0.1}_{-0.1}$	[0.0]	$1.58^{+0.01}_{-0.01}$	$0.08^{+0.01}_{-0.01}$	$0.28^{+0.01}_{-0.01}$	$1.69^{+0.01}_{-0.01}$

Notes. Based on the point-like (top) and extended (bottom) modeling of the sources, as described in Tables 3.1 and 3.2. Statistics are extracted from the final MCMC chains with 10^6 steps. To compare properly different models with different numbers of observables and degrees of freedom, we have rescaled the errors on the observed multiple images for each model, so that its χ^2_{min} value is approximately equal to that of the number of dof.

7", and presents two components. The other source (C), instead, does not have a spectroscopic redshift measurement, and its two multiple images represent the closest and the most distant images from the deflector center. Thus, the introduction of this source is key to the reconstruction of the total mass profile of the lens in its inner and outer regions, approximately from 15 to 63 kpc, and to the reduction of some degeneracies among the model parameters.

We have developed several strong lensing models of the deflector with the software **GLEE**, combining (cored or singular) PIEMD and SPEMD total mass profiles with or without an external shear component. At the beginning, we considered the sources as point-like objects and modeled the lensed source positions. We took advantage of the eight observed positions of source AB (four multiple images for each of the two components) and of the two observed positions of source C. The redshift of source C was also included as a free parameter in the models.

Then, we considered the sources as extended objects and reconstructed their SB distributions. With this improvement, we were able to exploit the image structure and the extended arcs in which they are distorted, over ~ 7200 HST pixels. We finally used the reconstructed sources to measure their sizes and have discussed how much they can be affected by the adopted total mass profile for the deflector.

The main results of this chapter can be summarized as follows:

- We combined the available multiband photometry from Pan-STARRS, NOT, and HST to model the SED of the main lens galaxy. The best-fit model results in a stellar mass value of $(1.5 \pm 0.3) \times 10^{12} M_\odot$. By using the public software GALFIT on the HST image in the F160W band of the system, we modeled the light distribution of the lens with a combination of two Sérsic profiles. Starting from them, we measured the cumulative luminosity profile and then converted it into a stellar mass profile by assuming a constant stellar mass-to-light-ratio.
- We used the public software pPXF to estimate the value of the stellar velocity dispersion, σ , of the main lens galaxy from its X-Shooter spectrum. We find $\sigma = (451 \pm 37)$ km s $^{-1}$, which is consistent with the very large values of the galaxy stellar mass and of the mean distance

between the observed multiple images, confirming that SDSS J0100+1818 is among the rarest, most massive elliptical galaxies (Loeb & Peebles 2003).

- With the point-like source modeling, we have found a total mass value projected within the Einstein radius (of approximately 42 kpc) of $(1.16 \pm 0.01) \times 10^{13} M_{\odot}$, consistent for the PIEMD+rc and SPEMD models (Fig. 3.9). Source C is predicted at $z_C = 1.72$ (1.98) for the PIEMD+rc (SPEMD) model (Table 3.1). The best-fit value of the logarithmic slope of the SPEMD model is shallower than for a singular isothermal profile. However, we remark the observation of the expected degeneracies between the values of the γ' , θ_E , and z_C parameters (Fig. 3.7).
- With the extended source modeling, we have confirmed a projected total mass value enclosed within the Einstein radius of $1.16 \times 10^{13} M_{\odot}$ with both the PIEMD+rc and SPEMD models. Source C is predicted at $z_C = 1.69$ (2.04) for the PIEMD+rc (SPEMD) model (Table 3.2). By considering the extended structure of the sources and of their multiple images, the number of observables increases to approximately 7200 (compared to the 20 observables of the point-like source modeling). As a consequence, the statistical uncertainties on the parameter values and on the derived quantities are strongly reduced (see Fig. 3.15).
- In Dutton & Treu (2014) and Newman et al. (2015), the value of γ_{tot} was defined as the 3D mass-weighted mean value of the density slope within r_e . They investigated how this value varies by considering a sample of 59 galaxy-scale lenses from the Sloan Lens ACS (SLACS; Auger et al. 2009, 2010) survey ($\langle z \rangle = 0.20$), 10 group-scale lenses ($\langle z \rangle = 0.36$), and 7 central galaxies of massive clusters ($\langle z \rangle = 0.25$; Newman et al. 2013b,a). We measured the value of γ_{tot} from the projected total mass profiles, $M(R)$, presented in Sects. 3.4 and 3.5. Thus, we could only directly compare the results for the models with a constant slope, the SPEMD profiles with $r_{\text{core}} = 0$ in our study. We obtained a γ_{tot} value of $1.89^{+0.22}_{-0.09}$ for the point-like source SPEMD model and $1.68^{+0.01}_{-0.01}$ for the extended source SPEMD model, considering the A, B, and C background sources. In both cases, we observed that the introduction of source C slightly increases the value of γ_{tot} , by 0.03 and 0.05, respectively. These values are consistent with those found by Newman et al. (2015) for group-scale systems with $r_e \approx 10$ kpc, which lie between the values obtained for galaxy-scale (2.09 ± 0.03) and cluster-scale ($1.18 \pm 0.07^{+0.05}_{-0.07}$) systems.
- Newman et al. (2015) exploited the samples introduced above to compare the values of the projected stellar-over-total mass fraction within r_e , defined as

$$f_{*, \text{Salp}} = \frac{M_*(r_e)}{M_T(r_e)}, \quad (3.12)$$

where the subscript clarifies that the stellar mass values were estimated assuming a Salpeter stellar IMF. They also showed that the value of the projected stellar-over-total mass fraction decreases with increasing Einstein radius and halo mass, and that galaxy-, group-, and cluster-scale systems populate different regions in these parameter spaces. They measured a mean projected stellar-over-total fraction value of 0.60 for galaxy-scale lenses, 0.17 for group-scale lenses, and 0.06 for cluster-scale lenses. In this work, for SDSS J0100+1818, we measured fractions of 0.55 ± 0.23 and 0.38 ± 0.09 for the PIEMD+rc and SPEMD models, respectively (see Fig. 3.10).

- We have explored the possible presence of other group members and estimated photometric redshifts over the $2.5' \times 2.5'$ field-of-view covered by our multiband images. It has not been possible to gather quantitative conclusions, due to a lack of spectroscopy. However, we qualitatively observed an overdensity of candidate members in the northeast direction, which corresponds to a shear position angle, ϕ_{ext} , of about 20° (note the different orientation of the compass in Fig. 3.1 and of the GLEE x -axis). This is in relatively good agreement with the best-fit values of ϕ_{ext} , which range from 16° to 71° . We note that the value of ϕ_{ext} shows some expected degeneracies, mainly with the values of b/a , θ , and γ_{ext} .
- We reconstructed the SB distributions of the background sources and measured their half-light radii from the luminosity profiles. We have successfully recovered the two-peaked structure of the AB source, with a small physical separation between 1.4 and 2.9 kpc (at $z = 1.880$) from all the models (Table 3.3). We have found that, when considering different models with similar $\chi^2_{\text{min}}/\text{dof}$ values, the sizes of the reconstructed sources can vary by a factor of about 2. These results can have important consequences on the strong lensing modeling of more complicated lens mass distributions (i.e., on cluster scales). However, we remark that in this study the models with a SPEMD or a PIEMD+rc lens total mass profile have the lowest χ^2_{min} values, and they predict reconstructed sources with consistent sizes (confirmed also with the extended source modeling).
- We have measured values of the effective radius between 0.5 and 1 kpc at $z = 1.880$ for the A and B components, depending on the adopted model. Approximately 60% of $z \sim 2$ galaxies show bright star-forming regions, dubbed “clumps” (e.g., Cowie et al. 1995; Elmegreen & Elmegreen 2005; Elmegreen et al. 2009a, 2013; Guo et al. 2015, 2018; Zanella et al. 2019). Our measured sizes are in agreement with those of strongly lensed clumps in star-forming galaxies at $z \sim 1 - 3$, with similar, moderately magnified sources ($\mu \sim 3 - 10$). Hydrodynamic simulations suggest that the measured clump sizes depend on the spatial resolution of the observations (e.g., Oklopčić et al. 2017; Behrendt et al. 2016, 2019; Tamburello et al. 2017; Faure et al. 2021), and thus that the measured size upper limit decreases with an increasing magnification factor (Meštrić et al. 2022; Claeysens et al. 2022). In high amplification regimes, recent observations have been able to explore clumps with sizes of ~ 100 pc (Dessauges-Zavadsky et al. 2019; Livermore et al. 2015; Cava et al. 2018), down to $\lesssim 20$ pc in some extremely magnified cases (Rigby et al. 2017; Vanzella et al. 2020a; Meštrić et al. 2022; Claeysens et al. 2022; Messa et al. 2022). Hence, considering the measured magnification factors for the multiple images of the SDSS J0100+1818 system, it remains unclear whether A and B are monolithic, isolated clumps or blends of smaller clumps (or, in general, subcomponents) unresolved with HST.

This study could be improved in several ways with additional integral field spectroscopy. With these data, we could: (1) measure the redshift value of source C, which would be crucial for breaking the degeneracy between the values of θ_E and γ' . A measurement of the lens total mass enclosed within two (different) Einstein radii would indeed allow us to estimate the values of θ_E and γ' with a precision of a few percent. The measured redshift of C would also allow us to perform a multiplane lensing analysis, in which the light emitted by source AB is also deflected by the total mass distribution of C (or vice versa, if $z_C > 1.88$); (2) confirm or reject the hypothesis of the group nature of SDSS J0100+1818. If some neighbor galaxies were confirmed at redshifts similar to that of the main deflector, we would be able to include them individually in the strong lensing model (and not simply as an external shear component); (3) measure the velocity dispersion profile of the main lens galaxy and combine kinematics and strong lensing information. The previous points would also pave the way to the confirmation and inclusion of the additional

background source we mentioned in Sect. 3.3. If confirmed, the introduction of another source, at a different redshift, strongly lensed into four multiple images, would greatly improve our strong lensing model and make SDSS J0100+1818 one of the few galaxy-scale systems known to date with three lensed sources at different redshifts (see, e.g., [Collett & Smith 2020](#)). We present such improvements in the following chapter.

CHAPTER 4

Cosmography from accurate mass modeling of the lens group SDSS J0100+1818: five sources at three different redshifts

The results reported in this chapter have been described in the manuscript: “Cosmography from accurate mass modeling of the lens group SDSS J0100+1818: five sources at three different redshifts”, **Bolamperti A.**, Grillo C., Caminha G. B., Granata, G., Suyu S. H., Cañameras R., Christensen L., Vernet J., Zanella A. 2024 (accepted for publication in A&A, arXiv:2411.07289)

4.1 Introduction

In the currently accepted Λ cold dark matter (CDM) scenario, the Universe is almost flat and expanding, and the expansion is accelerating (Riess et al. 1998; Perlmutter et al. 1999). The Universe is composed of baryons and dark matter (DM) for $\approx 30\%$ ($\Omega_m \approx 0.3$), and the cosmic acceleration is due to the remaining $\approx 70\%$ ($\Omega_\Lambda \approx 0.7$), represented by the so-called dark energy. Our understanding of dark energy is very poor. We believe that it exerts a negative pressure, and it has an equation of state with $w \approx -1$, where w is defined as the ratio between pressure and energy density, $p/\rho c^2$. The Λ CDM model successfully describes the Universe at large scales ($\gtrsim 1$ Mpc), but presents difficulties in explaining some properties related to the formation of structures at smaller scales, like the sub-halo structures in galaxy clusters (Grillo et al. 2015; Meneghetti et al. 2020) and the value of the inner slope of DM halos (e.g., Gnedin et al. 2004; Newman et al. 2013a,b; Martizzi et al. 2012). Moreover, in extended cosmological models, currently available data cannot accurately measure the values of Ω_m and Ω_Λ , and different models can be reconciled with the observations (e.g., Motta et al. 2021). This motivates the continuous investigation and testing of the Λ CDM model, through new projects and observations. In this context, the use of different and independent cosmological probes is crucial, as they are subject to different systematics and degeneracies. Thus, they can offer valuable help in investigating the current tensions in cosmology (Verde et al. 2019; Moresco et al. 2022).

Strong gravitational lensing is an extremely powerful tool for extragalactic and cosmological studies (e.g., Bartelmann 2010; Treu 2010). Among the many applications, such as characterizing the total and DM mass distributions of clusters of galaxies (Acebron et al. 2022; Bergamini et al. 2023a; Granata et al. 2023) and galaxies (Vegetti et al. 2012; Schuldt et al. 2019; Ballard et al. 2024) acting as lenses, gravitational lensing can be used to probe the geometry of the Universe. Beside being particularly effective in measuring the value of the current expansion rate of the

Universe (the Hubble constant, H_0) through the observations of multiply lensed variable sources, such as quasars or supernovae, both on galaxy and cluster scales (e.g., [Refsdal 1964c](#); [Suyu et al. 2017](#); [Grillo et al. 2018](#); [Birrer et al. 2019](#); [Grillo et al. 2020](#); [Wong et al. 2020](#); [Rusu et al. 2020](#); [Shajib et al. 2023](#); [Grillo et al. 2024](#)), it also allows one to measure the values of Ω_m , w , and Ω_k (the latter parametrizing the curvature of the Universe, $\Omega_k = 0$ in a flat geometry), when kinematic data for lens galaxies are available (e.g., [Grillo et al. 2008](#); [Cao et al. 2012](#)) or in systems where two or more sources are multiply imaged by the same deflector ([Tu et al. 2009](#); [Collett & Auger 2014](#); [Tanaka et al. 2016](#); [Smith & Collett 2021](#), and with clusters of galaxies).

Massive clusters of galaxies can produce tens to hundreds of multiple images from several background sources and in the last decade they have been employed to measure the values of Ω_m , Ω_Λ , w , and Ω_k (e.g., [Jullo et al. 2010](#); [Caminha et al. 2016, 2022](#); [Grillo et al. 2024](#)), also thanks to the advent of very deep Integral Field Spectroscopic (IFS) observations, that represent the most effective way to spectroscopically confirm and discover lensed sources. For instance, the number of spectroscopically confirmed multiple images lensed by the Hubble Frontier Field galaxy cluster MACS J0416.1-2403 has increased, in less than 10 years, from 10 sources observed in 30 multiple images ([Grillo et al. 2015](#)) to 88 sources lensed into 237 multiple images ([Bergamini et al. 2023b](#)).

Unfortunately, the total mass distribution of clusters of galaxies is usually very complex, and this requires several mass components to properly model it, whose parameters may be degenerate with the cosmological ones. On the other hand, galaxy-scale systems are in general easier to model and the lens can often be described with an effective single total mass profile, but the limited number of background sources, usually ≤ 2 , makes them prone to be affected by the mass-sheet degeneracy ([Schneider 2014](#)). Galaxy or group-scale systems with a larger number (≥ 3) of lensed background sources might represent the best compromise between these two regimes to learn about the geometry of the Universe. They allow one to measure the values of Ω_m and w , independently of that of H_0 , but only a few of these systems are known to date and are suitable for cosmological studies (e.g., [Smith & Collett 2021](#)). Their analysis, even individually, can offer competitive estimates of the cosmological parameter values, and will pave the way to the exploitation of a larger number of systems of this kind, that are foreseen to be discovered with Euclid and the Vera C. Rubin Observatory - LSST ([Collett & Auger 2014](#); [Li et al. 2024](#)).

In this chapter, we extend the study presented in Chapter 3 on SDSS J010049.18+181827.7 (hereafter, SDSS J0100+1818), a rare strong lensing system (Fig. 4.1) included in the Cambridge And Sloan Survey Of Wide ARcs in the skY (CASSOWARY) survey ([Belokurov et al. 2009](#); [Stark et al. 2013](#)) as a candidate fossil system at $z = 0.581$ ([Johnson et al. 2018b](#)). In the previous chapter, we developed a strong lensing model of the system from the observed positions of the four multiple images of sources A and B (spectroscopically confirmed) and of the two multiple images of source C (with its redshift as a free parameter), and from the extended surface brightness distributions of the multiple images from the Hubble Space Telescope (HST) data. We employed the best-fit models to measure the cumulative total mass profile of the deflector, disentangle the DM and baryonic mass distributions, and to reconstruct the background sources. Now, we leverage on new data taken with the Multi Unit Spectroscopic Explorer (MUSE) on the Very Large telescope (VLT). These IFS observations allow us to measure the redshift of source C, discover two additional strongly lensed objects (E and F), spectroscopically confirm the group members in the MUSE field of view, and measure the stellar velocity dispersion profile of the brightest galaxy. We develop enhanced strong lensing models by including this information, that also allow us to measure the posterior probability distributions of the cosmological parameters Ω_m and w .

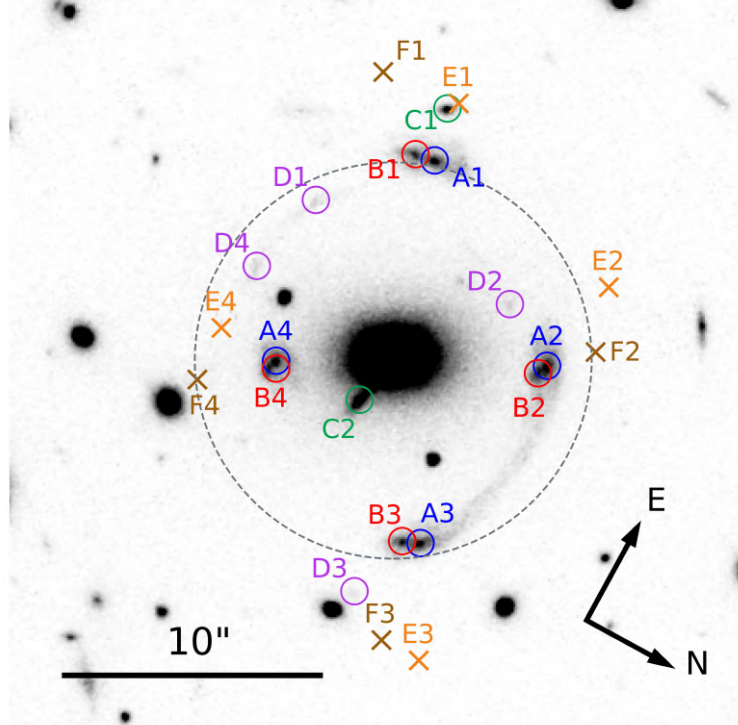


Figure 4.1: HST F160W image of the SDSS J0100+1818 strong lensing system studied in this work. Letters label multiple images of the same background source. E and F do not show continuum in the HST image and the orange and brown crosses mark the position of their Ly α emission line peaks, as detected with MUSE. The grey dashed circle represents an aperture of 50 kpc, the approximate average Einstein radius of the system.

This chapter is organized as follows. In Section 4.2, we summarize the currently available data for SDSS J0100+1818, focusing on the MUSE data reduction and spectra extraction. In Section 4.3, we describe the SDSS J0100+1818 system, characterizing the multiply imaged sources A, B, C, E, and F (excluding D that is not a secure system), the deflector with its velocity dispersion profile, and the group members. In Section 4.4, we describe the enhanced strong lensing models developed and the relative results. In Section 4.5, we show the strong lensing models with variable values of the cosmological parameters Ω_m and w . We discuss the results in Section 4.6, and draw conclusions in Section 4.7.

4.2 Observations and data reduction

4.2.1 Ancillary data

SDSS J0100+1818 benefits from a large sample of both photometric and spectroscopic observations, detailed, with the adopted data reduction procedures, in the previous chapter. In particular, we observed SDSS J0100+1818 with the HST Wide Field Camera 3 (WFC3; program GO-15253; PI: R. Cañameras), spending one orbit in each of the two F438W and F160W filters, resulting in PSF FWHMs of $0.086''$ and $0.187''$ in F438W and F160W, respectively. We complemented photometric observations with VLT/X-Shooter (Vernet et al. 2011) spectroscopy (program 091.A-0852, PI: L. Christensen), obtaining the spectrum of the main deflector and of

three out of four multiple images of the families A and B, being able to spectroscopically confirm them and to measure the lens stellar velocity dispersion.

4.2.2 Integral field spectroscopy observations with VLT/MUSE

We added IFS data of SDSS J0100+1818, by observing it for 5 hours with VLT/MUSE, from October to December 2022 (program 0110.245R, PI: A. Bolamperti). The observations were taken with seeing $\lesssim 1''$, clear sky conditions, airmass $\lesssim 1.4$ and with the Wide Field mode, resulting in a $1' \times 1'$ field of view and a spatial sampling of $0.2'' \text{ pix}^{-1}$. We divided the observations into five different observation blocks (OBs) of 1 hour each, taken with four different rotation angles (90° apart) and applying small offsets to the center, to optimize the final data quality.

We reduced the data with the standard MUSE pipeline v2.8.9 (Weilbacher et al. 2020), following the procedure detailed in Caminha et al. (2019), through the ESO Recipe Execution Tool (EsoRex; ESO CPL Development Team 2015) pipeline. In summary, we corrected all the raw exposures using the associated **BIAS**, **FLAT**, and **ILLUMINATION** calibrations. We then applied wavelength and flux calibrations and created a **PIXTABLE** relative to each exposure. At the end, we combined all of them into a final stacked datacube, and defined the astrometry with respect to the HST F160W image. To enhance the background sky subtraction, we made use of the Zurich Atmosphere Purge (ZAP; Soto et al. 2016) tool.

The resulting datacube spans in wavelength from 4750 \AA to 9350 \AA , with a constant $1.25 \text{ \AA} \text{ pix}^{-1}$ sampling. The final reduced MUSE data cube has a PSF FWHM of $0.8''$, covers a square of approximately 400 kpc on a side at the redshift of the main deflector, and it is centered on it. This pointing includes all the multiple images previously identified, as well as the most likely group members from our photometric analysis.

We identified and measured the source redshifts following the multi-step procedure described in Caminha et al. (2019). Firstly, we ran **SExtractor** (v2.28.0, Bertin & Arnouts 1996) on a cutout of the HST F160W image that covers the final MUSE datacube field of view (shown in Fig. 4.2), to detect the position of all the sources. We then extracted a spectrum from the datacube within a circular aperture with radius of $0.8''$ centered on each detected position. This aperture was chosen to represent a good compromise between collecting as much signal as possible and not including nearby contaminants in the most crowded regions. For some particular systems of distorted arcs hosting multiple images, or with faint and extended objects, we assumed specifically-designed regions to extract the spectra, that allowed us to obtain a better S/N . We complemented this catalog by adding sources that present clear emission lines in the MUSE datacube, but are not detected in the HST F160W continuum, through visual inspection and the use of the Cube Analysis and Rendering Tool for Astronomy (CARTA; Comrie et al. 2021) tool. We extracted their spectra within circular apertures with radius of $0.8''$ centered on the luminosity peak of the detected emission lines.

We measured the redshift values of the objects in the catalog with a dual automatic and visual procedure, identifying clear spectral features like emission and/or absorption lines, and continuum breaks. We made use of the software **Marz** (Hinton et al. 2016), that performs an automatic fitting of each spectrum with different templates. We found the automatic procedure reliable in the high S/N regime (e.g., to identify the bright group members), while we visually inspected the faint objects or those with only emission lines detected. We assigned for each redshift measurement a quality flag (QF), defined to be QF = 1 for non-reliable measurements, QF = 2 for possible measurements based on faint spectral features, QF = 3 for secure measure-

ments from more than one absorption and/or emission lines, and $QF = 9$ for measurements based on a single narrow line emission. In some cases, with a single emission line but with clear features that allow us to identify its nature, like the Ly α line or a doublet, we assigned a $QF = 3$. The catalog used in this chapter contains 133 redshift measurements with $QF \geq 2$ (65 with $QF \geq 3$), divided into 3 (3) stars, 22 (19) group members, 27 (10) foreground galaxies, 80 (32) background galaxies and 1 (1) background quasar.

4.3 The SDSS J0100+1818 system

SDSS J0100+1818, (RA, dec) = (01:00:49.18, +18:18:27.79), was introduced in a later release of the CASSOWARY catalog. In Chapter 3, we determined a robust lens redshift, $z = 0.581$, and a stellar mass value of $(1.5 \pm 0.3) \times 10^{12} M_{\odot}$ for the most luminous galaxy. We assumed different mass distributions for the main lens and, through a strong lensing analysis, we measured the total mass profile of the deflector.

4.3.1 Multiple images of A and B

We confirm the joint redshift measurement of $z = 1.880$ for the two source components forming image families A and B (Fig. 4.1) that we found in the previous chapter. Previously, based on X-Shooter data, we performed a joint analysis of the targeted multiple images, A1/B1, A3/B3, and A4/B4. We made use of lines detected at about 10740 in the binned 2D spectra, whose width is consistent with the [OII] $\lambda\lambda 3727, 3729$ doublet, of a faint detection of [OIII] $\lambda 5007$ in A3/B3, and of the lack of additional line detections over the spectral range covered by X-Shooter. In the MUSE cube, we extract the spectra over four regions, shown in Fig. 4.2, that include the compact and extended emission from all four images. We detect the MgII $\lambda 2800$ doublet at about 8065, five absorption features of FeII (FeII $\lambda\lambda 2344, 2374, 2382, 2586, 2600$), three of Al (AlII $\lambda 1671$, AlIII $\lambda 1854$, AlIII $\lambda 1862$), and a tentative detection of HeI $\lambda 3188$ and [CII] $\lambda 2326$. These features are shown, for each of the A1/B1, A2/B2, A3/B3, A4/B4 images and stacked, in Fig. 4.3.

4.3.2 Multiple images of C

By combining observations in the HST F160W and F438W filters with the first strong lensing models of the system, we previously identified another candidate lensed background source, with two multiple images labeled as C1 and C2 in Fig. 4.1. Since C1 and C2 have similar colors and their positions were correctly predicted by our initial strong lensing models, it was highly likely that a single source was observed multiple times. Although we lacked spectroscopic confirmation, as they were not included in the X-Shooter pointing, we considered the redshift value of source C as a free parameter in the strong lensing analysis. The two best models presented in Chapter 3 predicted, in the point-like approximation and in the extended source reconstruction, best-fit redshift values of respectively 1.72 and 1.69. They also showed that the value of z_C was degenerate with those of other parameters, mainly the Einstein radius (θ_E) and the 3D logarithmic total mass density slope (γ') of the deflector. We extract the spectra of C1 and C2 from the apertures shown in Fig. 4.2, and measure a redshift value of 1.698, from the detection of the Mg II at about 7550, with some evidence of a P-Cygni line profile of the doublet, five absorption features of FeII (FeII $\lambda\lambda 2344, 2374, 2382, 2586, 2600$), and the emission lines of CIII] $\lambda\lambda 1907, 1909$ and [OII] $\lambda 2470$, shown in Fig. 4.4.

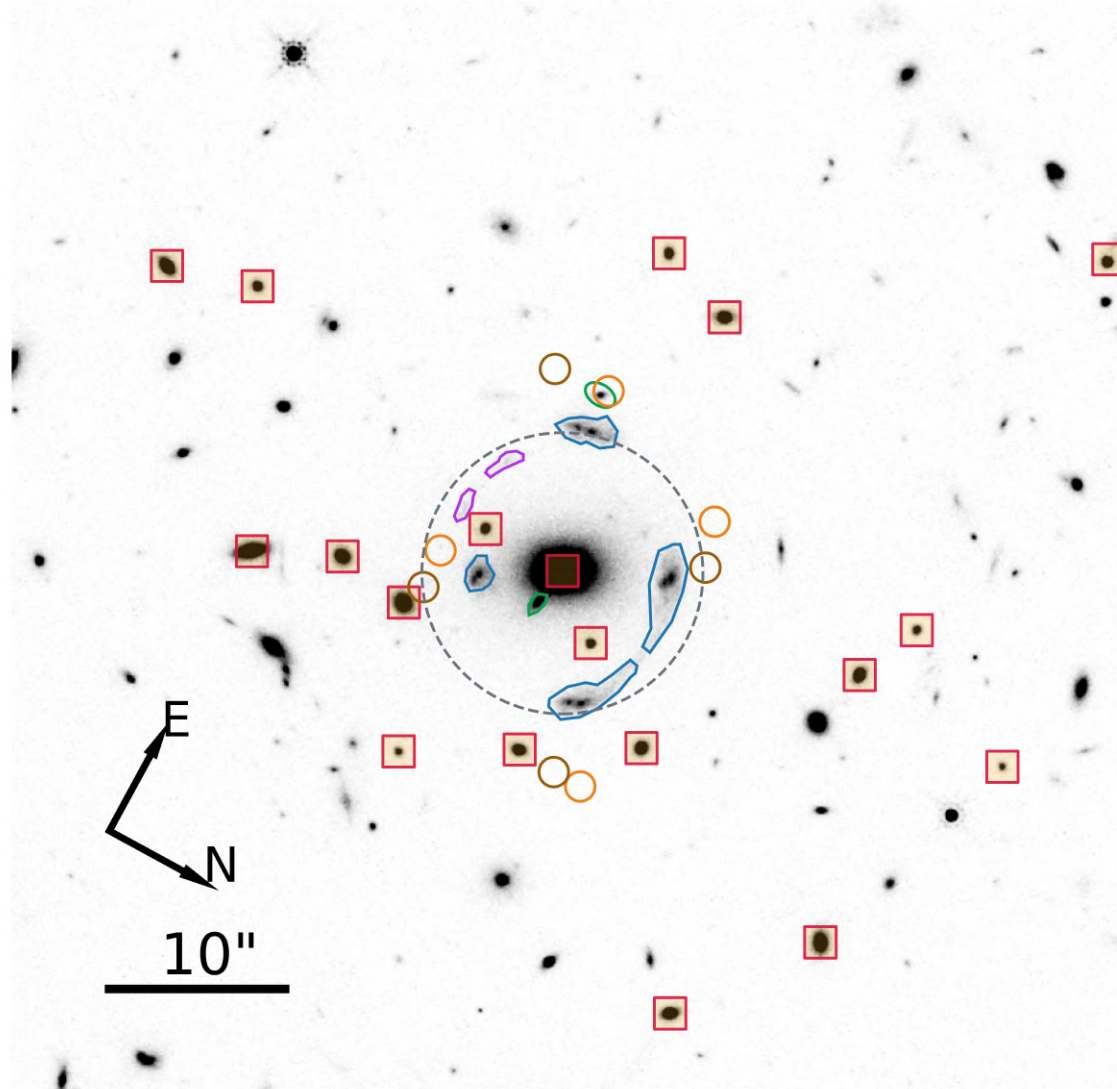


Figure 4.2: Group members (squares) identified as those galaxies whose redshift is within 0.581 ± 0.011 , equivalent to the mean redshift of the group with a spread of 2000 km s^{-1} (rest-frame). The colored regions represent the apertures within which we extracted the spectra of the multiple images of A and B (blue), C (green), D (purple), E (orange) and F (brown). The spectra of E and F, that do not present HST-detected continuum, are extracted within circular apertures with radius of $0.8''$. The grey dashed curve shows a circle with a radius of 50 kpc, which represents approximately the average Einstein radius of the system.

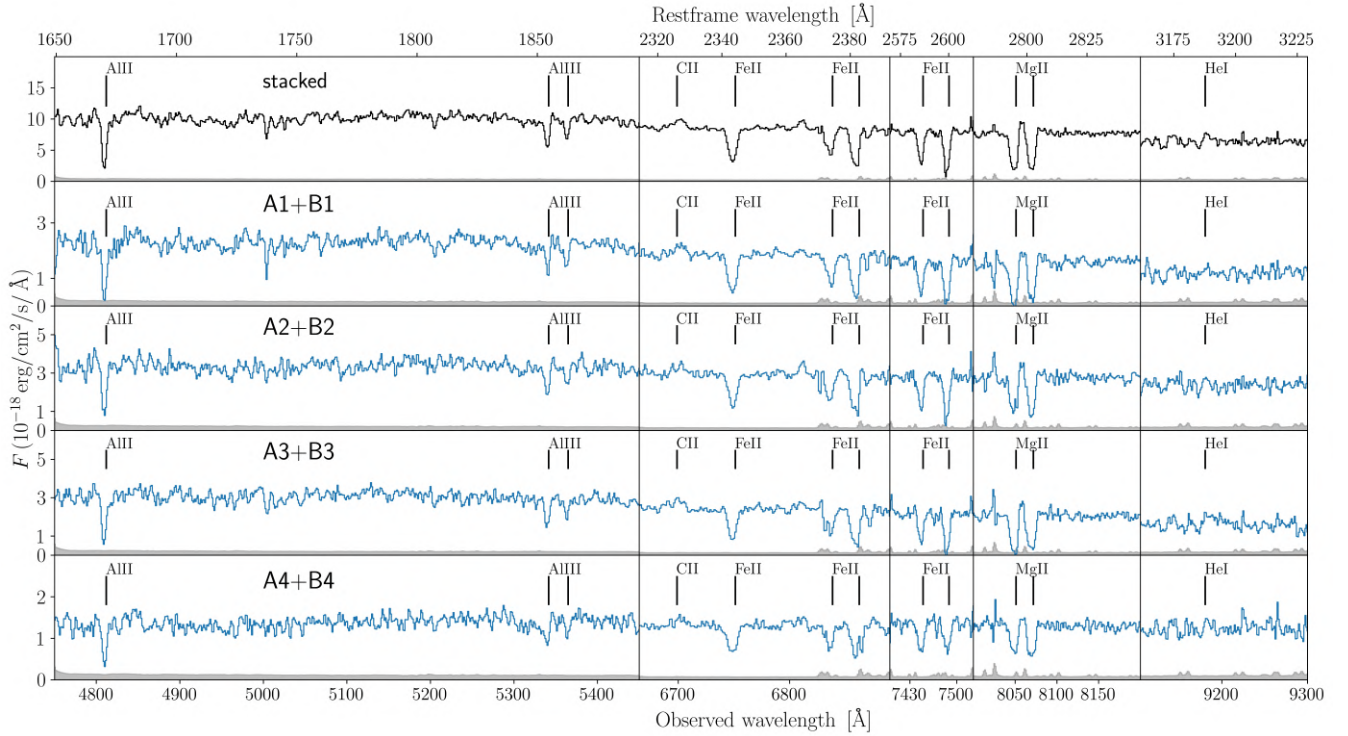


Figure 4.3: MUSE 1D spectra of the multiple images A1+B1, A2+B2, A3+B3, A4+B4, and stacked (top row), extracted within the blue apertures highlighted in Fig. 4.2. The spectra are smoothed with a ~ 2.5 boxcar filter. We zoom in around five wavelength ranges where we observe the main absorption and emission lines used to confirm the redshift measurement of 1.880. The blue lines represent the observed spectra in units of $10^{-18} \text{ erg s}^{-1} \text{ cm}^{-2} \text{ s}^{-1}$, and the gray regions indicate the 1σ uncertainties.

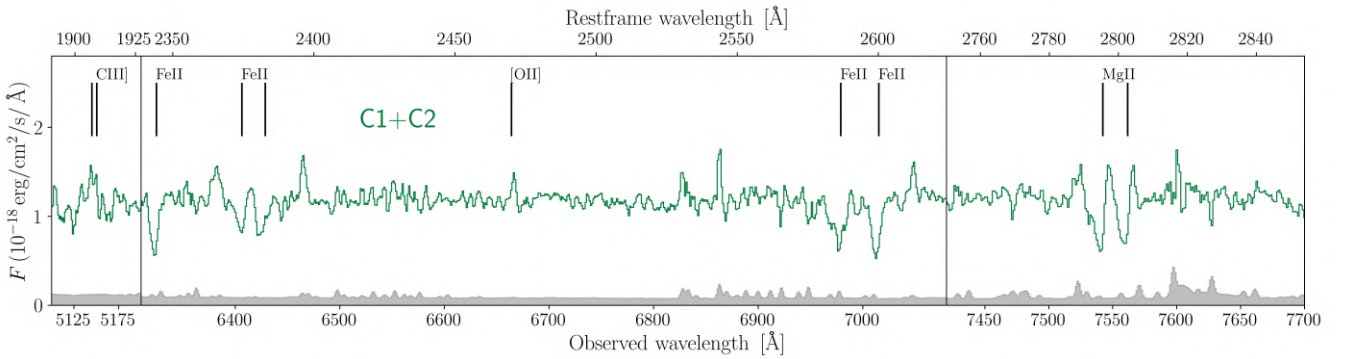


Figure 4.4: MUSE 1D spectrum of the multiple images C1 and C2 (stacked), extracted within the green apertures highlighted in Fig. 4.2. The spectrum is smoothed with a ~ 2.5 boxcar filter. We zoom in around three wavelength ranges where we observe the main absorption and emission lines used to confirm the redshift measurement of 1.698. The green line represents the observed spectra in units of $10^{-18} \text{ erg s}^{-1} \text{ cm}^{-2} \text{ s}^{-1}$, and the gray regions indicate the 1σ uncertainties.

4.3.3 Multiple images of E and F

With MUSE we identify two additional multiply imaged background sources, labeled as E and F in Fig. 4.1, that do not show any stellar continuum counterpart in HST F160W. They are detected through a strong emission line at $\approx 7231\text{ }\text{\AA}$, as it often happens in deep MUSE observations of similar fields (e.g., Collett & Smith 2020). Based on the asymmetric line profile with a clear blue cutoff, this line is interpreted as the Ly α line at $z = 4.95$. E and F have four multiple images each, whose spectrum around the observed emission line is shown in Fig. 4.5. Their position coordinates are reported in Table 4.1.

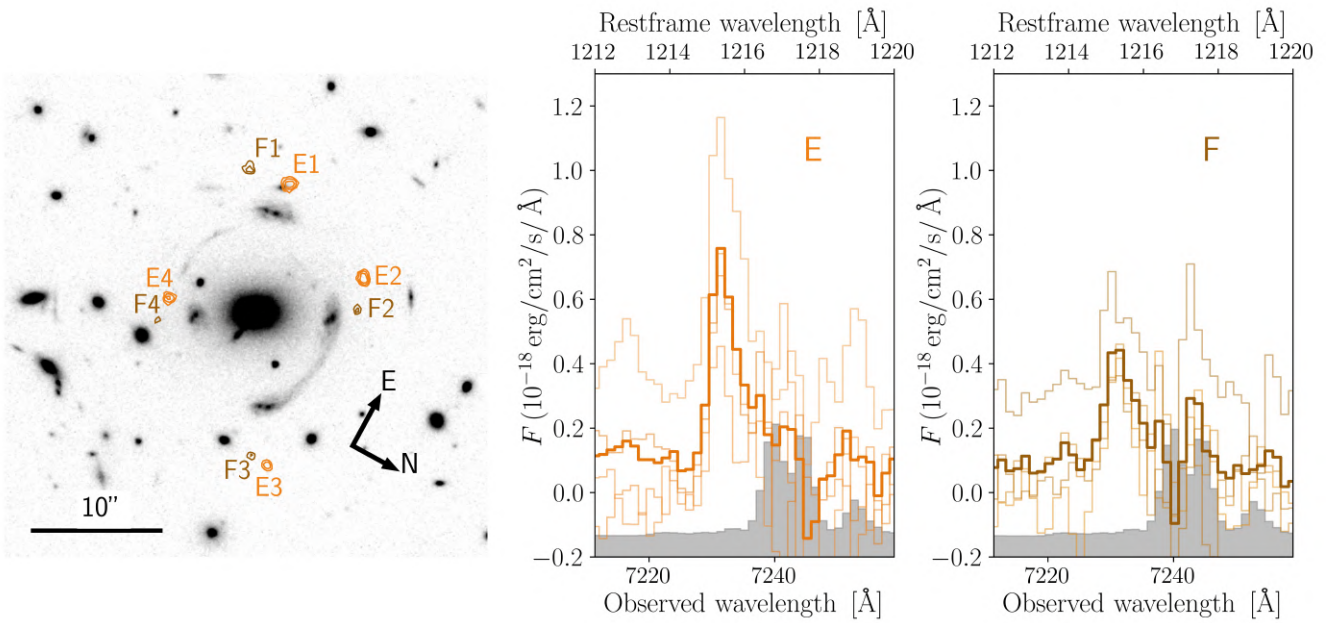


Figure 4.5: Left: contours from a continuum-subtracted narrow band image, centered on the emission line detected at $\approx 7231\text{ }\text{\AA}$, identified as the Ly α emission at $z = 4.95$. The contours are superimposed on the HST F160W image, to show that continuum counterparts are not detected. Center: zoom-in of the MUSE 1D spectra of the multiple images E1, E2, E3, E4, and stacked (thicker line), around the detected emission line. Right: same as in the center for F1, F2, F3 and F4. The spectra are extracted within the orange (E) and brown (F) apertures in Fig. 4.2, consisting of circular apertures with radius of $0.8''$, and are smoothed with a ~ 2.5 boxcar filter.

4.3.4 Discussion on system D

We identify an additional system with four multiple images, labeled as D1-4 in Fig. 4.1. D1 and D4 are distorted into an extended arc South-East to the main elliptical deflector, D2 is faint in the North-East direction, and D3 lies between B3 and F3 in the West direction, angularly close to a group member with a F160W magnitude of 21.32 mag. We extracted the D spectrum from an elongated region that includes the D1/D4 arc, shown in Fig. 4.2. We also extracted the spectra of D2 and D3 within circular apertures, but they revealed to be too faint and too contaminated, respectively. We do not detect any clear spectral feature that allows us to obtain a secure redshift measurement for D. The lack of strong emission lines in MUSE and the positions of the multiple images suggest that D lies at a redshift between approximately 1.5 and 2, but further observations will be needed to confirm the nature of this system. The D system was hypothesized also in our previous study, but did not enter in the analysis. We anticipate here

Table 4.1: Right ascension (RA) and declination (dec), redshift (z), and distance in projection from the brightest group galaxy (BGG) center (d) of the detected multiple images.

ID	RA	dec	z	d ['']
BGG	01:00:49.18	+18:18:27.79	0.581	0.00
A1	01:00:49.71	+18:18:25.50	1.880	7.54
A2	01:00:49.36	+18:18:33.05	1.880	5.86
A3	01:00:48.78	+18:18:32.06	1.880	7.37
A4	01:00:49.03	+18:18:23.85	1.880	4.56
B1	01:00:49.69	+18:18:24.74	1.880	7.67
B2	01:00:49.33	+18:18:32.89	1.880	5.54
B3	01:00:48.76	+18:18:31.40	1.880	7.23
B4	01:00:48.99	+18:18:23.75	1.880	4.86
C1	01:00:49.84	+18:18:24.98	1.698	9.60
C2	01:00:49.04	+18:18:27.38	1.698	2.25
E1	01:00:49.87	+18:18:25.27	4.95	10.01
E2	01:00:49.63	+18:18:33.69	4.95	8.64
E3	01:00:48.50	+18:18:34.15	4.95	11.70
E4	01:00:49.03	+18:18:21.41	4.95	6.70
F1	01:00:49.85	+18:18:22.15	4.95	10.91
F2	01:00:49.46	+18:18:34.43	4.95	7.72
F3	01:00:48.50	+18:18:32.52	4.95	10.90
F4	01:00:48.88	+18:18:21.55	4.95	7.59

Notes. The coordinates of the multiple images of families A, B, and C are measured with **SExtractor** in the HST F160W image, while the positions of the multiple images of the E and F sources, whose continuum is not detected in HST, are taken as the brightest pixels in a narrow-band image centered around their Ly α emission lines.

that we continue to exclude the multiple images of source D in the strong lensing modeling described in the following for different reasons. The lack of a secure redshift measurement, the fact that it is not possible to clearly identify a position and a brightest pixel for image D2, and the position of D3 that is strongly perturbed by the mass distribution of a group member angularly very close, make the inclusion of family D strongly uncertain. Furthermore, our best-fit strong lensing model currently disfavors the inclusion of this system, based on the noisy observables. For these reasons, we leave the inclusion of system D for future strong lensing modeling efforts, may its redshift and its spatial positions be confirmed with deeper observations.

4.3.5 Group members

In Chapter 3, given the large estimated value of the deflector total mass, we considered the possibility of SDSS J0100+1818 being a group of galaxies, and we found 53 galaxies in a $2.5' \times 2.5'$ field of view with photometric redshifts consistent, at the 2σ level, with the spectroscopic redshift of the main elliptical galaxy. Thanks to the MUSE data, we securely select and consider as part of the same group all the galaxies with spectroscopic redshift in the 0.581 ± 0.011 range, corresponding to the mean redshift of the overdensity at $z \approx 0.6$, with a spread of $\pm 2000 \text{ km s}^{-1}$ (rest-frame). With this method, we select 19 group members (with $\text{QF} \geq 3$), including the main elliptical galaxy, hereafter referred to as brightest group galaxy (BGG), whose positions are

shown in Fig. 4.2. They are distributed through the entire MUSE field of view. The closest and the furthest group members lie approximately $4''$ (27 kpc) and $33''$ (220 kpc) away in projection from the BGG, respectively. Three group members are located within $7''$ (approximately the physical Einstein radius of system AB), eight within $15''$, and thirteen within $20''$. We measure their F160W Kron magnitudes with `SExtractor`, ranging from 17.05 mag to 22.96 mag. We note that the second brightest member has a magnitude of 19.94, almost three magnitudes fainter than the BGG.

4.3.6 Velocity dispersion profile

With the new MUSE data, we are able not only to confirm the extremely large stellar velocity dispersion value, σ_* , that elects the main deflector to be one of the most massive galaxies known at intermediate redshift, but also to measure a stellar velocity dispersion profile, considering the first aperture of $0.4''$ of radius and then different annuli with the same center (see Fig. 4.6). The spectral S/N is larger than 15 in all the selected bins and the corresponding velocity dispersion values are partially correlated, given the observational PSF FWHM. We measured the value of the stellar line-of-sight velocity dispersion of each bin following the procedure presented in [Granata et al. \(2023\)](#). We used pPXF (penalized pixel-fitting, [Cappellari & Emsellem 2004b](#); [Cappellari 2017b, 2023](#)) to compare the observed spectra with a combination of stellar templates chosen from a set of 463 UVB stellar spectra with $S/N > 100^{-1}$ from the X-shooter Spectral Library (XSL) DR2 ([Gonneau et al. 2020](#)), convolved with a line-of-sight velocity distribution. The obtained global stellar velocity dispersion presents a value that is consistent, but systematically lower than the previous estimate with X-Shooter. The difference can be explained mainly by the different S/N of the two datasets (significantly higher for MUSE), in addition to the different spectral resolution of the instruments and stellar templates adopted to model the spectra. In the following, we will refer to the MUSE estimate, given that it is more robust. Moreover, this value will result consistent with the BGG mass obtained from the strong lensing analysis (see Sections 4.4 and 4.5).

4.4 Lensing modeling

We performed our strong lensing modeling with the Gravitational Lens Efficient Explorer (GLEE; [Suyu & Halkola 2010](#)) software, that allows one both to optimize the parameter values and to infer their probability distributions, through Bayesian analyses like simulated annealing and Markov chain Monte Carlo (MCMC), respectively. GLEE supports several types of mass and light profiles, whose parameters can be optimized by reproducing the observed positions, fluxes, and/or time delays of multiple images. In this study, we employed the positions of the 18 multiple images from the five background sources A, B, C, E, and F, listed in Table 4.1. For A, B, and C, we considered each multiple image position as that of its brightest pixel in the HST F160W image, with an uncertainty of one HST pixel ($0.066''$). For E and F, that do not show continuum in the HST images, we considered the brightest pixel in a narrow-band image centered around the Ly α emission line. For these images, we adopted a positional uncertainty of $0.15''$. In this chapter, we only performed a point-like source modeling, given that the images of the sources E and F do not present any HST continuum. We leave the extended source modeling approach for a future work, where we will treat properly the weighing of a combination of extended and point-like sources.

The best-fit values of the parameters of each model were estimated with a simulated annealing technique, structured in several steps, first minimizing the χ^2 value on the source plane, and then

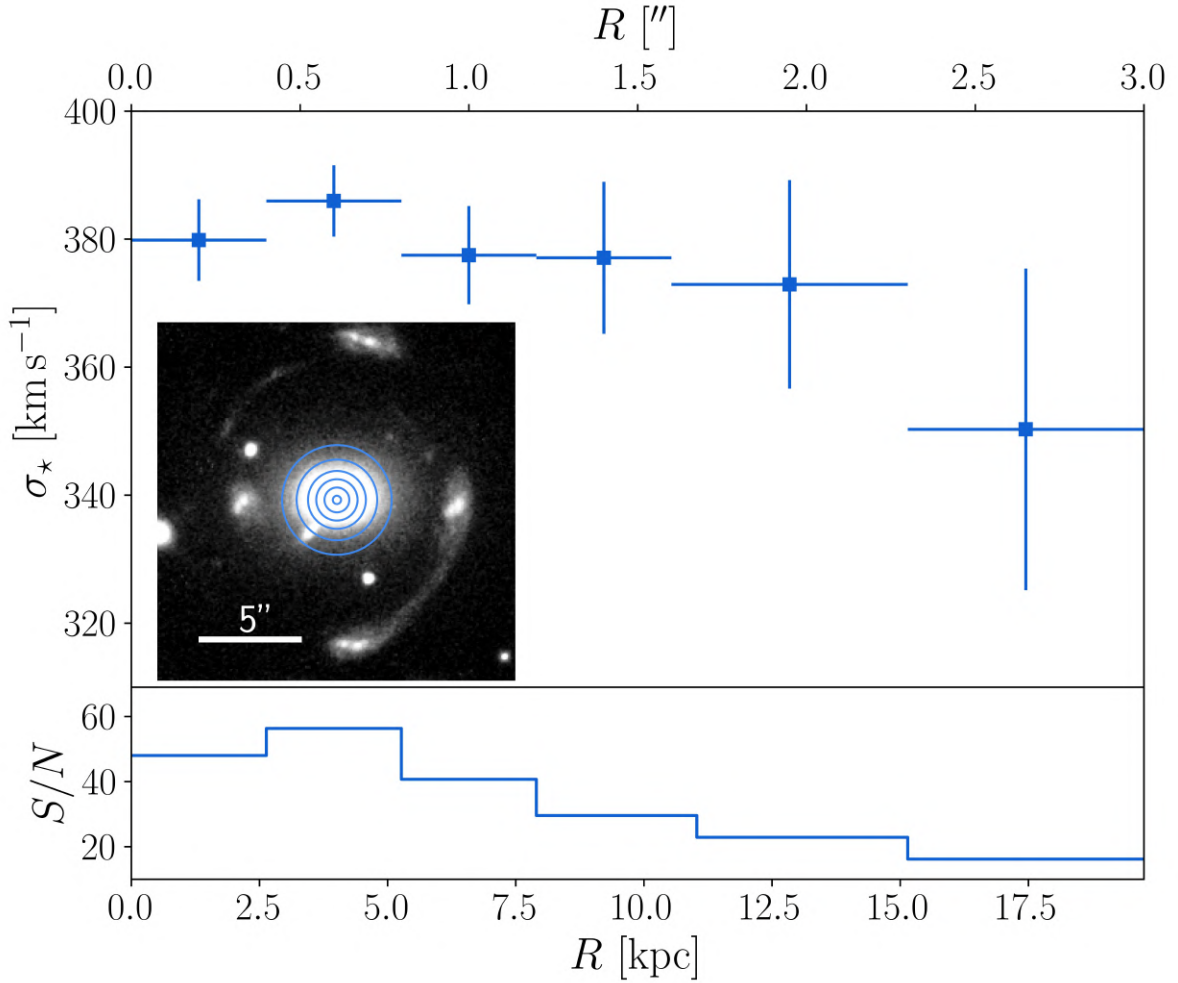


Figure 4.6: Stellar velocity dispersion profile of the main deflector. The apertures (the first $0.4''$ -radius aperture and then different annuli with the same center) used to extract the spectra relative to each bin are shown in the inset. In the bottom panel, we show the spectral S/N of each bin, that is larger than 15 in all of them, peaking at around 60. Given the value of the observational PSF FWHM and of the chosen bin widths, the σ_* values of the profile are partially correlated.

on the deflector plane. We assumed different total mass profiles for the deflector, and evaluated their goodness by considering different statistical estimators, often employed in similar strong lensing studies (see, e.g., [Acebron et al. 2017](#); [Mahler et al. 2018](#)). We took into account: (1) the number of degrees of freedom (ndof), defined as the difference between the number of observables and the number of free parameters, (2) the value of the minimum χ^2 , defined as

$$\chi^2 = \sum_{i=1}^N \frac{|\boldsymbol{\theta}_i^{\text{obs}} - \boldsymbol{\theta}_i^{\text{pred}}|^2}{\sigma_i^2}, \quad (4.1)$$

where $\boldsymbol{\theta}_i^{\text{obs}}$ are the positions of the observed images, $\boldsymbol{\theta}_i^{\text{pred}}$ are their positions as predicted by the model, N is the total number of multiple images and σ_i is the positional uncertainty relative to the i -th image, (3) the value of the root-mean-square difference (rms) between the observed and the model predicted positions of the multiple images, defined as

$$\text{rms} = \sqrt{\frac{1}{N} \sum_{i=1}^N |\boldsymbol{\theta}_i^{\text{obs}} - \boldsymbol{\theta}_i^{\text{pred}}|^2}, \quad (4.2)$$

(4) the Bayesian Information Criterion (BIC, [Schwarz 1978](#)), given by

$$\text{BIC} = k \ln N_{\text{obs}} + \chi^2, \quad (4.3)$$

where k is the number of free parameters and N_{obs} is the number of data points ($= 2N$, for the x and y coordinates of the multiple images), and (5) the corrected Akaike Information Criterion (AICc, [Akaike 1974](#); [Cavanaugh 1997](#)), defined as

$$\text{AICc} = 2k + \chi^2 + \frac{2k(k+1)}{N_{\text{obs}} - k - 1}. \quad (4.4)$$

The BIC and AICc estimators penalize models with an increasing number of free parameters, to contrast overfitting. Thus, models with lower BIC and AICc (as well as rms and minimum χ^2) values are preferred.

Additionally, we estimated median values and uncertainties for the model parameters from MCMCs of 10^7 steps, with acceptance rates between 20% and 30%, and rejecting the first 10% burn-in steps. These chains are the final step of a sequence in which each intermediate chain is used to estimate the covariance matrix of the model parameters and to extract the starting point for the following one. To obtain sensible confidence intervals for the values of the parameters from the chains, we rescaled the positional uncertainties until the χ^2 value is similar to the number of degrees of freedom.

Thanks to the relatively simple structure of group-scale systems, we described the total mass distribution of SDSS J0100+1818 and disentangled the different mass contributions by assuming a straightforward composite model, with different mass components describing those of the BGG, of the group members, and of the extended DM halo. In the following subsections, we will detail the different parametrizations considered, that will give rise to the four models presented in Section 4.4.3.

4.4.1 Inclusion of group members

We modeled the dimensionless surface mass density (convergence, κ) of each group member as a dual pseudoisothermal elliptical mass distribution (dPIE; [Elíasdóttir et al. 2007](#)). In GLEE, this

profile is described by six parameters: the x and y coordinates of the center, the semiminor (b) to semimajor (a) axis ratio $q = b/a$, the position angle θ (measured counter clockwise from $+x$), the Einstein radius θ_E , the core radius r_{core} , and the truncation radius r_T . Through this work, we assumed the total mass distribution of the members to be spherical ($q = 1$), and without a core radius ($r_{\text{core}} = 0$). Within these approximations, the convergence becomes

$$\kappa_{\text{dPIE}}(x, y) = \frac{\theta_E}{2} \left(\frac{1}{R} - \frac{1}{\sqrt{R^2 + r_T^2}} \right), \quad (4.5)$$

where $R = \sqrt{x^2 + y^2}$, and

$$\theta_E = \frac{4\pi\sigma^2}{c^2}, \quad (4.6)$$

with σ representing the effective velocity dispersion of the deflector. In our analysis, we weighed the total mass of each group galaxy based on its luminosity, L , as it is commonly done in cluster-scale strong lensing modeling (e.g., Grillo et al. 2015; Caminha et al. 2019; Acebron et al. 2022; Bergamini et al. 2023b). We estimated L from the Kron magnitude measured with **SExtractor** in the HST F160W band, and we linked the i -th galaxy total mass, described by the values of the Einstein radius, $\theta_{E,i}$ and truncation radius, $r_{T,i}$, and its luminosity via the following scaling relations:

$$\theta_{E,i} = \theta_{E,\text{ref}} \left(\frac{L_i}{L_{\text{ref}}} \right)^\alpha \quad \text{and} \quad r_{T,i} = r_{T,\text{ref}} \left(\frac{L_i}{L_{\text{ref}}} \right)^\beta, \quad (4.7)$$

where $\theta_{E,\text{ref}}$ and $r_{T,\text{ref}}$ are reference values relative to a galaxy at the redshift of the group. In particular, we selected the BGG as the reference galaxy, when it is included in the scaling relations, and the second brightest group member at (RA, dec) = (1:00:48.68, +18:18:12.67) ($m = 19.94$ mag), when the BGG is parametrized separately, i.e. without its parameter values following the scaling relations. In this latter case, the models will be labeled with "+BGG" at the end of the name.

We fixed $\alpha = 0.7$ and $\beta = 0.5$ (e.g., Grillo et al. 2015; Wang et al. 2022). Given that for a dPIE profile the total mass, M_T , is proportional to θ_E and r_T , the total mass-to-light ratio, for the assumed values of α and β , increases with the luminosity as

$$\frac{M_T}{L} \sim \frac{\theta_{E,T}}{L} \sim \frac{L^{0.7} L^{0.5}}{L} \sim L^{0.2}, \quad (4.8)$$

corresponding to the “tilt of the Fundamental Plane” observed in elliptical galaxies (Faber et al. 1987; Bender et al. 1992; Ciotti et al. 1996; Bernardi et al. 2003; Grillo & Gobat 2010).

4.4.2 Dark matter halo

We completed the total mass modeling of the group with the inclusion of an additional mass component, representing, in particular, the group-scale DM halo and all the contributions not associated to the member galaxies. We explored two different mass profiles describing the extended and smooth mass distribution of the group. The first one is a pseudo-isothermal elliptical mass distribution (PIEMD; Kneib et al. 1996). In **GLEE**, it is defined by six parameters: the x and y coordinates of the center, the semi-minor (b) to semi-major (a) axis ratio $q = b/a$, the position angle θ (measured counter clockwise from $+x$), the Einstein radius θ_E , and the core radius r_{core} . We stress that the value of θ_E is defined for a source at $z = \infty$ and does not correspond to that of the Einstein radius of the system, which should be nearly independent of

the mass modeling details. The value of θ_E is a parameter which describes the lens strength and enters the dimensionless surface mass density κ_{PIEMD} as

$$\kappa_{\text{PIEMD}}(x, y) = \frac{\theta_E}{2\sqrt{r_{\text{core}}^2 + \frac{x^2}{(1+e)^2} + \frac{y^2}{(1-e)^2}}}, \quad (4.9)$$

where the ellipticity $e = \frac{1+q}{1-q}$. The second profile is a singular power law elliptical mass distribution (SPEMD; Barkana 1998). In GLEE, it is characterized by seven parameters: the first six are in common with the PIEMD profile, and the seventh is the slope g , which is related to the three-dimensional logarithmic mass density slope $\gamma' = -d\log[\rho(r)]/d\log(r)$ (i.e., $\rho \propto r^{-\gamma'}$) through $\gamma' = 2g + 1$ (i.e., an isothermal profile corresponds to $\gamma' = 2$ and $g = 0.5$). In the following, we will refer to the physical parameter γ' . Similarly to the PIEMD case, θ_E is a parameter of the mass distribution introduced in the dimensionless surface mass density κ_{SPEMD} as

$$\kappa_{\text{SPEMD}}(x, y) = \theta_E \left(x^2 + \frac{y^2}{q^2} + \frac{4r_{\text{core}}^2}{(1+q)^2} \right)^{-\frac{\gamma'-1}{2}}. \quad (4.10)$$

Following the definitions implemented in GLEE, the values of the θ_E parameters adopted in the PIEMD and in the SPEMD cases differ by a factor of $(1+q)$.

4.4.3 Mass models and results

We tested four different mass models, exploring two alternative profiles for the smooth, extended group mass distribution (PIEMD and SPEMD) and two options for the BGG in terms of scaling relations. Given the nature of the group, with the BGG being almost three magnitudes brighter than the second brightest galaxy and likely including a large fraction of the total mass of the group members, we tried two different options for the BGG: one in which the BGG follows the scaling relations of Eq. (4.7), and another one in which the total mass of the BGG is still parametrized by a dPIE profile, but independently of the other members. This second option allows the model to associate with more freedom the total mass contribution related to the BGG and to the other group members. To employ the lowest number of free parameters, we fixed the BGG position to its luminosity center, $q = 1$, and $r_{\text{core}} = 0$, leaving its total mass described only by θ_E and r_T . The four considered models are thus:

- **PIEMD:** This model includes a PIEMD mass distribution for the extended halo, and dPIEs for all the group members. The BGG is included in the scaling relations, so that the total mass of each group member is related to that of the BGG. This mass model is described by 8 free parameters: 6 relative to the extended halo and 2 to the scaling relations. Given that for all the models the number of observables is equal to 36 (x and y coordinates of each of the 18 total multiple images), this model has $\text{ndof} = 18$.
- **SPEMD:** Similar to the PIEMD model, this model includes a SPEMD mass distribution for the extended halo, and dPIEs for the group members, including the BGG. It is described by 9 free parameters (adding γ'), and has $\text{ndof} = 17$.
- **PIEMD+BGG:** This model includes a PIEMD mass distribution for the extended halo, an independent dPIE for the BGG, and dPIEs for the group members, linked through the scaling relations. This mass model is described by 10 free parameters: 6 relative to the extended halo, 2 relative to the dPIE of the BGG, and 2 to the scaling relations, and has $\text{ndof} = 16$.

- **SPEMD+BGG:** This model considers a SPEMD mass distribution for the extended halo, an independent dPIE for the BGG, and dPIEs for the group members linked through the scaling relations. It is described by 11 free parameters and has $\text{ndof} = 15$.

The best-fit values of the parameters corresponding to each model are reported in Table 4.2. By comparing the best-fit parameter values of these different models, we noticed that the center of the total mass approximately coincides with the luminosity center, when the BGG is modeled inside the scaling relations, while it is shifted by $\approx 0.2''$ in the $-x$ -direction, when it is not. The value of the axis ratio q of the extended halo does not vary significantly among all the different models, as well as that of the position angle θ . The PIEMD and SPEMD models predict similar values of the Einstein radii, which describe the strength of the lens, both for the extended halo and the BGG ($\theta_{\text{E, ref}}$). This latter value of approximately $4.7''$ is found also when the BGG is modeled outside of the scaling relations (in the PIEMD+BGG and SPEMD+BGG models), thus strengthening its robustness. The core radius of the diffuse halo increases by $\approx 15\%$, when it is parametrized with a SPEMD mass distribution, whose best-fit slope ($\gamma' \sim 2.2$) is slightly steeper than isothermal. The BGG has a truncation radius ($r_{\text{T, ref}}$ in PIEMD and SPEMD, and r_{T} in PIEMD+BGG and SPEMD+BGG) larger than the distance over which the multiple images appear (see Table 4.1).

Summarizing, we have found that the best-fit values of the parameters are stable when the BGG is modeled outside of the scaling relations. We note that, by reducing the number of degrees of freedom from 18 of the PIEMD model to 15 of the SPEMD+BGG one, the χ^2_{\min} value decreases from 86.63 to 76.82, with a corresponding reduction of the rms value from $0.23''$ to $0.21''$.

4.4.4 Mass profiles of the deflectors

We measured the cumulative total mass (M_{T}) profile for each model by randomly extracting 1000 parameter value sets from the last MCMC chains of 10^7 steps described above. GLEE can create the convergence maps, that we converted into total mass maps. Then, we summed up the contribution of all the pixels within circular apertures centered on the brightest pixel of the main lens galaxy, with a step of 0.5 pixels, to obtain the cumulative total mass profiles that are presented in the following. For each aperture, we estimated the 1σ uncertainties as the 16th and 84th percentile values of the distribution of the total mass values of all the 1000 random models. We separated the total mass contribution of the extended halo (PIEMD or SPEMD) from that of the group members (dPIE), by considering the relevant free parameters in the MCMC chains. The resulting cumulative mass profiles are shown in Fig. 4.7. The four models predict fully consistent total mass profiles, with mean relative uncertainties of only 2%. The total mass value projected within 50 kpc, approximately equivalent to the Einstein radius of the system, is $(1.55 \pm 0.01) \times 10^{13} M_{\odot}$, while within the projected distance of the furthest multiple image ($R \approx 77$ kpc) is $(2.78 \pm 0.04) \times 10^{13} M_{\odot}$.

The mass component associated with the diffuse halo presents a slightly larger mean uncertainty of around 10% in all the four models. For this component, the models predict a projected total mass value of $9.2_{-3.1}^{+1.2} \times 10^{12} M_{\odot}$, at $R = 50$ kpc, and of $1.9_{-0.7}^{+0.2} \times 10^{13} M_{\odot}$, at $R = 77$ kpc. As visible in Fig. 4.7, the profiles show that, in the central regions, the total mass is dominated by the group member contribution, while from $R \approx 35$ kpc outwards the extended halo prevails. The different models predict consistent relative weights for the different mass components, with the models with the BGG outside of the scaling relations assigning to the extended halo a slightly lower contribution.

Table 4.2: Results obtained for the deflector total mass distribution from the four adopted models.

PIEMD						
x ["]	y ["]	q	θ [rad]	θ_E ["]	r_{core} ["]	
-0.01	0.03	0.69	-0.02	20.35	7.19	
Scaling rel.	$\theta_{E,\text{ref}}$ ["]	$r_{T,\text{ref}}$ ["]				
	4.67	11.27				
	$N_{\text{obs}} = 36$		ndof = 18	$\chi^2_{\text{min}} = 86.63$		
	BIC = 151.13		AICc = 162.87	rms = 0.23"		
SPEMD						
x ["]	y ["]	q	θ [rad]	θ_E ["]	r_{core} ["]	γ'
0.05	0.05	0.70	-0.01	20.53	8.36	2.18
Scaling rel.	$\theta_{E,\text{ref}}$ ["]	$r_{T,\text{ref}}$ ["]				
	4.71	11.28				
	$N_{\text{obs}} = 36$		ndof = 17	$\chi^2_{\text{min}} = 86.62$		
	BIC = 154.71		AICc = 172.12	rms = 0.23"		
PIEMD+BGG						
x ["]	y ["]	q	θ [rad]	θ_E ["]	r_{core} ["]	
-0.20	0.04	0.68	-0.02	19.50	7.23	
dPIE BGG	θ_E ["]	r_T ["]				
	4.65	17.94				
Scaling rel.	$\theta_{E,\text{ref}}$ ["]	$r_{T,\text{ref}}$ ["]				
	2.74	0.65				
	$N_{\text{obs}} = 36$		ndof = 16	$\chi^2_{\text{min}} = 76.85$		
	BIC = 148.52		AICc = 172.85	rms = 0.21"		
SPEMD+BGG						
x ["]	y ["]	q	θ [rad]	θ_E ["]	r_{core} ["]	γ'
-0.19	0.05	0.68	-0.02	19.45	8.47	2.17
dPIE BGG	θ_E ["]	r_T ["]				
	4.71	18.05				
Scaling rel.	$\theta_{E,\text{ref}}$ ["]	$r_{T,\text{ref}}$ ["]				
	2.69	0.69				
	$N_{\text{obs}} = 36$		ndof = 15	$\chi^2_{\text{min}} = 76.82$		
	BIC = 152.07		AICc = 184.82	rms = 0.21"		

Notes. For each model, we show the best-fit values of the parameters, the number of degrees of freedom (ndof), the minimum chi-square (χ^2_{min}), and the rms values. The values of the x and y coordinates are referred to the center of light of the main elliptical lens galaxy, i.e., to its brightest pixel. The position angle θ is measured counter clockwise from the x -axis, aligned following the horizontal direction of Fig. 4.1. We report in the table only the values of the optimized parameters, while for each group member we fix its total mass center to its luminosity center ($\equiv (0, 0)$ for the BGG), and the axis ratio and core radius values to $q = 1$ and $r_{\text{core}} = 0$, respectively.

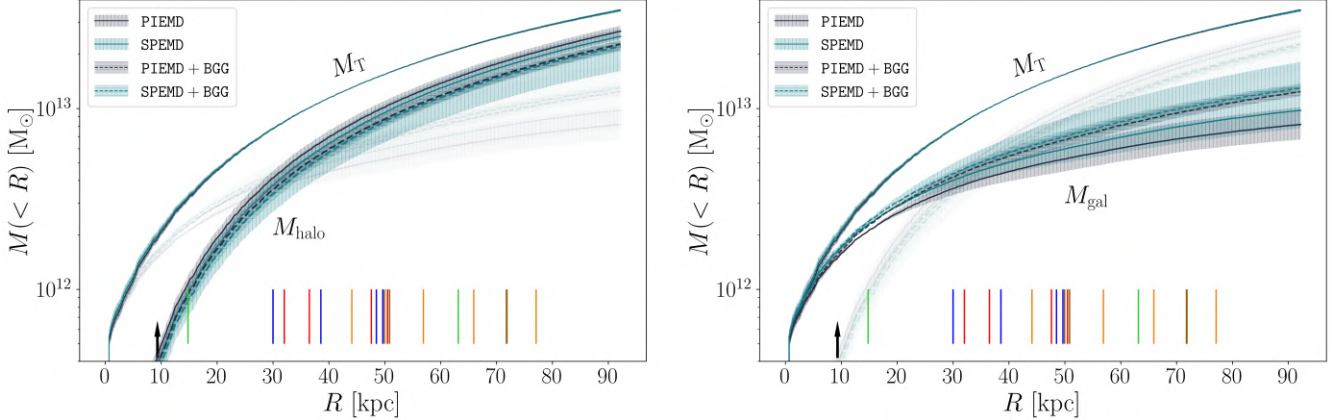


Figure 4.7: Cumulative projected total mass profiles for the PIEMD (solid black), SPEMD (solid blue), PIEMD+BGG (dashed black) and SPEMD+BGG (dashed blue) models with $\pm 1\sigma$ uncertainties (differently hatched shaded areas). The curves on top, labeled with M_T , are relative to the total mass, and they are divided into the halo component (M_{halo} , left panel) and the galaxy member component (M_{gal} , right panel), identified by the same linestyle. For comparison, we leave M_{gal} and M_{halo} as faint lines in the left and right panels, respectively. The vertical lines close to the x -axis locate the distances from the lens galaxy center of the different multiple images, color-coded following Fig. 4.1. The black line at $R = 9.32$ kpc shows the effective radius of the BGG.

We measured the stellar mass (M_*) profile of the BGG in Chapter 3 from its reconstructed luminosity profile, by assuming a constant stellar mass-to-light ratio estimated through a spectral energy distribution (SED) fitting. We assume here the same value for the stellar mass-to-light ratio of the other galaxy members and convert the HST F160W image into a M_* map, by multiplying it by the BGG mass-to-light ratio and by a mask designed to include only the pixels associated to the 19 group members (including the BGG). This is justified by the fact that all the group members show similar spectra and colors in the MUSE and photometric data, and thus they are likely early-type galaxies hosting similar stellar populations. From the resulting image, we measured the cumulative projected stellar mass profile of the group by summing the contribution of the pixels within circular apertures centered on the brightest pixel of the main lens galaxy, with a step of 0.5 pixels. The profile is shown in the top panel of Fig. 4.8. The BGG clearly dominates the light (and thus the stellar mass) distribution, and the inclusion in the external apertures of the other group members is visible as steps in the profile. Given that we can measure the stellar mass distribution of the group all across the MUSE field of view, it is possible to explore the outer regions, up to $R \approx 30'' \approx 180$ kpc. We note that the total stellar mass value of the group at $R = 180$ kpc is approximately equal to 1.5 times that of the BGG and, at the largest distance where the multiple images appear ($R \approx 77$ kpc), the total stellar mass of the group is $(1.7 \pm 0.3) \times 10^{12} M_\odot$, and the BGG contributes with almost 90% of it, namely with $(1.5 \pm 0.3) \times 10^{12} M_\odot$. We remark that the cumulative stellar mass profile is between 1.5 and 5 times smaller than the total one associated with the galaxy member components, shown in the right panel of Fig. 4.7. This difference is mainly due to the presence of DM, in the form of galaxy-scale halos, in the group members.

In the bottom panel of Fig. 4.8, we plot the cumulative projected stellar-over-total mass fraction profiles relative to each model. They are all in very good agreement, differing only by less than 2% in the inner region, and by a fraction of percent from $R > 20$ kpc outwards. We

measured a stellar-over-total mass fraction value of $45.6^{+8.7\%}_{-8.3\%}$ at the lens galaxy effective radius ($R_e = 9.32$ kpc), decreasing to $(11.1 \pm 1.9)\%$ at $R = 50$ kpc and to $(6.6 \pm 1.1)\%$ at $R \approx 77$ kpc.

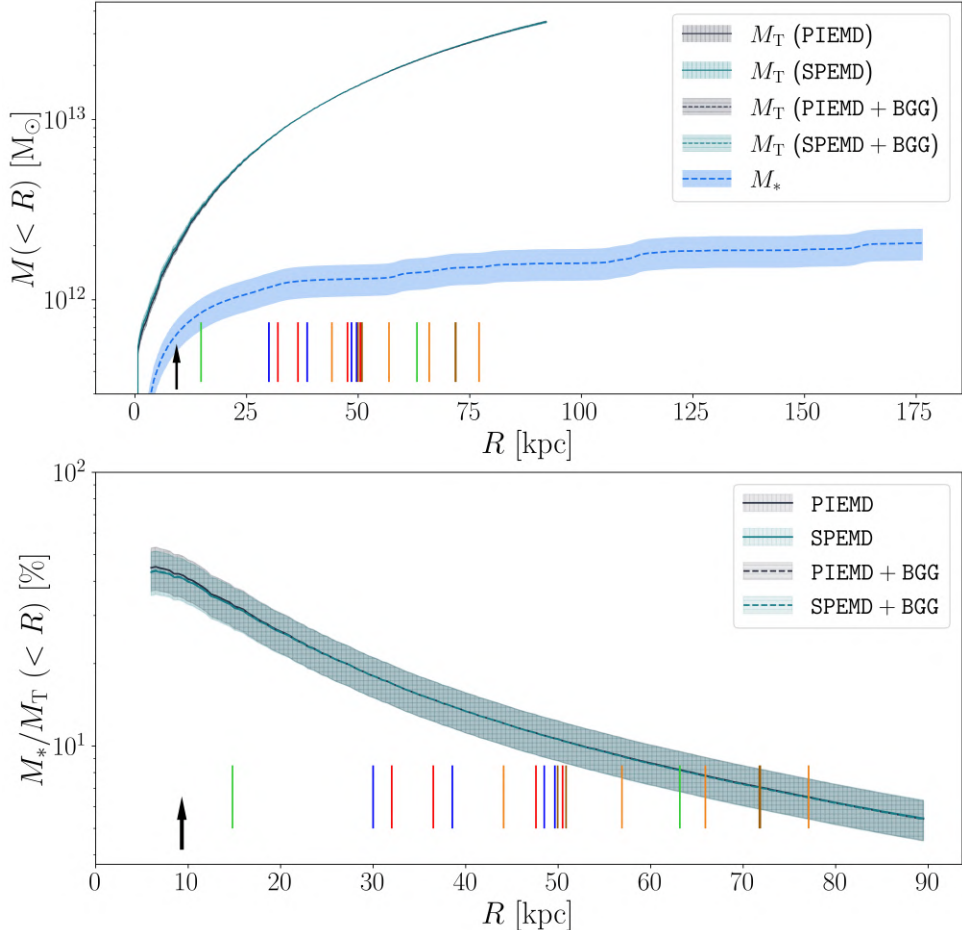


Figure 4.8: Top: cumulative projected total mass profiles for the PIEMD (solid black), SPEMD (solid blue), PIEMD+BGG (dashed black) and SPEMD+BGG (dashed blue) models with $\pm 1\sigma$ uncertainties (differently hatched shaded areas), as in Fig. 4.7, compared with the cumulative projected stellar mass profile with $\pm 1\sigma$ uncertainties, represented by the light blue dashed curve and shaded area, respectively. Bottom: cumulative projected stellar-over-total mass fraction profiles, color coded for each model according to the top panel. In both panels, the vertical lines close to the x -axis locate the distances from the lens galaxy center of the different multiple images, color-coded following Fig. 4.1. The black line at $R = 9.32$ kpc shows the effective radius of the BGG.

4.5 Strong lensing models with variable cosmology

The observed positions of the lensed multiple images of a system depend both on the total mass distribution of the lens and on the cosmological angular-diameter distances between the observer, the lens, and the sources. Systems where multiple sources at different redshifts are strongly lensed by the same foreground deflector allow one to break the mass-cosmology degeneracy, and thus to learn about the geometry of the Universe. By measuring the ratio of different Einstein radii in a multiple-source system, and assuming a cosmological model, it is possible to estimate the values of the cosmological parameters defining the global geometry of the Universe, without

any dependence on the value of H_0 (Collett et al. 2012). The same parameter values can be measured thanks to other cosmological probes (Eisenstein et al. 2005; Komatsu et al. 2014; Treu et al. 2022b). In light of the results of the statistical estimators adopted and discussed in the previous sections, we decided to consider in the following only the PIEMD and SPEMD models. We assumed a flat ($\Omega_\Lambda + \Omega_m = 1$) Λ CDM cosmology and reoptimized the PIEMD $_{\Omega_m}$ and SPEMD $_{\Omega_m}$ models, where Ω_m was introduced as a free parameter. We further reconsidered the PIEMD $_{\Omega_m w}$ and SPEMD $_{\Omega_m w}$ models in a flat w CDM cosmology, where both Ω_m and w were free to vary. We reran the same procedure described above, starting from a χ^2 minimization on the lens plane and then obtaining a sequence of MCMC chains, resulting in a final one composed of 10^7 steps. We adopted uniform priors on the values of Ω_m and w , respectively, between 0 and 1, and -2 and 0.

To fully exploit our observational dataset and alleviate possible degeneracies between the values of the cosmological and lens total mass distribution parameters, we used the available kinematic information on the BGG to impose a Gaussian prior on the value of its Einstein radius $\theta_{E,\text{ref}}$. As we wished to probe the inner kinematics of the BGG, we weighed the MUSE cube with its observed surface brightness in the HST F160W band, degraded and re-binned to the PSF and pixel-scale of MUSE. We then extracted a spectrum within an aperture with a radius of $3''$, centered on the BGG. This light-weighted extraction procedure yields measured velocity dispersion values equivalent to those that would be obtained from a non-weighted spectrum extracted within the galaxy effective radius (Granata et al. in prep.). By doing so, we measured a stellar velocity dispersion value of $(380.5 \pm 4.4) \text{ km s}^{-1}$. We converted this value, with a conservative uncertainty of 10 km s^{-1} , to the corresponding Einstein radius for an isothermal profile, through Eq. 4.6. We note that the value obtained in this way is very similar to the best-fit values of $\theta_{E,\text{ref}}$ and θ_E of the BGG reported in Table 4.2, as well as consistent within about 1σ with the results from the respective posterior probability distributions (e.g., $(409 \pm 29) \text{ km s}^{-1}$ for the PIEMD+BGG model). Furthermore, we checked that the introduction of this prior does not have any significant impact on the lens mass profiles reconstructed through the different models. In detail, all the profiles shown in Figs. 4.7 and 4.8 did not vary appreciably.

We report in Table 4.3 the median values, with the 68% confidence level (CL) uncertainties, of the cosmological parameters Ω_m and w , and show in Fig. 4.9 their posterior probability distributions for the PIEMD $_{\Omega_m w}$ and SPEMD $_{\Omega_m w}$ models. The average 1σ uncertainty is on the order of 0.1 for Ω_m and 0.4 for w . The Ω_m distributions are skewed towards the lower limit of our uniform prior (i.e., zero), thus in the table we also include the 95.4% quantile upper limits. The models with w as a free parameter predict median values of w smaller than -1 , with relative uncertainties of approximately 30%. In particular, we found $w = -1.27^{+0.43}_{-0.48}$ and $w = -1.38^{+0.38}_{-0.41}$ for the PIEMD $_{\Omega_m w}$ and SPEMD $_{\Omega_m w}$ models, respectively. The considered statistical estimators did not reveal a strongly preferred model, as all of them reproduced the observed positions of the multiple images with the same rms of $0.23''$ (and thus had very similar χ^2_{min} values). Consequently, the PIEMD $_{\Omega_m}$ model, given its smallest number of free parameters, is moderately preferred by both the BIC and AICc metrics, followed by the PIEMD $_{\Omega_m w}$ model.

4.5.1 Multi-plane approach

Given the presence of galaxies (i.e., mass concentrations) at different redshifts, we additionally adopted a multi-plane strong lensing approach (Blandford & Narayan 1986b; Schneider et al. 1992b), to take into account the fact that the light rays coming from the furthest sources are deflected not only once, by the main group at $z = 0.581$, but instead multiple times by other

Table 4.3: Cosmological parameters Ω_m and w from the six adopted strong lensing models with variable cosmology.

Model	Ω_m	Ω_m 95.4% upper limit	w
PIEMD_ Ω_m			
	$0.14^{+0.16}_{-0.09}$	0.47	
	$N_{\text{obs}} = 36$	ndof = 17	$\chi^2_{\min} = 85.95$
	BIC = 154.04	AICc = 171.45	rms = 0.23''
SPEMD_ Ω_m			
	$0.09^{+0.10}_{-0.06}$	0.29	
	$N_{\text{obs}} = 36$	ndof = 16	$\chi^2_{\min} = 85.94$
	BIC = 157.61	AICc = 181.94	rms = 0.23''
PIEMD_ $\Omega_m w$			
	$0.19^{+0.17}_{-0.10}$	0.59	$-1.27^{+0.43}_{-0.48}$
	$N_{\text{obs}} = 36$	ndof = 16	$\chi^2_{\min} = 85.68$
	BIC = 157.35	AICc = 181.68	rms = 0.23''
SPEMD_ $\Omega_m w$			
	$0.15^{+0.10}_{-0.07}$	0.34	$-1.38^{+0.38}_{-0.41}$
	$N_{\text{obs}} = 36$	ndof = 15	$\chi^2_{\min} = 85.68$
	BIC = 160.93	AICc = 193.68	rms = 0.23''
MP-PIEMD_ Ω_m			
	$0.18^{+0.29}_{-0.12}$	0.76	
	$N_{\text{obs}} = 36$	ndof = 16	$\chi^2_{\min} = 84.45$
	BIC = 156.12	AICc = 180.45	rms = 0.23''
MP-PIEMD_ $\Omega_m w$			
	$0.19^{+0.30}_{-0.11}$	0.81	$-1.39^{+0.49}_{-0.41}$
	$N_{\text{obs}} = 36$	ndof = 15	$\chi^2_{\min} = 84.42$
	BIC = 159.67	AICc = 192.42	rms = 0.23''

Notes. The median values, with the 68% CL uncertainties, of the cosmological parameters Ω_m and w were extracted as the 50th quantiles, and from the 16th and 84th quantiles of the posterior probability distributions from the MCMC chains. Given that the Ω_m distributions are skewed towards values approaching zero, we also include the 95.4% quantile upper limits. For each model, we also report the adopted metrics describing the goodness of the best-fit models. The two bottom entries are based on the multi-plane approach, with an additional mass distribution at $z = 1.880$ (see Sect. 4.5.1).

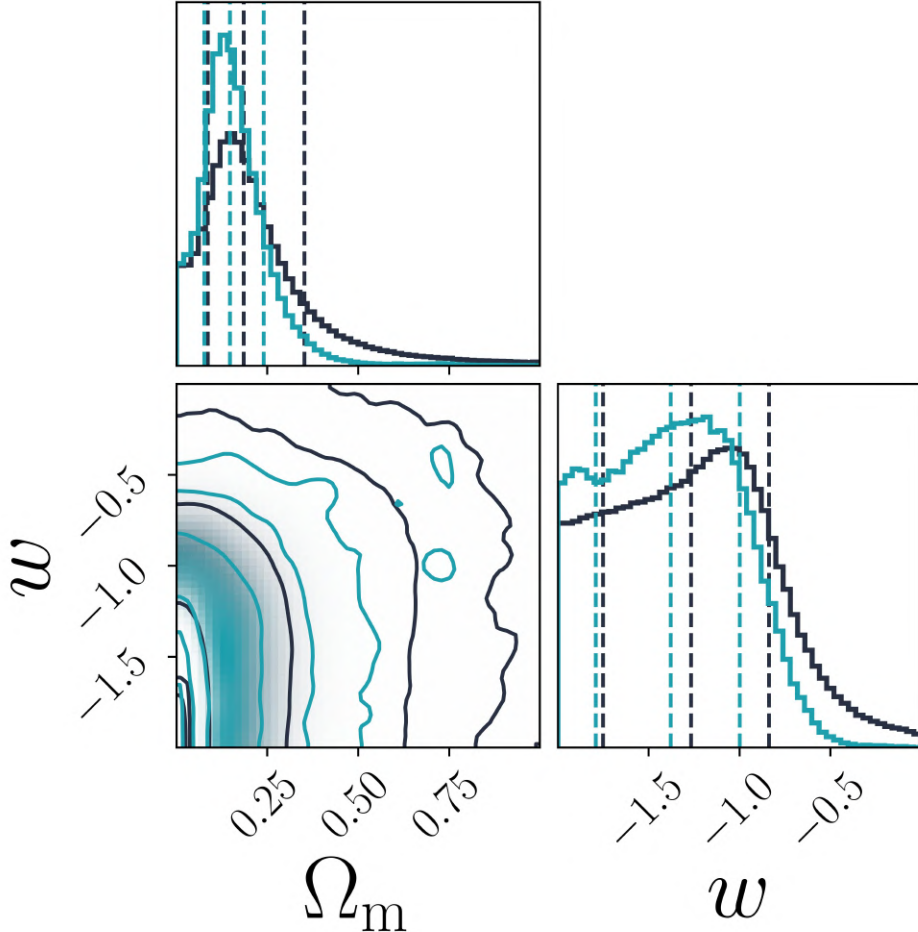


Figure 4.9: Probability density distributions of the cosmological parameters Ω_m and w in the `PIEMD_Ωmw` (black) and `SPEMD_Ωmw` (blue) models. We show the marginalized 1D histograms of each parameter and their joint 2D probability distribution. The vertical dashed lines in the 1D histograms represent the 16th, 50th, and 84th percentiles, while the solid lines in the 2D distributions represent the 0.68, 0.95 and 0.99 contour levels.

secondary deflectors at different redshifts. In particular, we explored the impact of such an approach on the inferred values of the cosmological parameters.

In the multi-plane formalism, the total deflection angle is a suitable sum of all the deflection angles relative to the different deflector planes (see, e.g., Gavazzi et al. 2008). This approach has been used to model both different foreground and background deflectors at distances different from that of the primary lens (e.g., Chirivì et al. 2018; Schuldt et al. 2024, Acebron et al., in prep.) and to assign mass to multiply imaged background sources, where several sources at different redshifts are lensed by the same deflector (e.g., Gavazzi et al. 2008; Schuldt et al. 2019; Collett & Smith 2020; Wang et al. 2022).

The lens models described above predict that the sources A, B, E, and F are located angularly close to the optical axis (i.e., the center of the BGG), while C lies $\sim 2''$ away. Considering the mutual angular distances, and the pixelated source reconstructions developed in the previous chapter, it is likely that the second largest contribution to the total deflection is that happening

at the plane of A and B on the light rays coming from sources E and F. Thus, we developed the MP-PIEMD $_{\Omega_m}$ and MP-PIEMD $_{\Omega_m w}$ models, that extended the PIEMD $_{\Omega_m}$ and PIEMD $_{\Omega_m w}$ models, respectively, by adding an additional PIEMD mass distribution at the redshift of A and B, $z = 1.880$. We imposed it to be spherical ($q = 1$) and with a vanishing core radius. Thus, this mass structure is described by three parameters: the coordinates (x_2, y_2) of the center of mass and θ_{E2} , where the subscripts indicate that these parameters are referred to the secondary lens. We repeated the procedure described above, minimizing the χ^2 on the lens plane, and then running a set of MCMC chains, resulting in a final one of 10^7 steps. The value of θ_{E2} was extracted with a uniform large prior, while the values of x_2 and y_2 were linked to the position of source A (that is brighter and more extended than B). The MP-PIEMD $_{\Omega_m}$ and MP-PIEMD $_{\Omega_m w}$ models are able to reproduce the observed positions of the multiple images with rms values of $0.23''$ (as for the PIEMD $_{\Omega_m}$ and PIEMD $_{\Omega_m w}$ models), but they are penalized by their BIC and AICc scores, due to the inclusion of the additional free parameter (the position of source A was optimized also in the previous models). From the posterior probability distributions, we observed a clear degeneracy between the parameters describing the centroids of the main halo at $z = 0.581$, (x, y) , and of the secondary lens, (x_2, y_2) . No clear degeneracy is observed with the cosmological parameters, that present consistent median values and uncertainties similar for w and boosted by a factor of ~ 1.5 for Ω_m , due to the more extended tails towards large values (see Fig. 4.10 and the bottom rows of Table 4.3). We also notice that these extended models predict cumulative total mass profiles for the main deflector that are fully consistent with those shown in Fig. 4.7.

4.6 Discussion

4.6.1 An enhanced model for SDSS J0100+1818

We compare here our results with those obtained in Chapter 3, highlighting the improvements and the overall consistency. The new MUSE data allowed us to:

- spectroscopically confirm the redshift of source C ($z_C = 1.698$). This value is fully consistent with the best-fit measurements of 1.72 and 1.69 of the previous chapter. This spectroscopic confirmation enabled to reduce some degeneracies found in the previous chapter between z_C and the parameters (in particular θ_E and γ') describing the total mass distribution of the deflector;
- characterize the deflector plane. We identified 18 group members (excluding the BGG), that were included in the strong lensing model as individual mass components, instead of as an external shear term, and we measured the BGG stellar velocity dispersion profile with an accuracy of $\lesssim 8\%$ (approximately 3% in the four inner bins);
- reduce the relative uncertainties on the cumulative total mass profiles from 17%, 1%, and 5%, to 3%, < 1%, and 1%, at $R \approx 15, 42$, and 63 kpc, respectively, thanks to the increased number of multiple images from additional sources at different redshifts;
- enlarge the radial interval probed by strong gravitational lensing with the discovery of the systems E and F, from the closest multiple image (C2, at $R \approx 15$ kpc) to the furthest (E3 at $R \approx 77$ kpc, previously C1 at $R \approx 63$ kpc). This allowed us to robustly reconstruct the total mass profile at previously unexplored physical distances from the group center with a precision of just a few percent;
- confirm the measured median and $\pm 1\sigma$ cumulative total mass profiles (Fig. 4.7), as well as the stellar-over-total mass profiles (Fig. 4.8), found in the previous chapter over the explored radial distances. In particular, we measure here (measured in Chapter 3) a projected total mass value of $(1.20 \pm 0.01) \times 10^{13} M_\odot$ ($(1.16 \pm 0.01) \times 10^{13} M_\odot$) within 42 kpc, and a stellar-over-total

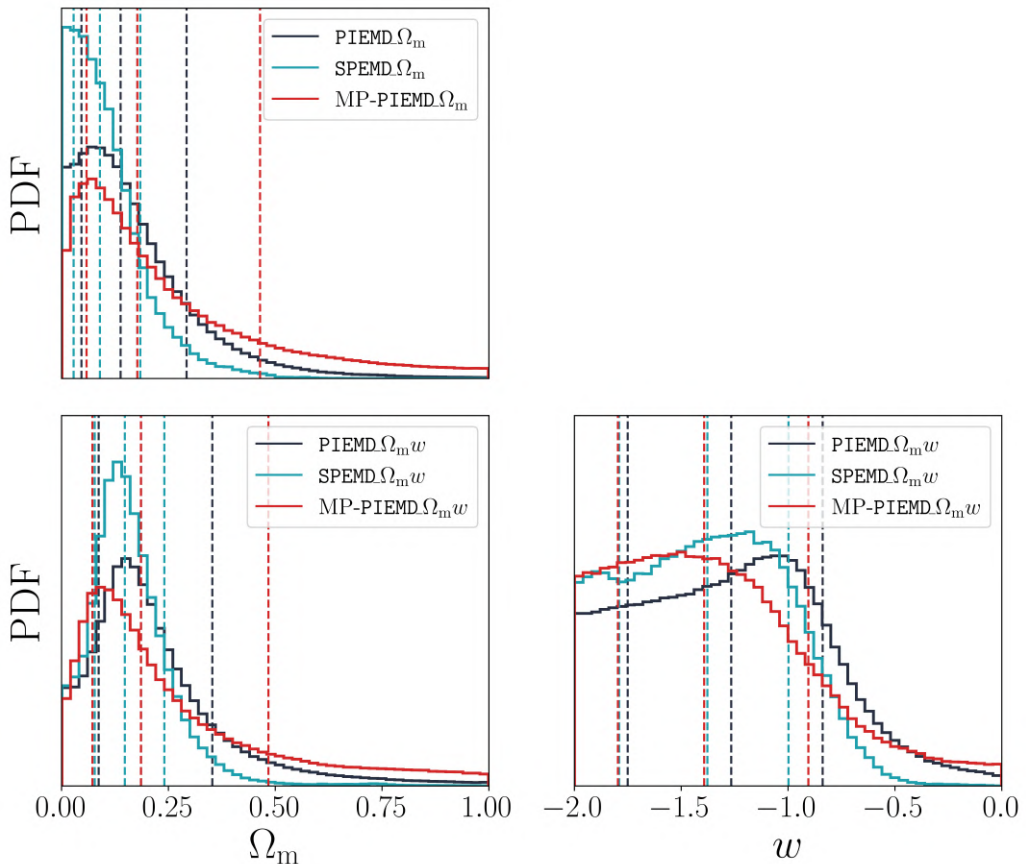


Figure 4.10: Marginalized 1D probability density distributions of the cosmological parameters Ω_m and w in the $\text{PIEMD}_\Omega \Omega_m$ (black), $\text{SPEMD}_\Omega \Omega_m$ (blue), and $\text{MP-PIEMD}_\Omega \Omega_m$ (red) models (top row), and $\text{PIEMD}_\Omega \Omega_m w$ (black), $\text{SPEMD}_\Omega \Omega_m w$ (blue), and $\text{MP-PIEMD}_\Omega \Omega_m w$ (red) models (bottom row). The vertical dashed lines represent the 16th, 50th, and 84th percentiles for each distribution.

mass fraction of $45.6^{+8.7\%}_{-8.3\%}$ at the lens galaxy effective radius, decreasing to $(13.6 \pm 2.3)\%$ at $R = 42$ kpc ($(38 \pm 9)\%$ decreasing to $(12 \pm 2)\%$)).

4.6.2 SDSS J0100+1818 as a fossil system

The hierarchical evolution of structures predicted by the Λ CDM scenario implies that, in the case of some compact groups of galaxies, all the main galaxies of a group could merge into a single one (Ponman & Bertram 1993). As this central galaxy cannibalizes more galaxies, the luminosity gap between it and the remaining galaxies increases with time. Jones et al. (2003) firstly gave an operational definition of the so-called “fossil” groups, namely systems where the magnitude gap in the r -band between the first two brightest galaxies, Δm_{12} , lying at a projected distance smaller than half the value of the virial radius, is larger than 2. Later, Dariush et al. (2010) proposed to consider the magnitude gap between the first and the fourth brightest galaxies, requiring $\Delta m_{14} > 2.5$. This criterion was shown to be more robust in classifying the groups with a small number of members, where the serendipitous infall of a bright galaxy would change the fossil status. Simulations show that the fossil system status is a phase in the evolution of a group rather than a class itself, as it can be lost if a bright galaxy is included in the system, but also acquired if the BGG merges with other members. Both definitions also include the presence of a diffuse X-ray emission, with $L_X \geq 10^{42}$ erg s $^{-1}$. The growing mechanism of fossil groups, given the typical angular momentum loss rates via dynamical friction, occurs over long timescales, and thus the discovery of fossil systems as old, undisturbed groups at intermediate redshift (approximately half of the age of the Universe) can act as a probe for galaxy evolution models. Moreover, fossil systems have a mass concentration in their center that is higher than that of normal galaxy groups (Johnson et al. 2018a), and this makes them particularly efficient as strong gravitational lenses.

Given the dominance of the BGG in its center, the SDSS J0100+1818 group was identified as a candidate fossil system in the CASSOWARY survey, but the lack of observations did not allow one to draw firm conclusions. Even now, we would need additional data to securely assign it the status: future deep X-ray data would be necessary to accurately measure the virial radius and confirm whether SDSS J0100+1818 is a dynamically evolved system immersed in a fairly undisturbed hot gas halo, as imposed by the criterion. This X-ray condition was originally imposed to guarantee the presence of an extended halo in which the group is immersed, and this results clear from the outcomes of the strong lensing modeling and from the total mass parametrization assumed (see also the studies Grillo et al. 2013; Wang et al. 2022, about CSWA31, a similar system included in the CASSOWARY survey). Additionally, SDSS J0100+1818 fulfills both the Jones et al. (2003) and Dariush et al. (2010) criteria, presenting $\Delta m_{12} = 2.89$ and $\Delta m_{14} = 3.35$. The confirmation of SDSS J0100+1818 as a fossil system would be decisive to put new constraints on the mechanisms that drive the formation and evolution of fossil systems and of extremely massive early-type galaxies, given that it would be the most distant system known so far (Khosrroshahi et al. 2006; Aguerri & Zarattini 2021, and references therein). SDSS J0100+1818 redshift is similar to that of the system studied by Ulmer et al. (2005), which only partially satisfies the condition of Jones et al. (2003), with $\Delta m_{12} = 1.93$.

4.6.3 The values of Ω_m and w from multi-plane strong lensing systems

We compare here the cosmological measurements obtained in this chapter with those from the galaxy-scale multi-source-plane strong lensing system SDSS J0946+1006 (also known as the “Jackpot”; Gavazzi et al. 2008; Smith & Collett 2021). The latter is composed of a galaxy at

$z_l = 0.222$ that acts as a strong lens on three background sources, at redshifts 0.609, 2.035, and 5.975. Even if the Jackpot deflector redshift is lower than that of SDSS J0100+1818, the lensed sources span very similar redshift intervals, with the D_{ds}/D_s ratios ranging from 0.54 to 0.72 for SDSS J0100+1818 and from 0.60 to 0.89 for the Jackpot (in the standard cosmological model). As shown in Collett et al. (2012), the best configuration to learn about cosmology from a double-source system is one with the first source at low redshift, close to the deflector, and with the second one at high redshift. We find that our measurements of Ω_m and w with SDSS J0100+1818 are comparable, in terms of values and accuracy, to those obtained from the Jackpot in Collett & Smith (2020) and Smith & Collett (2021), where they were combined though with priors from *Planck* (Planck Collaboration et al. 2014).

Given the group nature of SDSS J0100+1818 and the relatively large number of background sources and their multiple images, we also compare our results with those obtained with lens clusters of galaxies. These systems can rely on a large number of multiple images, from several sources located at different redshifts, that help in breaking the mass-sheet and mass-cosmology degeneracies, making them excellent cosmological probes. On the other hand, cosmographic measurements are hindered by the complex total mass distribution of clusters: in order to accurately reproduce the observed positions of many multiple images, distributed over wide spatial regions, several mass components, tracing both the baryonic (stars and hot-gas) and DM distributions, are usually needed. This complexity can introduce some systematic uncertainties associated to the specific choice of the total mass parametrization. On the contrary, galaxy and group-scale systems have the advantage that the lens is usually successfully modeled with a few mass components, with an immediate physical interpretation, like the simple DM halo, BGG, and group member contributions in SDSS J0100+1818.

Caminha et al. (2022) exploited five strong lensing clusters (with redshift from 0.234 to 0.587), with 7-20 multiply imaged sources per system, with redshift from 0.68 to 6.85. They combined the results from the lens clusters in the sample and found $\Omega_m = 0.30^{+0.09}_{-0.11}$ and $w = -1.12^{+0.17}_{-0.32}$ but, when considering the individual clusters, they obtained 1σ uncertainties on Ω_m ranging from 0.2 to 0.4. This relative uncertainty is fully consistent with that obtained from SDSS J0100+1818, showing that the lower number of multiple images is balanced by the simpler total mass distribution. Moreover, Caminha et al. (2022) also noticed that the typical "L-shape" they observed in the Ω_m - w plane (also visible for SDSS J0100+1818 in Fig. 4.9) is less pronounced, as the redshift of the deflector increases. Only one of the clusters they studied is at a redshift larger than that of SDSS J0100+1818, suggesting that, together with the comparable accuracy level reached, massive galaxy- and group-scale systems can complement cosmographic studies through strong lensing performed with clusters.

4.7 Summary and conclusions

In this chapter, we have exploited new VLT/MUSE data to expand the study of Chapter 3 about the strong lensing system SDSS J0100+1818. This system consists of a group of galaxies, dominated by a central massive early-type galaxy (BGG), at redshift $z = 0.581$, which acts as a strong gravitational deflector for five background sources, all spectroscopically confirmed. The sources are lensed into a total of 18 multiple images, located between $2.25''$ (≈ 15 kpc) and $11.70''$ (≈ 77 kpc) in projection from the BGG.

We have built, with the software GLEE, different strong lensing models of the deflector, consisting in an extended component (whose total mass distribution has been parametrized with either a PIEMD or a SPEMD profile), representing the DM halo in which the group is immersed, and

several dPIE components for the member galaxies. We have measured the best-fit parameter values, and their posterior probability distribution, by reproducing the observed position of all the 18 multiple images.

Taking advantage of the multi-plane nature of the system, with several sources at different redshifts lensed by the same deflector, we have developed some additional models varying also the geometry of the Universe. In fact, by considering the distance ratios between the observer, the lens, and the different sources, and assuming a model of the Universe (flat Λ CDM or w CDM models) the values of Ω_m and w can be inferred.

The main results of this chapter can be summarized as follows:

- We have confirmed the redshift of the background sources A and B, at $z = 1.880$. We have also measured the redshift of source C, at $z = 1.698$. Furthermore, we have discovered two additional background sources, E and F at $z = 4.95$, that do not show any HST continuum, but do have clear Ly α emission lines.
- We have securely measured the redshifts of 65 objects in the field of view, identifying 19 group members (including the BGG) on the deflector plane, 3 stars, 10 foreground galaxies, 32 background galaxies, and 1 background quasar.
- We have measured the stellar velocity dispersion profile of the BGG over six bins with $S/N > 15$ up to an aperture of $3''$ radius (≈ 20 kpc, approximately twice the value of the effective radius). The profile has a peak of $(386 \pm 6) \text{ km s}^{-1}$, and slightly decreases to $(350 \pm 25) \text{ km s}^{-1}$ in the outer regions.
- We have developed different strong lensing models for the system. We have modeled the projected dimensionless surface mass density of each group member as a dPIE mass distribution, and weighed the total mass of each group galaxy based on its luminosity. We have included an additional mass component, representing all the contributions not associated to the group galaxies. In particular, this main group-scale DM halo has been parametrized with either a PIEMD or a SPEMD total mass distribution. Given the dominance of the BGG, we have also considered models in which the total mass of the BGG was still parametrized by a dPIE profile, but not weighed through the scaling relations adopted for all the other members. The results of these models, summarized in Table 4.2, show that we could reproduce the observed positions of the 18 multiple images with a rms value between $0.21''$ and $0.23''$.
- We have accurately measured a total mass profile for the deflector with an average relative uncertainty of only 2% between 15 and 77 kpc. In particular, we have measured a total mass of $(1.55 \pm 0.01) \times 10^{13} M_\odot$ ($(2.78 \pm 0.04) \times 10^{13} M_\odot$) within an aperture of $R = 50$ kpc ($R \approx 77$ kpc). The total mass of the extended halo within the same apertures are, respectively, $9.2_{-3.1}^{+1.2} \times 10^{12} M_\odot$ and $1.9_{-0.7}^{+0.2} \times 10^{13} M_\odot$.
- By adopting the stellar mass-to-light ratio estimated in the previous chapter, we have measured the group cumulative stellar mass profile up to $R \approx 30'' \approx 180$ kpc. We have employed this profile to obtain the stellar over total mass fraction profiles for each model. They have

resulted in a value of $45.6^{+8.7\%}_{-8.3\%}$ at the BGG effective radius, decreasing to $(11.1 \pm 1.9)\%$ at $R = 50$ kpc, and to $(6.6 \pm 1.1)\%$ at $R \approx 77$ kpc.

- We have developed strong lensing models with the values of Ω_m and w free to vary, in flat Λ CDM and w CDM models for the Universe. The average 1σ uncertainty is on the order of 0.1 for Ω_m , and of 0.4 for w . We have measured $\Omega_m = 0.14^{+0.16}_{-0.09}$ (with a 95.4% upper limit of 0.47) in the flat Λ CDM case, and $\Omega_m = 0.19^{+0.17}_{-0.10}$ (with a 95.4% upper limit of 0.59) and $w = -1.27^{+0.43}_{-0.48}$ in the flat w CDM case.
- We have considered the MP-PIEMD- Ω_m and MP-PIEMD- $\Omega_m w$ models, by adopting a multi-plane strong lensing modeling approach. These models have included an additional PIEMD mass distribution at $z = 1.880$, representing the total mass term associated to sources A and B, and contributing to the total deflection angle. We have found consistent median values for the cosmological parameters Ω_m and w , with a similar uncertainty on w and an increased uncertainty on Ω_m by a factor of approximately 1.5.
- We have checked that the accuracy on the cosmological measurements obtained with SDSS J0100+1818 is similar to that obtained with the galaxy-scale multi-source-plane strong lensing system known as the “Jackpot” (Collett & Auger 2014; Collett & Smith 2020; Smith & Collett 2021). Given the group nature of SDSS J0100+1818 and the quite large number of multiple images, we have also compared the accuracy of our estimates with those provided by lens clusters of galaxies. By comparing with the sample presented in Caminha et al. (2022), we have found that SDSS J0100+1818 performs as a typical cluster of galaxies, showing that the lower number of multiple images is balanced by the simpler total mass distribution. As an advantage, SDSS J0100+1818 has a lens redshift that is larger than the average one for the lens clusters, and this reduces the degeneracy between the values of Ω_m and w .

CHAPTER 5

UV-continuum β slopes of individual $z \sim 2 - 6$ clumps and their evolution

The results reported in this chapter have been described in:

the manuscript “UV-continuum β slopes of individual $z \sim 2 - 6$ clumps and their evolution”, **Bolamperti A.**, Zanella A., Meštrić U., Vanzella E., Castellano M., Bergamini P., Calura F., Grillo C., Meneghetti M., Mercurio A., Rosati P., Devereaux T., Iani E., Vernet J., 2023, MNRAS, 526, 5263.

5.1 Introduction

In the last years, the characterization of observed (e.g., [Madau & Dickinson 2014](#); [Förster Schreiber et al. 2009](#); [Dunlop 2012](#); [Murata et al. 2014](#); [Zanella et al. 2015](#); [Bouwens et al. 2015](#); [Stott et al. 2016](#); [Guo et al. 2018](#); [Oesch et al. 2018](#); [Romano et al. 2021](#); [Sommovigo et al. 2021](#); [Vanzella et al. 2022](#)) and simulated (e.g., [Bournaud et al. 2014](#); [Tamburello et al. 2015](#); [Buck et al. 2017](#); [Lovell et al. 2021](#); [Zanella et al. 2021](#); [Pallottini et al. 2022](#); [Vizgan et al. 2022](#); [Calura et al. 2022](#)) galaxies at high redshift represented a key step in the study of galaxy evolution in the early Universe. Recently, thanks to the first data from the James Webb Space Telescope (*JWST*), some studies have reached new and unexplored epochs, discovering galaxies up to $z \sim 10 - 17$ ([Atek et al. 2022](#); [Castellano et al. 2022](#); [Donnan et al. 2022](#); [Finkelstein et al. 2022](#); [Harikane et al. 2022](#)), just approximately 200–500 Myr after the Big Bang in the standard cosmological model.

Galaxies at high- z show a morphology different from local ones. They consist of turbulent disk-like structures, i.e., marginally-stable rotating discs with a significant contribution of random motions to the dynamical support of the system ([Elmegreen et al. 2007](#); [Glazebrook 2013](#); [Guo et al. 2015](#); [Ferreira et al. 2022](#)). These galaxies are dominated by bright blue knots, dubbed *clumps*, visible also in the latest *JWST* images (e.g., [Treu et al. 2022a](#)). Observations showed that clumps have stellar mass values between 10^7 and $10^9 M_\odot$ ([Förster Schreiber et al. 2011a](#); [Guo et al. 2012](#); [Soto et al. 2017](#)), star-formation rate values between 0.1 and $10 M_\odot \text{ yr}^{-1}$ ([Guo et al. 2012](#); [Soto et al. 2017](#)) and are star-forming regions, i.e., with a specific star-formation rate considerably larger than their host galaxy ([Bournaud et al. 2015](#); [Zanella et al. 2015, 2019](#)). Clumps in field galaxies are unresolved ($\text{FWHM} < 1 \text{ kpc}$) ([Elmegreen et al. 2007](#); [Förster Schreiber et al. 2011b](#); [Genzel et al. 2011](#)), and it has been shown, through simulations and observations with different resolutions ([Oklopčić et al. 2017](#); [Behrendt et al. 2016, 2019](#); [Tamburello et al. 2017](#); [Faure et al. 2021](#); [Meštrić et al. 2022](#); [Claeyssens et al. 2023](#)), that the detectability and the measured

sizes of clumps depend on the observational resolution. Thanks to gravitational lensing, we can observe clump sizes of the order of hundreds of pc (Livermore et al. 2015; Rigby et al. 2017; Cava et al. 2018; Dessauges-Zavadsky et al. 2017, 2019), down to a few tens of pc in extremely high-magnification regimes (Johnson et al. 2017; Vanzella et al. 2019, 2020b; Calura et al. 2021; Vanzella et al. 2022; Meštrić et al. 2022; Messa et al. 2022; Claeysens et al. 2023). Although gravitational lensing remains the best opportunity to explore compact and faint structures, a proper correction of the observed properties to infer the intrinsic ones, i.e., the *delensed* ones, requires the most accurate lensing models of cluster of galaxies developed nowadays, with the largest number of constraints (e.g., Caminha et al. 2017; Bonamigo et al. 2018; Bergamini et al. 2021, 2022). Their accuracy critically depends on the number of spectroscopically-confirmed multiple images, to minimize the number of misidentified systems and the degeneracy between the observer-deflector-source relative distances and the total mass distribution of the deflector (Johnson et al. 2014; Grillo et al. 2015; Caminha et al. 2019; Bolamperti et al. 2023a).

In this framework, the investigation of the physical properties of galactic substructures and individual clumps hosted by high- z galaxies down to the smallest scales gives unique hints to study galaxy evolution. One of the most important quantities exploited to characterize young stellar populations is the UV-continuum slope. This can be estimated directly from multi-band rest-frame UV measurements, or from spectral energy distribution (SED) fitting. The UV-continuum slope is commonly referred to as “ β slope”, because it has been shown that the UV part of the spectrum can reasonably be fitted with a simple power-law relation, i.e., $f_\lambda \propto \lambda^\beta$ (Calzetti et al. 1994). Despite some degeneracy with the metallicity of a galaxy (e.g. Castellano et al. 2014; Calabro et al. 2021) and with its star formation history (SFH, Bouwens et al. 2016), the value of β can give important insights on the stellar population, in particular about the presence of young stars. It is also a common indicator of dust attenuation (Calzetti et al. 1994), allowing the study of the evolution and build-up of dust in galaxies, from $z \sim 2$ to 10 (Reddy et al. 2018). The intrinsic slope is the combination of different factors defining the stellar population in the galaxy, such as the total amount and composition of dust grains, the metallicity, the stellar initial mass function (IMF), and the star formation history (SFH). It is not possible to constrain all these physical parameters separately, but a robust measurement of the β slope is necessary to characterize the global properties of galaxies. As a reference, a galaxy with a dust-free stellar population with solar metallicity and constant star formation rate has a value of $\beta \simeq -2.2$. Several studies, based on HST data up to $z \sim 8$, show average β values $\lesssim -2$, a sign of young and metal-poor stellar populations (e.g., Dunlop et al. 2013; Finkelstein et al. 2012; Bouwens et al. 2014; Castellano et al. 2023). In fact, the bluest $z = 2 - 4$ (Castellano et al. 2012; McLure et al. 2018) and local (Calzetti et al. 1994; Vázquez et al. 2004) galaxies usually show slopes between -2.5 and -2 . Great efforts have been dedicated to the search for the bluest galaxies at high- z . Within the photometric uncertainties increasing for the bluest slopes, the discovery of robust $\beta \simeq -3$ candidates, indicating stellar populations formed from pristine gas with a large ionizing photon escape fraction, would provide important insights into the composition and characteristics of the most distant galaxies. Many models predict that, in principle, slopes of -3 would be produced by extremely low metallicity and young stellar populations (Raiter et al. 2010; Bouwens et al. 2010; Topping et al. 2022). However, we do not expect to observe them because of the presence of nebular continuum emission from the ionized gas around young stars, that reddens the slopes up to $\Delta\beta \sim 0.5$ (Raiter et al. 2010; Bouwens et al. 2010; Trussler et al. 2022), even if this effect may be mitigated if the ionizing radiation leaks directly into the intergalactic medium (IGM). Despite this, some studies presented $\beta \lesssim -3$ slopes, not always reproducible with stellar population models (Bouwens et al. 2010; Labb   et al. 2010; Ono et al. 2010; Jiang et al. 2020; Topping et al. 2022). Particular attention has been dedicated to the

identification of reionization-era galaxies with very blue UV slopes, whose young, low-metallicity stellar populations and large escape fraction of ionizing photons into the IGM can be interpreted as the presence of zero metallicity, massive PopIII stars (Wise et al. 2012; Dayal & Ferrara 2018).

So far, no systematic studies on the β slopes of individual star-forming clumps have been done. The building of a significant sample of individual star-forming clumps over a broad redshift range would be essential to characterize their physical properties and the interplay with their host galaxies, which is also a key ingredient in high-resolution hydrodynamical simulations.

In this chapter we investigate the UV-continuum slope of individual clumps between redshift of approximately 2 and 6, and discuss several factors that can affect these measurements. This chapter is organized as follows. In Section 2, we present the ancillary data, discuss the sample selection, and summarize the algorithm used to identify individual clumps. In Section 3, we detail the process we used to extract photometric measurements and to measure the β slope. In Section 4, we do the same with spectroscopic data, and compare the results with the photometric slopes. In Section 5, we compare our individual clump results with those for galaxies from the literature, and discuss trends of β with magnitude and redshift. At the end of the section, we also discuss some cases that exhibit an extremely blue slope ($\beta \lesssim -2.7$), analyzing the physical scenarios that can explain them. Finally, in Section 6 we summarize the results and draw conclusions, discussing the caveats of this study.

5.2 Sample selection and ancillary data

5.2.1 *HST* data

MACS J0416.1–2403 (hereafter, MACS J0416), (RA, dec) = (04:16:08.9, −24:04:28.7) at $z = 0.396$, is one of the galaxy clusters which act as gravitational lenses with the largest number of observed multiple images (Zitrin et al. 2013), likely because of its highly elongated and irregular structure. It has been included in the Hubble Frontier Field (HFF) program and thus observed in seven *HST* filters. We make use of the deep, multi-wavelength observations in the MACS J0416 field, which are publicly available (Lotz et al. 2017; Koekemoer et al. 2014), and of ASTRODEEP PSF matched images in the *HST*/ACS F435W, F606W, F814W, and *HST*/WFC3 F105W, F125W, F140W, and F160W bands (Merlin et al. 2016; Castellano et al. 2016). In the following, we will refer to *HST*/ACS F435W, F606W, F814W, and *HST*/WFC3 F105W, F125W, F140W, and F160W bands as, respectively, *B*₄₃₅, *V*₆₀₆, *I*₈₁₄, *Y*₁₀₅, *J*₁₂₅, *JH*₁₄₀, *H*₁₆₀. Merlin et al. (2016) complemented the HFF data with imaging from the CLASH survey (PI: M. Postman, Postman et al. 2012) and program 13386 (PI: S. Rodney), and use the final reduced and calibrated v1.0 mosaics released by the Space Telescope Science Institute (STScI), drizzled at 0.06'' pixel-scale. The *H*₁₆₀ image plays a key role in this framework, because it has the worst PSF FWHM (0.20''), which increases with increasing wavelength (e.g., from 0.11'' in the *B*₄₃₅ to 0.19'' in the *JH*₁₄₀ band). All the images in the remaining six filters have been PSF-matched to the *H*₁₆₀ one, with a convolution kernel that was obtained from the ratio of the PSFs of the respective pair of images in the Fourier space. Furthermore, Merlin et al. (2016) performed a multi-step procedure with the program GALFIT (Peng et al. 2002) in all the images, to subtract the light contribution from the foreground objects and the intracluster light.

5.2.2 VLT/MUSE data

Thanks to its unique properties as a gravitational lens, MACS J0416 benefits from an excellent spectroscopic coverage, which is essential to build a robust strong lensing model. We make use

of the latest ground-based Integral Field spectroscopic data, observed with MUSE at the Very Large Telescope (VLT) between November 2017 and August 2019 (Prog.ID 0100.A-0763(A), PI: E. Vanzella). These observations consist of 22.1 hours (including overheads) pointing in the north-east region of the galaxy cluster (see Fig. 5.1). This dataset was implemented with GTO observations taken in November 2014 (Prog.ID 094.A-0115B, PI: J. Richard), reaching a total on-sky integration time of 17.1 hours, and a final image quality of $0.6''$. MUSE data-cubes cover a field-of-view of 1 squared arcmin, spatially sampled with $0.2'' \times 0.2''$ pixels. The wavelength range extends from 4700\AA to 9350\AA , with a dispersion of 1.25\AA pix^{-1} , and a spectral resolution of $\sim 2.6\text{\AA}$ approximately constant across the entire spectral range. With these data and extending the catalogs by [Caminha et al. \(2017\)](#) and [Richard et al. \(2021\)](#), [Vanzella et al. \(2021\)](#) identified and measured the redshift of 48 background sources, with $0.9 < z < 6.2$, lensed into 182 multiple images, all of them spectroscopically confirmed.

5.2.3 Lensing model

The strong lensing model used in this work is described in [Bergamini et al. \(2021\)](#) and it is based on the spectroscopic catalog developed by [Vanzella et al. \(2021\)](#) and described above. The total mass distribution of MACS J0416 was accurately reconstructed, with a root-mean-square displacement of only $0.40''$ between the observed and model-predicted positions of the 182 multiple images. This result has been possible thanks also to the identification of 171 cluster galaxy members (80% of which spectroscopically confirmed) and to the measurement of the internal velocity dispersion for 64 of them, allowing to estimate the contribution of their subhalo mass components via the Faber-Jackson scaling relation ([Bergamini et al. 2019, 2021, 2023b](#)). They also quantify the uncertainties, in different locations, on the magnification maps that can be derived from the strong lensing model. This is a fundamental step in the study of lensed high- z sources, due to the fact that the local magnification factor is essential to infer the intrinsic properties from the observed ones. Since our sources are compact, when we mention the magnification factor of a clump, we refer to the average of the magnification maps from [Bergamini et al. \(2021\)](#), in a region of 2×2 pixels and centered on the clump.

5.2.4 Clumps identification

The procedure of clumps identification is detailed in [citetMestric2022](#) (hereafter, [Meštrić et al. \(2022\)](#)), who made use of the same *HST* PSF matched images exploited in this work. Summarizing, the clumps have been identified, and their emission deblended from that of the underlying diffuse host galaxy, by smoothing a cutout image centered on each clump through a boxcar filter with the *IRAF* ([Tody 1986](#)) task *MEDIAN*. The size of the smoothing box represents a key factor in this process, and [Meštrić et al. \(2022\)](#) optimized it by assuming a size $\sim 2\text{-}3$ times larger than each source, resulting typically on 21-31 pixels. Then, the smoothed image is subtracted from the original cutout to obtain a high-contrast image. With automatic (*SExtractor* v2.24, [Bertin & Arnouts 1996](#)) and visual inspection, it is possible to efficiently identify the individual clumps. This technique has been used in the literature in different fields, from the study of non-lensed clumps ([Guo et al. 2015](#)) to the subtraction of the contaminating host galaxy before modelling ultra-compact dwarfs ([Norris & Kannappan 2011](#)). [Meštrić et al. \(2022\)](#) found that while the majority ($\sim 70\%$) of the lensed galaxies host 1-2 clumps, there are systems harbouring up to 15-16 clumps. For more details on the distributions of clumps in number per system and redshift, we refer the readers to the [Meštrić et al. \(2022\)](#) paper.

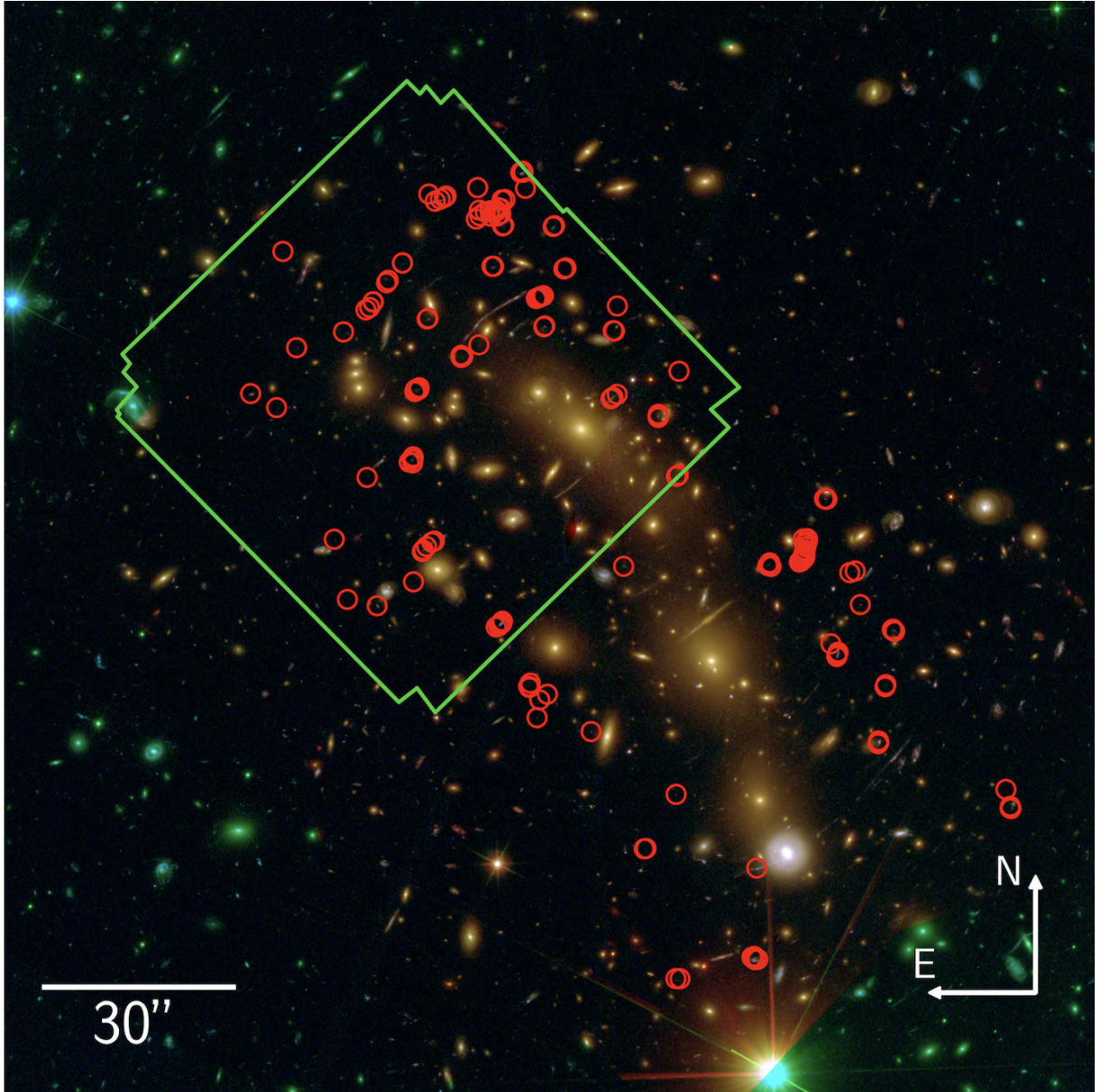


Figure 5.1: RGB image (R: F105W+F110W+F125W+F140W+F160W, G: F606W+F625W+F775W+F814W+F850LP, B: F435W+F475W) of MACS J0416 showing in green the north-east 17.1 h MUSE pointing (Vanzella et al. 2021). Red circles mark the position of the 166 individual clumps included in our sample. They all benefit from a spectroscopic redshift measurement, and 100 of them are covered by the deep MUSE pointing.

5.2.5 Sample

The resulting [Meštrić et al. \(2022\)](#) sample we analyze is composed of 166 star-forming clumps belonging to 67 galaxies strongly lensed by MACS J0416. The magnification factors of the clumps in our sample are distributed from $\simeq 2$ to $\simeq 82$, with a median value of approximately 4.6. About 80% of the clumps are magnified by a factor < 10 . Approximately 70% (48 over 67) of the galaxies has multiple images: for them, we consider the brightest system, that is the one with the largest value of the magnification factor, from the lensing model developed by [Bergamini et al. \(2021\)](#) and described above. When possible, we check the consistency of the presented results with those relative to the not considered multiple images. The properties of the sample are summarized in Fig. 5.2. All the clumps in the sample benefit from a spectroscopic redshift measurement, and they cover a redshift range from $z \sim 2$ to ~ 6.2 , with peaks around redshift 2, 3.5 and 6, due to clumps hosted by the same galaxy, or by different galaxies at approximately the same redshift, probably belonging to the same group or structure. Among the 166 clumps in the sample, 100 are included in the deep MUSE pointing of [Vanzella et al. \(2021\)](#), shown in Fig. 5.1.

5.3 Photometric β slopes

In this section we describe how we measure the fluxes relative to each clump, and the methodology exploited to measure the respective photometric β slopes. We then discuss how we estimate the robustness of the resulting measurements. After that, we present our β slopes measurements and their uncertainties. At the end of the section, we compare our results with those obtained by adopting the fluxes measured by the ASTRODEEP collaboration ([Merlin et al. 2016; Castellano et al. 2016](#)) for a subsample of 48 in-common objects.

5.3.1 Photometric measurements

We measure the photometric properties of clumps on the images reduced by the ASTRODEEP collaboration, where the intracluster light (ICL) and the foreground cluster members are subtracted and the images in each filter are PSF matched to the resolution of the *H160* one. We make use of the A-PHOT software ([Merlin et al. 2019](#)), developed to perform aperture photometry on astronomical images, which allows one to obtain multiple measurements within different circular or elliptical apertures, and to estimate and subtract the local background sky. A-PHOT computes the total flux within an aperture by summing up the flux of the pixels entirely included in the aperture, and dividing in $n \times n$ sub-pixels those crossed by the border, with n fixed by the user, and iterating the procedure. The local background is estimated through a recursive algorithm with a clipping procedure, considering the mean value of the pixels within an annulus centered on the aperture.

We measure the fluxes relative to each clump by considering circular apertures of diameter $0.27''$, centered on the center of each clump (see Table 1 of [Meštrić et al. \(2022\)](#) for the coordinates), and with the local background subtraction option implemented. The output magnitudes are computed as $m_i = -2.5 \log f_i + zp_i$, where i denotes each filter, f_i are the fluxes measured with A-PHOT and zp_i are the relative zeropoints.

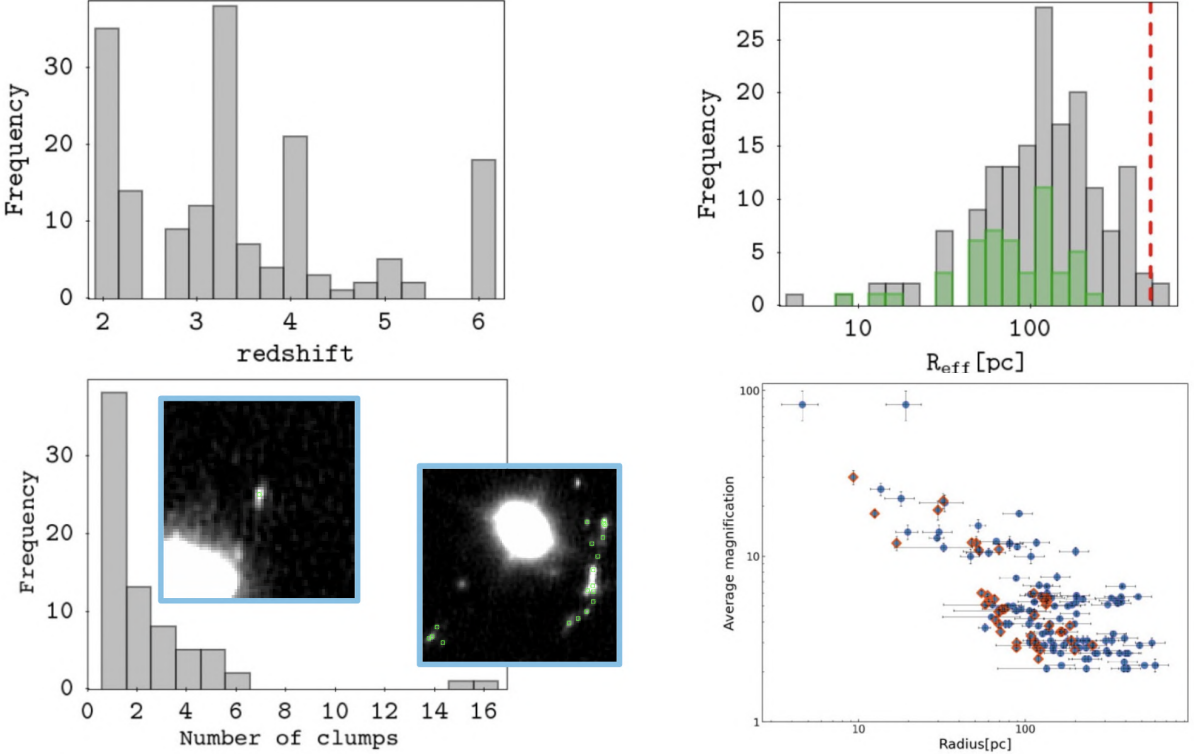


Figure 5.2: Properties of the sample of clumps, adapted from Meštrić et al. (2022). Top left: redshift distribution of the clumps, where peaks denote clumps belonging to the same host galaxy or group. Top right: size distribution of the clumps, where the green histogram indicated the clumps whose size is an upper limit. the red dashed vertical line denotes the typical smallest clump size detected in field, without strong lensing. Bottom left: Distribution of the number of clumps per system, with an example of a galaxy hosting one clump and hosting 16 clumps is shown in the onsets. Bottom right: Average magnification as a function of the effective radius of the clump. Orange diamonds represent upper limits. We note that, given that the effective radii are corrected for magnification, this correlation is, at least partially, artificial and dependent on the definitions.

5.3.2 Photometric β slopes

We measure the UV-continuum β slopes through the relation (Castellano et al. 2012)

$$m_i = -2.5(\beta + 2) \log(\lambda_i) + c , \quad (5.1)$$

where m_i is the measured magnitude in the i -th filter and λ_i is the corresponding wavelength, assumed to be the pivot wavelength¹ of each filter reported to rest-frame, i.e., divided by a factor $(1 + z)$. We fit the data with a weighted least squares technique, where the weights, w_i , depend on the magnitudes uncertainties, $\epsilon_{m,i}$ as $w_i = \epsilon_{m,i}^{-2}$. We correct the seven bands for Milky Way reddening by adopting the Cardelli et al. (1989) reddening law with $R_V = 3.1$ (Schlafly & Finkbeiner 2011; O'Donnell 1994).

For a given value of the redshift, only the fluxes measured in filters that are rest-frame included in the UV interval can be exploited to fit Eq. 5.1. We adopt the following criteria to select

¹defined, for each filter, as $\lambda_p = \sqrt{\frac{I(\lambda) d\lambda}{\int I(\lambda) \lambda^{-2} d\lambda}}$, where $I(\lambda)$ is the response of the filter.

Table 5.1: Summary of the HST filters used to fit Eq. 5.1 in each redshift interval

Redshift interval	# filters	Filters	# clumps
$z < 2.0$	3	$B435, V606, I814$	9
$2.0 < z < 2.8$	2	$V606, I814$	40
$2.8 < z < 3.0$	3	$V606, I814, Y105$	11
$3.0 < z < 3.8$	2	$I814, Y105$	51
$3.8 < z < 4.3$	3	$I814, Y105, J125$	25
$4.3 < z < 4.7$	4	$I814, Y105, J125, JH140$	4
$4.7 < z < 4.9$	3	$Y105, J125, JH140$	2
$4.9 < z$	4	$Y105, J125, JH140, H160$	24

Summary of the HST filters used to fit Eq. 5.1 in each redshift interval, following the criteria described in Eqs. 5.2 and 5.3. For each redshift interval, we report the number of included rest-frame UV filters, their names, and the respective number of clumps in our sample.

the redshift range in which each filter can be exploited: we measure the redshift limits, z_{inf} and z_{sup} , for each filter by considering the redshift values such that the pivot and the minimum wavelengths, λ_p and λ_{\min} , are included in the 1250-2600 Å range (Calzetti et al. 1994), as

$$z_{\text{inf}} = \frac{\lambda_p}{2600 \text{ Å}} - 1 \quad (5.2)$$

$$z_{\text{sup}} = \frac{\lambda_{\min}}{1216 \text{ Å}} - 1. \quad (5.3)$$

In particular, we use λ_{\min} towards the 1250 Å limit to avoid the possible inclusion in the filter of the Ly α emission line, that can significantly affect the measured magnitude. Considering that the clumps range from redshift 2 to 6, we divide our sample into seven redshift intervals, as described in Table 5.1 and showed in Fig. 5.3. Each interval differs for the number and the kind of exploitable filters. By following the described criteria, we find that in the redshift interval between 2.8 and 3.0, only one filter ($I814$) can be exploited, and thus no UV β slope measurement is possible for 11 clumps. Thus, we relax the conditions and include the $V606$ band, whose transmission at 1216 Å is $< 10\%$, and the $Y105$ band. We test the results by measuring the slopes with only the $V606$ - $I814$ and $I814$ - $Y105$ pairs in the same redshift interval, obtaining fully consistent results, differing only by a few percent. Thus, we present in the following the three-magnitude slope for the 11 clumps included in the redshift interval between 2.8 and 3.0. Similarly, we extend the redshift range of the $I814$ filter to lower values, to cover also 9 clumps at $z \sim 1.9$. We tested the consistency of the results with the only-two filter fit. In this case, the choice is supported and justified by the asymmetric shape of the $I814$ response, peaking at $\lambda_{\text{peak}} < \lambda_p$.

Hence, the β slope for each clump is computed by fitting Eq. 5.1 with two, three, or four magnitudes relative to the rest-frame UV filters. The procedure and the parameters used to measure the magnitudes can play a major role in the resulting β slopes. In the following, we describe the software we use and the procedure we follow.

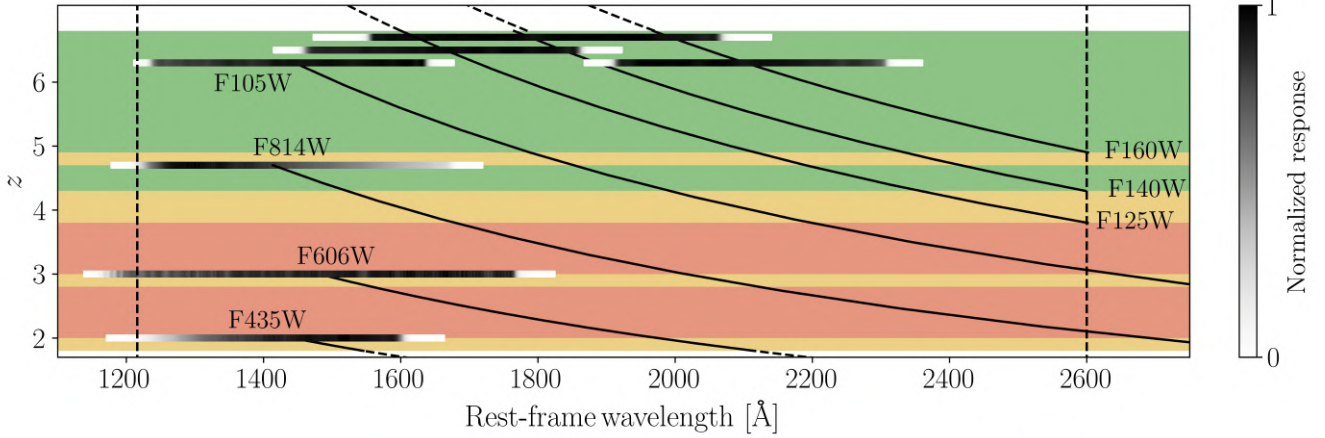


Figure 5.3: Scheme of the rest-frame UV coverage of each available HST filter, as a function of the redshift (vertical axis). The UV limits ($1216 - 2600 \text{ \AA}$, Calzetti et al. 1994) are displayed with vertical dashed lines. Each filter is entirely represented at the respective $z = z_{\text{sup}}$ with the intensity of the color proportional to the normalized response (colorbar on the right), while a solid line shows the position of its pivot wavelength as a function of the redshift. In this representation, a filter is defined as rest-frame UV in the redshift interval where the solid line is drawn. That is, fixing a value of the redshift (i.e., tracing an horizontal line), the included filters are those whose solid lines are crossed. The coloured backgrounds indicate the corresponding number of included filters: two (red), three (yellow) or four (green). For the F125W, F140W, and F160W filters, the dashed end of the lines indicates that the filter could potentially be further exploited to higher redshifts, out of the range of our sample. The solid lines relative to the F814W and F105W filters extend over the 2600 \AA limit because we relaxed the selection criteria, as justified in the main text. The filters and the number of clumps of the sample included in each redshift interval are also summarized in Table 5.1.

5.3.3 Robustness of the photometric and β slopes measurements

We choose this combination of parameters (circular apertures of diameter $0.27''$, centered on the center of each clump, with the local background subtraction option implemented) after performing several tests on the real clumps and on 50 mock clumps we injected in the images as PSF functions, in locations similar to those of the real clumps. In detail, we distribute them in the outer and inner regions of the cluster, to see the possible residuals from the intracenter light removal process, in isolated positions and angularly close to a bright object, to quantify the contribution of the contamination of foreground galaxies. For instance, in the latter case, we put the mock clump at the same angular distance to the contaminant as that of the real clump, but in an opposite direction, to avoid the real clumps to contaminate the simulation. The resulting locations of the 50 mock clumps are shown in the Appendix B.1, in Fig. B.1.

We test different apertures, from $0.2''$ to $0.54''$ in diameter, to switch on and off the A-PHOT local background estimation, and to manually fit and subtract with GALFIT the surface brightness distribution of a foreground contaminant and the background level. For each mock clump, we associate a “true” (β_{true}) UV slope value extracted from an uniform distribution in the $[-3, 0]$ interval, and a m_{I814} magnitude in the $I814$ band sampled from a Gaussian distribution with mean = 28.1 and $\sigma = 1.1$, resulted by fitting the magnitude distribution of the clumps in our original sample. From β_{true} and m_{I814} it is possible to uniquely assign m_{Y105} , the corresponding

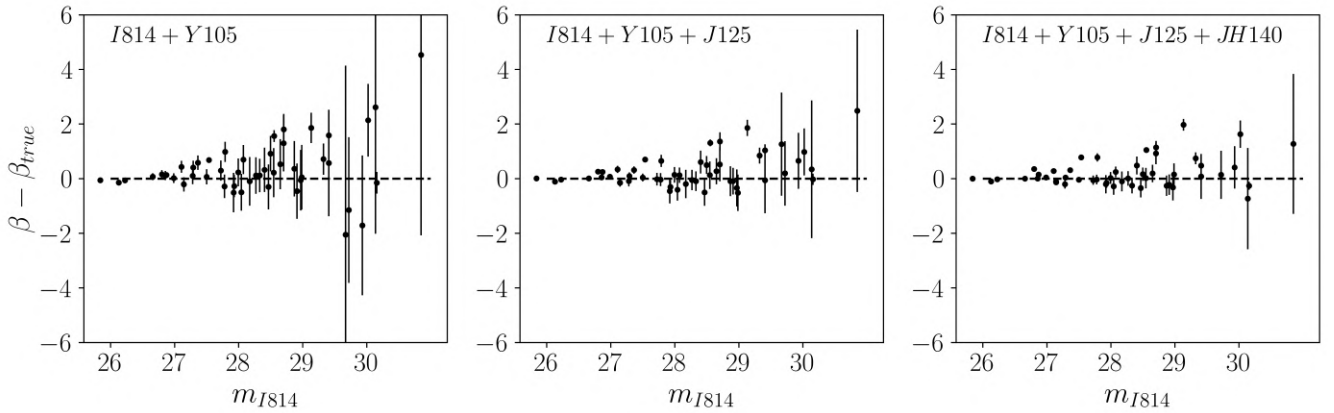


Figure 5.4: Difference between the measured and the injected β slopes ($\beta - \beta_{true}$) as a function of the magnitude m_{I814} , in the case with aperture of diameter $0.27''$, when β is measured using the magnitudes in two (left), three (center) or four (right panel) filters. The scatter around zero increases with the faintness of the sources, because of the less precise photometric measurements, but also with decreasing number of exploited bands, being however mostly consistent with zero within a 1σ uncertainty.

magnitude in the $Y105$ band. Analogously, in the next steps we assign the respective magnitudes in the $J125$ and in the $JH140$ filters. At the end of each step, we measure the magnitude of the mock clumps with A-PHOT, exploiting in sequence the two, three and four available bands.

We check how the photometric measurements change when modifying the aperture, the background subtraction, and the contaminants subtraction. We find good agreement between the measured β slopes with different apertures and the input β_{true} values. We show, in Fig. 5.4, the residuals ($\beta - \beta_{true}$) as a function of m_{I814} , in the selected case with aperture $0.27''$ -diameter. The scatter along the zero-residual line increases with the faintness of the sources, due to the less precise photometric measurements, but also with decreasing number of exploited bands, although remaining consistent with zero within 1σ uncertainties: we describe extensively how we estimated the uncertainties on the measured β values in Subsect. 5.3.5. We repeat the experiment by extracting the photometry from a circle with a larger aperture of diameter $0.4''$ and find that the measured β slopes are systematically redder (i.e., larger values) than those obtained with aperture of diameter $0.27''$, of typically $\Delta\beta \sim 0.2$, corresponding to $\sim 10\%$. There are two main reasons that can explain this result. Increasing the aperture means that a larger fraction of the light from the diffuse host galaxy is included, and it has typically a redder slope. Moreover, it also includes a larger light contribution from the ICL (or from the residuals of its subtraction) and from foreground contaminants. It is the case of several clumps in our sample, which are located in positions angularly close to a red galaxy. For this subsample, we model and then subtract the surface brightness distribution of the contaminant with GALFIT in the different bands involved in the β slope measurement. Then, we repeat the measurement on the cleaned images. With this procedure ($0.4''$ -diameter aperture, A-PHOT sky subtraction off, contaminants subtracted with GALFIT) we recover β values consistent with those obtained in our best case, which is $0.27''$ -diameter aperture and A-PHOT sky subtraction on. Finally, we adopt and present in the following the results obtained with this last configuration, to maintain the same aperture and being consistent with Meštrić et al. (2022).

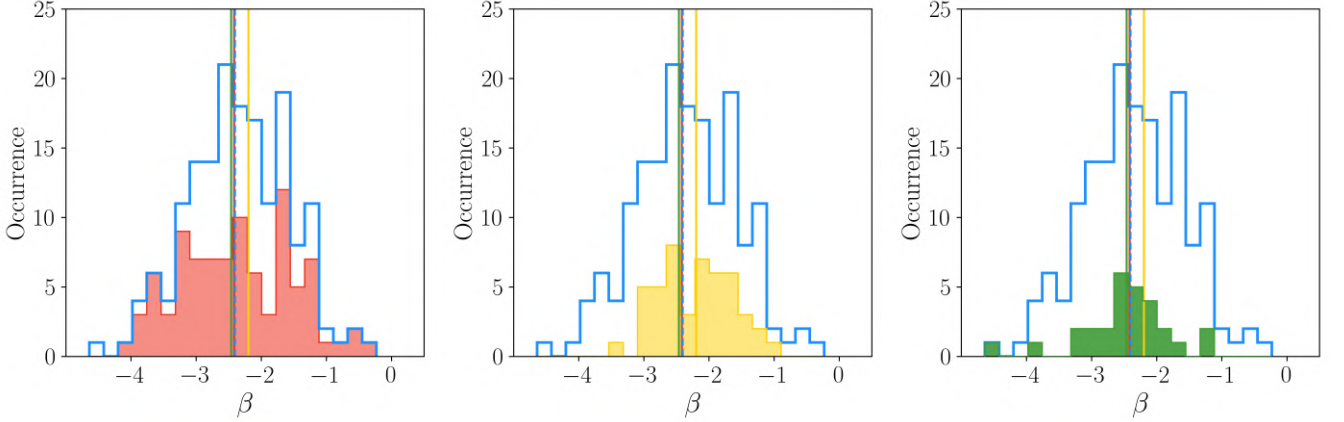


Figure 5.5: Distribution of the photometric β slopes measured (blue empty histogram), and split into subsamples with two (red), three (yellow), or four (green) available photometric measurements. The vertical lines represent the median value relative to each color-coded subsample, while the blue dashed one represents the median value of the entire sample.

5.3.4 β slopes measurements

The resulting UV-continuum β slopes are shown in Fig. 5.5. The β slopes distribution of our sample of individual clumps shows a median value of ~ -2.4 , with a standard deviation of 0.78. The low median value is expected, since UV bright clumps in high- z galaxies are well-known sites of star formation (e.g., Bournaud et al. 2014; Zanella et al. 2015, 2019; Meštrić et al. 2022). Thus, they are populated by young, massive OB stars, whose spectrum strongly emits in the UV, resulting in a blue β slope. There are several objects populating the tails of this distribution: 4 objects have a very red ($\beta > -1$) and 50 a very blue ($\beta < -2.7$) slope. We will discuss these extreme clumps in Subsect. 5.5.3. We observe that the majority of extremely blue slopes was measured with 2-magnitudes fits, that are more affected by systematics, but also 8 clumps with 3-magnitudes and 8 with 4-magnitudes fits are included. The median β slopes of each subsample are -2.45 , -2.20 , and -2.40 , when two, three, and four magnitude measurements are exploited in the fit, respectively.

5.3.5 Uncertainty estimates on β

The uncertainties associated to the β slopes primarily depend on the magnitude uncertainties (Fig. 5.4). A-PHOT computes the uncertainty associated to the flux of the object obj through the so-called “CCD Equation” (Mortara & Fowler 1981), which assumes the form

$$\sigma_{obj} = \sqrt{\sum_{i=1}^{N_{pixels}} \text{rms}_{i,obj}^2 + \frac{f_{obj}}{G}} \quad (5.4)$$

when the root-mean-square (rms) map is considered. Here, f_{obj} is flux received associated to the object and G is the gain.

We adopt these estimates as the 1σ uncertainty on the flux measurements, and use them to compute ϵ_m , the uncertainty relative to the corresponding magnitude value. Then, we use a bootstrap technique to estimate the uncertainties on the β slopes, by fitting, via Eqn. 5.1, 10^4 sets of magnitudes randomly extracted from a Gaussian distribution centered on the measured

values in each filter and with $\sigma = \epsilon_m$. We assess the 16th and the 84th percentile values of the resulting β distribution as the lower and upper 1σ uncertainties, respectively. We notice that clumps with 2-magnitudes fits generally lie at the lowest redshifts (Table 5.1) and consequently they dominate the bright end of the magnitude distribution of clumps. It results in β slopes of bright objects (i.e., with accurate flux measurements) with only two photometric measurements to have smaller uncertainties than those with three or four photometric points, which do not reflect the systematics that affect such two-point β slope measurements. To take into account systematics, we apply to all the 2-magnitudes fits the same bootstrap technique, but extracting a random value from a Gaussian distribution centered on the measured values in each filter and with $\sigma = 3\epsilon_m$. The uncertainties on the 2-point β slopes estimated in this way are consistent with those estimated for the 3- and 4-point fits.

5.3.6 Comparison with ASTRODEEP

The objects in the MACS J0416 field have been extensively detected and characterized by the ASTRODEEP collaboration (Merlin et al. 2016; Castellano et al. 2016), with a 5σ depth in the range 28.5-29.0 AB in 2 PSF-FWHM ($= 0.2''$) aperture. Meštrić et al. (2022) cross-matched our sample with the ASTRODEEP catalog, finding 48 in-common objects. For this subsample, we consider the fluxes measured by the ASTRODEEP collaboration in each HFF filter², and apply our pipeline to measure the associated β slope, using the same approach and band selection described above. The comparison with our β slopes is shown in Fig. B.2.

We find in general good agreement between the resulting β slopes. The ASTRODEEP slopes are systematically redder (median $\Delta\beta \sim 0.24$), but consistent with the 1:1 relation given the average uncertainty of approximately 0.27. Moreover, the redder ASTRODEEP slopes can be explained by the fact that the fluxes are measured in larger apertures and that the catalog is mainly composed of galaxies, and not of individual clumps. In almost all the cases, each ASTRODEEP object is composed by multiple clumps of our sample plus their diffuse host. For these cases, Meštrić et al. (2022) associated the ASTRODEEP object to the brightest clump of the group, but the correspondence is not exactly one-to-one, and also the centroids may be slightly shifted. The agreement of the results, within less than 1σ on average, represents an important consistency test for the robustness of our flux measurements, given that the ASTRODEEP fluxes are calculated with a different approach but exploiting exactly the same images, with subtracted ICL and PSF-matched to the $H160$ band.

5.4 Spectroscopic β slopes

Similarly to Calzetti et al. (1994), we exploit ten spectral windows in the rest-UV range, from 1200 to 2600 Å (see Table 5.2), to measure the spectroscopic β slope of the 100 clumps of our sample included in the MUSE pointing. These intervals are properly designed to remove from the fitting the main absorption and emission lines, as well as the strong telluric absorption residuals, that could bias the measurement of the continuum slope. For each window, we measure the integrated flux and associated uncertainty, correct them for Milky Way reddening (Cardelli et al. 1989 reddening law with $R_V = 3.1$, Schlafly & Finkbeiner 2011; O'Donnell 1994), and then fit Eqn. 5.1. Depending on the redshift of each clump, the MUSE wavelength coverage reported to rest-frame allows us to employ a different number of windows, that is, a different number of flux values for the fit. The majority of clumps can be fit with $\gtrsim 6$ windows, and we exclude the

²<http://astrodeep.u-strasbg.fr/f/>

Table 5.2: Rest-frame UV ten spectral windows used to measure the spectroscopic β slopes and the relative redshift range in which they can be exploited.

Window number	Wavelength range [Å]	Redshift range
1	1268 - 1284	$z \gtrsim 2.6$
2	1309 - 1316	$2.5 \lesssim z \lesssim 6.1$
3	1360 - 1371	$2.4 \lesssim z \lesssim 5.8$
4	1407 - 1515	$2.1 \lesssim z \lesssim 5.6$
5	1562 - 1583	$1.9 \lesssim z \lesssim 4.9$
6	1677 - 1725	$z \lesssim 4.4$
7	1760 - 1833	$z \lesssim 4.3$
8	1866 - 1890	$z \lesssim 4.0$
9	1930 - 1950	$z \lesssim 3.8$
10	2400 - 2580	$z \lesssim 2.9$

They are measured by adopting the spectral windows identified by [Calzetti et al. \(1994\)](#), properly designed to remove from the fitting the main absorption and emission lines.

clumps whose spectrum covers less than three windows, as it happens for $z > 5.7$. Hence, we extract the spectrum for 87 clumps in our sample.

We extract the spectra of each source by fixing circular apertures of $0.4''$ -diameter, centered on each clump. Since most of the sources in our catalog, in particular at higher redshifts, are very faint, we estimate the spectra signal-to-noise ratio (S/N), and we keep only those with $S/N \gtrsim 2$. After this selection, we measure the spectroscopic β slope for 37 clumps. They are distributed between redshift 1.99 and 3.29, corresponding to 6-9 exploited spectral windows.

5.4.1 Comparison with photometric β slopes

The spectroscopic β slopes are on average redder than the photometric ones, with a median $\Delta\beta = \beta_{\text{spec}} - \beta_{\text{phot}} \sim 0.7$. There are different factors that contribute to it. The main one is the contamination from some red foreground objects, the BCG, and the ICL, which are not subtracted in the MUSE datacube, unlike the HST images. Additionally, we estimated the photometric slopes using magnitudes extracted from $0.27''$ -diameter apertures, increased, given that the MUSE observations are seeing limited, to $0.4''$ -diameter for the spectroscopic ones. The larger aperture enhances the effect of contaminants, as we observe in photometric measurements, where the median difference between slopes measured with $0.4''$ and $0.27''$ -diameter aperture is 0.21. This effect can be seen in Fig. B.3, where we show the difference between the photometric and spectroscopic β slopes as a function of the position in the sky (i.e., of the presence of close by contaminants) and of the redshift. Thus, we discard the clumps with angular distance smaller than $5''$ from the closest foreground red galaxy, reducing the spectroscopic sample to 27 clumps with reliable both photometric and spectroscopic β slopes, and the difference between them is reduced to $\Delta\beta \sim 0.3$.

5.5 Results and discussion

5.5.1 Comparison with galaxy-integrated β slopes

We compare the resulting photometric β slopes for our sample of individual clumps with those of galaxies at $z \sim 4$, color-selected from the GOODS-ERS WFC3/IR dataset (Giavalisco et al. 2004) and HUDF WFC3/IR dataset (e.g. Oesch et al. 2010) by Castellano et al. (2012), and with a sample of galaxies from $z = 4$ to 8 from Bouwens et al. (2014). The comparison is shown in Fig. 5.6. The samples of galaxies reveal that most of them have blue UV slopes, with distributions peaking around $\beta \sim -2$, with some red slope interlopers ($\beta \gtrsim -0.5$). This has been interpreted as a suggestion of low dust environment in high- z galaxies (e.g., Dunlop et al. 2013). The β slopes distribution of our sample of individual clumps shows a bluer median value of ~ -2.4 , that is consistent with different scenarios. Firstly, it confirms that clumps are sites of intense star formation (e.g., Bournaud et al. 2014; Zanella et al. 2015, 2019; Meštrić et al. 2022), and are populated by young, massive OB stars, whose spectrum strongly emits in the UV. But, it can also point out different features between the host galaxies and their clumps. The same result can be indeed reproduced by assuming that the dust at the location of the clumps is lower than the average extinction of the galaxy. This implies that assuming a similar extinction for the clumps and the host would result in an overestimate of the clumps SFR. Also, a lower metallicity at the clumps location or a different IMF or SFH can explain the bluer median β slope, and would have a crucial role in estimating the age of the clumps.

5.5.2 Trends with M_{UV} and redshift

It has been shown in previous studies that the mean UV-continuum slope of galaxies shows a dependence on the UV luminosity, with an almost identical slope with redshift ranging from 4 to 10 (Bouwens et al. 2014; Yamanaka & Yamada 2019; Cullen et al. 2022). It suggests that UV-faint galaxies are typically younger, less metal-enriched, and less dust-obscured than their brighter analogs (e.g., Rogers et al. 2013; Bhatawdekar & Conselice 2021).

We show the results for our sample in Fig. 5.7, with superimposed the relation found by Bouwens et al. (2014). The UV magnitudes for our sample, M_{UV} , have been measured as the geometric mean absolute magnitude of each clump in all the *HST* bands that contribute to its UV-continuum β slope determination. The adoption of the geometric mean prevents one to give too much weight to the bluer or redder bands in measuring M_{UV} , that could artificially introduce a β - M_{UV} correlation (Bouwens et al. 2012). The observed magnitudes are converted to intrinsic through the local magnification factor, and then to absolute magnitudes via the luminosity distance, measured with the assumed cosmological model. We show the results dividing our sample in redshift bins, as $z \sim 4$, $z \sim 5$, and $z \sim 6$.

The clumps in our sample are consistent with the Bouwens et al. (2014) reference relation within 2.3σ ($z \sim 4$), 1.2σ ($z \sim 5$) and 0.5σ ($z \sim 6$)³, and with a median scatter of $\Delta\beta \sim 0.26$, 0.15, and 0.35, respectively. The increasing consistency at higher redshift is mainly due to the larger uncertainty of the $z \sim 6$ relation and to the increasing median uncertainties on the β

³We measured the consistency values, η , as

$$\eta = \frac{|\beta - \beta_{B14}|}{\sqrt{\epsilon_\beta^2 + \epsilon_{\beta_{B14}}^2}} ,$$

where β and ϵ_β are the measured slopes and their uncertainties, while the subscript B14 denotes the same quantities derived from the Bouwens et al. (2014) best-fit relation.

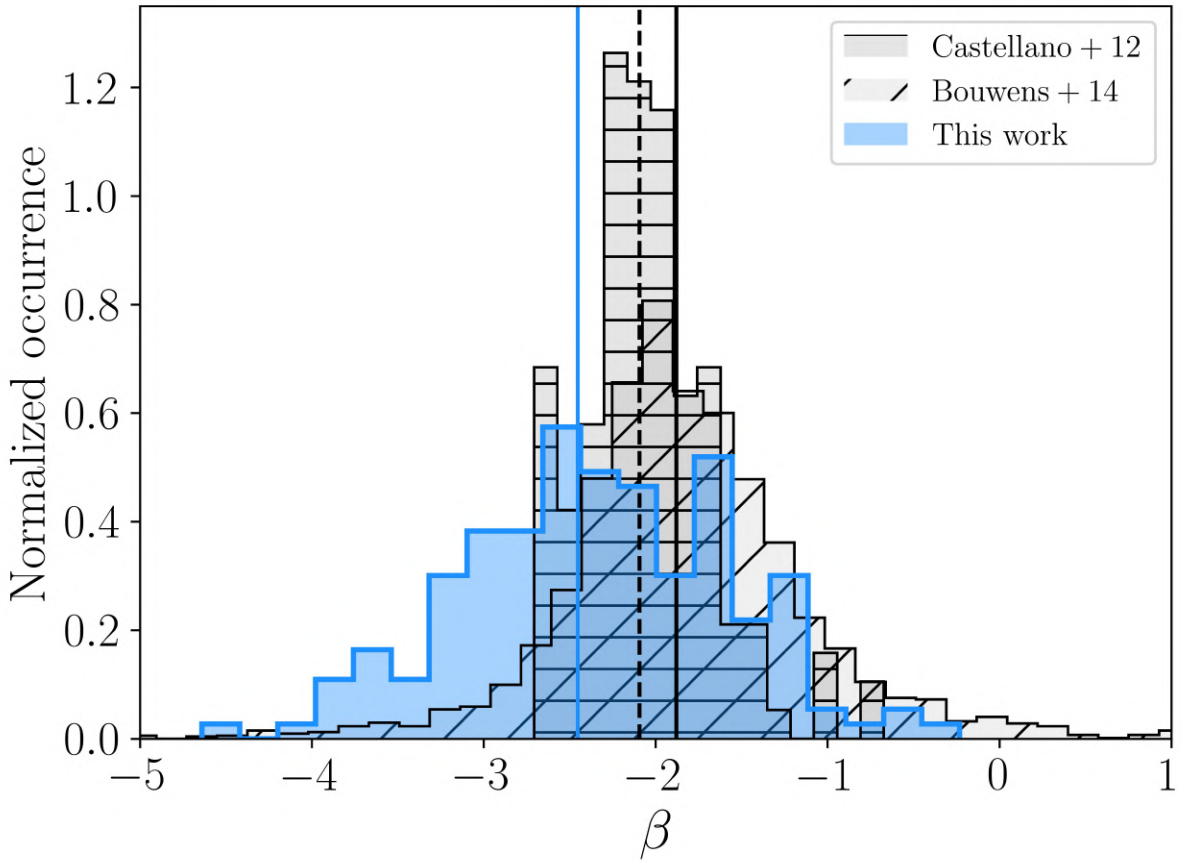


Figure 5.6: Distribution of the measured photometric β slopes. Our sample of clumps (in blue) is compared with two samples of high- z galaxies, from Castellano et al. (2012) and Bouwens et al. (2014) (hatched black histograms). The vertical lines represent the median values of the distributions, respectively in blue, dashed black and solid black.

measurements, but it may also suggest different evolutionary schemes. In fact, it may convey that clumps are bluer than their hosts especially at lower redshifts. It suggests that, at high- z , clumps and host have more similar stellar populations, dust content, SFH, and then the host changes properties over time more significantly than clumps do, presenting, at lower redshift, a dust rich environment and an evolved stellar population (resulting in a redder β slope) while the clumps maintain their blue β slopes thanks to the continuous star formation activity. Alternatively, due to the lack of resolution and to their faintness, high- z galaxy might rarely be resolved, and thus at the highest redshifts galaxies and isolated clumps can be misidentified or represent the same physical objects.

The reference relation has been measured for galaxies with M_{UV} ranging from -22 to -16 , while our sample of clumps covers M_{UV} values between -18 and -12 . It suggests that star-forming clumps follow the same β - M_{UV} relation of their host galaxies, and that it can be extended to fainter magnitudes (Fig. 5.7).

Several works (e.g., Stanway et al. 2005; Wilkins et al. 2011; Finkelstein et al. 2012; Castellano et al. 2012; Bhatawdekar & Conselice 2021) also report an evolution of the measured β slopes toward the blue with the increasing redshift, but it has not been confirmed uniformly with

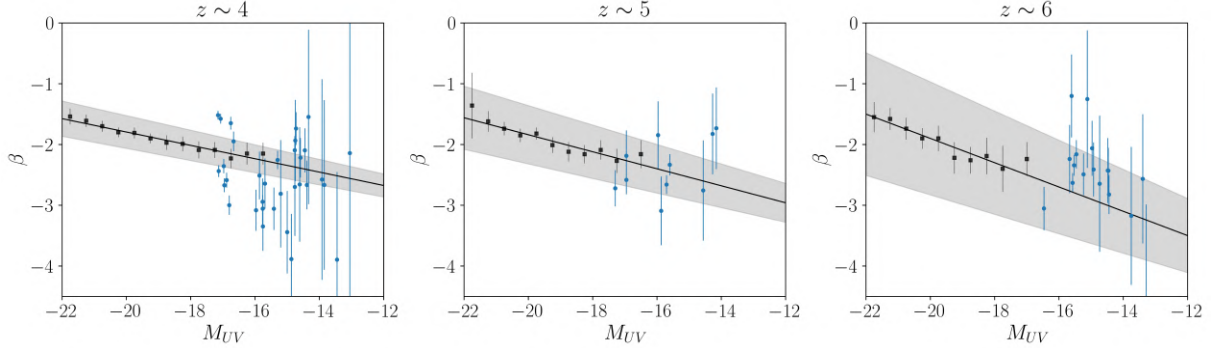


Figure 5.7: Measured β values as a function of the UV magnitude M_{UV} , in the $z \sim 4$ (left), $z \sim 5$ (center), $z \sim 6$ (right) redshift bin. The blue points, with 1σ uncertainties, are the clumps of our sample, while the bi-weighted binned mean of the sample of integrated galaxies from [Bouwens et al. \(2014\)](#) are shown in black. The black line represents the best-fit relation measured from this latter sample. The relation still holds at much fainter magnitudes, suggesting that star-forming clumps and their hosts follow the same relation.

most recent JWST data (e.g., [Nanayakkara et al. 2022](#)) and might be a result of observational limits. For the clumps of our sample, we observe a moderate reddening of the UV-continuum slopes with increasing cosmic time (Fig. 5.8). By fitting a linear relation between β and z , we measure $\beta = (-0.57 \pm 0.05)z + (-0.47 \pm 0.12)$. We stress however that the slope is strongly constrained by the clumps at $z \lesssim 3$, whose photometric measurements (and, consequently, β) are less uncertain. We fit the relation excluding the β measured with only two magnitudes, and find a fully consistent slope $d\beta/dz = -0.49 \pm 0.06$. Our relation shows a steeper slope than that measured by [Bouwens et al. \(2014\)](#) at $z \gtrsim 3.5$. If we limit our fit to the clumps in the same redshift range, we obtain a much flatter slope $d\beta/dz = -0.26 \pm 0.09$. We investigate the substantially different relations obtained in the two redshift intervals by assuming different subsets of the sample. When considering only the clumps in the most populated magnitude bins ($18 < M_{UV} < -15$) or with secure β measurement (uncertainty on $\beta < 0.5$) we find the best-fit parameters which are completely consistent with those obtained when fitting the entire sample (difference smaller than the typical 10% uncertainties). We do not consider other functional analytical forms to fit the data, like higher degree polynomials, given that they would not be physically motivated.

5.5.3 Extremely blue β slopes

Particular interest is recently devoted to extremely blue slopes, approaching values $\lesssim -3$. Such blue slopes would imply non-standard physical properties of high- z galaxies, and their analysis is crucial to characterize their stellar populations and put them in the context of galaxy formation and evolution. Several works have claimed the detection of robust $\beta \lesssim -2.7$ slopes for spectroscopically confirmed galaxies at high redshift (e.g., [Bouwens et al. 2010](#); [Labbé et al. 2010](#); [Zackrisson et al. 2013](#); [Maseda et al. 2020](#); [Jiang et al. 2020](#); [Marques-Chaves et al. 2022](#)), while there is not yet any reference for individual star-forming clumps.

In our sample, we selected eight clumps with robust photometric β measurements between -3.4 and -2.8 . We consider only the β slopes obtained with at least three flux measurements and without strong nearby contaminants. This subsample, presented in Table 5.3, results in the redshift range between approximately 4 and 6 (except for ID 253.3N at redshift ~ 3) and with a

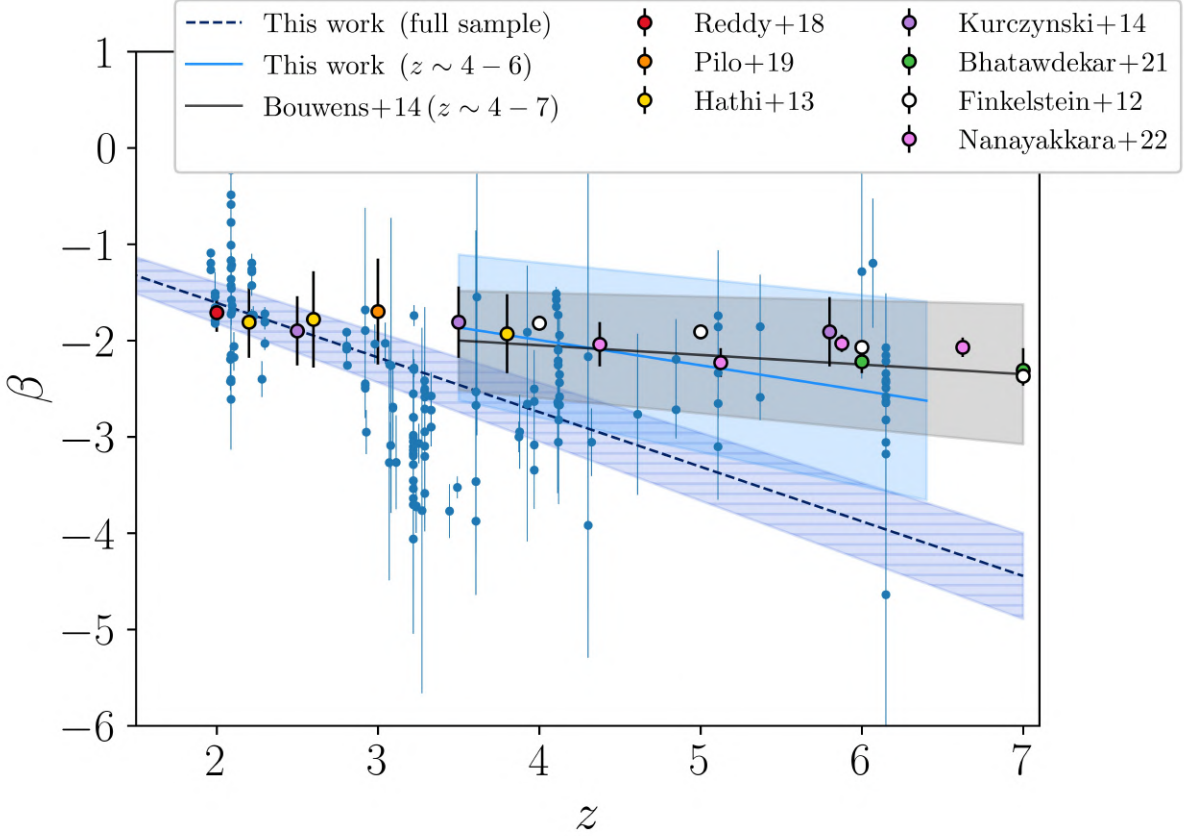


Figure 5.8: Measured β values as a function of the redshift z , with 1σ uncertainties. We report three different fits to a possible $\beta - z$ relation: in dashed blue the best-fit weighted relation of the entire sample of clumps, in black the relation found by Bouwens et al. (2014) for a sample of integrated galaxies at redshift between 4 and 7, and in solid blue the best-fit weighted relation to our sample of individual clumps limited to the same redshift range. The median value of β for galaxies at different redshifts reported in other studies is also shown (Reddy et al. 2018; Hathi et al. 2013; Pilo et al. 2019; Kurczynski et al. 2014; Finkelstein et al. 2012; Bhatawdekar & Conselice 2021; Nanayakkara et al. 2022).

typical β uncertainty of 0.4.

The flux measurements and the slopes are shown in Fig. 5.9. As shown in the previous section, generally the measured β slopes become bluer with increasing redshift and decreasing luminosity, and it has been shown that β measurements on photometrically-selected galaxies can likely introduce contamination and biases (Finlator et al. 2011; Ceverino et al. 2019). Together with the increasing number of claims of very blue slopes in high- z galaxies, the inspection of the physical properties of their stellar populations became necessary. Bouwens et al. (2010) could reproduce slopes of ~ -3 with standard (Leitherer et al. 1999; Bruzual & Charlot 2003) stellar population models only for very young (< 5 Myr) star-forming systems and ignoring the nebular continuum emission. The latter is caused by the ionized gas around young stars, and can redden the slopes up to $\Delta\beta \sim 0.5$ (Topping et al. 2022). If this component is included, the slope is not easily reducible below -2.7 . This suggests that very low metallicity (Z) values, or a different IMF, are needed to reproduce more extreme slopes. Some studies (e.g., Bouwens et al. 2010;

Table 5.3: The selected eight clumps with robust extremely blue slopes ($\beta \lesssim -2.7$)

ID	Redshift	β slope	V606	I814	Y105	J125	JH140	H160
2.1b	6.15	$-2.82^{+0.32}_{-0.32}$			28.58 ± 0.08	28.78 ± 0.12	28.85 ± 0.12	28.89 ± 0.12
17.1a	3.97	$-3.35^{+0.40}_{-0.40}$		28.76 ± 0.10	29.20 ± 0.13	29.35 ± 0.20		
17.3a	3.97	$-3.08^{+0.35}_{-0.33}$		28.61 ± 0.09	28.99 ± 0.11	29.06 ± 0.15		
18a	3.87	$-3.00^{+0.17}_{-0.16}$		27.90 ± 0.04	28.23 ± 0.06	28.32 ± 0.08		
70.7N	5.11	$-3.10^{+0.56}_{-0.55}$			29.11 ± 0.13	29.34 ± 0.20	29.44 ± 0.21	29.61 ± 0.23
103.1b	4.12	$-3.06^{+0.22}_{-0.23}$		28.23 ± 0.05	28.50 ± 0.07	28.78 ± 0.12		
122	6.15	$-3.06^{+0.36}_{-0.36}$			28.62 ± 0.08	28.75 ± 0.12	28.93 ± 0.14	29.07 ± 0.15
263.3N	2.93	$-2.95^{+0.24}_{-0.23}$	28.48 ± 0.09	28.69 ± 0.08	29.13 ± 0.13			

The first column contains the ID relative to the clump, as in the catalog by Meštrić et al. (2022). The second column displays their redshift, the third the β slope measured from photometry, making use of the magnitudes (and 1σ uncertainties) reported in the others column for the V606, I814, Y105, J125, JH140, H160 bands. Each clump has the measurements reported only for the three or four filters that are included in the useful UV rest-frame allowed by its redshift, described by Eqs. 5.2-5.3 and summarized in Table 5.1 and Fig. 5.3.

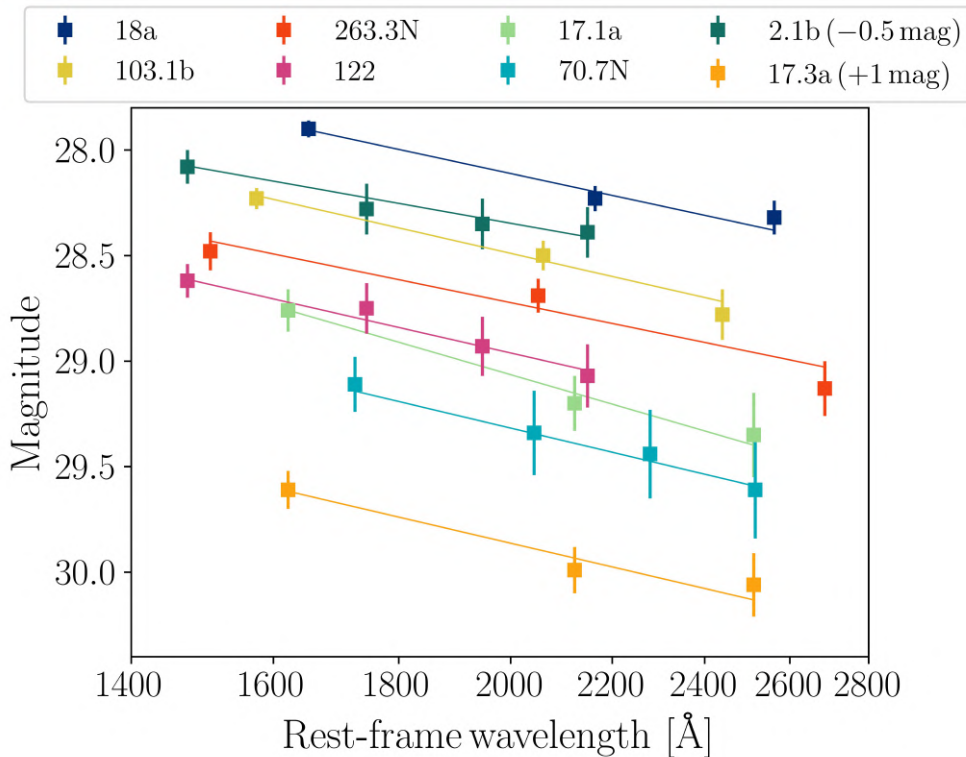


Figure 5.9: Measured magnitudes and the UV-continuum slope for eight selected clumps with $\beta \lesssim 2.7$, reported in Table 5.3. For each clump, represented with a different color, the symbols with the 1σ errorbars represent the magnitudes, while the lines show the best fit to the data. For clarity, the data relative to clump 2.1b and 17.3a have been shifted along the y -axis of -0.5 and $+1$ magnitudes, respectively.

Maseda et al. 2020) found that it is possible to reproduce slopes of about -3 with $Z < 10^{-2} Z_{\odot}$, but only for a limited range of ages, between 10 and 30 Myr. They conclude that very low metallicity values can explain part of the extremely blue slopes found, but the limited age range makes it unlikely to be the general explanation. They tested that the obtained slopes are comparable in the most extreme case of a single instantaneous burst with different IMFs and SFHs, like exponential declining or constant star formation. Jeřábková et al. (2017) demonstrated that the IMF assumption plays a secondary role in the resulting β slopes, but for the youngest ages (< 5 Myr), where it can account for up to $\Delta\beta = 0.2$. The IMF choice has also a stronger impact when the nebular emission is taken into account. The bluer slopes are related to the presence of the youngest and most massive stars, that would dominate the resulting stellar population if their IMF is top-heavy ($\alpha \sim 1.5$ in $dN/dm \propto m^{-\alpha}$, where $\alpha = 2.35$ in Salpeter 1955). The issue of this scenario is that the same stars are incredibly efficient at ionizing the surrounding gas, producing a nebular emission that would make the slope redder than in the young burst scenario with a standard IMF. The contribution from the nebular emission depends on a large number of factors, such as, for instance, the ionization parameter, the metallicity and the geometry. A promising way to decrease it, and thus being able to reproduce more extreme blue slopes, is to consider the case of ionizing radiation that leaks directly into the intergalactic medium (IGM). An escape fraction of ionizing photons into the IGM of 0.3 can easily reproduce the observed blue spectra (Bouwens et al. 2010; Zackrisson et al. 2013; Chisholm et al. 2022), but this value is considerably larger than the usually assumed ~ 0.1 , sufficient for galaxies to reionize the Universe. Similarly, Raiter et al. (2010) found that the contribution of the nebular emission strongly affects the slopes, even if also trends with the IMF, SFH, metallicity and age are observed. Topping et al. (2022) explored the possibility that the introduction of binary stars could generate significantly bluer slopes, but could reproduce slopes down to -3.15 , similar to the ~ -3.2 limit reached with single stars, concluding that binaries are not the main responsible for the extremely blue slopes.

We analyze the physical properties of our sample of extremely blue clumps making use of the publicly available Binary Population and Spectral Synthesis code (BPASS v2.3, Byrne et al. 2022; Eldridge et al. 2017) through its Python version Hoki (Stevance et al. 2020), which implements binary stellar evolution models and synthetic stellar populations to investigate the properties of the integrated light emitted from physically motivated distant stellar populations. We measured the β slopes of distant galaxies from their synthetic spectra with the same procedure described in Sect. 5.4. The different spectra are obtained by varying the main physical parameters that impact the β values: the metallicity, the age, the presence of binaries, and the IMF. We assumed four different IMFs: 1) a Salpeter IMF (Salpeter 1955) with $0.5\text{-}100 M_{\odot}$ mass range; 2) a Salpeter IMF with $0.5\text{-}300 M_{\odot}$ mass range; 3) a Chabrier IMF with $1\text{-}100 M_{\odot}$ mass range; and 4) a Chabrier IMF with $1\text{-}300 M_{\odot}$ mass range, and measured the β slopes over a grid of metallicity ($Z = 10^{-5}, 10^{-4}, 0.001, 0.002, 0.003, 0.004, 0.005, 0.006, 0.008, 0.010, 0.014, 0.020, 0.030, 0.040$) and age (from $\log_{10}(\text{age}/\text{yr}) = 6.0$ to 8.5 , with 0.1 steps) values. We repeat each configuration including the presence of binaries. In order to reproduce the bluer slopes, we focus only on pure stellar emission models, not considering the nebular emission. We obtain similar trends for all the models, and we show the results for two of them, with a Salpeter IMF with $0.5\text{-}300 M_{\odot}$ mass range, a Chabrier IMF with $1\text{-}300 M_{\odot}$ mass range and including binaries, in Fig. 5.10. The minimum β value we could reach is approximately -3.2 for all the models, with the absolute minimum -3.22 value obtained for the model showed on the left of Fig. 5.10. The introduction of binary systems makes on average the slopes bluer of $\Delta\beta \sim 0.08$ for all the IMFs, for all the age and metallicities. The extension of the IMF mass range from $1\text{-}100 M_{\odot}$ to $1\text{-}300 M_{\odot}$ makes

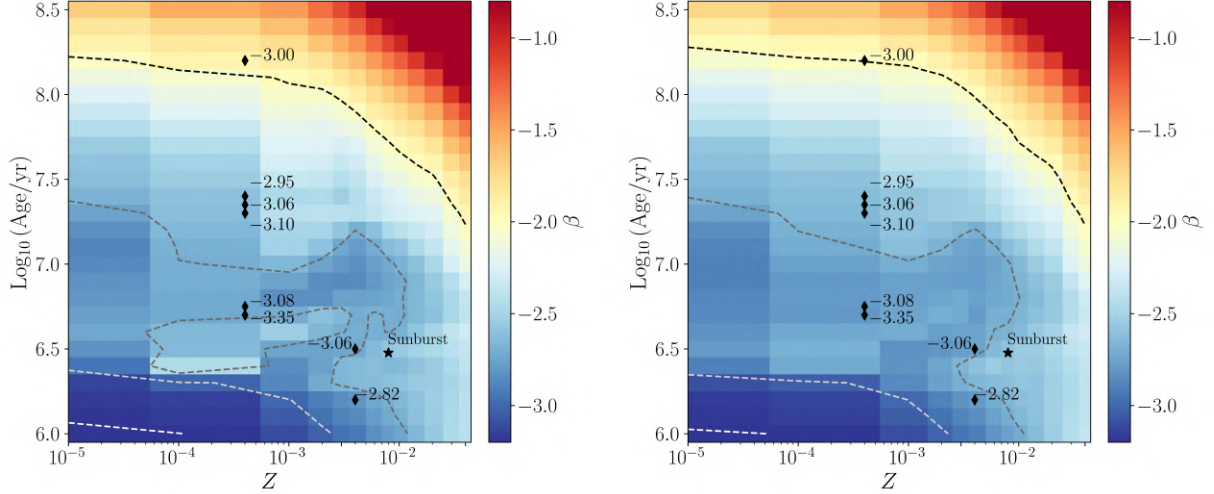


Figure 5.10: UV continuum β slopes (colormap) as a function of the age and metallicity, obtained with the synthetic spectra generated with the BPASS code, not including the nebular emission from the ionized gas around young stars. In this way, it is possible to reproduce the bluest observed slopes, down to -3.2 , by assuming extremely low metallicity and very young ages (bottom left part of each plot). The β values are measured by assuming a pure stellar emission and a Salpeter IMF with $0.5\text{-}300\,\mathrm{M}_\odot$ mass range (left) and a Chabrier IMF with $1\text{-}300\,\mathrm{M}_\odot$ mass range with the inclusion of binaries (right). In both panels, the black diamonds represent our eight extremely blue clumps, with their β slopes measured from photometry (see Table 5.3). The age and metallicity values are the best-fit measured by Meštrić et al. (2022) through SED modelling, with a typical uncertainty on the age of $+1.7$ and -0.7 dex. The black star represents the stellar cluster 5.1 of the Sunburst galaxy, at $z = 2.37$ (Dahle et al. 2016). We measure a photometric β slope of -2.41 ± 0.01 , exploiting the F555W, F606W, and F814W *HST* filters. The dashed lines, from black to white, represent the $[-2, -2.7, -3, -3.2]$ contours, respectively.

them bluer of $\Delta\beta \sim 0.02$. For all the models, this mean value affects uniformly all the ages and metallicities, but for $\log_{10}(\text{age/yr}) \lesssim 6.5$, where $\Delta\beta$ has a mean value of 0.2 , with a peak of 0.4 . In both the panels of Fig. 5.10, the black diamonds represent our eight extremely blue clumps according to the best-fit results obtained by Meštrić et al. (2022) through SED modelling, with a mean uncertainty on the age of $+1.7$ and -0.7 dex. The measurements of the age suffer from large uncertainties because of the young ages of these clumps, and we would need future spatially resolved spectroscopic observations to better constrain these quantities and directly compare models and observations. In the same plot, we mark, with a black star, the location of the stellar cluster 5.1 hosted by the Sunburst galaxy, at $z = 2.37$ (Dahle et al. 2016; Chisholm et al. 2019). This stellar cluster, with 12 multiple images, presents a multi-peaked Ly α emission that is consistent with an optically thin medium and Lyman continuum (LyC) leakage along the line of sight (Rivera-Thorsen et al. 2017). Additional studies revealed that this stellar cluster is younger than 3 Myr and presents a stellar metallicity of $0.4\,\mathrm{Z}_\odot$, with a physical size of $\approx 10\,\mathrm{pc}$ and a stellar mass of $\approx 10^7\,\mathrm{M}_\odot$ (Vanzella et al. 2022; Meštrić et al. 2023). The observed LyC leakage is consistent with low nebular emission, and it makes it possible to compare the β slope of this system with those measured from our BPASS models, where the nebular emission contribution is not included. Sunburst benefits from a comprehensive collection of photometric and spectroscopic data (Meštrić et al. 2023). To be fully consistent with the presented results, we measure the photometric β slope with the same approach described here, exploiting the F555W,

F606W, and F814W *HST* filters. The UV continuum slope we measure is $\beta = -2.41 \pm 0.01$.

5.5.4 Caveats

The measurement of the UV continuum β slope from photometry over a wide range of redshift values suffers from several well-known biases. In the study by Bouwens et al. (2014), a comprehensive examination of potential systematic uncertainties affecting the derived β slopes reveals a multitude of small factors. These factors include uncertainties in the effective PSFs of the HST observations, errors in accurately registering the observations with each other, the derivation of PSF kernels to ensure consistency across multiple bands, uncertainties in the HST zeropoints, the influence of light emitted by neighboring sources, and potential systematic errors in background subtraction. When the different images are PSF matched with the procedure we followed, Bouwens et al. (2014) estimate a total systematic uncertainty of about 3% in the measured colors.

One of the most relevant systematics effects is the “blue bias” (e.g., Dunlop 2012; Rogers et al. 2013; Bouwens et al. 2014; Jiang et al. 2020; Bhatawdekar & Conselice 2021; Cullen et al. 2022), that makes the faintest galaxies to have bluer slopes. This effect is due to the selection of candidate high- z galaxies by using filters close to the Lyman- α emission line, that enhances the flux in the short wavelength part of the spectrum and makes the slope bluer. In our study, the effect of this bias is absent, thanks to the spectroscopic confirmation of all the clumps. Furthermore, the selection of the exploitable filters that are included in the rest-frame UV, is properly designed to avoid Lyman- α contaminations (see Eqn. 5.2 and Calzetti et al. 1994). Despite this, our sample shows a correlation of the measured β slopes with the UV magnitude: it is usually interpreted as a change in the metallicity and in the dust extinction, but a contribution related to this bias cannot be excluded. Another observed systematic effect, of the order of $\Delta\beta \sim 0.2 - 0.3$, is related to the wavelength range in which the slopes are measured. In our study, and consistently with broad band measurements, we exploit the entire UV wavelength range, but it was shown that β values measured between 1300 – 1800 Å and 1800 – 2200 Å can be slightly different (e.g., Raiter et al. 2010; Chisholm et al. 2022). This effect may become particularly relevant when comparing the photometric β slopes with the spectroscopic ones or, depending on the redshift of the source, when the used photometric filters do not cover the entire UV range. This effect is stronger in the case of β slopes measured from a small number of available fluxes, as it can be the case of our fits with two or three magnitude measurements (e.g., Jiang et al. 2020; Mondal et al. 2023). We studied in detail the effects of the number of filters used in the fit, giving particular attention to the 2-magnitudes fits. Even if they are commonly employed in this kind of studies, given that no more than four HST broad filters can be simultaneously included in the relatively narrow restframe UV wavelength range, we observed significant trends, in particular regarding the uncertainties and the extreme β values. The 2-magnitude fits, even if they have been derived for the lowest redshift and brightest clumps, have the largest uncertainties. The tails of the distribution of the measured β slopes are strongly dominated by those clumps (see also Fig. 5.5). For this reason, we decided to exclude 2-magnitudes fits from some parts of the analysis, as described in the previous sections, and we checked whether all the results and correlations would importantly change by including or excluding them.

5.6 Summary and conclusions

We measured the UV-continuum β slopes of a sample of 166 individual star-forming clumps, belonging to 67 galaxies strongly lensed by the cluster of galaxies MACS J0416.1–2403, making

use of PSF-matched HST photometry for the entire sample, joint with deep MUSE spectroscopic observations for 100 clumps of the sample. We accurately analyzed and discussed the possible presence of biases and systematic uncertainties on the β measurements. The first aim of this study is to compare our novel measurements for individual clumps with those for integrated galaxies, in order to investigate possible physical differences between these regions and their hosts. We pursue it by measuring the value of the UV-continuum β slope ($f_\lambda \propto \lambda^\beta$), which depends on different key physical parameters, such as the age, metallicity, dust extinction, IMF and SFH. As is common in analogous studies referred to high- z galaxies, we investigate the trends of the β values as a function of the redshift and the UV luminosity. Our main conclusions can be summarized as follows.

- The β slope distribution of our sample of individual clumps shows a median value of ~ -2.4 , with a standard deviation of ~ 0.8 . This value is bluer than the ~ -2 value measured in literature for integrated galaxies in the same redshift range. The bluer median value for individual clumps confirms that they are sites of star formation, populated by young, massive OB stars, whose spectrum strongly emits in the UV, but can also point out different features between the host galaxy and their clumps. In fact, the bluer median slope can suggest a dishomogeneous dust distribution in the galaxy, and that the dust at the location of clumps is lower than the average extinction of the galaxy. Also, it can be explained by assuming a different SFH or SFR recipe for the clumps.
- The measured β values show a trend with the absolute magnitude in the restframe UV, M_{UV} , consistent with the relation expressed by [Bouwens et al. \(2014\)](#). They show a scatter of $\Delta\beta \sim 0.26$, 0.15, and 0.35, in the $z \sim 4$, $z \sim 5$ and $z \sim 6$ bin, respectively. The reference relation was measured for high- z galaxies, with M_{UV} ranging from -22 to -16 , while our sample of clumps covers M_{UV} from -18 to -12 . This implies that this relation can be extended to much fainter magnitudes, and that clumps follow the same relation as their host galaxies (see Fig. 5.7).
- We observe a weak trend of the β values with the redshift, as observed for integrated galaxies. We fit our entire sample and measure the relation $\beta = (-0.57 \pm 0.05)z + (-0.47 \pm 0.12)$, which is steeper than that measured by [Bouwens et al. \(2014\)](#). But, they are obtained in different redshift bins and, limiting our fit to the $z \gtrsim 3.5$ clumps, we obtain a much flatter slope of (-0.26 ± 0.09) , consistent with the results for integrated galaxies.
- In the β slopes distribution of our sample of individual clumps, several objects populate the tails of this distribution: 4 objects have a very red ($\beta > -1$) and 30 a very blue ($\beta < -2.7$) slope. We focused on eight objects with very blue robust β slope, obtained by fitting magnitude measurements in at least three different filters. We used the code BPASS, that simulates stellar populations and follows their evolution, to generate synthetic spectra of galaxies with different metallicities, SFHs, IMFs, and the possible presence of binaries. We were able to reproduce slopes down to $\beta \sim 3.2$, by assuming low metallicity ($Z \lesssim 10^{-3}$), young ($\log(\text{age}/\text{yr}) \lesssim 7$) and dust-poor regions, considering the absence of the nebular emission, whose presence would not allow us to reach so blue slopes, reddening them typically by $\Delta\beta \sim 0.5$.

CHAPTER 6

Constraining the geometry of the gas surrounding a typical galaxy at $z = 3.4$ with Ly α polarization

The results reported in this chapter have been mainly pursued during the 1-year Studentship period at the European Southern Observatory (ESO) in Garching bei München, Germany, and have been described in the manuscript “[Constraining the geometry of the gas surrounding a typical galaxy at \$z = 3.4\$ with Ly \$\alpha\$ polarization](#)”, **Bolamperti A.**, Zanella A., Vernet J., Chang S.-J., Gronke M., Arrigoni Battaia F., Calura F., Iani E., Vanzella E., submitted to A&A.

6.1 Introduction

The evolution of galaxies is impacted by the gas reservoirs around them, known as the circumgalactic medium (CGM; [Tumlinson et al. 2017](#)). The CGM plays a central role in the exchange of gas, dust and metals between the galaxy and its surroundings. It funnels toward galaxies the gas needed to form stars, it is the site where powerful galactic outflows end up and where gas recycling happens ([Putman et al. 2012](#); [Fox & Davé 2017](#); [Péroux & Howk 2020](#); [Veilleux et al. 2020](#)). The CGM presents a complex density and kinematic structure, that has been studied in the last decades thanks to multi-wavelength observations and simulations. They revealed that the CGM is “multiphase”, as it consists of different components ranging over wide intervals of density, temperature, and ionization state (e.g., [Péroux et al. 2019](#); [Wakker et al. 2012](#); [Ford et al. 2013](#); [Anderson et al. 2013](#); [Suresh et al. 2017](#); [Weng et al. 2022](#)). This complexity makes the modeling of the geometry and kinematics of the CGM challenging, in particular at high redshift, where it is usually modeled with simplified spherically or cylindrically symmetric static or expanding gas geometries (such as expanding ellipsoids) or with bipolar outflows (e.g., [Eide et al. 2018](#)), but the currently available data do not allow us to distinguish them. The Lyman- α (Ly α) line is one of the best observational signatures used in such studies, in particular at high- z , given its dependence on the structure, ionization, and kinematics of the H I gas where its photons propagate ([Osterbrock 1962](#); [Dijkstra et al. 2016](#); [Gronke & Dijkstra 2016](#)). It is the strongest tracer of recombining ionized hydrogen in young star-forming galaxies ([Partridge & Peebles 1967](#)) and is ubiquitously detected at high- z (e.g., [Zitrin et al. 2015](#); [Vanzella et al. 2017a](#); [Caminha et al. 2023](#); [Bunker et al. 2023](#); [Nakane et al. 2024](#)), but its interpretation is still debated. In fact, differently than other lines like the H α whose photons propagate undisturbed and reach us, Ly α has a resonant nature, and thus a Ly α photon can undergo a great number of scatterings after its emission. The number of scatterings that it experiences before being able

to leave its emission site depends on the H I column density, geometry, and kinematics (Adams 1972; Dijkstra 2014), on quantum mechanical probabilities (Stenflo 1980), and on the properties of the region where it originated. For instance, centrally emitted Ly α photons, e.g., created as nebular emission powered by star formation, significantly scatter before escaping, potentially giving rise to an observed spatially-extended Ly α emission. However, spatially-extended Ly α emission can also be produced by cooling gas (Haiman et al. 2000), gas that has been shock-heated by supernova explosions (Mori et al. 2004) and galactic winds (Taniguchi & Shioya 2000), fluorescent radiation from an external ionizing field (Hogan & Weymann 1987; Cantalupo et al. 2005), or extended star formation (Momose et al. 2016; Mas-Ribas et al. 2017). These features are encoded in the intensity spectrum of the source (Ahn et al. 2002, 2003; Verhamme et al. 2006; Dijkstra & Loeb 2008; Gronke et al. 2015), causing the broadening and shifting of its Ly α line profile (Neufeld 1990; Dijkstra et al. 2006). Moreover, the Ly α spectrum is also affected by radiative transfer effects at the interstellar medium (ISM) and CGM scales and is dependent on the inclination and evolutionary stage of the galaxy (see Blaizot et al. 2023, for a study on a simulated Ly α emitter galaxy at $z \sim 3 - 4$). The spectrum and the Ly α surface brightness profile, that reveals the spatial distribution of the Ly α emission and the diffusion process of Ly α photons, are the most frequently used observables embraced to investigate the nature of the Ly α emission. But, thanks to its resonant nature, we can additionally leverage on the Ly α degree and direction of linear polarization, typically represented by the Stokes parameters Q and U .

The Ly α degree of polarization increases if photons are scattered in a preferential direction, and the resulting value mainly depends on two fundamental factors: the production mechanism and site where the Ly α photons are created, and the geometry of the gas where they scatter before escaping, being in particular sensitive to the isotropy and homogeneity of the emission and gas distribution (e.g., Lee & Ahn 1998; Ahn et al. 2002; Eide et al. 2018). Theoretical studies showed that different models may present similar spectra, but different degrees of polarization of the Ly α line (e.g., Dijkstra & Loeb 2008; Gronke et al. 2015; Eide et al. 2018).

Due to the observational difficulty of measuring the Ly α degree of polarization of distant sources and the limited number of available (spectro-) polarimeters intended for extragalactic use (Hayes & Scarlata 2011; Beck et al. 2016), only a few studies that map the polarization of Ly α are currently present, and mostly with the narrow-band imaging mode. Moreover, they all target bright ($L_{\text{Ly}\alpha} > 10^{43} \text{ erg s}^{-1}$) and extended (up to ~ 150 kpc) Ly α emissions at $z \sim 2 - 3$ in dense environments, with no clear central powering sources (the so-called “Ly α blobs”; LAB) or around extreme environments, such as high- z quasars, overdense regions (clusters or protoclusters) and AGN or radio galaxies. The results are still controversial. Koratkar et al. (1995) made use of the HST Faint Object Spectrograph (FOS) spectropolarimeter to observe three QSOs at $z = 0.5 - 1.6$ including PG 1630+377, which presents an increase of the degree of polarization up to $\sim 20\%$ blueward the Lyman break, and a Ly α line polarization of $(7.3 \pm 1.6)\%$, that can be explained with the presence of two sources, one completely obscured and producing the scattered polarized signal, and a secondary unpolarized redder source. Vernet & Cimatti (2001) presented low resolution VLT/FORS1 spectropolarimetry of the submillimeter-selected galaxy SMM J02399–0136, finding a Ly α degree of polarization of $2.1_{-0.5}^{+0.9}\%$. Vernet et al. (2001) measured Ly α degrees of polarization $< 2\%$ in nine radio galaxies at $z \sim 2.5$ with Keck II/Low Resolution Imaging Spectrometer (LRIS). Prescott et al. (2011) observed the LAB LABd05, containing an obscured AGN at $z = 2.656$. Due to the coarse spatial resolution, they could only put an upper limit of $\approx 5\%$ on the Ly α degree of polarization within an aperture of 65 kpc. With deeper data, Kim et al. (2020) found a consistent polarization fraction of $(6.2 \pm 0.9)\%$ within the same aperture, but could also detect a spatially resolved polarization varying from 5% at the

$\text{Ly}\alpha$ peak to 20% 45 kpc away, consistent with $\text{Ly}\alpha$ photons not being scattered in the central region between the AGN and the $\text{Ly}\alpha$ peak, but only in the outer gas surrounding the nebula. Similarly, [Humphrey et al. \(2013\)](#) measured a low ($< 5\%$) polarization fraction in the center of the LAB hosting the TXS 0211–122 radio galaxy at $z = 2.34$, increasing to $(16.4 \pm 4.6)\%$ in the eastern section. [You et al. \(2017\)](#) found no polarized signal in the center of the LAB B3, which surrounds a radio-loud AGN at $z = 3.09$, and a degree of polarization of 3% (17%) at 10 (25) kpc, with an asymmetric distribution. [Hayes et al. \(2011\)](#) observed LAB1, in the SSA22 protocluster at $z = 3.09$, and did not detect polarized signal in the center, but a 20%-polarized ring at approximately 45 kpc. The results were confirmed by using spectropolarimetric observations by [Beck et al. \(2016\)](#), who found increasing polarization towards the wings of the $\text{Ly}\alpha$ spectral profile, which can be explained by the presence of outflows. Finally, [North et al. \(2024\)](#) did not detect polarized signal in the LAB hosting the radio-quiet quasar SDSS J1240+145, at $z = 3.11$.

Additionally, state-of-the-art models and simulations are needed to interpret the observations. In the last few years, significative steps forward have been done in such studies, with the implementation of $\text{Ly}\alpha$ polarization in advanced $\text{Ly}\alpha$ radiative transfer codes (e.g., [Ahn et al. 2000](#); [Dijkstra & Loeb 2008](#); [Ahn & Lee 2015](#); [Chang et al. 2017](#); [Eide et al. 2018](#); [Seon et al. 2022](#); [Chang et al. 2023](#); [Chang & Gronke 2024](#)), that allow us to predict the polarization behavior in different geometries (spherically symmetric like the expanding shell, and non spherically symmetric like the expanding ellipsoids or biconical outflows) and with different physical properties (density and clumpiness of the gas) and kinematics.

In this chapter we present the first study of the degree of polarization of the $\text{Ly}\alpha$ emission line for a typical clumpy, star-forming galaxy (Abell 2895a in [Livermore et al. 2015](#)) at $z \sim 3.4$, strongly lensed by the cluster of galaxies Abell 2895 (A2895) into three multiple images. Thanks to the image multiplicity and the lensing magnification, we are able to study the properties of this source in great detail using the available multi-wavelength dataset, which includes ancillary observations taken with the Hubble Space Telescope (HST), the Multi Unit Spectroscopic Explorer (MUSE), the Enhanced Resolution Imager and Spectrograph (ERIS), and the Spectrograph for INtegral Field Observations in the Near Infrared (SINFONI) at the Very Large Telescope (VLT), the Atacama Large Millimeter/submillimeter Array (ALMA), and new observations taken with VLT/FOcal Reducer/low dispersion Spectrograph 2 (FORS2) instrument, with its Polarimetric Multi Object Spectroscopy (PMOS) mode.

The chapter is organized as follows. In Section 6.2, we present the data available for this system, summarizing the ancillary archival data and then focusing on the new FORS2 PMOS observations. We also describe the pipeline and the step followed in the data reduction. In Section 6.3, we describe the 1D spectra extraction, the dilution correction, the measurement of the Stokes parameters and polarization fraction as a function of the wavelength, and the assumed bins in wavelength. In Section 6.4 we expose the radiative transfer models we developed to interpret the results, and we compare observations and models in Section 6.4.3. In Section 6.5 we discuss our results and the future perspectives. In Section 6.6, we summarize our results.

6.2 Data

6.2.1 Our target galaxy and its ancillary data

Our target, Abell 2895a, is a clumpy star-forming galaxy at $z \sim 3.4$, strongly lensed by the galaxy cluster A2895 into three multiple images with coordinates (M1; M2; M3) (RA, dec) = (01:18:11.19, $-26:58:04.4$; 01:18:10.89, $-26:58:07.5$; 01:18:10.57 $-26:58:20.5$) ([Livermore et al.](#)

2015; Iani et al. 2021). They are located in the inner region of the A2895 cluster, angularly close to the brightest cluster galaxy (BCG; at $z = 0.227$). Through this chapter, we will focus on the two most magnified images, M1 and M2, whose average lensing magnifications are $\mu = 5.5 \pm 0.7$ and $\mu = 4.5 \pm 0.3$, respectively (Iani et al. 2021; Zanella et al. 2024).

Abell 2895a has a redshift of $z_{\text{opt}} = 3.39535 \pm 0.00025$, estimated from optical emission lines (Iani et al. 2021), which is consistent with the $z_{[\text{C II}]} = 3.39548 \pm 0.00007$ estimated from the [C II] far-infrared line (Zanella et al. 2024). It presents a clumpy morphology in the UV continuum and in [C II] emission line observations. At least four star-forming clumps within a diffuse emission are detected in the UV continuum, one of which is also observed in the [C II] data. Two additional clumps, without a detected UV counterpart, are identified in [C II], whereas no dust continuum is detected.

Abell 2895a offers a suite of ancillary data, presented in Iani et al. (2021) and Zanella et al. (2024). The rest-frame UV HST imaging (SNAP program 10881, PI: G. Smith) has FWHM $\sim 0.13''$ resolution in the F606W filter, obtained with a total exposure time of 0.33 hours. The VLT/SINFONI spectra (Livermore et al. 2015), targeting H β and [O III], are taken with a total exposure time of 5.33 hours, and are seeing limited with FWHM $\sim 0.6''$. New VLT/ERIS observations (program IDs 110.2576, 112.25HA, 114.273Y, PI: A. Zanella), aimed at spatially-resolving the [O III] and H β emissions, are ongoing. The VLT/MUSE observations are taken with the Adaptive Optics (AO) Wide Field Mode (WFM) with a total integration time of 5 hours, and have a resolution of FWHM $\sim 0.4''$. They have targeted the Ly α emission, that appears spatially offset with respect to the clumps visible in the UV continuum and the optical emission lines, suggesting the presence of dust and neutral gas, that absorb and scatter the Ly α photons. This offset is not due to astrometry issues, as the MUSE and HST data were aligned, and the HST astrometry was registered against Gaia DR3 (Iani et al. 2021). The HST rest-frame UV and the Ly α contours are shown in Fig. 6.1. Finally, ALMA Band 8 observed Abell 2895a in October 2019 for 1.9 hours on source (program ID 2019.1.01676.S, PI: E. Iani) to detect the [C II] emission line and the underlying continuum (Zanella et al. 2024). The beam size (assuming a natural weighting) is FWHM = $0.31'' \times 0.26''$.

A2895 also benefits from a robust strong lensing model, introduced by Iani et al. (2021). The 2D-projected total mass distribution of the cluster is modeled as a combination of an extended cluster-scale halo and multiple galaxy-scale double pseudo-isothermal elliptical components (dPIE, Elíasdóttir et al. 2007), whose centers and shapes are constrained by the respective surface brightness centroids, ellipticities, and position angles from the HST F606W image. The cluster members are selected through the color–magnitude diagram method (e.g. Richard et al. 2014), and the total mass associated to each member is computed from its luminosity, through the Faber–Jackson relation for elliptical galaxies (Faber & Jackson 1976), as is usual in strong lensing modeling on cluster scales (e.g., Caminha et al. 2023; Bergamini et al. 2023b). The model is constrained by using the location of the multiple images of Abell 2895a and those of another triply imaged system with spectroscopic redshift $z = 3.721$ (Livermore et al. 2015; Iani et al. 2023), shown in Fig. 6.1. The best-fit model reproduces the location of the multiple images with a root-mean-square (rms) displacement of $0.09''$ between the observed and modeled multiple images positions. The convergence maps derived from this strong lensing model are exploited to estimate the magnification factors in the locations of M1 and M2, that we use to derive the magnification-corrected quantities adopted in the following.

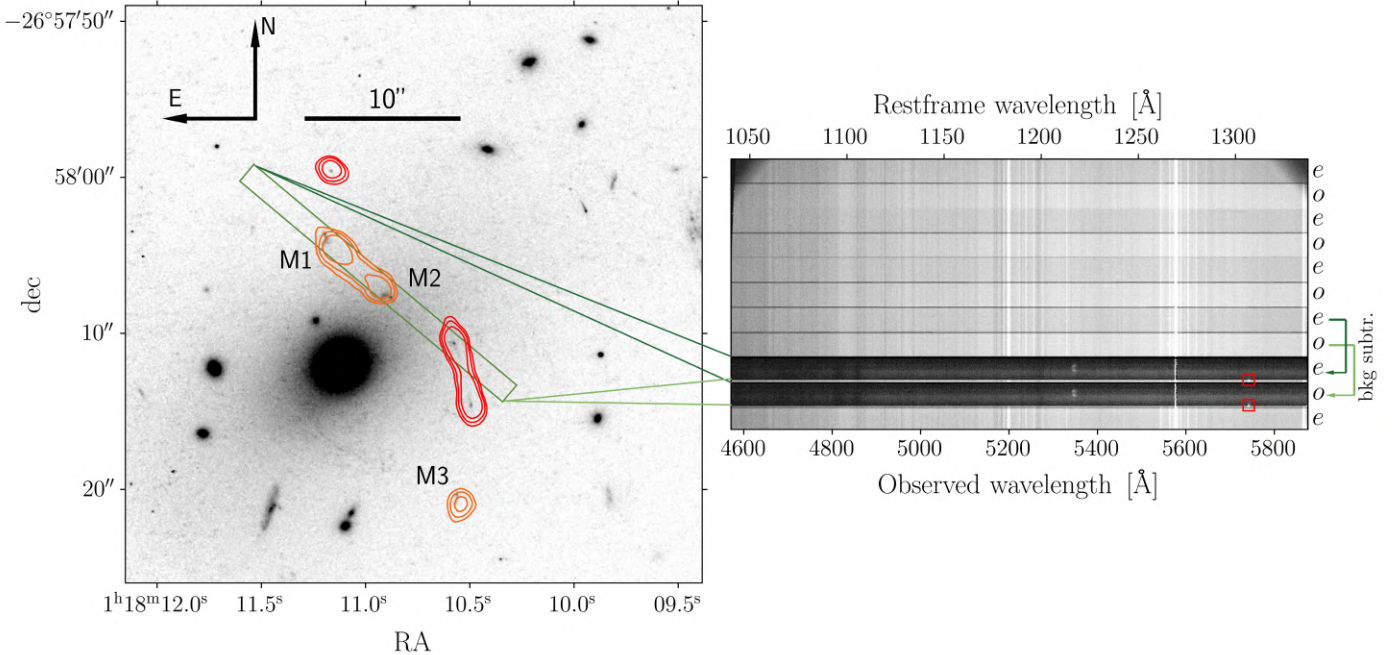


Figure 6.1: Left: HST F606W image of the inner part of A2895, where the three multiple images of Abell 2895a (M1, M2, and M3) appear. It represents the rest-frame UV at the redshift of Abell 2895a, $z \sim 3.4$. In orange, we show the 2, 3, and 5σ contours of the Ly α emission, detected with MUSE. The green box represents the FORS2 $1.4'' \times 22''$ adopted slit, that includes M1 and M2, and one image of another source at $z \sim 3.7$ (Iani et al. 2023), whose Ly α 2, 3, and 5σ contours are shown in red. Thanks to the PMOS mode, the signal included in the slit is split in an ordinary (o) and extraordinary (e) ray, with orthogonal polarizations, shown with different tones of green. Right: stacked 2D spectrum with $\varphi = 0.0^\circ$ obtained after calibration, cosmic ray rejection, and sky subtraction. In particular, the sky is subtracted only in the relevant slits which contain Abell 2895a, and appear darker. Each slit has a spatial (vertical) width of $22''$, and the sky level is estimated and then subtracted from the closest ordinary and extraordinary slits (see the e and o labels on the right), respectively, as shown by the green arrows on the right. In the slits including the target, we detect the extended Ly α emission associated with M1 and M2, at approximately 5340 Å, the continuum from the nearby BCG, in the bottom part, and the Ly α emission of the source at $z \sim 3.7$ (red squares, close to the edge of the slitlets). We only show here the 2D spectrum taken with the 0.0° position of the half-wave plate in the CHIP1 (Norma) CCD.

6.2.2 FORS2 PMOS observations and data reduction

Abell2895a was observed with VLT/FORS2 (Appenzeller et al. 1998) between September 2021 and August 2022 (program ID 108.2260, PI: A. Zanella), for a total of 18.1 hours in PMOS mode. The polarization optics are composed of a superachromatic half-wave plate mosaic followed by a Wollaston prism, that separates the light into two beams with orthogonal polarization (the "ordinary" (o) and "extraordinary" (e) rays). Half of the MOS mask slitlets in front of the polarization optics are fully closed to avoid the overlap of the o and the e beams, leaving eight $22''$ high slitlets for science targets.

Observations were executed with seeing $< 0.9''$, clear sky conditions, fraction of lunar illumination

< 0.4 , and airmass $\lesssim 1.6$. The run was divided into twelve sets of four 1200 s exposures with the half wave plate position angles (φ) set successively to 0° , 22.5° , 45° , and 67.5° . We used the MIT red CCD together with the 1400V grism and a slit width of $1.4''$ for all observations providing an effective spectral resolution of about 3.6 \AA FWHM covering the wavelength range from 4560 to 5860 \AA . The slit was oriented at 40° so that both M1 and M2 fit in a single slitlet (see Fig. 6.1), which also includes one multiple image of another source at $z \sim 3.7$ (Iani et al. 2023). However, this galaxy is too close to the edge of the slit and the slit losses are too important to analyze the polarization of this second target too, that is not considered in the following analysis.

We reduced the data with the standard FORS2 PMOS pipeline v5.14, making use of the ESO Recipe Execution Tool (EsoRex, ESO CPL Development Team 2015) pipeline. We reduced separately the observations of each of the twelve OBs and combined them as the last step. We focused on the data taken with the CHIP1 (Norma) CCD, which contains the spectrum of Abell 2895a in the bottom part. We ran the calibration recipe to correct all the raw exposures using the associated BIAS frames, identify the slitlets limits, the dispersion relation, and the spatial distortion, and correct for the FLAT fields. These products were used as inputs in the science recipe, that produces as output wavelength-calibrated optical distortion-corrected 2D spectra. Given the faintness of our target in the single OB, we disabled the sky subtraction automatically performed by the pipeline, as it may affect the resulting signal-to-noise ratio (S/N) of the target. We detected and subtracted the cosmic ray traces with the Astro-SCRAPPY (McCully et al. 2018) Python package, based on L.A.Cosmic (van Dokkum 2001). To properly subtract the sky background contribution for the o and e beams, we estimated the median flux at each wavelength in the two respective closest slits, located $22''$ apart (Fig. 6.1, right panel, arrows on the right). We did not use the slits containing the target themselves to estimate the sky as they are dominated by the emission of M1, M2, and the BCG contribution. We checked that, after subtracting the median sky flux from the target slits, the residuals did not show systematics or gradients. Three OBs presented a polarized background contamination, likely due to the presence of the moon, and thus with a not robust sky subtraction. We decided to exclude them so as not to bias our analysis. These OBs were the only ones taken with the moon above the horizon, and had the lowest angular separation between the target and the Moon ($\sim 90^\circ$ instead of the $140^\circ - 150^\circ$ of the rest of the OBs). We stacked the remaining nine OBs by spatially matching the position of the Ly α peak. We computed, for each OB, a profile in the spatial y -direction around the Ly α line and identified the peaks of the two Ly α glows, relative to M1 and M2. We noticed that, in the selected OBs, the peaks do not show significant shifts ($\lesssim 0.5''$, much smaller than the extraction aperture used for 1D spectra in the following), and thus we directly stacked them, obtaining four 2D spectra, one for each of the four φ values (one of the four 2D spectra, relative to the $\varphi = 0.0^\circ$ case, is shown as an example in Fig. 6.1). We measured the 2D variance spectra by converting the stacked spectra from ADU/s to counts, and propagating the uncertainties associated to the object, the sky, and the readout noise assuming Poissonian statistics.

The four resulting 2D spectra of the o and e channels including Abell 2895a consist of $22''$ slits, with a spatial resolution of $\sim 0.25'' \text{ pix}^{-1}$ and spanning in wavelength from 4560 \AA to 5860 \AA , with an effective spectral resolution of about 3.6 \AA FWHM, and with a $0.64 \text{ \AA} \text{ pix}^{-1}$ dispersion.

6.3 Analysis

6.3.1 Intensity spectrum of Abell 2895a and dilution correction

To maximize the S/N , we extracted the 1D spectra by summing, for each wavelength, the signal included in an aperture of $7.5''$, designed to encompass both the M1 and M2 Ly α emission. The eight resulting 1D spectra, with intensities $I_{\varphi}^{o,e}(\lambda)$, relative to the o and e channels with $\varphi = 0.0^\circ, 22.5^\circ, 45.0^\circ$, and 67.5° , showed a significant contribution from the flux of the angularly close BCG. This signal is not polarized and it does not directly affect the polarization measurements of the Ly α line of Abell 2895a, but dilutes it. Thus, the maximum polarization fraction we could measure was limited by the dilution factor, f_d . We firstly estimated the total intensity spectrum $I(\lambda)$ within the extraction aperture, that is equivalent to the total intensity Stokes parameter spectrum, as the sum of the eight 1D spectra. Then, we evaluated the total intensity spectrum associated with the BCG, $I_{\text{BCG}}(\lambda)$, by applying the same procedure to eight spectra extracted within $4''$ -apertures centered on the bottom part of each slit, where there is no contribution from the Ly α blobs. We normalized the $I(\lambda)$ and $I_{\text{BCG}}(\lambda)$ spectra, and smoothed $I_{\text{BCG}}(\lambda)$ to mitigate noise features. The $I(\lambda)$ spectrum, before and after subtracting $I_{\text{BCG}}(\lambda)$, is shown in the left panels of Fig. 6.2. We derived the dilution factor, defined as the fraction between the total intensity spectrum from the underlying continuum, mainly due to the BCG, and that of Abell 2895a only, as

$$f_d(\lambda) = \frac{I_{\text{BCG}}(\lambda)}{I(\lambda) - I_{\text{BCG}}(\lambda)}. \quad (6.1)$$

We measured $f_d(\lambda)$ values ranging from approximately 2 at the peak of the Ly α to 10 in the tails.

6.3.2 The reduced Stokes parameters q , u , and P spectra and variance spectra

We combined the measured $I_{\varphi}^o(\lambda)$ and $I_{\varphi}^e(\lambda)$ intensities to measure the reduced Stokes parameters q and u ¹ as a function of the wavelength. Combining observations taken with four different position angles is crucial to correctly handle the different gain factors in the o and e channels, and to extract reliable $q(\lambda)$ and $u(\lambda)$ spectra (Cohen et al. 1997). The degree of polarization is then measured as

$$P(\lambda) = \sqrt{q^2(\lambda) + u^2(\lambda)}, \quad (6.2)$$

and the uncertainties on $q(\lambda)$, $u(\lambda)$, and $P(\lambda)$ are estimated through the propagation of the uncertainties associated with each of the eight $I_{\varphi}^o(\lambda)$ and $I_{\varphi}^e(\lambda)$ 1D intensity spectra. In principle, $q(\lambda)$ and $u(\lambda)$ allow us to measure also the polarization angle but, given the low S/N regime, we could not obtain significant measurements, and will not consider the polarization angle in the following.

The degree of polarization measured through Eq. 6.2 is, by definition, a positive quantity. In low S/N regimes, the uncertainties on $q(\lambda)$ and $u(\lambda)$ lead to an increase of the biased measured value of $P(\lambda)$, that will differ from the true unbiased value $P_0(\lambda)$. We applied the correction

¹ $q(\lambda)$ and $u(\lambda)$ are measured as

$$q(\lambda) = \frac{R_Q(\lambda) - 1}{R_Q(\lambda) + 1}, \quad \text{where } R_Q^2(\lambda) = \frac{I_{0.0^\circ}^o(\lambda)/I_{0.0^\circ}^e(\lambda)}{I_{45.0^\circ}^o(\lambda)/I_{45.0^\circ}^e(\lambda)},$$

$$u(\lambda) = \frac{R_U(\lambda) - 1}{R_U(\lambda) + 1}, \quad \text{where } R_U^2(\lambda) = \frac{I_{22.5^\circ}^o(\lambda)/I_{22.5^\circ}^e(\lambda)}{I_{67.5^\circ}^o(\lambda)/I_{67.5^\circ}^e(\lambda)}.$$

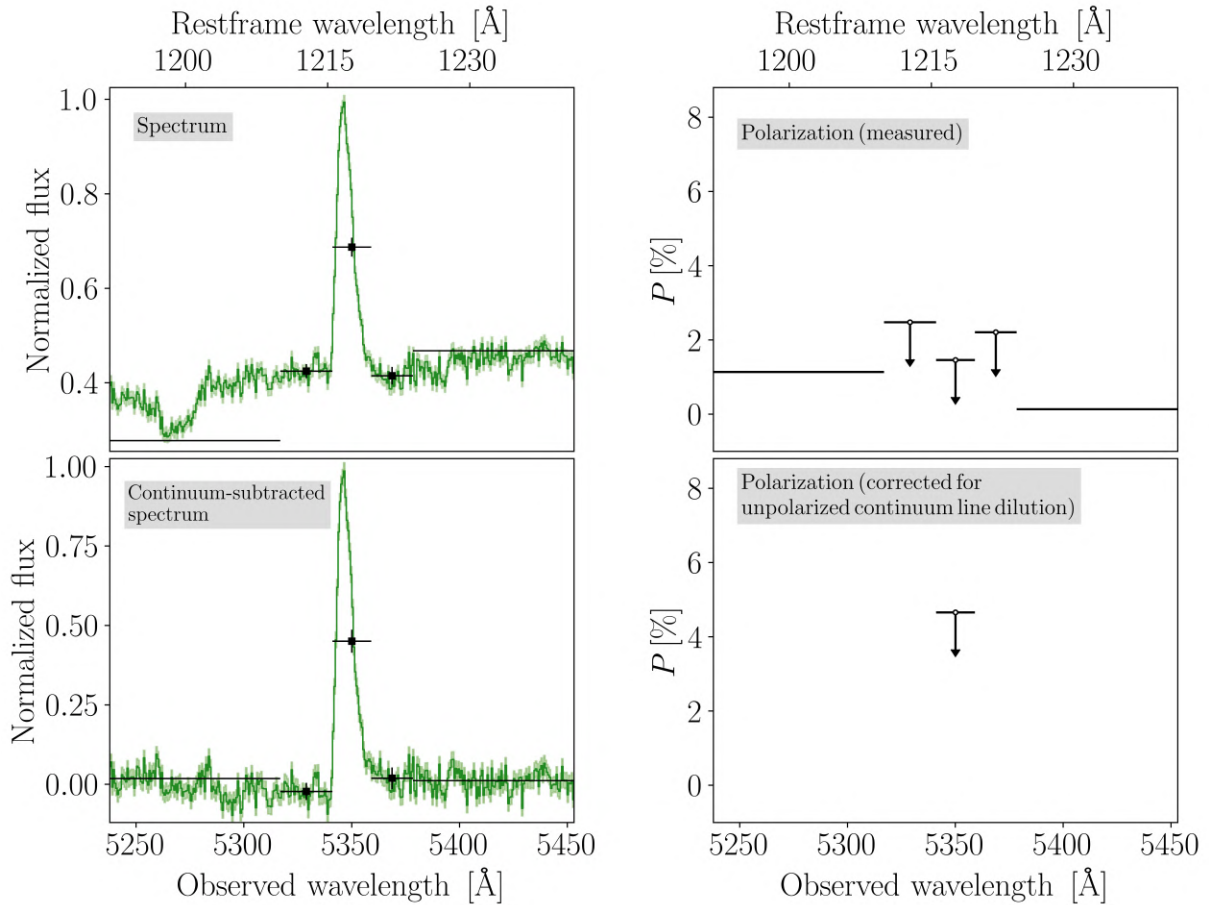


Figure 6.2: Left panels: total intensity spectra (green solid line) and 1σ uncertainties (light green shaded region) in the spectral region around the Ly α line. The top (bottom) panel shows the normalized spectrum before (after) the subtraction of the BCG contribution. The black filled squares, with 1σ uncertainties, represent the binned data. Right panels: polarization (P) measurements obtained before (top) and after (bottom) the dilution correction described in Eq. 6.1. The black open circles represent the 1σ upper limits obtained by applying the correction of [Simmons & Stewart \(1985\)](#). In the bottom right panel, only one datapoint is visible, as the others are outside the plotted range (upper limits for $P \sim 80\% - 95\%$).

by [Simmons & Stewart \(1985\)](#), that proposed, for different S/N regimes, four different possible methods to estimate $P_0(\lambda)$ (the average estimator from [Serkowski 1958](#), the [Wardle & Kronberg 1974](#) estimator, the maximum likelihood estimator, and the median estimator) and their uncertainties. In high S/N regimes all the four methods predict consistent results, while they are particularly effective in estimating $P_0(\lambda)$ in low S/N regimes, like those presented in this chapter. In this regime, the quality of the measured $q(\lambda)$, $u(\lambda)$, and $P(\lambda)$ can be moreover enhanced by binning the spectra in a number of bins that depends on the target S/N and on the spectral resolution needed for a proper interpretation of the data. We adopted two different approaches: we included the entire Ly α line in a single bin, integrating from 1215.5 Å to 1219.6 Å, or we divided it into three bins, one including the blue tail (1215.5-1216.3 Å), a central one including the peak (1216.3-1217.9 Å) and one including the red tail (1217.9-1219.6 Å). We also included two bins to sample the continuum blueward (one narrower and closer to the Ly α , from 1210.0 Å to 1215.5 Å, and one broader, from 1037 Å to 1210 Å) and redward (similarly, from 1219.6 Å to 1224.0 Å, and from 1224 Å to 1260 Å) the Ly α emission. These are partially visible in Fig. 6.2 as the horizontal black lines. In the following, we will refer to the case with a single bin for the Ly α , while the results for the other case are shown in Appendix C.1, as they are equivalent and bring to the same conclusions.

We applied Eq. 6.2, and measured low P values, consistent with zero. After the positive bias correction and the binning, we obtained observational upper limits on P_0 in the considered bins. We multiplied these upper limits by the dilution factor $f_d(\lambda)$, correspondingly binned within the same chosen spectral windows (e.g., $f_d \approx 3$ in the Ly α bin). The measured polarization fractions before and after the dilution correction are shown in the right panels of Fig. 6.2. The P_0 values revealed that we can put tighter constraints on the polarization fraction at the peak of the Ly α line, where the S/N is at its maximum, and increasingly shallower ones moving towards the tails. Far from the line, in the continuum where $I(\lambda) \approx I_{BCG}(\lambda)$, it is not possible to put informative constraints. After the dilution correction, we measure for the bin including the Ly α 1σ , 2σ and 3σ unbiased upper limits on the degree of polarization, $P_{Ly\alpha}$, of 4.6%, 5.8%, 6.5%, respectively. Due to the large dilution factor of approximately 35 (100), the degree of polarization is barely (not) constrained for the narrow (broad) continua bins.

We checked whether the $P_{Ly\alpha}$ measurements could be affected by our choice of the aperture adopted to extract the spectra, including two multiple images of Abell 2895a. In fact, the strong lensing critical lines at the redshift of Abell 2895a pass between the two images, that result fairly mirrored (as can be seen from the UV morphology and the Ly α contours on the left panel of Fig. 6.1). We extracted the spectra separately from the the extended Ly α of M1 and M2, visible on the right panel of Fig. 6.1, with apertures of 4'' centered on the peaks (against the 7.5''aperture that includes both peaks). By adopting the same Ly α bin and corrections, we obtained consistent 1σ $P_{Ly\alpha}$ upper limits of 7.4% and 5.8%, that are less stringent due to the lower S/N .

6.4 Radiative transfer models for Ly α

[Iani et al. \(2021\)](#) modeled the spectral profile of Ly α through Ly α radiative transfer modeling ([Dijkstra 2019](#)), using the fitting pipeline of [Gronke et al. \(2015\)](#), adopting the shell model (e.g., [Ahn et al. 2000; Verhamme et al. 2006](#)), which is composed of a thin H I shell with a single constant radial velocity and a central Ly α source. However, due to the symmetry of the shell model, the integrated Ly α spectrum is always unpolarized. If the scattering medium is not symmetric, such as a bipolar wind or ellipsoidal halo, the integrated Ly α can be polarized ([Dijkstra & Loeb 2008](#);

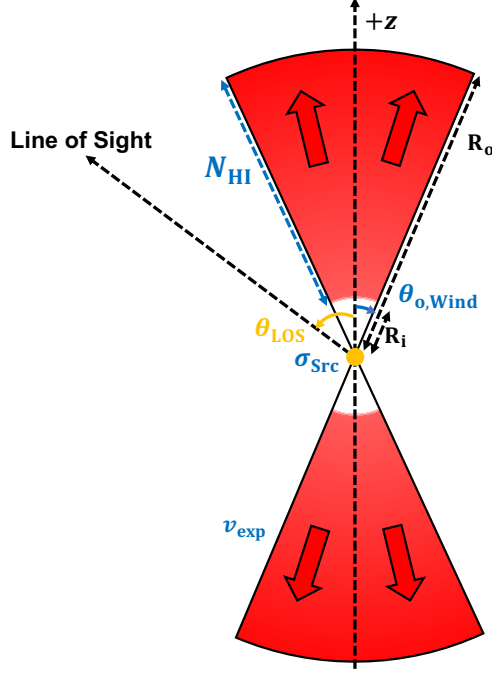


Figure 6.3: Schematic illustration of the wind model composed of a central point source (orange) and a bipolar outflow with the radius R_o (red). The central source emits Ly α photons, following a Gaussian profile with a width σ_{Src} . The bipolar outflow is characterized by the H I column density N_{HI} , the opening angle $\theta_{o,\text{Wind}}$ (increasing from the $+z$ -axis, as the blue solid arrow), and the expansion velocity v_{exp} parameters. The inner radius of the outflow R_i is fixed at $0.1R_o$. As the wind model is symmetric about the z -axis, the line of sight angle θ_{LOS} is the angle from the $+z$ -axis following the orange arrow, and thus with $\theta_{\text{LOS}} = 0^\circ$ meaning observing in the direction of the outflow, and $\theta_{\text{LOS}} = 90^\circ$ representing the equatorial view.

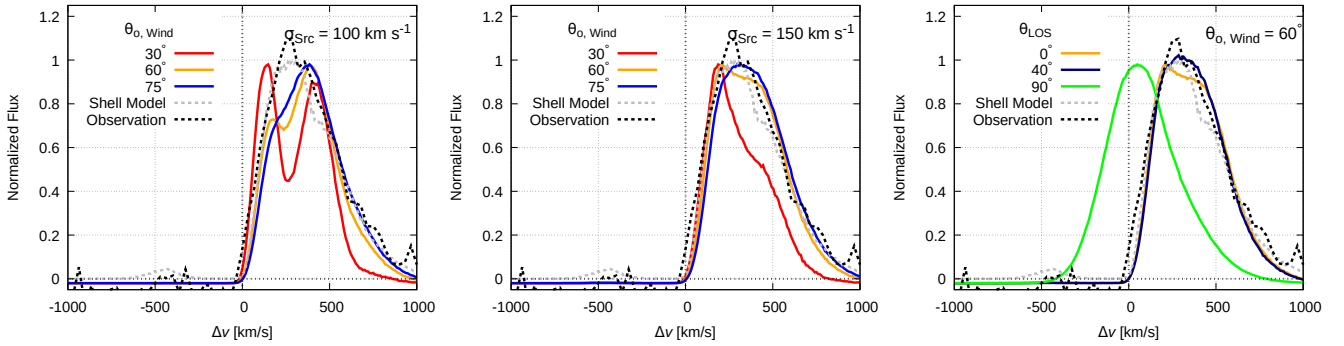


Figure 6.4: Comparisons between observed and simulated Ly α spectra. The simulated spectra of the wind models are normalized by setting the same peak height as the observed spectrum. The black dashed line is the observed Ly α spectrum, which is continuum subtracted. The grey dashed line is the simulated Ly α spectrum of the shell model from Iani et al. (2021). In the left and middle panels line colors represent, for σ_{Src} equal to, respectively, 100 km s^{-1} and 150 km s^{-1} , $\theta_{o,\text{Wind}} = 30^\circ$ (red), 60° (orange), and 75° (blue), with θ_{LOS} fixed to 0° . In the right panel, $\theta_{o,\text{Wind}}$ is fixed to 60° , and line colors represent $\theta_{\text{LOS}} = 0^\circ$ (orange), 40° (blue), and 90° (green).

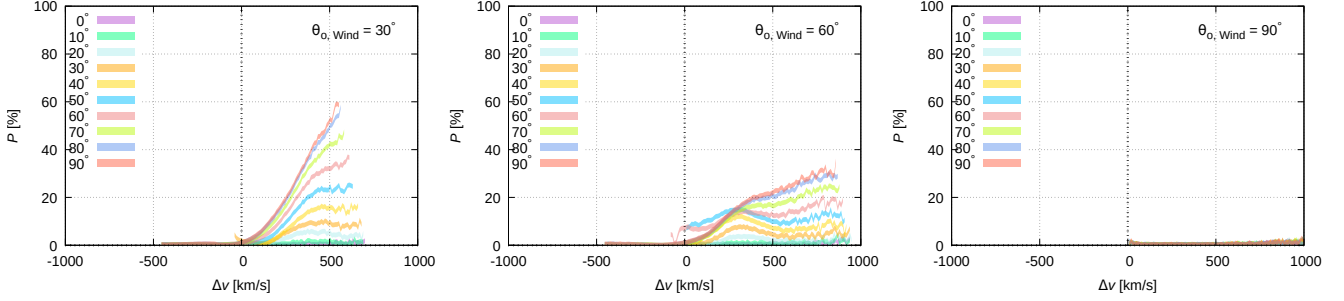


Figure 6.5: The degree of polarization P for models with θ_{LOS} from 0° to 90° , with steps of 10° . Given its low significance, we do not display the degree of polarization when the flux in the simulated intensity spectrum is smaller than 5% of the peak flux of the Ly α line. The left, middle, and right panels show the results for $\theta_{\text{o,Wind}} = 30^\circ$, 60° , and 90° , respectively. The overall degree of polarization increases with increasing θ_{LOS} and decreasing $\theta_{\text{o,Wind}}$.

Eide et al. 2018). Thus, to explore polarized Ly α , we adopt a new asymmetric model using the radiative transfer code *RT-scat* (Chang et al. 2023; Chang & Gronke 2024). We describe the geometry of our wind model and the resulting Ly α spectrum in Section 6.4.1 and polarization in Section 6.4.2. We extensively compare observations and models in Section 6.4.3.

6.4.1 Ly α spectrum in the wind model

Our new model is composed of a bipolar wind and a point Ly α source. We show a schematic illustration of the model in Fig. 6.3. The wind model is characterized by four main parameters: the H I column density, N_{HI} , the expansion velocity, v_{exp} , the half opening angle of the bipolar wind, $\theta_{\text{o,Wind}}$, and the width of intrinsic Ly α , σ_{Src} . The bipolar wind outflows expand radially with a constant velocity v_{exp} , similar to the shell model. The wind's H I number density is constant, and its inner radius is fixed to 10% of the outer radius. We adopt this geometry as the bipolar wind is intended to represent the outflows outside of the galaxy, and thus extending in the simulations from ~ 10 kpc to ~ 100 kpc. In our model we assumed that there is no H I outside the wind outflows, although some H I from inflowing gas or satellites might be present. Given that different H I properties can have opposite effects on the resulting polarization and that we do not have any evidence to constrain these properties, we excluded the presence of additional H I outside the wind outflows, leaving it for future spatially resolved studies (see the discussion in Section 6.5.2). The central source emits Ly α with a Gaussian profile with a width of σ_{Src} . This assumption is chosen as it represents the most general case, and is supported by the observational evidence that there is no dust in the galaxy (both from the study of optical lines in Iani et al. 2021 and from ALMA observations in Zanella et al. 2024), that could suppress or modify the Ly α shape (Laursen et al. 2009). Additionally, we consider the angle of the line of sight θ_{LOS} , the azimuthal angle from the $+z$ -axis, as the bipolar wind is symmetric about the z -axis. In the simulations, we consider 10^6 photons and extract the escaping Ly α spectrum for various θ_{LOS} .

In our new model we assumed a simplified geometry as it allows us to focus on the physical processes that originate polarization. This approach is analogous to that commonly employed to analyze the spectra, where the shell model is usually adopted as the standard model and, even if it does not reflect reality and can be affected by many degeneracies (e.g., Gronke et al. 2016; Li & Gronke 2022), it can help us to decrypt the information in the Ly α line. Currently,

there is not a similar standard in the joint study of polarization and spectra together, and we decided to adopt the bipolar wind model as it allows us to explore a large variety of scenarios in a well-motivated physical frame.

Fig. 6.4 shows the observed $I(\lambda)$ spectrum around the Ly α line, the simulated spectrum from the shell model, and the simulated spectra of the wind model. Iani et al. (2021) estimated the physical properties of the shell model ($N_{\text{HI}} \sim 10^{20} \text{ cm}^{-2}$, $v_{\text{exp}} \sim 200 \text{ km s}^{-1}$, and $\sigma_{\text{Src}} \sim 100 \text{ km s}^{-1}$), that we adopted as the starting point of our wind model. We found that all the simulated spectra of the wind model for different $\theta_{\text{o,Wind}}$ values (e.g., we show $\theta_{\text{o,Wind}} = 30^\circ$, 60° , and 75° in the left panel of Fig. 6.4) do not match the observed spectrum, especially near the red peak of the Ly α . This is because scattered photons escape outside the outflow opening angle, in the equatorial direction, unlike in the shell model.

To address this discrepancy, we assumed a broader intrinsic Ly α ($\sigma_{\text{Src}} = 150 \text{ km s}^{-1}$) to better reproduce the observations. This wider intrinsic spectrum can stem from radiative transfer effects within the inner ISM (e.g., Gronke et al. 2018). With this assumption, simulated spectra for $\theta_{\text{o,Wind}} = 60^\circ$ and 75° are similar to those of the previous shell modeling and to the observations, as can be seen in the middle panel of Fig. 6.4.

The right panel of Fig. 6.4 shows the simulated spectra for three θ_{LOS} at $\theta_{\text{o,Wind}} = 60^\circ$. The spectra at $\theta_{\text{LOS}} = 0^\circ$ and 40° match the observed spectrum well. On the contrary, the spectrum at $\theta_{\text{LOS}} = 90^\circ$ does not resemble the observed spectrum and has enhanced flux in the vicinity of the systemic velocity. In the case of a large θ_{LOS} , as this one, intrinsic photons are observed directly, without scattering, resulting in a central peak and enhanced red wing in the simulated spectrum. In summary, to reproduce the red peak and the suppressed blue peak of the observed Ly α , we need a larger $\sigma_{\text{Src}} = 150 \text{ km s}^{-1}$ and θ_{LOS} to be smaller than $\theta_{\text{o,Wind}}$. The larger σ_{Src} allows Ly α photons to be emitted over a wider velocity range, broadening the red peak, while the smaller θ_{LOS} ensures that most intrinsic photons undergo scattering within the wind cone, suppressing the blue Ly α peak emission.

6.4.2 Polarization of Ly α in the wind model

Dijkstra & Loeb (2008) showed that different models, that assume different production mechanisms of the Ly α photons and different geometries of the gas surrounding the emitting source, give rise to different polarization levels. For an individual Ly α photon, we expect to detect no polarization if the entire nebula is photoionized, and if it does not experience subsequent scattering. On the contrary, if the Ly α photon is produced in the inner parts of the nebula and then escapes it through scattering, it would be polarized.

From an observational point of view, we detect the signal from an ensemble of photons and not from individual ones, hence the main factor influencing the detected polarization is the geometry of the scattering medium and the presence of a preferential polarization direction, as the signal from highly polarized individual photons may result in an average not polarized signal if their polarization angles are not aligned. Thus, to understand the polarization behavior of scattered Ly α , two fundamental mechanisms to develop polarization are important.

First, the polarization of the integrated Ly α strongly depends on the symmetry of the scattering geometry (Eide et al. 2018). Thus, in Fig. 6.5, at $\theta_{\text{LOS}} = 0^\circ$, the total degree of polarization P becomes zero due to symmetry, regardless of $\theta_{\text{o,Wind}}$. Similarly, in the right panel, the total P at $\theta_{\text{o,Wind}} = 90^\circ$ is zero for any line of sight. The overall P at $\theta_{\text{LOS}} = 0^\circ$ and those at $\theta_{\text{o,Wind}} = 90^\circ$ are approximately zero. Additionally, as $\theta_{\text{o,Wind}}$ increases, the simulated Ly α halo becomes

Table 6.1: Values of the parameters describing the bipolar wind model adopted in our simulations.

Param.	Adopted values	Description
N_{HI}	10^{20} cm^{-2}	H I column density
v_{exp}	200 km s^{-1}	Wind expansion velocity
σ_{Src}	150 km s^{-1}	Width of intrinsic Ly α
$\theta_{\text{o,Wind}}$	$0^\circ, 15^\circ, 30^\circ, 45^\circ, 60^\circ, 75^\circ, 90^\circ$	Bipolar wind opening angle
θ_{LOS}	$0^\circ, 10^\circ, 20^\circ, 30^\circ, 40^\circ, 50^\circ, 60^\circ, 70^\circ, 80^\circ, 90^\circ$	Line of sight angle

Notes. We fix the values of N_{HI} , v_{exp} , and σ_{Src} (see the main text), while explored different possibilities for $\theta_{\text{o,Wind}}$ and θ_{LOS} , where $\theta_{\text{LOS}} = 0^\circ$ means observing in the direction of the outflow.

more symmetric, leading to a decrease in P (panels from left to right in Fig. 6.5).

Second, the degree of polarization P of scattered photons increases when the scattering angle, defined as the angle between the incident and scattered directions, approaches 90° (e.g., [Chandrasekhar 1960](#); [Chang et al. 2017](#); [Seon et al. 2022](#)). Scattering at angles close to 0° (forward scattering) or 180° (backward scattering) causes the P of the scattered photon to be identical to that of the incident photon. Based on this mechanism, when θ_{LOS} is close to 90° , the fraction of photons undergoing perpendicular scattering increases, leading to a higher P . This behavior is evident in the left and middle panels of Fig. 6.5, where the overall P increases with increasing θ_{LOS} . As a result, P decreases with increasing $\theta_{\text{o,Wind}}$ and decreasing θ_{LOS} , making the information on geometrical properties of the H I medium imprinted in the polarization of the Ly α line.

6.4.3 Comparing observations and models

We compared our observations of Abell 2895a with the simulated results by using both their total intensity spectra $I(\lambda)$, and the polarization fraction of the Ly α , $P_{\text{Ly}\alpha}$. To properly compare the $I(\lambda)$, we convolved those from simulations with a Gaussian function, to take into account the instrumental spectral resolution of ~ 3.6 ($R \sim 1500$). We adopted the following physical properties of the wind model (also summarized in Table 6.1): $N_{\text{HI}} = 10^{20} \text{ cm}^{-2}$, $v_{\text{exp}} = 200 \text{ km s}^{-1}$, and $\sigma_{\text{Src}} = 150 \text{ km s}^{-1}$. We considered a large variety of geometries for the modeled biconical outflows, varying the wind opening angles $\theta_{\text{o,Wind}}$ from 0° to 90° with steps of 15° and the line of sight angles θ_{LOS} from 0° to 90° with steps of 10° . We evaluated the goodness of the matching of their total intensities I by adopting a reduced χ^2_ν metric over $N = 136$ wavelength elements around the Ly α emission line, defined as

$$\chi^2_\nu = \frac{1}{N} \sum_{\lambda=1206}^{1225} \left[\frac{I(\lambda) - I_{\text{model}}(\lambda)}{\sigma_I(\lambda)} \right]^2, \quad (6.3)$$

where $I(\lambda)$, $\sigma_I(\lambda)$, and $I_{\text{model}}(\lambda)$ are, respectively, the observed, its uncertainty, and the modeled normalized total intensity spectra. Thus, models with lower χ^2_ν values were preferred, as they indicate that the observed and modeled spectra are more in agreement. We remark that, given that the flux measurements are correlated between several pixels, the χ^2_ν values must not be interpreted in an absolute way, but rather qualitatively. We decided to adopt this metric because it can offer a straightforward and clear visualization of the goodness of the agreement, and allows one to directly compare different models, and evaluate those ruled out by $I(\lambda)$.

The observed Ly α shows an asymmetric profile that is redshifted with a relative velocity $\Delta v = 403 \pm 4 \text{ km s}^{-1}$ with respect to the systemic redshift ([Iani et al. 2021](#)), as it is typical for outflows.

In Fig. 6.6, we compared observed data and simulated results from the wind models for various θ_{LOS} and $\theta_{\text{o,Wind}}$. As we discussed in Section 6.4.1, only the models with $\theta_{\text{LOS}} < \theta_{\text{o,Wind}}$ are able to reproduce these spectral features (see the top panels of Fig. 6.6). At $\theta_{\text{LOS}} > \theta_{\text{o,Wind}}$, the peak of the simulated spectrum is centered on $\Delta v = 0 \text{ km s}^{-1}$, due to directly escaping photons from the central source. However, at $\theta_{\text{o,Wind}} \leq 15^\circ$, even if $\theta_{\text{LOS}} < \theta_{\text{o,Wind}}$, the spectrum does not reproduce the observed red wing since a small $\theta_{\text{o,Wind}}$ induces less scattering.

The cases with $\theta_{\text{o,Wind}} = 45^\circ$ and 60° are those better representing the observations, for $\theta_{\text{LOS}} < \theta_{\text{o,Wind}}$, and have the lowest χ^2_ν values. They present an asymmetric profile and can well reproduce the observed red tail, in particular for $\theta_{\text{LOS}} \lesssim 40^\circ$. The case with $\theta_{\text{o,Wind}} = 30^\circ$ (75°) has a slightly larger χ^2_ν value, because the peak is less (more) redshifted than the observations, but consistent within 1σ . The trend continues to the $\theta_{\text{o,Wind}} = 90^\circ$ case, that is the one resembling the expanding ellipsoid geometry of the gas, only marginally consistent with the observed total intensity spectrum. The observed and modeled $I(\lambda)$ spectra for all the models can be seen in the top panels of Fig. 6.6, while their χ^2_ν values are shown in Fig. 6.7 in the greyscale, where lighter tones represent better agreement.

We binned the degree of polarization from the models with the same binning adopted for the observations, and considered the polarization of the bin including the observed Ly α peak, from 1215.5 Å to 1219.6 Å. Given that we only had upper limits on $P_{\text{Ly}\alpha}$ from the observations, we considered as consistent those models whose Ly α polarization fraction, within 1σ , is lower than the observational upper limit. We show the $P_{\text{Ly}\alpha}$ from the models and from the observations in the bottom row of Fig. 6.6. As discussed in Section 6.4.2, the low $P_{\text{Ly}\alpha}$ value suggests that the observed system is fairly symmetric, and thus the perfectly symmetric $\theta_{\text{o,Wind}} = 0^\circ$ and 90° cases with $P_{\text{Ly}\alpha} \simeq 0$ are fully consistent with observations. The case with $\theta_{\text{o,Wind}} = 15^\circ$ (30°) presents a $P_{\text{Ly}\alpha}$ value that increases with θ_{LOS} , always consistent (consistent for $\theta_{\text{LOS}} < 60^\circ$) with the observational constraint. In the cases with $\theta_{\text{o,Wind}} = 45^\circ$, 60° , and 75° , the binned $P_{\text{Ly}\alpha}$ values do not increase with increasing θ_{LOS} , due to the non-vanishing polarization close to the systemic redshift ($\Delta v \approx 0$), that can be seen also in the center panel of Fig. 6.5 (in particular for the $\theta_{\text{LOS}} = 50^\circ$ and 60° curves). It results in larger degrees of polarization, that can exceed the observational upper limit for the models with $\theta_{\text{o,Wind}} \sim \theta_{\text{LOS}}$. The models ruled out by the observational constraints (at the 1σ level) on the polarization are in hatched red in Fig. 6.7. We highlight that the $I(\lambda)$ and $P_{\text{Ly}\alpha}$ constraints rule out complementary regions in the $\theta_{\text{LOS}}\text{-}\theta_{\text{o,Wind}}$ plane, proving the effectiveness of combining these different tracers to investigate the geometry of the scattering H I gas around star-forming galaxies at high redshift and the mechanism of production of the Ly α photons.

6.5 Discussion

6.5.1 Origin mechanisms of the Ly α

As introduced in Section 6.4.2, there are two main mechanisms that originate the Ly α photons that we observe from distant sources. The first, usually referred to as “in situ”, includes both the recombination (in photo-ionized gas) and collisional excitation scenarios. Recombination happens when an electron is captured by a proton, resulting in a hydrogen atom in an excited state that can eventually decay to the ground state, emitting Ly α (Haiman & Rees 2001; Cantalupo et al. 2005; Arrigoni Battaia et al. 2019). The probability of emitting Ly α mainly depends on the temperature and density of the medium and, in the usually adopted B-case recombination regime, the probability is as large as approximately 68% at $T = 10^4$ K (e.g.,

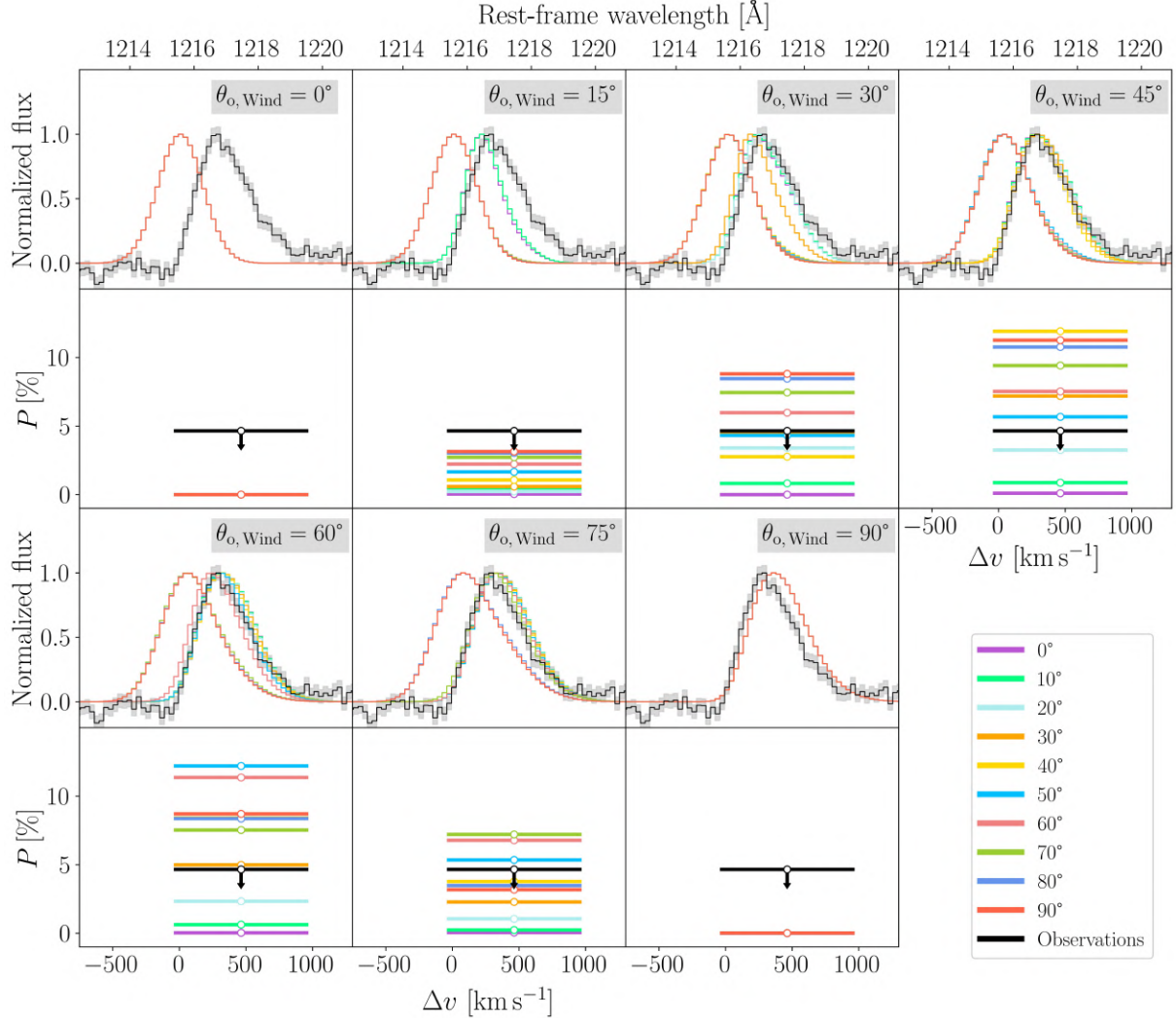


Figure 6.6: Top and third rows: observed (black, with 1σ uncertainties in grey) and modeled (with different colors denoting different line-of-sight angles, θ_{LOS} , reported in the legend) normalized total intensity spectra I , assuming a H I column density N_{HI} of 10^{20} cm^{-2} , an outflow velocity v_{exp} of 200 km s^{-1} , and a Gaussian width of intrinsic Ly α σ_{Src} of 150 km s^{-1} , in the case of $\theta_{\text{o, Wind}} = 0^\circ, 15^\circ, 30^\circ, 45^\circ, 60^\circ, 75^\circ, 90^\circ$, from left to right, as indicated in the grey labels. Second and bottom rows: Polarization fraction relative to the model described in the corresponding row above. The black open circles represent the observational 1σ upper limit of $P_{\text{Ly}\alpha} = 4.6\%$. The uncertainties for the models are smaller than the linewidths.

Dijkstra 2014), also explaining why the Ly α is the intrinsically stronger emission line in star-forming galaxies. The collisional process involves instead an electron and a hydrogen atom, that is left in an excited state after the close encounter. This process converts thermal energy of the electrons into radiation, and is thus also called “Ly α emission by cooling radiation”. The second mechanism is related to the scattering, as the Ly α photons that are created by a central source (e.g., a star-forming galaxy or AGN), can then escape the production site after numerous scatters in the surrounding H I cloud (Hayes et al. 2011; Beck et al. 2016), causing them to propagate far from their production site. Likely these two mechanisms act simultaneously (e.g., Kim et al. 2020). Polarization can be detected in the photoionization case, if enough neutral

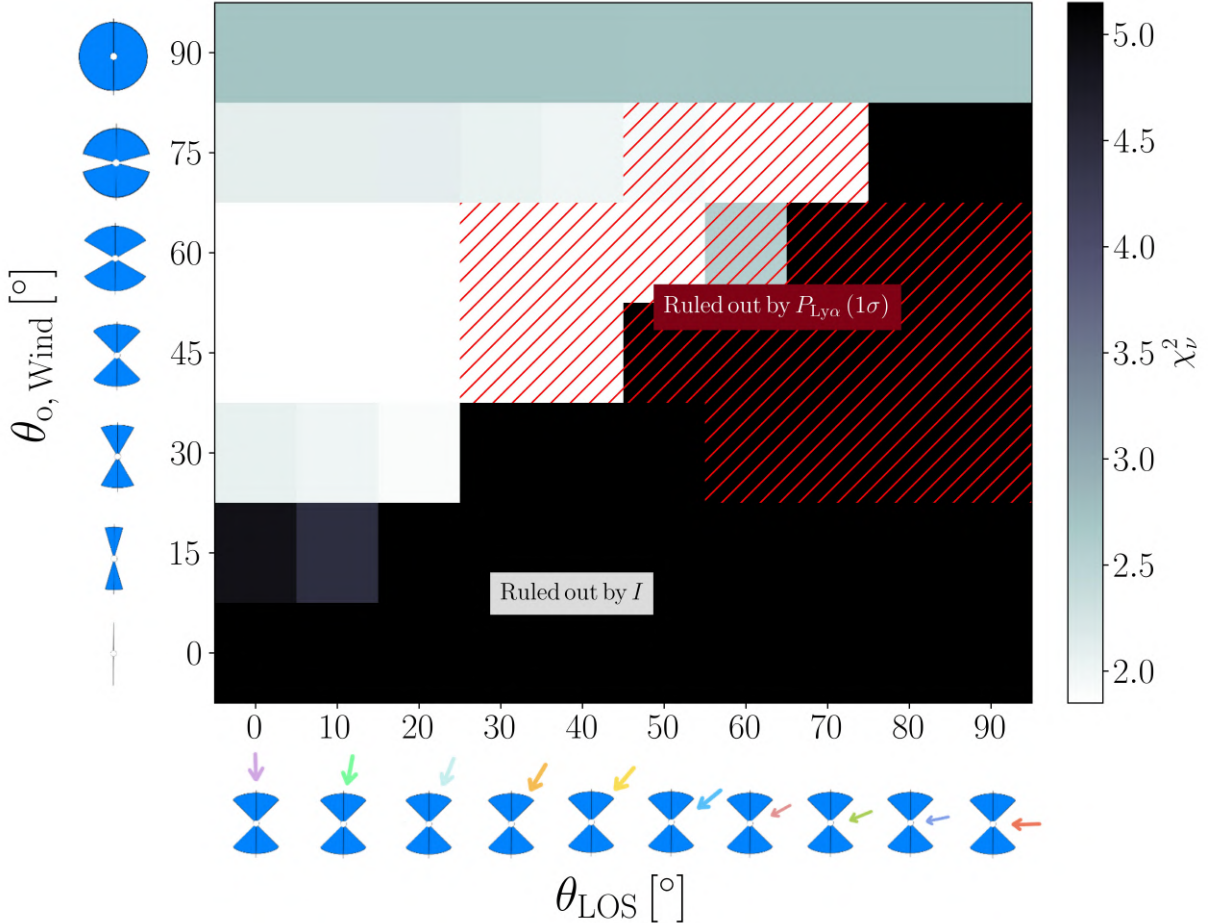


Figure 6.7: Comparison between observations and wind models at $N_{\text{HI}} = 10^{20} \text{ cm}^{-2}$, $v_{\text{exp}} = 200 \text{ km s}^{-1}$, $\sigma_{\text{Src}} = 150 \text{ km s}^{-1}$. The sketches along the axes give a visual representation of the models, with increasing $\theta_{\text{o},\text{Wind}}$ along the y -axis and increasing θ_{LOS} along the x -axis, represented with arrows colored according to Fig. 6.6. The grey scale indicates the agreement between the observed and modeled total intensities I , evaluated through the χ^2_ν value (colorbar on the right), with lighter tones representing better agreement (see the top row of Fig. 6.6). Red hatched regions rule out models whose degree of polarization $P_{\text{Ly}\alpha}$ is larger than (and thus not consistent with) the observational 1σ upper limit $P_{\text{Ly}\alpha}$ (see the bottom row of Fig. 6.6).

hydrogen is present in extended regions, producing a considerable scattering probability. We can thus conclude that, if the Ly α is polarized, there is photon scattering, while if the Ly α is not (or low) polarized, there is no scattering or the gas has a specific geometry.

The Ly α intensity spectrum of Abell 2895a requires a scattering contribution to explain the asymmetric profile and the redshifted peak of the line with respect to the systemic redshift. On the other hand, the low polarization upper limit, $P_{\text{Ly}\alpha}$, is also consistent with photoionization only and no scatter, or with scatter in a fairly symmetric medium that, given the lack of a preferential scattering direction, would result in a measured low polarization signal, even if the individual photons might be highly polarized. For example, as described in Section 6.4.3 for Abell 2895a, centrally emitted photons that experience scattering can give rise to an integrated $P_{\text{Ly}\alpha} \sim 0$, consistent mostly with the large $\theta_{\text{o},\text{Wind}}$ and low θ_{LOS} cases, that are the most

symmetric ones. Deep spatially resolved polarization observations, that we discuss in the next section, are needed to reconstruct in detail the production site of Ly α photons and the geometry of the scattering medium, allowing us to disentangle between the different possible production mechanisms of the Ly α .

6.5.2 Spatially resolved observations and future perspectives

Scattering of Ly α photons through a geometrically asymmetric medium give rise to polarized signal (Angel 1969; Lee & Ahn 1998), detectable also without resolving the system (Eide et al. 2018), as we described in Sections 6.3 and 6.4 for Abell 2895a. However, as discussed in Section 6.5.1, this leaves the question about the origin of the Ly α photons (and thus the region from where they are emitted) and the geometry and orientation of the scattering medium. This degeneracy can be broken by learning the geometry of the galaxy from other independent probes, or by using spatially resolved and deeper spectropolarimetric observations. Spatially resolved observations can put constraints on the polarization over different regions that we can compare with models predicting different degrees of polarization ranging, for example in a biconical wind geometry, from $P_{\text{Ly}\alpha} \sim 0\%$ in the center to $P_{\text{Ly}\alpha}$ up to 80% in the outflows (Eide et al. 2018). Additionally, deeper observations can help putting tighter constrains to the measured polarization levels, and achieving observational S/N high enough to measure also the polarization angle, that is predicted to significantly change between different models, giving hints on, for example, the direction of the outflow in a biconical wind geometry (Eide et al. 2018).

Currently, Abell 2895a is the only distant star-forming galaxy with Ly α spectropolarimetric observations. The main reasons for the lack of such observations are the typical low luminosity of high- z star-forming galaxies and the fact that the light beam has to be split in two components (its o and e components, with orthogonal polarizations) and rotated, significantly increasing the observational exposure time necessary to reach sufficient S/N values, even with the most advanced spectropolarimeters mounted on cutting-edge telescopes. This issue can be mitigated by observing galaxies at $z \sim 2 - 4$ (with redshifted Ly α line included in the instrument's wavelength coverage) that are strongly lensed (i.e., magnified and distorted) with a large magnification factor ($\mu \gtrsim 10$), that would sensibly lower the needed exposure time. The observation of the most magnified and distorted sources lying across the lensing critical lines would allow us to zoom-in and study the spatial variation of the polarization across the Ly α emission on sub-kpc scales and put more stringent limits to the origin of the Ly α emission and the scattering H I geometry. Additionally, extending such observations to a small sample of galaxies will also allow us to put the results obtained for Abell 2895a in a broader context.

6.5.3 Polarization of other resonant lines

In principle, the study presented in this chapter can be executed by employing different resonant line emissions than the Ly α , like the Mg II, C IV, O VI, N V, Si IV doublets, commonly used in astrophysics (e.g., Prochaska et al. 2011; Hayes et al. 2016; Henry et al. 2018; Berg et al. 2019; Katz et al. 2022; Dutta et al. 2023). The scattering processes of such resonance doublets are very similar to those of the Ly α line, because they present similar atomic properties with one electron in the outer orbit and have the same atomic structure composed of two transitions, called “K” ($S_{1/2} - P_{3/2}$) and “H” ($S_{1/2} - P_{1/2}$). Due to their resonance nature, metal resonance doublets are also spatially extended and polarized via scattering. The inclusion of such lines would allow us to expand the usable redshift range (atomic line center wavelengths from ~ 1032 for the O VI to ~ 2800 for the Mg II) and to explore the multi-phase nature of the CGM, exploring

gas temperatures from 10^{3-4} K (ionization energies of 13.6 eV for the Ly α and 15 eV for the Mg II) to 10^{5-6} K (138 eV of the O VI). Moreover, the two K and H transitions, that are not possible to observationally disentangle for the Ly α line, because of the small ionization difference of $\sim 10^{-4}$ eV $\approx 1.5 \text{ km s}^{-1}$, are resolved for other lines, like the Mg II (transition K at 2796.4 Å and H at 2803.5 Å, with a separation of 760 km s^{-1}) or the Si IV (K at 1393.8 Å and H at 1402.8 Å, with the largest separation of 1926 km s^{-1} between the above-mentioned resonant lines).

Recently, radiative transfer models that include the Mg II doublet have been developed, also including polarization (Seon 2023; Chang & Gronke 2024). In particular, Chang & Gronke (2024) considered three-dimensional shell, sphere, and clumpy sphere geometries, and studied the joint Ly α and Mg II escape using *RT-scat*. They reveal that, despite being driven by similar atomic processes, the emerging Mg II and Ly α spectra are very different, because of the different Mg II and H I column densities, with $N_{\text{H}_1} \gg N_{\text{MgII}}$. Moreover, they confirmed a correlation between the escape of LyC radiation and the Mg II doublet ratio, the ratio of the K and H lines (also see, Henry et al. 2018; Chisholm et al. 2020; Izotov et al. 2022; Katz et al. 2022; Xu et al. 2023). They also found that the Mg II degree of polarization decreases with increasing column density N_{MgII} , because the multiple scatterings without a preferential direction decrease the resulting polarization. This results in a low (< 5%) degree of polarization in the center, growing up to 10% (25%) with $N_{\text{MgII}} = 10^{14} \text{ cm}^{-2}$ ($N_{\text{MgII}} = 10^{13} \text{ cm}^{-2}$). Consequently, they suggested that the Mg II polarization can be used to estimate the doublet ratio of the extended halo. Unfortunately, the Mg II emission is much fainter than the Ly α , making it challenging to resolve and measure its degree of polarization, and requiring extremely large amount of observational time, especially at high redshift. Again, strongly lensed candidates would allow us to obtain spatially extended and spectropolarimetric observations and to pursue this kind of studies.

6.6 Summary and conclusions

In this chapter we put novel constraints on the geometry of the H I region surrounding a clumpy star-forming galaxy at $z \approx 3.4$, Abell 2895a (Livermore et al. 2015; Iani et al. 2021; Zanella et al. 2024), strongly lensed into three multiple images by the cluster of galaxies Abell 2895. We made use of new VLT/FORS2 observations taken with the Polarimetric Multi Object Spectroscopy (PMOS) mode to extract the spectra relative to the ordinary (o) and extraordinary (e) beams in four different half-wave plate angles, from an aperture including the M1 and M2 multiple images of Abell 2895a. We combined the different spectra to measure the total intensity 1D spectrum, $I(\lambda)$. We focused on the Ly α emission line, and we computed the Stokes parameters q and u , used to measure the polarization fraction $P_{\text{Ly}\alpha}$, corrected both for the positive bias of polarization and for the dilution effect due to the contamination of the angularly close, unpolarized, BCG of the Abell 2895 cluster. We obtained $P_{\text{Ly}\alpha}$ upper limits of 4.6%, 5.8%, and 6.5% at the 1σ , 2σ , and 3σ level. We showed that polarization constraints are complementary to those usually achieved by using only the total Ly α intensity and line profile, demonstrating the effectiveness of this novel technique.

To interpret the observational constraints, we developed a Ly α radiative transfer model including a bipolar wind geometry (characterized by the half opening angle $\theta_{\text{o, Wind}}$, the radial expansion velocity v_{exp} , and the H I column density N_{H_1} parameters) and a central source that emits Ly α photons with a Gaussian profile with a width of σ_{Src} . We assumed $N_{\text{H}_1} \sim 10^{20} \text{ cm}^{-2}$, $v_{\text{exp}} \sim 200 \text{ km s}^{-1}$, and $\sigma_{\text{Src}} \sim 150 \text{ km s}^{-1}$ and tried different $\theta_{\text{o, Wind}}$ values (from 0° to 90° with steps of 15°) and simulated different line of sight angles (θ_{LOS} from 0° to 90° with steps of 10°).

In order to reproduce the spectral profile and shift with respect to the systemic velocity of the Ly α line, we needed Ly α photons that are created in the inner regions and that undergo several scattering events before escaping, and $\theta_{\text{LOS}} < \theta_{\text{o, Wind}}$ and $\theta_{\text{o, Wind}} > 15^\circ$. Models with $\theta_{\text{o, Wind}}$ of 45° , 60° , or 75° with θ_{LOS} of $30^\circ - 60^\circ$ can well reproduce the Ly α spectral profile, but the combination of $\theta_{\text{o, Wind}}$ and θ_{LOS} resulting in an asymmetric geometry and the scattering due to the larger $\theta_{\text{o, Wind}}$, make the predicted polarization much larger than the low observed $P_{\text{Ly}\alpha}$, that is consistent with no scattering or with scattering in a fairly symmetric medium, and thus are excluded.

Summarizing, the models that satisfy both the Ly α spectral profile and polarization requirements are those with $\theta_{\text{o, Wind}} \sim 30^\circ$ for $\theta_{\text{LOS}} \leq 20^\circ$, $\theta_{\text{o, Wind}} \sim 45^\circ$ for $\theta_{\text{LOS}} \leq 20^\circ$, $\theta_{\text{o, Wind}} \sim 60^\circ$ for $\theta_{\text{LOS}} \leq 20^\circ$, $\theta_{\text{o, Wind}} \sim 75^\circ$ for $\theta_{\text{LOS}} \leq 40^\circ$, and $\theta_{\text{o, Wind}} \sim 90^\circ$ for any θ_{LOS} , where $\theta_{\text{LOS}} = 0^\circ$ means observing in the direction of the outflow. These results will pave the way to future spatially resolved spectropolarimetric observations, needed to discriminate between the different production mechanisms of the Ly α and the geometry of the scattering medium.

Conclusions and future prospects

I have summarized and described extensively the conclusions at the end of each chapter, in Sections 3.6, 4.7, 5.6, and 6.6. Here, I come back to the main questions drawn in Section 1.5, summarizing the main findings.

Chapter 3: How well can we measure the total mass cumulative profiles of extremely massive early-type galaxies that act as lenses at intermediate redshift, and how are their baryonic and dark matter components distributed? How can we reconstruct and characterize the background sources, thanks to spatially-extended strong lensing modeling?

I measured the total mass profile of SDSS J0100 with a 1% accuracy ($(1.16 \pm 0.01) \times 10^{13} M_{\odot}$) within the Einstein radius, assuming the background sources as point-like. I confirmed the results with the extended source modeling. In this case, thanks to the large number of observables, the statistical errors are further reduced by a factor of approximately 10, and the systematic uncertainties dominate. I also measured the stellar-over-total mass fraction profile, finding it to be $(38 \pm 9)\%$ at the lens galaxy effective radius, decreasing to $(12 \pm 2)\%$ at $R = 42$ kpc. In this case, the dominating uncertainties are from the stellar mass profile, that is obtained by combining the light profile and the total stellar mass from SED fitting. I reconstructed the surface brightness distributions of the background sources and measured their half-light radii, resulting in effective radii between 0.5 and 1 kpc at $z = 1.880$ for the A and B components depending on the adopted model. I have found that the sizes of the reconstructed sources can vary by a factor of about 2, if different models that can reasonably well fit the data are assumed, but I remark that our preferred models, with the lowest χ^2 , produced consistent results. The measured sizes are consistent with those of strongly lensed clumps in star-forming galaxies at $z \sim 1-3$.

Chapter 4: How can we develop an enhanced strong lensing model thanks to new MUSE data? What constraints can we put from such models to the values of the cosmological parameters? What is the impact on such values of multi-plane lensing, where additional deflection planes are introduced?

I refer to Section 4.6.1 for a detailed description of how I enhanced the SDSS J0100 strong lensing model thanks to new MUSE data, with the spectroscopic confirmation of C, the discovery of E and F, and the inclusion in the model of 19 group members, to complement the group-scale extended halo. One of the main improvements is the possible characterization of the cosmological parameters. In particular, I measured $\Omega_m = 0.14_{-0.09}^{+0.16}$ in a flat Λ cold dark matter (CDM) model, and $\Omega_m = 0.19_{-0.10}^{+0.17}$ and $w = -1.27_{-0.48}^{+0.43}$ in a flat w CDM model. Moreover, given the

presence of different sources angularly close in projection, I quantified through a multi-plane approach their impact on the inferred values of the cosmological parameters. I obtained consistent median values, with uncertainties for only Ω_m increasing by approximately a factor of 1.5. In conclusion, I found that such systems can give cosmological constraints similar to those obtained from individual typical clusters of galaxies, showing that the lower number of multiple images is balanced by the simpler total mass distribution. Group-scale systems that act as lenses for $\gtrsim 3$ background sources at different redshifts will represent a valuable cosmological probe in the future, when we expect to discover tens of them.

Chapter 5: What is the distribution of UV-continuum β slopes of the individual clumps we observe in high- z galaxies, and how does it evolve with the UV magnitude and the redshift? How can we reproduce and interpret the extremely slopes ($\beta \lesssim -2.7$) we observe?

I found a median value of $\beta \sim -2.4$ for the sample of clumps, lower than that of integrated galaxies ($\beta \sim -2$). This result confirms that clumps are sites of intense star formation, populated by young, massive stars, whose spectrum strongly emits in the UV. This is also consistent with the assumption that the dust extinction at the location of the clumps is lower than the average extinction of the galaxy, or that clumps have a different initial mass function (IMF) or star-formation history (SFH). I made use of the correlations, discovered for high- z galaxies, of the β value with those of redshift and UV magnitude, M_{UV} , finding that clumps follow the same relations, extended to much fainter magnitudes ($M_{\text{UV}} < -13$). I also found evidence of eight clumps with extremely blue ($\beta \lesssim -2.7$) slopes, that I was able to reproduce (down to $\beta \sim 3.2$) as extremely low-metallicity ($Z \lesssim 10^{-3}$), young ($\log(\text{age}/\text{yr}) \lesssim 7$) and dust-poor regions, considering the absence of the nebular emission, whose presence would not allow us to reach so blue slopes, reddening them typically by $\Delta\beta \sim 0.5$.

Chapter 6: What is the origin of the (resonant) Ly α emission in a typical clumpy star-forming galaxy at high- z ? How can we use Ly α polarization to constrain between different models, that assume different physical properties of the scattering medium and its geometry?

I measured a Ly α degree of polarization 1σ upper limit of 4.6%. Such low polarization upper limit is consistent with photoionization only and no scatter, or with scatter in a fairly symmetric medium that, given the lack of a preferential scattering direction, would result in a measured low polarization signal, even if the individual photons might be highly polarized. To investigate such geometry, I developed new Ly α radiative transfer models assuming a biconical outflow geometry aimed at reproducing the observations. I found that they can be explained by assuming the star-forming galaxy being embedded in a circum-galactic medium (CGM) with a biconical outflow geometry (with H I column density $N_{\text{HI}} = 10^{20} \text{ cm}^{-2}$, expansion velocity $v_{\text{exp}} = 200 \text{ km s}^{-1}$, and the width of intrinsic Ly α $\sigma_{\text{Src}} = 150 \text{ km s}^{-1}$, from the Ly α line spectral fitting) with an opening angle of the wind $\theta_{\text{o, Wind}} \sim 30^\circ$ for line-of-sight angles $\theta_{\text{LOS}} \leq 20^\circ$, $\theta_{\text{o, Wind}} \sim 45^\circ$ for $\theta_{\text{LOS}} \leq 20^\circ$, $\theta_{\text{o, Wind}} \sim 60^\circ$ for $\theta_{\text{LOS}} \leq 20^\circ$, and $\theta_{\text{o, Wind}} \sim 75^\circ$ for $\theta_{\text{LOS}} \leq 40^\circ$, where $\theta_{\text{LOS}} = 0^\circ$ means observing in the direction of the outflow.

For each of the described projects, I plan to further investigate, and answer some other open questions. The work presented in Chapter 4, that is itself an improvement of those presented in Chapter 3, can be enhanced with already available and future data. For instance, the kinematics of the BGG and of the brightest group members could be included to refine the strong lensing analysis, new models could be developed considering not only the point-like position but also

the extended structure of the multiple images, and the background sources could be further characterized, by using their morphology and kinematics. Moreover, the extended radial profile shown in Fig. 4.6 will allow us to develop a joint strong lensing and dynamics model, to better characterize the total mass distribution in the inner regions of the group. Additional new deep rest-frame infrared spectroscopic observations could allow us to measure the redshift of source D, making it the first group-scale system, dominated by a central BGG, with 6 lensed sources on 4 different redshift planes, and possibly discover other distant lensed line emitters, like E and F. Furthermore, deep X-ray observations could confirm the fossil nature of SDSS J0100+1818, and enable us to put constraints on the extended halo in which the group is immersed. A detailed study of SDSS J0100+1818 will pave the way to the characterization of tens of such rare galaxy and group scale systems that will be employed for cosmography and that will be discovered with new and upcoming facilities, like Euclid and Rubin-LSST. Finally, I discovered absorption lines (FeII and Mg II) in the spectra of AB, at the redshift of source C. By reconstructing the impact parameters of the AB rays on the plane of C, and estimating the elemental abundances from their equivalent widths for the four multiple images separately, it would be possible to reconstruct an abundance profile of FeII and Mg II of the source C.

Regarding the work presented in Chapter 5, the sample of individual clumps can be enhanced by including both other fields lensed by cluster of galaxies, and non-lensed galaxies. Moreover, it will allow us to improve the measured distributions by adding catalogs with similar depths and redshift ranges. Then, the redshift and the magnitude ranges can be enlarged thanks to infrared coverage of JWST, that will be able to measure β slopes with approximately $\sigma_\beta \sim 0.2$ uncertainty for $M_{UV} < -20$ at $z > 8$. Additionally, thanks to new NIRCam slitless spectroscopy data, it will be possible to investigate the spectral properties of clumps (e.g., emission line ratios giving information about reddening, ionization parameter, metallicity, SFR). Concerning the extremely blue slopes, an extension of the synthetic models explored and a broad-wavelength spectroscopic follow up with ground (e.g., VLT/X-Shooter) or space (i.e., JWST/NIRSpec) instruments of the bluest and brightest clumps represent essential steps in the study of the first galaxies and of the epoch of reionization. A first robust confirmation of galaxies, or isolated clumps, with uncommonly low metallicity or dust extinction values can reshape and deepen our comprehension on how galaxies were born, how they evolve, as well as the fate of their star-forming clumps.

Finally, regarding the results of Chapter 6, the main improvement is linked to the spatially resolved polarization measurements, described in Section 6.5.2. Studying Abell 2895a, I put constraints on the geometry of the scattering medium, finding it to be fairly symmetric, and thus, adopting a biconical outflow model, consistent with large opening angles of the outflows, or with small line-of-sight angles, i.e., observing it in the direction of the outflow. It was not possible to disentangle between them, and the different mechanisms that origin the Ly α photons, because of the non sufficient spatial resolution and S/N achieved. With the observation of arcs that are strongly lensed and distorted, I would be able to understand the origin of the Ly α emission through: 1) A spatially resolved analysis: simulations show that different regions have different polarization levels, from $\lesssim 10\%$ in the center up to 50–80% in the outflows (Eide et al. 2018). The tangential stretch would allow us to resolve structures that are just a fraction of arcsecond away on the source plane; 2) A spectrally resolved analysis: models predict that different geometries can have similar Ly α polarization fractions in the center, but significantly different in the tails. For example, both the expanding ellipsoid and the biconical outflow can reproduce low polarizations in the center, but then have different $\leq 15\%$ and up to 80%, respectively, polarizations in the blue and red tails (Eide et al. 2018). The large magnification factor provides a boost of the flux that allows us to reach a S/N sufficiently large to separate the flux from the tails and explore such differences.

Acknowledgements

I acknowledge the support from the University of Padova, the Istituto Nazionale di Astrofisica (INAF), and the European Southern Observatory (ESO).

I would like first to thank my PhD supervisor, Anita. Your energy and enthusiasm motivated me from the first day. You offered me several opportunities and responsibility that were decisive in achieving the results described in this thesis and in professionally growing up. You made my PhD a beautiful journey, thank you.

Secondly, I would like to thank my PhD co-supervisors. Once again, thank you Claudio for your guidance over the last years and for being an inspiration for me constantly. You have always represented an example to follow, and I owe you a large part of the scientist I am today.

Finally, thank you Joël for having me introduced with your passion to new and beautiful sides of astronomy. I really enjoyed and learned a lot in our long chats until late afternoon, where I could see your patience and dedication in making me understand.

To all three of you, I could not ask for anything better, thank you. I hope our academic and beyond collaborations are just at the beginning.

I would then like to thank all my collaborators, that made the work exposed in this thesis, and not only, possible. In particular, thank you Ana, Eros, Matteo, Pietro, Sherry, Uroš, Edoardo, Francesco, Gabriel, Giovanni, Piero, and Raoul. I really enjoyed working together and I hope these were just the first steps in a long path.

I would also like to express my gratitude to the many people I met during these years and with whom I shared a part of them.

To all my colleagues and friends in Padova, for welcoming me again and again after every period I had far from there. In particular, thank you Amelia, Biagio, Edoardo, Eric, and Irene, for your support, in different ways.

To the colleagues and friends met during my year at ESO, that made it so special. In particular, to Ellie, Adrien, Chiara, Josh, Ivanna, and Tommy, for our shared moments that I will always keep with me. To Nelma, because I was not used to having such a careful safe spot in an institute. To all my colleagues and friends in Milan and in the lensing group. In particular, to Ana, I lost count of how many times I felt supported and helped by you.

To some of my flatmates, and in particular Matti in Munich and Giulia in Padova, for the daily support. To Elizabeth, my friend from conferences, who seems like we have known for years.

I also acknowledge my old Ghiffa friends, we grew up together, and even if the PhD brought me a bit far, it is always as time never passed. And Antonello, with whom we finally manage to meet more often but always never enough.

A major thank to my parents, my first supporters to whom I owe a lot, and my sisters. You make me proud every day and fill my life with joy, even when I am far away.

Finally, to Alice. The PhD gave us the opportunity to meet again and I couldn't be luckier and more grateful. Thank you for making everything we have together so special.

The research described in this thesis is based on observations made with the NASA/ESA Hubble Space Telescope obtained from the Space Telescope Science Institute, which is operated by the Association of Universities for Research in Astronomy, Inc. It is also based on observations collected at the European Organization for Astronomical Research in the Southern Hemisphere under the ESO programs mentioned in each chapter, and on observations with the Nordic Optical Telescope, operated by the Nordic Optical Telescope Scientific Association at the Observatorio del Roque de los Muchachos, La Palma, Spain, of the Instituto de Astrofisica de Canarias.

I acknowledge the use of `numpy` ([Harris et al. 2020](#)), `matplotlib` ([Hunter 2007](#)), `astropy` ([Astropy Collaboration et al. 2022](#)), `pandas` ([pandas development team 2023](#)), `corner.py` ([Foreman-Mackey 2016](#)), and `CARTA` ([Comrie et al. 2021](#)).

Bibliography

- Abadi, M. G., Navarro, J. F., Fardal, M., Babul, A., & Steinmetz, M. 2010, Monthly Notices of the RAS, 407, 435
- Acebron, A., Grillo, C., Bergamini, P., et al. 2022, Astronomy and Astrophysics, 668, A142
- Acebron, A., Jullo, E., Limousin, M., et al. 2017, Monthly Notices of the RAS, 470, 1809
- Adamo, A., Bradley, L. D., Vanzella, E., et al. 2024, arXiv e-prints, arXiv:2401.03224
- Adams, T. F. 1972, Astrophysical Journal, 174, 439
- Aguerri, J. A. L. & Zarattini, S. 2021, Universe, 7, 132
- Ahn, S.-H. & Lee, H.-W. 2015, Journal of Korean Astronomical Society, 48, 195
- Ahn, S.-H., Lee, H.-W., & Lee, H. M. 2000, Journal of Korean Astronomical Society, 33, 29
- Ahn, S.-H., Lee, H.-W., & Lee, H. M. 2002, Astrophysical Journal, 567, 922
- Ahn, S.-H., Lee, H.-W., & Lee, H. M. 2003, Monthly Notices of the RAS, 340, 863
- Akaike, H. 1974, IEEE Transactions on Automatic Control, 19, 716
- Anderson, M. E., Bregman, J. N., & Dai, X. 2013, Astrophysical Journal, 762, 106
- Angel, J. R. P. 1969, Astrophysical Journal, 158, 219
- Annunziatella, M., Bonamigo, M., Grillo, C., et al. 2017, Astrophysical Journal, 851, 81
- Appenzeller, I., Fricke, K., Fürting, W., et al. 1998, The Messenger, 94, 1
- Arrigoni Battaia, F., Hennawi, J. F., Prochaska, J. X., et al. 2019, Monthly Notices of the RAS, 482, 3162
- Astropy Collaboration, Price-Whelan, A. M., Lim, P. L., et al. 2022, Astrophysical Journal, 935, 167
- Atek, H., Shuntov, M., Furtak, L. J., et al. 2022, arXiv e-prints, arXiv:2207.12338
- Auger, M. W., Treu, T., Bolton, A. S., et al. 2009, Astrophysical Journal, 705, 1099
- Auger, M. W., Treu, T., Bolton, A. S., et al. 2010, Astrophysical Journal, 724, 511

- Bacon, R., Accardo, M., Adjali, L., et al. 2010, in Society of Photo-Optical Instrumentation Engineers (SPIE) Conference Series, Vol. 7735, Ground-based and Airborne Instrumentation for Astronomy III, ed. I. S. McLean, S. K. Ramsay, & H. Takami, 773508
- Ballard, D. J., Enzi, W. J. R., Collett, T. E., Turner, H. C., & Smith, R. J. 2024, Monthly Notices of the RAS, 528, 7564
- Barkana, R. 1998, *Astrophysical Journal*, 502, 531
- Barnabè, M., Czoske, O., Koopmans, L. V. E., Treu, T., & Bolton, A. S. 2011, *Monthly Notices of the RAS*, 415, 2215
- Barnabè, M., Spiniello, C., Koopmans, L. V. E., et al. 2013, *Monthly Notices of the RAS*, 436, 253
- Bartelmann, M. 2003, arXiv e-prints, astro
- Bartelmann, M. 2010, *Classical and Quantum Gravity*, 27, 233001
- Bartelmann, M. & Schneider, P. 2001, *Physics Reports*, 340, 291
- Beck, M., Scarlata, C., Hayes, M., Dijkstra, M., & Jones, T. J. 2016, *Astrophysical Journal*, 818, 138
- Behrendt, M., Burkert, A., & Schartmann, M. 2016, *Astrophysical Journal Letters*, 819, L2
- Behrendt, M., Schartmann, M., & Burkert, A. 2019, *Monthly Notices of the RAS*, 488, 306
- Belokurov, V., Evans, N. W., Hewett, P. C., et al. 2009, *Monthly Notices of the RAS*, 392, 104
- Bender, R., Burstein, D., & Faber, S. M. 1992, *Astrophysical Journal*, 399, 462
- Benítez, N. 2000, *Astrophysical Journal*, 536, 571
- Berg, D. A., Chisholm, J., Erb, D. K., et al. 2019, *Astrophysical Journal Letters*, 878, L3
- Bergamini, P., Acebron, A., Grillo, C., et al. 2022, arXiv e-prints, arXiv:2207.09416
- Bergamini, P., Acebron, A., Grillo, C., et al. 2023a, *Astrophysical Journal*, 952, 84
- Bergamini, P., Grillo, C., Rosati, P., et al. 2023b, *Astronomy and Astrophysics*, 674, A79
- Bergamini, P., Rosati, P., Mercurio, A., et al. 2019, *Astronomy and Astrophysics*, 631, A130
- Bergamini, P., Rosati, P., Vanzella, E., et al. 2021, *Astronomy and Astrophysics*, 645, A140
- Bernardi, M., Sheth, R. K., Annis, J., et al. 2003, *Astronomical Journal*, 125, 1866
- Bertin, E. 2006, in *Astronomical Society of the Pacific Conference Series*, Vol. 351, *Astronomical Data Analysis Software and Systems XV*, ed. C. Gabriel, C. Arviset, D. Ponz, & S. Enrique, 112
- Bertin, E. 2010, SWarp: Resampling and Co-adding FITS Images Together
- Bertin, E. & Arnouts, S. 1996, *Astronomy and Astrophysics*, Supplement, 117, 393
- Bhatawdekar, R. & Conselice, C. J. 2021, *Astrophysical Journal*, 909, 144

- Birrer, S., Millon, M., Sluse, D., et al. 2024, *Space Science Reviews*, 220, 48
- Birrer, S., Treu, T., Rusu, C. E., et al. 2019, *Monthly Notices of the RAS*, 484, 4726
- Blaizot, J., Garel, T., Verhamme, A., et al. 2023, *Monthly Notices of the RAS*, 523, 3749
- Blandford, R. & Narayan, R. 1986a, *Astrophysical Journal*, 310, 568
- Blandford, R. & Narayan, R. 1986b, *Astrophysical Journal*, 310, 568
- Blumenthal, G. R., Faber, S. M., Flores, R., & Primack, J. R. 1986, *Astrophysical Journal*, 301, 27
- Bolamperti, A., Grillo, C., Cañameras, R., Suyu, S. H., & Christensen, L. 2023a, *Astronomy and Astrophysics*, 671, A60
- Bolamperti, A., Zanella, A., Meštrić, U., et al. 2023b, *Monthly Notices of the RAS*, 526, 5263
- Bonamigo, M., Grillo, C., Ettori, S., et al. 2018, *Astrophysical Journal*, 864, 98
- Boquien, M., Burgarella, D., Roehlly, Y., et al. 2019, *Astronomy and Astrophysics*, 622, A103
- Bournaud, F., Daddi, E., Elmegreen, B. G., et al. 2008, *Astronomy and Astrophysics*, 486, 741
- Bournaud, F., Daddi, E., Weiß, A., et al. 2015, *Astronomy and Astrophysics*, 575, A56
- Bournaud, F., Perret, V., Renaud, F., et al. 2014, *Astrophysical Journal*, 780, 57
- Bouwens, R. J., Aravena, M., Decarli, R., et al. 2016, *The Astrophysical Journal*, 833, 72
- Bouwens, R. J., Illingworth, G. D., Oesch, P. A., et al. 2012, *Astrophysical Journal*, 754, 83
- Bouwens, R. J., Illingworth, G. D., Oesch, P. A., et al. 2014, *Astrophysical Journal*, 793, 115
- Bouwens, R. J., Illingworth, G. D., Oesch, P. A., et al. 2015, *Astrophysical Journal*, 803, 34
- Bouwens, R. J., Illingworth, G. D., Oesch, P. A., et al. 2010, *Astrophysical Journal Letters*, 708, L69
- Bowler, R. A. A., McLure, R. J., Dunlop, J. S., et al. 2017, *Monthly Notices of the RAS*, 469, 448
- Bruzual, G. & Charlot, S. 2003, *Monthly Notices of the RAS*, 344, 1000
- Buck, T., Macciò, A. V., Obreja, A., et al. 2017, *Monthly Notices of the RAS*, 468, 3628
- Bunker, A. J., Saxena, A., Cameron, A. J., et al. 2023, *Astronomy and Astrophysics*, 677, A88
- Burgarella, D., Buat, V., & Iglesias-Páramo, J. 2005, *Monthly Notices of the RAS*, 360, 1413
- Byrne, C. M., Stanway, E. R., Eldridge, J. J., McSwiney, L., & Townsend, O. T. 2022, *Monthly Notices of the RAS*, 512, 5329
- Cañameras, R., Nesvadba, N., Kneissl, R., et al. 2017a, *Astronomy and Astrophysics*, 604, A117
- Cañameras, R., Nesvadba, N. P. H., Kneissl, R., et al. 2017b, *Astronomy and Astrophysics*, 600, L3

- Calabrò, A., Castellano, M., Pentericci, L., et al. 2021, *Astronomy and Astrophysics*, 646, A39
- Calura, F., Lupi, A., Rosdahl, J., et al. 2022, *Monthly Notices of the RAS*, 516, 5914
- Calura, F., Vanzella, E., Carniani, S., et al. 2021, *Monthly Notices of the RAS*, 500, 3083
- Calzetti, D., Kinney, A. L., & Storchi-Bergmann, T. 1994, *Astrophysical Journal*, 429, 582
- Caminha, G. B., Grillo, C., Rosati, P., et al. 2016, *Astronomy and Astrophysics*, 587, A80
- Caminha, G. B., Grillo, C., Rosati, P., et al. 2017, *Astronomy and Astrophysics*, 600, A90
- Caminha, G. B., Grillo, C., Rosati, P., et al. 2023, *Astronomy and Astrophysics*, 678, A3
- Caminha, G. B., Rosati, P., Grillo, C., et al. 2019, *Astronomy and Astrophysics*, 632, A36
- Caminha, G. B., Suyu, S. H., Grillo, C., & Rosati, P. 2022, *Astronomy and Astrophysics*, 657, A83
- Campbell, W. W. & Trumpler, R. 1923, *Publications of the ASP*, 35, 158
- Cantalupo, S., Porciani, C., Lilly, S. J., & Miniati, F. 2005, *Astrophysical Journal*, 628, 61
- Cao, S., Pan, Y., Biesiada, M., Godlowski, W., & Zhu, Z.-H. 2012, *Journal of Cosmology and Astroparticle Physics*, 2012, 016
- Cappellari, M. 2017a, *MNRAS*, 466, 798
- Cappellari, M. 2017b, *Monthly Notices of the RAS*, 466, 798
- Cappellari, M. 2023, *Monthly Notices of the RAS*, 526, 3273
- Cappellari, M., Bacon, R., Bureau, M., et al. 2006, *Monthly Notices of the RAS*, 20, 127
- Cappellari, M. & Emsellem, E. 2004a, *Publications of the ASP*, 116, 138
- Cappellari, M. & Emsellem, E. 2004b, *Publications of the ASP*, 116, 138
- Cardelli, J. A., Clayton, G. C., & Mathis, J. S. 1989, *Astrophysical Journal*, 345, 245
- Castellano, M., Amorín, R., Merlin, E., et al. 2016, *Astronomy and Astrophysics*, 590, A31
- Castellano, M., Belfiori, D., Pentericci, L., et al. 2023, The ionizing photon production efficiency of bright $z \sim 2-5$ galaxies
- Castellano, M., Fontana, A., Grazian, A., et al. 2012, *Astronomy and Astrophysics*, 540, A39
- Castellano, M., Fontana, A., Treu, T., et al. 2022, arXiv e-prints, arXiv:2207.09436
- Castellano, M., Sommariva, V., Fontana, A., et al. 2014, *Astronomy and Astrophysics*, 566, A19
- Cava, A., Schaefer, D., Richard, J., et al. 2018, *Nature Astronomy*, 2, 76
- Cavanaugh, J. E. 1997, *Statistics & Probability Letters*, 33, 201
- Ceverino, D., Dekel, A., & Bournaud, F. 2010, *Monthly Notices of the RAS*, 404, 2151
- Ceverino, D., Klessen, R. S., & Glover, S. C. O. 2019, *Monthly Notices of the RAS*, 484, 1366

- Chandrasekhar, S. 1960, Radiative transfer
- Chang, S.-J. & Gronke, M. 2024, arXiv e-prints, arXiv:2403.11524
- Chang, S.-J., Lee, H.-W., & Yang, Y. 2017, Monthly Notices of the RAS, 464, 5018
- Chang, S.-J., Yang, Y., Seon, K.-I., Zabludoff, A., & Lee, H.-W. 2023, Astrophysical Journal, 945, 100
- Charlot, S. & Fall, S. M. 2000, Astrophysical Journal, 539, 718
- Chirivì, G., Suyu, S. H., Grillo, C., et al. 2018, Astronomy and Astrophysics, 614, A8
- Chisholm, J., Prochaska, J. X., Schaefer, D., Gazagnes, S., & Henry, A. 2020, Monthly Notices of the RAS, 498, 2554
- Chisholm, J., Rigby, J. R., Bayliss, M., et al. 2019, Astrophysical Journal, 882, 182
- Chisholm, J., Saldana-Lopez, A., Flury, S., et al. 2022, Monthly Notices of the RAS, 517, 5104
- Chwolson, O. 1924, Astronomische Nachrichten, 221, 329
- Ciotti, L., Lanzoni, B., & Renzini, A. 1996, Monthly Notices of the RAS, 282, 1
- Claeyssens, A., Adamo, A., Richard, J., et al. 2022, arXiv e-prints, arXiv:2208.10450
- Claeyssens, A., Adamo, A., Richard, J., et al. 2023, Monthly Notices of the RAS, 520, 2180
- Clarke, D. & Stewart, B. G. 1986, Vistas in Astronomy, 29, 27
- Cohen, M. H., Vermeulen, R. C., Ogle, P. M., Tran, H. D., & Goodrich, R. W. 1997, Astrophysical Journal, 484, 193
- Collett, T. E. & Auger, M. W. 2014, Monthly Notices of the RAS, 443, 969
- Collett, T. E., Auger, M. W., Belokurov, V., Marshall, P. J., & Hall, A. C. 2012, Monthly Notices of the RAS, 424, 2864
- Collett, T. E., Buckley-Geer, E., Lin, H., et al. 2017, Astrophysical Journal, 843, 148
- Collett, T. E. & Smith, R. J. 2020, Monthly Notices of the RAS, 497, 1654
- Comrie, A., Wang, K.-S., Hsu, S.-C., et al. 2021, CARTA: The Cube Analysis and Rendering Tool for Astronomy
- Conroy, C., Dutton, A. A., Graves, G. J., Mendel, J. T., & van Dokkum, P. G. 2013, Astrophysical Journal, Letters, 776, L26
- Conselice, C. J. 2014, Annual Review of Astron and Astrophys, 52, 291
- Conselice, C. J., Grogin, N. A., Jogee, S., et al. 2004, Astrophysical Journal, Letters, 600, L139
- Cowie, L. L., Hu, E. M., & Songaila, A. 1995, Astronomical Journal, 110, 1576
- Cullen, F., McLure, R. J., McLeod, D. J., et al. 2022, arXiv e-prints, arXiv:2208.04914
- Dahle, H., Aghanim, N., Guennou, L., et al. 2016, Astronomy and Astrophysics, 590, L4

- Dariush, A. A., Raychaudhury, S., Ponman, T. J., et al. 2010, Monthly Notices of the RAS, 405, 1873
- Dayal, P. & Ferrara, A. 2018, Physics Reports, 780, 1
- Dekel, A., Ishai, G., Dutton, A. A., & Maccio, A. V. 2017, Monthly Notices of the RAS, 468, 1005
- DESCollaboration, Abbott, T. M. C., Aguena, M., et al. 2021, Dark Energy Survey Year 3 Results: A 2.7% measurement of Baryon Acoustic Oscillation distance scale at redshift 0.835
- Dessauges-Zavadsky, M., Richard, J., Combes, F., et al. 2019, Nature Astronomy, 3, 1115
- Dessauges-Zavadsky, M., Schaefer, D., Cava, A., Mayer, L., & Tamburello, V. 2017, Astrophysical Journal, Letters, 836, L22
- Diego, J. M., Adams, N. J., Willner, S., et al. 2023, arXiv e-prints, arXiv:2312.11603
- Diego, J. M., Broadhurst, T., Molnar, S. M., Lam, D., & Lim, J. 2015, Monthly Notices of the RAS, 447, 3130
- Dijkstra, M. 2014, Publications of the Astron. Soc. of Australia, 31, e040
- Dijkstra, M. 2019, Saas-Fee Advanced Course, 46, 1
- Dijkstra, M., Gronke, M., & Sobral, D. 2016, Astrophysical Journal, 823, 74
- Dijkstra, M., Haiman, Z., & Spaans, M. 2006, Astrophysical Journal, 649, 14
- Dijkstra, M. & Loeb, A. 2008, Monthly Notices of the RAS, 386, 492
- Donnan, C. T., McLeod, D. J., Dunlop, J. S., et al. 2022, arXiv e-prints, arXiv:2207.12356
- Dunlop, J. S. 2012, in The First Galaxies (Springer Berlin Heidelberg), 223–292
- Dunlop, J. S., Rogers, A. B., McLure, R. J., et al. 2013, Monthly Notices of the RAS, 432, 3520
- Dutta, R., Fossati, M., Fumagalli, M., et al. 2023, Monthly Notices of the RAS, 522, 535
- Dutton, A. A. & Treu, T. 2014, Monthly Notices of the RAS, 438, 3594
- Dyson, F. W., Eddington, A. S., & Davidson, C. 1920, Philosophical Transactions of the Royal Society of London Series A, 220, 291
- Dyson, F. W., Eddington, A. S., & Davidson, C. 1920, Philosophical Transactions of the Royal Society of London. Series A, Containing Papers of a Mathematical or Physical Character, 220, 291
- Eddington, A. S. 1919, The Observatory, 42, 119
- Eddington, A. S. 1920, Space, time and gravitation. an outline of the general relativity theory
- Efstathiou, G., Moody, S., Peacock, J. A., et al. 2002, Monthly Notices of the RAS, 330, L29
- Eide, M. B., Gronke, M., Dijkstra, M., & Hayes, M. 2018, Astrophysical Journal, 856, 156
- Einstein, A. 1911, Annalen der Physik, 340, 898

- Einstein, A. 1915, Sitzungsberichte der Königlich Preussischen Akademie der Wissenschaften, 844
- Einstein, A. 1916, Sitzungsberichte der Königlich Preussischen Akademie der Wissenschaften, 688
- Einstein, A. 1917, Sitzungsberichte der Königlich Preussischen Akademie der Wissenschaften, 142
- Einstein, A. 1936, Science, 84, 506
- Eisenstein, D. J., Zehavi, I., Hogg, D. W., et al. 2005, Astrophysical Journal, 633, 560
- El-Zant, A., Shlosman, I., & Hoffman, Y. 2001, Astrophysical Journal, 560, 636
- El-Zant, A. A., Hoffman, Y., Primack, J., Combes, F., & Shlosman, I. 2004, Astrophysical Journal, Letters, 607, L75
- Eldridge, J. J., Stanway, E. R., Xiao, L., et al. 2017, Publications of the Astron. Soc. of Australia, 34, e058
- Elíasdóttir, Á., Limousin, M., Richard, J., et al. 2007, arXiv e-prints, arXiv:0710.5636
- Elmegreen, B. G. & Elmegreen, D. M. 2005, Astrophysical Journal, 627, 632
- Elmegreen, B. G., Elmegreen, D. M., Fernandez, M. X., & Lemonias, J. J. 2009a, Astrophysical Journal, 692, 12
- Elmegreen, B. G., Elmegreen, D. M., Sánchez Almeida, J., et al. 2013, Astrophysical Journal, 774, 86
- Elmegreen, D. M., Elmegreen, B. G., Marcus, M. T., et al. 2009b, Astrophysical Journal, 701, 306
- Elmegreen, D. M., Elmegreen, B. G., Ravindranath, S., & Coe, D. A. 2007, Astrophysical Journal, 658, 763
- ESO CPL Development Team. 2015, EsoRex: ESO Recipe Execution Tool, Astrophysics Source Code Library, record ascl:1504.003
- Faber, S. M., Dressler, A., Davies, R. L., et al. 1987, in Nearly Normal Galaxies. From the Planck Time to the Present, ed. S. M. Faber, 175
- Faber, S. M. & Jackson, R. E. 1976, Astrophysical Journal, 204, 668
- Faure, B., Bournaud, F., Fensch, J., et al. 2021, Monthly Notices of the RAS, 502, 4641
- Ferreira, L., Conselice, C. J., Sazonova, E., et al. 2022, arXiv e-prints, arXiv:2210.01110
- Finkelstein, S. L., Bagley, M., Song, M., et al. 2022, Astrophysical Journal, 928, 52
- Finkelstein, S. L., Papovich, C., Salmon, B., et al. 2012, Astrophysical Journal, 756, 164
- Finlator, K., Oppenheimer, B. D., & Davé, R. 2011, Monthly Notices of the RAS, 410, 1703
- Fiorentino, G., Bellazzini, M., Ciliegi, P., et al. 2017, arXiv e-prints, arXiv:1712.04222

- Fisher, D. B., Glazebrook, K., Damjanov, I., et al. 2017, Monthly Notices of the RAS, 464, 491
- Florentin-Nielsen, R. 1984, Astronomy and Astrophysics, 138, L19
- Ford, A. B., Oppenheimer, B. D., Davé, R., et al. 2013, Monthly Notices of the RAS, 432, 89
- Foreman-Mackey, D. 2016, The Journal of Open Source Software, 1, 24
- Foreman-Mackey, D., Hogg, D. W., Lang, D., & Goodman, J. 2013, Publications of the ASP, 125, 306
- Förster Schreiber, N. M., Genzel, R., Bouché, N., et al. 2009, Astrophysical Journal, 706, 1364
- Förster Schreiber, N. M., Shapley, A. E., Erb, D. K., et al. 2011a, Astrophysical Journal, 731, 65
- Förster Schreiber, N. M., Shapley, A. E., Genzel, R., et al. 2011b, Astrophysical Journal, 739, 45
- Fox & Davé. 2017, in Astrophysics and Space Science Library, Vol. 430, Gas Accretion onto Galaxies
- Freudling, W., Romaniello, M., Bramich, D. M., et al. 2013, Astronomy and Astrophysics, 559, A96
- Fruchter, A. S., Hack, W., Dencheva, N., Droettboom, M., & Greenfield, P. 2010, in 2010 Space Telescope Science Institute Calibration Workshop, 382–387
- Gallazzi, A., Bell, E. F., Zibetti, S., Brinchmann, J., & Kelson, D. D. 2014, Astrophysical Journal, 788, 72
- Gao, L., Navarro, J. F., Frenk, C. S., et al. 2012, Monthly Notices of the RAS, 425, 2169
- Gavazzi, R., Treu, T., Koopmans, L. V. E., et al. 2008, Astrophysical Journal, 677, 1046
- Gavazzi, R., Treu, T., Rhodes, J. D., et al. 2007, Astrophysical Journal, 667, 176
- Genzel, R., Burkert, A., Bouché, N., et al. 2008, Astrophysical Journal, 687, 59
- Genzel, R., Newman, S., Jones, T., et al. 2011, Astrophysical Journal, 733, 101
- Gerhard, O., Kronawitter, A., Saglia, R. P., & Bender, R. 2001, Astronomical Journal, 121, 1936
- Giavalisco, M., Dickinson, M., Ferguson, H. C., et al. 2004, Astrophysical Journal, Letters, 600, L103
- Glazebrook, K. 2013, Publications of the Astronomical Society of Australia, 30, e056
- Gnedin, O. Y., Kravtsov, A. V., Klypin, A. A., & Nagai, D. 2004, Astrophysical Journal, 616, 16
- Golse, G. & Kneib, J. P. 2002, Astronomy and Astrophysics, 390, 821
- Gonneau, A., Lyubenova, M., Lançon, A., et al. 2020, Astronomy and Astrophysics, 634, A133
- Governato, F., Brook, C., Mayer, L., et al. 2010, Nature, 463, 203

- Graham, A. W., Merritt, D., Moore, B., Diemand, J., & Terzić, B. 2006, *Astronomical Journal*, 132, 2701
- Granata, G., Bergamini, P., Grillo, C., et al. 2023, *Astronomy and Astrophysics*, 679, A124
- Grillo, C. 2010, *Astrophysical Journal*, 722, 779
- Grillo, C., Christensen, L., Gallazzi, A., & Rasmussen, J. 2013, *Monthly Notices of the RAS*, 433, 2604
- Grillo, C. & Gobat, R. 2010, *Monthly Notices of the RAS*, 402, L67
- Grillo, C., Gobat, R., Lombardi, M., & Rosati, P. 2009, *Astronomy and Astrophysics*, 501, 461
- Grillo, C., Karman, W., Suyu, S. H., et al. 2016, *Astrophysical Journal*, 822, 78
- Grillo, C., Lombardi, M., & Bertin, G. 2008, *Astronomy and Astrophysics*, 477, 397
- Grillo, C., Pagano, L., Rosati, P., & Suyu, S. H. 2024, arXiv e-prints, arXiv:2401.10980
- Grillo, C., Rosati, P., Suyu, S. H., et al. 2018, *Astrophysical Journal*, 860, 94
- Grillo, C., Rosati, P., Suyu, S. H., et al. 2020, *Astrophysical Journal*, 898, 87
- Grillo, C., Suyu, S. H., Rosati, P., et al. 2015, *Astrophysical Journal*, 800, 38
- Gronke, M., Bull, P., & Dijkstra, M. 2015, *Astrophysical Journal*, 812, 123
- Gronke, M. & Dijkstra, M. 2016, *Astrophysical Journal*, 826, 14
- Gronke, M., Dijkstra, M., McCourt, M., & Oh, S. P. 2016, *Astrophysical Journal, Letters*, 833, L26
- Gronke, M., Girichidis, P., Naab, T., & Walch, S. 2018, *Astrophysical Journal, Letters*, 862, L7
- Guo, Y., Ferguson, H. C., Bell, E. F., et al. 2015, *Astrophysical Journal*, 800, 39
- Guo, Y., Giavalisco, M., Ferguson, H. C., Cassata, P., & Koekemoer, A. M. 2012, *Astrophysical Journal*, 757, 120
- Guo, Y., Rafelski, M., Bell, E. F., et al. 2018, *Astrophysical Journal*, 853, 108
- Gustafsson, M., Fairbairn, M., & Sommer-Larsen, J. 2006, *Physical Review D*, 74, 123522
- Haiman, Z. & Rees, M. J. 2001, *Astrophysical Journal*, 556, 87
- Haiman, Z., Spaans, M., & Quataert, E. 2000, *Astrophysical Journal, Letters*, 537, L5
- Harikane, Y., Ouchi, M., Oguri, M., et al. 2022, arXiv e-prints, arXiv:2208.01612
- Harris, C. R., Millman, K. J., van der Walt, S. J., et al. 2020, *Nature*, 585, 357
- Hathi, N. P., Cohen, S. H., Ryan, R. E., J., et al. 2013, *Astrophysical Journal*, 765, 88
- Hayes, M., Melinder, J., Östlin, G., et al. 2016, *Astrophysical Journal*, 828, 49

- Hayes, M. & Scarlata, C. 2011, in SF2A-2011: Proceedings of the Annual meeting of the French Society of Astronomy and Astrophysics, ed. G. Alecian, K. Belkacem, R. Samadi, & D. Valls-Gabaud, 129–133
- Hayes, M., Scarlata, C., & Siana, B. 2011, *Nature*, 476, 304
- Henry, A., Berg, D. A., Scarlata, C., Verhamme, A., & Erb, D. 2018, *Astrophysical Journal*, 855, 96
- Hewitt, J. N., Turner, E. L., Schneider, D. P., Burke, B. F., & Langston, G. I. 1988, *Nature*, 333, 537
- Hezaveh, Y. D., Dalal, N., Marrone, D. P., et al. 2016, *Astrophysical Journal*, 823, 37
- Hinojosa-Goñi, R., Muñoz-Tuñón, C., & Méndez-Abreu, J. 2016, *Astronomy and Astrophysics*, 592, A122
- Hinshaw, G., Larson, D., Komatsu, E., et al. 2013, *Astrophysical Journal, Supplement*, 208, 19
- Hinton, S. R., Davis, T. M., Lidman, C., Glazebrook, K., & Lewis, G. F. 2016, *Astronomy and Computing*, 15, 61
- Hirano, S., Hosokawa, T., Yoshida, N., Omukai, K., & Yorke, H. W. 2015, *Monthly Notices of the RAS*, 448, 568
- Hoag, A., Huang, K. H., Treu, T., et al. 2016, *Astrophysical Journal*, 831, 182
- Hogan, C. J. & Weymann, R. J. 1987, *Monthly Notices of the RAS*, 225, 1P
- Hopkins, P. F., Narayanan, D., & Murray, N. 2013, *Monthly Notices of the RAS*, 432, 2647
- Huchra, J., Gorenstein, M., Kent, S., et al. 1985, *Astronomical Journal*, 90, 691
- Huertas-Company, M., Iyer, K. G., Angeloudi, E., et al. 2024, *Astronomy and Astrophysics*, 685, A48
- Humphrey, A., Vernet, J., Villar-Martín, M., et al. 2013, *Astrophysical Journal, Letters*, 768, L3
- Hunter, J. D. 2007, *Computing in Science & Engineering*, 9, 90
- Iani, E., Zanella, A., Vernet, J., et al. 2023, *Monthly Notices of the RAS*, 518, 5018
- Iani, E., Zanella, A., Vernet, J., et al. 2021, *Monthly Notices of the RAS*, 507, 3830
- Immeli, A., Samland, M., Gerhard, O., & Westera, P. 2004a, *Astronomy and Astrophysics*, 413, 547
- Immeli, A., Samland, M., Westera, P., & Gerhard, O. 2004b, *Astrophysical Journal*, 611, 20
- Inoue, A. K. 2011, *Monthly Notices of the RAS*, 415, 2920
- Inoue, S., Dekel, A., Mandelker, N., et al. 2016, *Monthly Notices of the RAS*, 456, 2052
- Izotov, Y. I., Chisholm, J., Worseck, G., et al. 2022, *Monthly Notices of the RAS*, 515, 2864
- Jauzac, M., Clément, B., Limousin, M., et al. 2014, *Monthly Notices of the RAS*, 443, 1549

- Jester, S., Schneider, D. P., Richards, G. T., et al. 2005, *Astronomical Journal*, 130, 873
- Jeřábková, T., Kroupa, P., Dabringhausen, J., Hilker, M., & Bekki, K. 2017, *Astronomy and Astrophysics*, 608, A53
- Jiang, L., Cohen, S. H., Windhorst, R. A., et al. 2020, *Astrophysical Journal*, 889, 90
- Johnson, L. E., Irwin, J. A., White, Raymond E., I., Wong, K.-W., & Dupke, R. A. 2018a, *Astrophysical Journal*, 869, 170
- Johnson, L. E., Irwin, J. A., White, Raymond E., I., et al. 2018b, *Astrophysical Journal*, 856, 131
- Johnson, T. L., Rigby, J. R., Sharon, K., et al. 2017, *Astrophysical Journal Letters*, 843, L21
- Johnson, T. L., Sharon, K., Bayliss, M. B., et al. 2014, *Astrophysical Journal*, 797, 48
- Jones, L. R., Ponman, T. J., Horton, A., et al. 2003, *Monthly Notices of the RAS*, 343, 627
- Jullo, E., Kneib, J. P., Limousin, M., et al. 2007, *New Journal of Physics*, 9, 447
- Jullo, E., Natarajan, P., Kneib, J. P., et al. 2010, *Science*, 329, 924
- Kalita, B. S., Silverman, J. D., Daddi, E., et al. 2024, *Astrophysical Journal*, 960, 25
- Kashikawa, N., Nagao, T., Toshikawa, J., et al. 2012, *Astrophysical Journal*, 761, 85
- Katz, H., Garel, T., Rosdahl, J., et al. 2022, *Monthly Notices of the RAS*, 515, 4265
- Kausch, W., Noll, S., Smette, A., et al. 2015, *Astronomy and Astrophysics*, 576, A78
- Kelly, P. L., Rodney, S. A., Treu, T., et al. 2016, *The Astrophysical Journal*, 819, L8
- Khosroshahi, H. G., Maughan, B. J., Ponman, T. J., & Jones, L. R. 2006, *Monthly Notices of the RAS*, 369, 1211
- Kim, E., Yang, Y., Zabludoff, A., et al. 2020, *Astrophysical Journal*, 894, 33
- Klimov, Y. G. 1963, *Astronomicheskii Zhurnal*, 40, 874
- Kneib, J. P., Ellis, R. S., Smail, I., Couch, W. J., & Sharples, R. M. 1996, *Astrophysical Journal*, 471, 643
- Koekemoer, A. M., Avila, R. J., Hammer, D., et al. 2014, in American Astronomical Society Meeting Abstracts, Vol. 223, American Astronomical Society Meeting Abstracts #223, 254.02
- Komatsu, E., Bennett, C. L., Barnes, C., et al. 2014, *Progress of Theoretical and Experimental Physics*, 2014, 06B102
- Koopmans, L. V. E., Bolton, A., Treu, T., et al. 2009, *Astrophysical Journal Letters*, 703, L51
- Koratkar, A., Antonucci, R. R. J., Goodrich, R. W., Bushouse, H., & Kinney, A. L. 1995, *Astrophysical Journal*, 450, 501
- Kurczynski, P., Gawiser, E., Rafelski, M., et al. 2014, *Astrophysical Journal Letters*, 793, L5
- Können, G. P. 1985, *Polarized light in nature*

- Labbé, I., González, V., Bouwens, R. J., et al. 2010, *Astrophysical Journal, Letters*, 716, L103
- Langston, G. I., Schneider, D. P., Conner, S., et al. 1989, *Astronomical Journal*, 97, 1283
- Laporte, C. F. P. & White, S. D. M. 2015, *Monthly Notices of the RAS*, 451, 1177
- Laursen, P., Sommer-Larsen, J., & Andersen, A. C. 2009, *Astrophysical Journal*, 704, 1640
- Lee, H.-W. & Ahn, S.-H. 1998, *Astrophysical Journal, Letters*, 504, L61
- Leitherer, C., Schaerer, D., Goldader, J. D., et al. 1999, *Astrophysical Journal, Supplement*, 123, 3
- Li, T., Collett, T. E., Krawczyk, C. M., & Enzi, W. 2024, *Monthly Notices of the RAS*, 527, 5311
- Li, Y., Ruszkowski, M., & Bryan, G. L. 2017, *Astrophysical Journal*, 847, 106
- Li, Z. & Gronke, M. 2022, *Monthly Notices of the RAS*, 513, 5034
- Liebes, S. 1964, *Physical Review*, 133, 835
- Livermore, R. C., Jones, T. A., Richard, J., et al. 2015, *Monthly Notices of the RAS*, 450, 1812
- Lodge, O. J. 1919, *Nature*, 104, 354
- Loeb, A. & Peebles, P. J. E. 2003, *Astrophysical Journal*, 589, 29
- Loewenstein, M. & Mushotzky, R. 2003, *Nuclear Physics B - Proceedings Supplements*, 124, 91, proceedings of the 5th International UCLA Symposium on Sources and Detection of Dark Matter and Dark Energy in the Universe
- Lombardi, M. 2024, arXiv e-prints, arXiv:2406.15280
- Lotz, J. M., Koekemoer, A., Coe, D., et al. 2017, *Astrophysical Journal*, 837, 97
- Lovell, C. C., Vijayan, A. P., Thomas, P. A., et al. 2021, *Monthly Notices of the RAS*, 500, 2127
- Madau, P. & Dickinson, M. 2014, *Annual Review of Astron and Astrophys*, 52, 415
- Magain, P., Surdej, J., Swings, J. P., Borgeest, U., & Kayser, R. 1988, *Nature*, 334, 325
- Mahler, G., Richard, J., Clément, B., et al. 2018, *Monthly Notices of the RAS*, 473, 663
- Marques-Chaves, R., Schaerer, D., Álvarez-Márquez, J., et al. 2022, *Monthly Notices of the RAS*, 517, 2972
- Martizzi, D., Teyssier, R., & Moore, B. 2013, *Monthly Notices of the RAS*, 432, 1947
- Martizzi, D., Teyssier, R., Moore, B., & Wentz, T. 2012, *Monthly Notices of the RAS*, 422, 3081
- Mas-Ribas, L., Dijkstra, M., Hennawi, J. F., et al. 2017, *Astrophysical Journal*, 841, 19
- Maseda, M. V., Bacon, R., Lam, D., et al. 2020, *Monthly Notices of the RAS*, 493, 5120
- McCully, C., Crawford, S., Kovacs, G., et al. 2018, *astropy/astroscrappy: v1.0.5 Zenodo Release*

- McCully, C. & Tewes, M. 2019, Astro-SCRAPPY: Speedy Cosmic Ray Annihilation Package in Python
- McLure, R. J., Dunlop, J. S., Cullen, F., et al. 2018, Monthly Notices of the RAS, 476, 3991
- Meneghetti, M. 2021, Introduction to Gravitational Lensing; With Python Examples, Vol. 956
- Meneghetti, M., Davoli, G., Bergamini, P., et al. 2020, Science, 369, 1347
- Merlin, E., Amorín, R., Castellano, M., et al. 2016, Astronomy and Astrophysics, 590, A30
- Merlin, E., Pilo, S., Fontana, A., et al. 2019, Astronomy and Astrophysics, 622, A169
- Messa, M., Dessauges-Zavadsky, M., Richard, J., et al. 2022, Monthly Notices of the RAS, 516, 2420
- Meštrić, U., Vanzella, E., Upadhyaya, A., et al. 2023, Astronomy and Astrophysics, 673, A50
- Meštrić, U., Vanzella, E., Zanella, A., et al. 2022, Monthly Notices of the RAS, 516, 3532
- Michell, J. 1784, Philosophical Transactions of the Royal Society of London, 74, 35
- Mieda, E., Wright, S. A., Larkin, J. E., et al. 2016, Astrophysical Journal, 831, 78
- Modigliani, A., Goldoni, P., Royer, F., et al. 2010, in Society of Photo-Optical Instrumentation Engineers (SPIE) Conference Series, Vol. 7737, Observatory Operations: Strategies, Processes, and Systems III, ed. D. R. Silva, A. B. Peck, & B. T. Soifer, 773728
- Momose, R., Ouchi, M., Nakajima, K., et al. 2016, Monthly Notices of the RAS, 457, 2318
- Mondal, C., Saha, K., Windhorst, R. A., & Jansen, R. A. 2023, Astrophysical Journal, 946, 90
- Moresco, M., Amati, L., Amendola, L., et al. 2022, Living Reviews in Relativity, 25, 6
- Mori, M., Umemura, M., & Ferrara, A. 2004, Astrophysical Journal, Letters, 613, L97
- Mortara, L. & Fowler, A. 1981, in Society of Photo-Optical Instrumentation Engineers (SPIE) Conference Series, Vol. 290, Society of Photo-Optical Instrumentation Engineers (SPIE) Conference Series, ed. J. C. Geary & D. W. Latham, 28
- Motta, V., García-Aspeitia, M. A., Hernández-Almada, A., Magaña, J., & Verdugo, T. 2021, Universe, 7, 163
- Munari, U., Sordo, R., Castelli, F., & Zwitter, T. 2005, Astronomy and Astrophysics, 442, 1127
- Murata, K. L., Kajisawa, M., Taniguchi, Y., et al. 2014, Astrophysical Journal, 786, 15
- Nakajima, K. & Maiolino, R. 2022, Monthly Notices of the RAS, 513, 5134
- Nakane, M., Ouchi, M., Nakajima, K., et al. 2024, Astrophysical Journal, 967, 28
- Nanayakkara, T., Glazebrook, K., Jacobs, C., et al. 2022, arXiv e-prints, arXiv:2207.13860
- Narayan, R. & Bartelmann, M. 1996, Lectures on gravitational lensing, Tech. Rep. astro-ph/9606001
- Navarro, J. F., Frenk, C. S., & White, S. D. M. 1996, Astrophysical Journal, 462, 563

- Navarro, J. F., Frenk, C. S., & White, S. D. M. 1997, *Astrophysical Journal*, 490, 493
- Navarro, J. F., Ludlow, A., Springel, V., et al. 2010, *Monthly Notices of the RAS*, 402, 21
- Neufeld, D. A. 1990, *Astrophysical Journal*, 350, 216
- Newman, A. B., Ellis, R. S., & Treu, T. 2015, *Astrophysical Journal*, 814, 26
- Newman, A. B., Treu, T., Ellis, R. S., & Sand, D. J. 2013a, *Astrophysical Journal*, 765, 25
- Newman, A. B., Treu, T., Ellis, R. S., et al. 2013b, *Astrophysical Journal*, 765, 24
- Newton, I. 1704, *Opticks* (Dover Press)
- Nightingale, J. W. & Dye, S. 2015, *Monthly Notices of the Royal Astronomical Society*, 452, 2940
- Nipoti, C., Treu, T., Ciotti, L., & Stiavelli, M. 2004, *Monthly Notices of the RAS*, 355, 1119
- Noguchi, M. 1999, *Astrophysical Journal*, 514, 77
- Noll, S., Burgarella, D., Giovannoli, E., et al. 2009, *Astronomy and Astrophysics*, 507, 1793
- Norris, M. A. & Kannappan, S. J. 2011, *Monthly Notices of the RAS*, 414, 739
- North, P., Hayes, M., Millon, M., et al. 2024, *Astronomy and Astrophysics*, 684, A147
- O'Donnell, J. E. 1994, *Astrophysical Journal*, 422, 158
- Oesch, P. A., Bouwens, R. J., Illingworth, G. D., et al. 2010, *Astrophysical Journal, Letters*, 709, L16
- Oesch, P. A., Bouwens, R. J., Illingworth, G. D., Labb  , I., & Stefanon, M. 2018, *Astrophysical Journal*, 855, 105
- Oguri, M. 2010, *Publications of the ASJ*, 62, 1017
- Oke, J. B. 1974, *Astrophysical Journal, Supplement*, 27, 21
- Oklop  i  , A., Hopkins, P. F., Feldmann, R., et al. 2017, *Monthly Notices of the RAS*, 465, 952
- Ono, Y., Ouchi, M., Shimasaku, K., et al. 2010, *Astrophysical Journal*, 724, 1524
- Osterbrock, D. E. 1962, *Astrophysical Journal*, 135, 195
- Pallottini, A., Ferrara, A., Gallerani, S., et al. 2022, *Monthly Notices of the RAS*, 513, 5621
- pandas development team, T. 2023, *pandas-dev/pandas: Pandas*
- Partridge, R. B. & Peebles, P. J. E. 1967, *Astrophysical Journal*, 148, 377
- Pedrosa, S., Tissera, P. B., & Scannapieco, C. 2009, *Monthly Notices of the RAS*, 395, L57
- Peirani, S., Kay, S., & Silk, J. 2008, *Astronomy and Astrophysics*, 479, 123
- Peng, C. Y., Ho, L. C., Impey, C. D., & Rix, H.-W. 2002, *Astronomical Journal*, 124, 266
- Peng, C. Y., Ho, L. C., Impey, C. D., & Rix, H.-W. 2010, *Astronomical Journal*, 139, 2097

- Perlmutter, S., Aldering, G., Goldhaber, G., et al. 1999, *Astrophysical Journal*, 517, 565
- Péroux, C. & Howk, J. C. 2020, *Annual Review of Astron and Astrophys*, 58, 363
- Péroux, C., Zwaan, M. A., Klitsch, A., et al. 2019, *Monthly Notices of the RAS*, 485, 1595
- Pilo, S., Castellano, M., Fontana, A., et al. 2019, *Astronomy and Astrophysics*, 626, A45
- Planck Collaboration, Ade, P. A. R., Aghanim, N., et al. 2014, *Astronomy and Astrophysics*, 571, A16
- Planck Collaboration, Aghanim, N., Akrami, Y., et al. 2020, *Astronomy and Astrophysics*, 641, A6
- Ponman, T. J. & Bertram, D. 1993, *Nature*, 363, 51
- Pontzen, A. & Governato, F. 2012, *Monthly Notices of the RAS*, 421, 3464
- Postman, M., Coe, D., Benítez, N., et al. 2012, *Astrophysical Journal, Supplement*, 199, 25
- Prescott, M. K. M., Smith, P. S., Schmidt, G. D., & Dey, A. 2011, *Astrophysical Journal, Letters*, 730, L25
- Prochaska, J. X., Kasen, D., & Rubin, K. 2011, *Astrophysical Journal*, 734, 24
- Puech, M. 2010, *Monthly Notices of the RAS*, 406, 535
- Puech, M., Hammer, F., Flores, H., Neichel, B., & Yang, Y. 2009, *Astronomy and Astrophysics*, 493, 899
- Putman, M. E., Peek, J. E. G., & Joung, M. R. 2012, *Annual Review of Astron and Astrophys*, 50, 491
- Raiter, A., Schaefer, D., & Fosbury, R. A. E. 2010, *Astronomy and Astrophysics*, 523, A64
- Reddy, N. A., Oesch, P. A., Bouwens, R. J., et al. 2018, *Astrophysical Journal*, 853, 56
- Refsdal, S. 1964a, *Monthly Notices of the RAS*, 128, 307
- Refsdal, S. 1964b, *Monthly Notices of the RAS*, 128, 307
- Refsdal, S. 1964c, *Monthly Notices of the RAS*, 128, 295
- Ribeiro, B., Le Fèvre, O., Cassata, P., et al. 2017, *Astronomy and Astrophysics*, 608, A16
- Richard, J., Claeysens, A., Lagattuta, D., et al. 2021, *Astronomy and Astrophysics*, 646, A83
- Richard, J., Jauzac, M., Limousin, M., et al. 2014, *Monthly Notices of the RAS*, 444, 268
- Riess, A. G., Filippenko, A. V., Challis, P., et al. 1998, *Astronomical Journal*, 116, 1009
- Rigby, J. R., Johnson, T. L., Sharon, K., et al. 2017, *Astrophysical Journal*, 843, 79
- Rihtaršić, G., Bradač, M., Desprez, G., et al. 2024, arXiv e-prints, arXiv:2406.10332
- Ritondale, E., Vegetti, S., Despali, G., et al. 2019, *Monthly Notices of the RAS*, 485, 2179
- Rivera-Thorsen, T. E., Dahle, H., Gronke, M., et al. 2017, *Astronomy and Astrophysics*, 608, L4

- Rizzo, F., Vegetti, S., Fraternali, F., Stacey, H. R., & Powell, D. 2021, Monthly Notices of the RAS, 507, 3952
- Rogers, A. B., McLure, R. J., & Dunlop, J. S. 2013, Monthly Notices of the RAS, 429, 2456
- Romano, M., Cassata, P., Morselli, L., et al. 2021, Astronomy and Astrophysics, 653, A111
- Romano-Díaz, E., Shlosman, I., Hoffman, Y., & Heller, C. 2008, Astrophysical Journal, Letters, 685, L105
- Rubin, V. C. 1983, Scientific American, 248, 96
- Rubin, V. C. & Ford, W. Kent, J. 1970, Astrophysical Journal, 159, 379
- Rusu, C. E., Wong, K. C., Bonvin, V., et al. 2020, Monthly Notices of the RAS, 498, 1440
- Salpeter, E. E. 1955, Astrophysical Journal, 121, 161
- Sand, D. J., Treu, T., Smith, G. P., & Ellis, R. S. 2004, Astrophysical Journal, 604, 88
- Schaerer, D. 2002, Astronomy and Astrophysics, 382, 28
- Schlafly, E. F. & Finkbeiner, D. P. 2011, Astrophysical Journal, 737, 103
- Schneider, P. 2014, Astronomy and Astrophysics, 568, L2
- Schneider, P., Ehlers, J., & Falco, E. 1992a, Gravitational Lenses (Springer-Verlag Berlin Heidelberg)
- Schneider, P., Ehlers, J., & Falco, E. E. 1992b, Gravitational Lenses
- Schneider, P., Kochanek, P., & Wambsganss, J. 2006, Gravitational Lensing: Strong, Weak and Micro (Springer-Verlag Berlin Heidelberg), 552
- Schuldt, S., Chirivì, G., Suyu, S. H., et al. 2019, Astronomy and Astrophysics, 631, A40
- Schuldt, S., Grillo, C., Caminha, G. B., et al. 2024, arXiv e-prints, arXiv:2405.12287
- Schwarz, G. 1978, Annals of Statistics, 6, 461
- Scolnic, D. M., Jones, D. O., Rest, A., et al. 2018, Astrophysical Journal, 859, 101
- Sellwood, J. A. & McGaugh, S. S. 2005, Astrophysical Journal, 634, 70
- Selsing, J., Malesani, D., Goldoni, P., et al. 2019, Astronomy and Astrophysics, 623, A92
- Seon, K.-i. 2023, arXiv e-prints, arXiv:2310.17908
- Seon, K.-i., Song, H., & Chang, S.-J. 2022, Astrophysical Journal, Supplement, 259, 3
- Serkowski, K. 1958, Acta Astronomica, 8, 135
- Sérsic, J. L. 1963, Boletin de la Asociacion Argentina de Astronomia La Plata Argentina, 6, 41
- Shajib, A. J., Mozumdar, P., Chen, G. C. F., et al. 2023, Astronomy and Astrophysics, 673, A9
- Shibuya, T., Ouchi, M., Harikane, Y., et al. 2018, Publications of the ASJ, 70, S15

- Shibuya, T., Ouchi, M., Kubo, M., & Harikane, Y. 2016, *Astrophysical Journal*, 821, 72
- Shu, Y., Bolton, A. S., Brownstein, J. R., et al. 2015, *Astrophysical Journal*, 803, 71
- Simmons, J. F. L. & Stewart, B. G. 1985, *Astronomy and Astrophysics*, 142, 100
- Smette, A., Sana, H., Noll, S., et al. 2015, *Astronomy and Astrophysics*, 576, A77
- Smith, R. J. & Collett, T. E. 2021, *Monthly Notices of the RAS*, 505, 2136
- Smoot, G. F., Bennett, C. L., Kogut, A., et al. 1992, *Astrophysical Journal, Letters*, 396, L1
- Sobral, D., Matthee, J., Brammer, G., et al. 2019, *Monthly Notices of the RAS*, 482, 2422
- Sobral, D., Matthee, J., Darvish, B., et al. 2015, *Astrophysical Journal*, 808, 139
- Sommer-Larsen, J. & Limousin, M. 2010, *Monthly Notices of the RAS*, 408, 1998
- Sommovigo, L., Ferrara, A., Carniani, S., et al. 2021, *Monthly Notices of the RAS*, 503, 4878
- Sonnenfeld, A., Jaelani, A. T., Chan, J., et al. 2019, *Astronomy and Astrophysics*, 630, A71
- Sonnenfeld, A., Treu, T., Marshall, P. J., et al. 2015, *Astrophysical Journal*, 800, 94
- Soto, E., de Mello, D. F., Rafelski, M., et al. 2017, *Astrophysical Journal*, 837, 6
- Soto, K. T., Lilly, S. J., Bacon, R., Richard, J., & Conseil, S. 2016, *Monthly Notices of the RAS*, 458, 3210
- Stanway, E. R., McMahon, R. G., & Bunker, A. J. 2005, *Monthly Notices of the RAS*, 359, 1184
- Stark, D. P., Auger, M., Belokurov, V., et al. 2013, *Monthly Notices of the RAS*, 436, 1040
- Stenflo, J. O. 1980, *Astronomy and Astrophysics*, 84, 68
- Stevance, H., Eldridge, J., & Stanway, E. 2020, *The Journal of Open Source Software*, 5, 1987
- Stokes, G. G. 1851, *Transactions of the Cambridge Philosophical Society*, 9, 399
- Stott, J. P., Swinbank, A. M., Johnson, H. L., et al. 2016, *Monthly Notices of the RAS*, 457, 1888
- Straughn, A. N., Voyer, E. N., Eufrasio, R. T., et al. 2015, *Astrophysical Journal*, 814, 97
- Sunnquist, B. 2018, WFC3/IR Blob Monitoring, Space Telescope WFC Instrument Science Report
- Suresh, J., Rubin, K. H. R., Kannan, R., et al. 2017, *Monthly Notices of the RAS*, 465, 2966
- Suyu, S. H., Auger, M. W., Hilbert, S., et al. 2013, *Astrophysical Journal*, 766, 70
- Suyu, S. H., Bonvin, V., Courbin, F., et al. 2017, *Monthly Notices of the RAS*, 468, 2590
- Suyu, S. H. & Halkola, A. 2010, *Astronomy and Astrophysics*, 524, A94
- Suyu, S. H., Hensel, S. W., McKean, J. P., et al. 2012, *Astrophysical Journal*, 750, 10

- Suyu, S. H., Marshall, P. J., Hobson, M. P., & Blandford, R. D. 2006, Monthly Notices of the RAS, 371, 983
- Tamburello, V., Mayer, L., Shen, S., & Wadsley, J. 2015, Monthly Notices of the RAS, 453, 2490
- Tamburello, V., Rahmati, A., Mayer, L., et al. 2017, Monthly Notices of the RAS, 468, 4792
- Tanaka, M., Wong, K. C., More, A., et al. 2016, Astrophysical Journal, Letters, 826, L19
- Taniguchi, Y. & Shioya, Y. 2000, Astrophysical Journal, Letters, 532, L13
- Tody, D. 1986, in Proceedings of the SPIE, Vol. 627, Instrumentation in astronomy VI, ed. D. L. Crawford, 733
- Tonini, C., Lapi, A., & Salucci, P. 2006, Astrophysical Journal, 649, 591
- Topping, M. W., Stark, D. P., Endsley, R., et al. 2022, Astrophysical Journal, 941, 153
- Treu, T. 2010, Annual Review of Astron and Astrophys, 48, 87
- Treu, T., Calabro, A., Castellano, M., et al. 2022a, arXiv e-prints, arXiv:2207.13527
- Treu, T. & Koopmans, L. V. E. 2002, Astrophysical Journal, 575, 87
- Treu, T. & Marshall, P. J. 2016, Astronomy and Astrophysics Reviews, 24, 11
- Treu, T., Suyu, S. H., & Marshall, P. J. 2022b, Astronomy and Astrophysics Reviews, 30, 8
- Trumpler, R. 1928, Publications of the ASP, 40, 130
- Trussler, J. A. A., Conselice, C. J., Adams, N. J., et al. 2022, arXiv e-prints, arXiv:2211.02038
- Tu, H., Gavazzi, R., Limousin, M., et al. 2009, Astronomy and Astrophysics, 501, 475
- Tumlinson, J., Peeples, M. S., & Werk, J. K. 2017, Annual Review of Astron and Astrophys, 55, 389
- Tyson, J. A., Valdes, F., & Wenk, R. A. 1990, Astrophysical Journal, Letters, 349, L1
- Ulmer, M. P., Adami, C., Covone, G., et al. 2005, Astrophysical Journal, 624, 124
- van Dokkum, P. G. 2001, Publications of the ASP, 113, 1420
- Vanzella, E., Calura, F., Meneghetti, M., et al. 2019, Monthly Notices of the RAS, 483, 3618
- Vanzella, E., Calura, F., Meneghetti, M., et al. 2017a, Monthly Notices of the RAS, 467, 4304
- Vanzella, E., Caminha, G. B., Calura, F., et al. 2020a, Monthly Notices of the RAS, 491, 1093
- Vanzella, E., Caminha, G. B., Calura, F., et al. 2020b, Monthly Notices of the RAS, 491, 1093
- Vanzella, E., Caminha, G. B., Rosati, P., et al. 2021, Astronomy and Astrophysics, 646, A57
- Vanzella, E., Castellano, M., Bergamini, P., et al. 2022, Astronomy and Astrophysics, 659, A2
- Vanzella, E., Castellano, M., Meneghetti, M., et al. 2017b, Astrophysical Journal, 842, 47
- Vanzella, E., Loiacono, F., Bergamini, P., et al. 2023, Astronomy and Astrophysics, 678, A173

- Vázquez, G. A., Leitherer, C., Heckman, T. M., et al. 2004, *Astrophysical Journal*, 600, 162
- Vegetti, S., Lagattuta, D. J., McKean, J. P., et al. 2012, *Nature*, 481, 341
- Veilleux, S., Maiolino, R., Bolatto, A. D., & Aalto, S. 2020, *Astronomy and Astrophysics Reviews*, 28, 2
- Verde, L., Treu, T., & Riess, A. G. 2019, *Nature Astronomy*, 3, 891
- Verhamme, A., Schaerer, D., & Maselli, A. 2006, *Astronomy and Astrophysics*, 460, 397
- Vernet, J. 2001, PhD thesis, Universite de Paris Diderot (Paris VII), France
- Vernet, J. & Cimatti, A. 2001, *Astronomy and Astrophysics*, 380, 409
- Vernet, J., Dekker, H., D'Odorico, S., et al. 2011, *Astronomy and Astrophysics*, 536, A105
- Vernet, J., Fosbury, R. A. E., Villar-Martín, M., et al. 2001, *Astronomy and Astrophysics*, 366, 7
- Vizgan, D., Greve, T. R., Olsen, K. P., et al. 2022, *Astrophysical Journal*, 929, 92
- von Soldner, J. G. 1804, *Astronomisches Jahrbuch für das Jahr 1804*, 161
- Wakker, B. P., Savage, B. D., Fox, A. J., Benjamin, R. A., & Shapiro, P. R. 2012, *Astrophysical Journal*, 749, 157
- Walsh, D., Carswell, R. F., & Weymann, R. J. 1979, *Nature*, 279, 381
- Wang, H., Cañameras, R., Caminha, G. B., et al. 2022, arXiv e-prints, arXiv:2203.13759
- Wardle, J. F. C. & Kronberg, P. P. 1974, *Astrophysical Journal*, 194, 249
- Weilbacher, P. M., Palsa, R., Streicher, O., et al. 2020, *Astronomy and Astrophysics*, 641, A28
- Welch, B., Coe, D., Zitrin, A., et al. 2023, *Astrophysical Journal*, 943, 2
- Weng, S., Sadler, E. M., Foster, C., et al. 2022, *Monthly Notices of the RAS*, 512, 3638
- Wilkins, S. M., Bunker, A. J., Stanway, E., Lorenzoni, S., & Caruana, J. 2011, *Monthly Notices of the RAS*, 417, 717
- Will, C. M. 1988, *American Journal of Physics*, 56, 413
- Wise, J., Turk, M., Norman, M., Abel, T., & Smith, B. 2012, in APS Meeting Abstracts, Vol. 2012, APS April Meeting Abstracts, D7.006
- Wise, J. H. 2019, arXiv e-prints, arXiv:1907.06653
- Wong, K. C., Suyu, S. H., Chen, G. C. F., et al. 2020, *Monthly Notices of the RAS*, 498, 1420
- Wuyts, E., Rigby, J. R., Gladders, M. D., & Sharon, K. 2014, *Astrophysical Journal*, 781, 61
- Xu, X., Heckman, T., Henry, A., et al. 2023, *Astrophysical Journal*, 948, 28
- Yamanaka, S. & Yamada, T. 2019, *Publications of the ASJ*, 71, 51
- You, C., Zabludoff, A., Smith, P., et al. 2017, *Astrophysical Journal*, 834, 182

- Zackrisson, E., González, J., Eriksson, S., et al. 2015, Monthly Notices of the RAS, 449, 3057
- Zackrisson, E., Inoue, A. K., & Jensen, H. 2013, Astrophysical Journal, 777, 39
- Zanella, A., Daddi, E., Le Floc'h, E., et al. 2015, Nature, 521, 54
- Zanella, A., Iani, E., Dessauges-Zavadsky, M., et al. 2024, Astronomy and Astrophysics, 685, A80
- Zanella, A., Le Floc'h, E., Harrison, C. M., et al. 2019, Monthly Notices of the RAS, 489, 2792
- Zanella, A., Pallottini, A., Ferrara, A., et al. 2021, Monthly Notices of the RAS, 500, 118
- Zitrin, A., Labb  , I., Belli, S., et al. 2015, Astrophysical Journal, Letters, 810, L12
- Zitrin, A., Meneghetti, M., Umetsu, K., et al. 2013, Astrophysical Journal, Letters, 762, L30
- Zitrin, A., Rosati, P., Nonino, M., et al. 2012, Astrophysical Journal, 749, 97
- Zwicky, F. 1937a, Physical Review, 51, 290
- Zwicky, F. 1937b, Physical Review, 51, 290

APPENDIX A

Appendix of “Studying the most massive early-type galaxies acting as strong gravitational lenses at intermediate redshift”

A.1 Spectra of the multiple images

We show here the 1D spectra of the multiple images of the AB source that are covered by the X-Shooter data (as described at the beginning of Section 3.3).

A.2 Spectrum of the main deflector

We show here the 1D spectrum of the main lens galaxy.

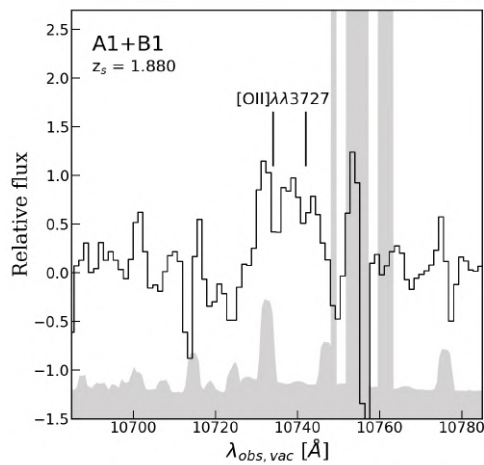


Figure A.1: X-Shooter 1D spectra of the multiple images A1 and B1. Zoom in of the wavelength range where we observe the main emission lines used to confirm the redshift measurement. The black lines are the observed spectra in units of 10^{-17} erg s $^{-1}$ cm $^{-2}$ Å $^{-1}$, and the gray regions indicate the data variance.

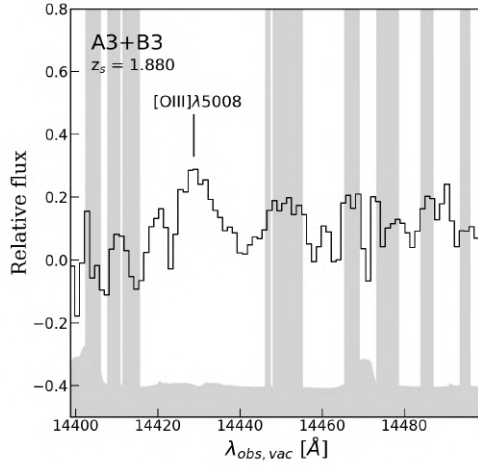


Figure A.2: X-Shooter 1D spectra of the multiple images A3 and B3. See the caption of Fig. A.1 for further details.

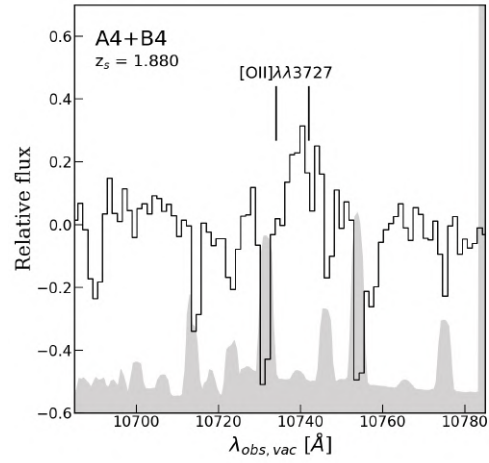


Figure A.3: X-Shooter 1D spectra of the multiple images A4 and B4. See the caption of Fig. A.1 for further details.

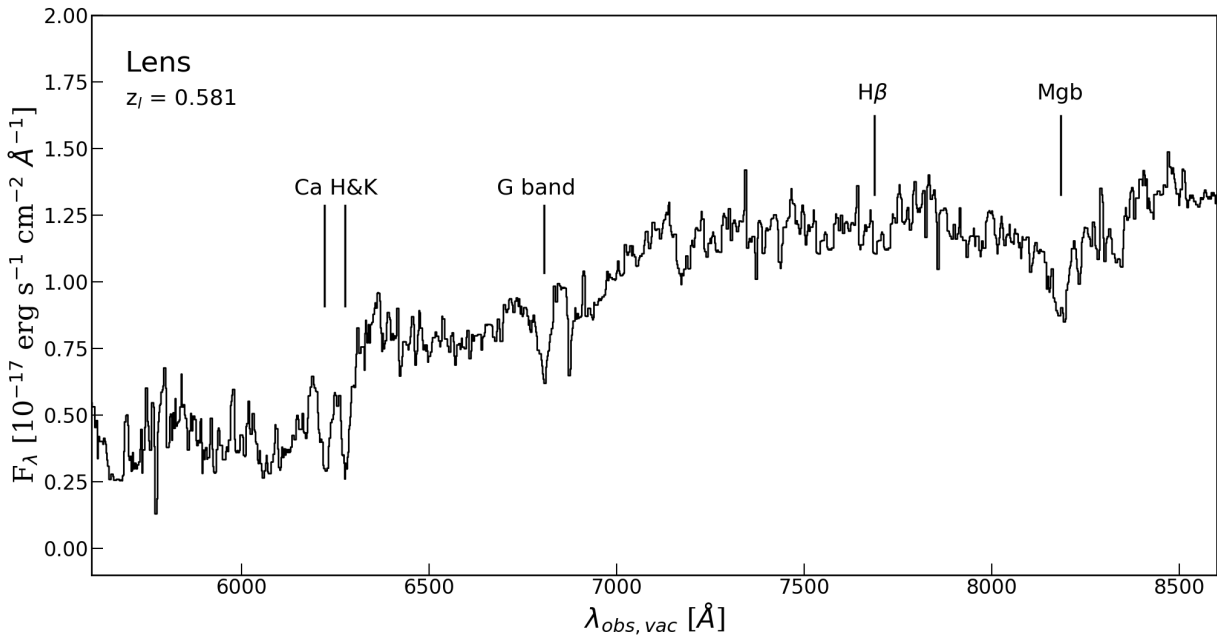


Figure A.4: X-Shooter 1D spectrum of the main lens galaxy. It is smoothed with a boxcar filter, and the most prominent spectral features are marked.

APPENDIX B

Appendix of “UV-continuum β slopes of individual $z \sim 2 - 6$ clumps and their evolution”

B.1 Location of the mock clumps in the simulation

In order to find the best combination of parameters to measure the β slope of the clumps in our sample, we test the possible presence of systematics on a sample of 50 mock clumps, placed in different locations around the lens cluster MACS J0416, as shown in Fig. B.1. They are not randomly distributed, but their positions are accurately chosen to investigate where the β measurements might be biased. In particular, we check the impact of the contribution of the ICL and of the presence on angularly close foreground bright objects. Then, we look for the best combination of A-PHOT parameters that is able to minimize the difference between the injected β slope and that measured. In particular, we test different apertures, from a diameter of $0.2''$ to $0.54''$, to switch on and off the A-PHOT local background estimation, and to manually fit the light and subtract the possible foreground contaminant and the background level with GALFIT.

B.2 Comparison with ASTRODEEP

We apply our pipeline to estimate the β slopes of our sample but making use of the photometric measurements by the ASTRODEEP collaboration (Merlin et al. 2016; Castellano et al. 2016), that detected and characterized the objects in the MACS J0416 field. Meštrić et al. (2022) cross-matched our sample with the ASTRODEEP catalog, finding 48 objects in common. The comparison with the β slopes obtained with our photometric measurements is shown in Fig. B.2.

B.3 Comparison between photometric and spectroscopic β slopes

We compare the β slopes measured with photometry and with spectroscopy for a subsample of 37 clumps, whose spectrum has $S/N \gtrsim 2$. We observe that spectroscopic ones result to be systematically redder. We explain this result by considering the contamination from some red foreground objects, the BCG, and the ICL, which are not subtracted in the MUSE datacube, unlike the HST images, and the larger aperture (photometry extracted from a $0.27''$ -diameter aperture, spectra extracted from $0.4''$ -diameter ones) that enhance this effect. We show, in Fig. B.3, that indeed, the most discordant slopes are measured for clumps angularly close to a foreground contaminant or located in the central regions of the cluster of galaxies.

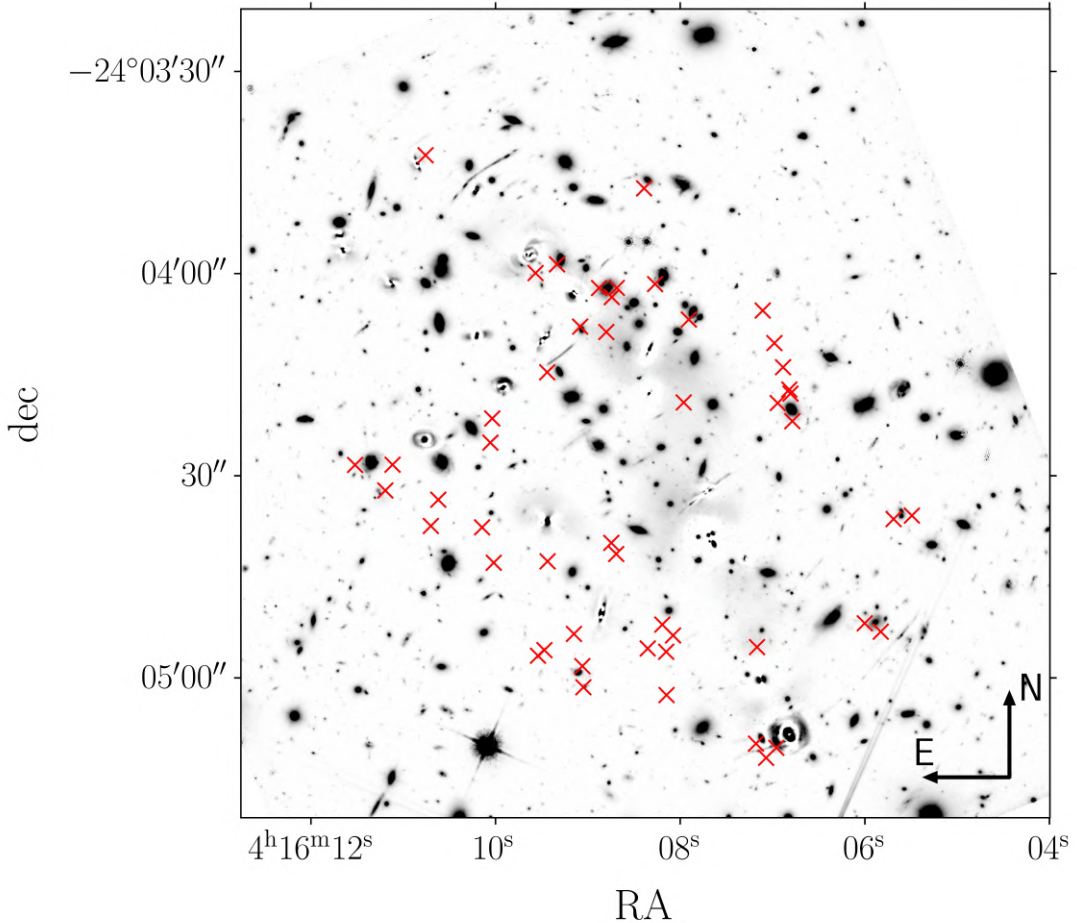


Figure B.1: Location of the 50 mock clumps (red crosses) superimposed to the F105W image of the lens cluster MACS 0416. We locate them in positions similar to those of the real clumps. Hence, we choose the outer and inner regions of the cluster, to see the possible residuals from the intracluster light removal, in isolated positions, and angularly close to a bright object, to quantify the contribution of the contamination of foreground galaxies. In this case, we put the mock clump at the same angular distance to the contaminant as that of the real clump, but in an opposite direction, to avoid the real clumps to contaminate the simulation.

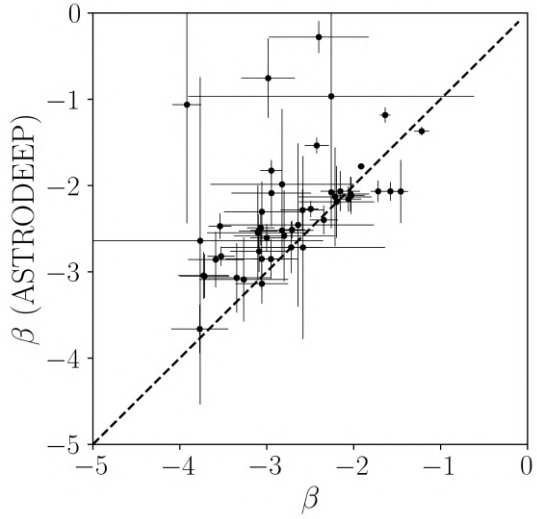


Figure B.2: Comparison between the β slopes measured with the magnitudes measured from the ASTRODEEP collaboration (y -axis) and in this work (x -axis). ASTRODEEP slopes are systematically redder (median $\Delta\beta \sim 0.24$), and thus lay above the 1:1 relation (dashed line), but they are referred to integrated galaxies extracted from larger apertures, while we isolated individual hosted clumps.

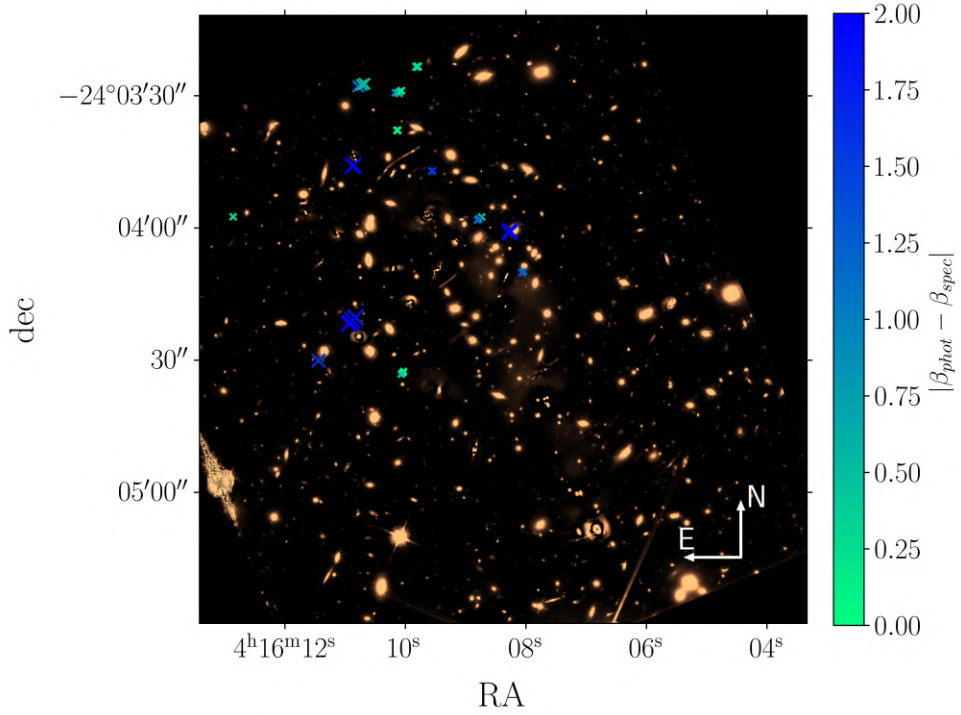


Figure B.3: Location of the 37 clumps whose spectra have $S/N \gtrsim 2$, on the $I814$ image. The marker size depends on the redshift, increasing from 1.99 to 3.29. They are color-coded following the difference between the spectroscopic (β_{spec}) and photometric (β_{phot}) β slopes. The most discrepant clumps appear angularly close to bright contaminants, which are subtracted in the photometric images but not in the MUSE datacube.

APPENDIX C

Appendix of “Constraining the geometry of the gas surrounding a typical galaxy at $z = 3.4$ with Ly α polarization”

C.1 Ly α polarization measured in the three-bin case

We show here the results obtained by dividing the Ly α line over three bins, one including the blue tail (1215.5-1216.3 Å), a central one including the peak (1216.3-1217.9 Å) and one including the red tail (1217.9-1219.6 Å). The binning is completed by sampling the blue and red continua with two bins: one narrower and closer to the line and one broader, from 1210.0 Å to 1215.5 Å, and from 1037 Å to 1210 Å for the blue, respectively, and from 1219.6 Å to 1224.0 Å, and from 1224 Å to 1260 Å for the blue, respectively. The bins are shown in the left panels of Fig. C.1. For the blue tail, central, and red tail bins, we measure 1σ upper limits on $P_{\text{Ly}\alpha}$ of 6.6%, 4.2%, and 13.1%, respectively. Due to the large dilution factor, the polarization degree is barely (not) constrained for the narrow (broad) continua bins.

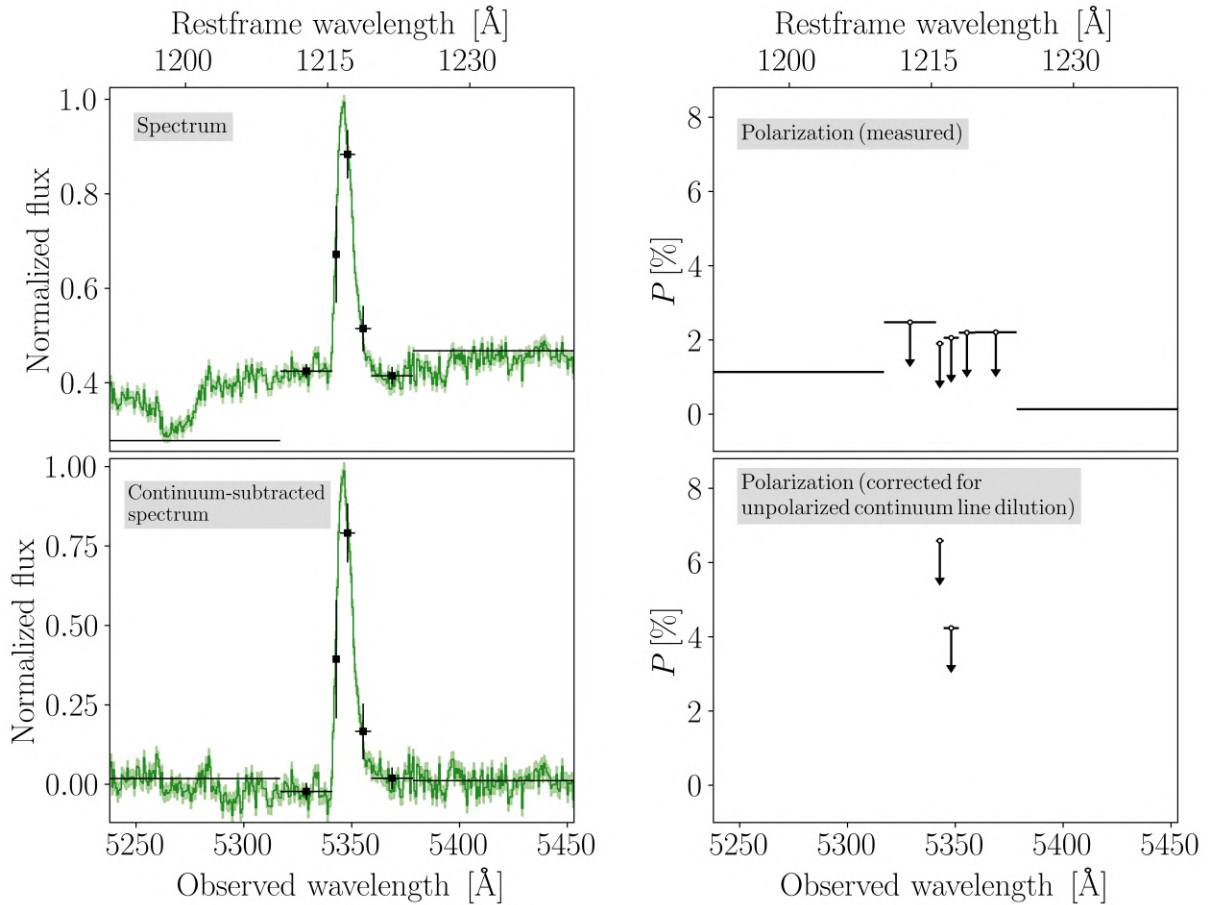


Figure C.1: Left panels: total intensity spectra (green solid line) and 1σ uncertainties (light green shaded region) in the spectral region around the Ly α line, similar to those presented in Fig. 6.2, but in the three-bin case. The top (bottom) panel shows the normalized spectrum before (after) the subtraction of the BCG contribution. The black filled squares, with 1σ uncertainties, represent the binned data. Right panels: polarization (P) measurements obtained before (top) and after (bottom) the dilution correction described in Eq. 6.1. The black open circles represent the 1σ upper limits obtained by applying the correction of [Simmons & Stewart \(1985\)](#). In the bottom right panel, only two datapoints are visible, as the others are outside the plotted range (upper limits for P from 13 to 95%).

